Simulations and Observations of Galaxies Constrained through Scaling Relations

by

Nikhil Arora

A thesis submitted to the
Department of Physics, Engineering Physics & Astronomy
in conformity with the requirements for
the degree of Doctor of Philosophy

Queen's University
Kingston, Ontario, Canada
August 2022

Abstract

Understanding galaxy formation and evolution requires robust comparisons of observations and simulations of galaxies. This thesis contrasts rich observations of galaxies with simulations (hydrodynamical and semi-analytical models, hereafter SAMs[1]) to study structural galaxy scaling relations and star formation quenching. The role of AGN feedback on galaxy quenching is studied for central galaxies at $z = 0$ through the comparison of 500,000 SDSS galaxies with SAMs (L-GALAXIES and SAGE). We find that galaxy passive fractions measured for observations and the SAGE SAMs correlate with the stellar mass of the bulge component; for the L-GALAXIES SAMs, passive fractions correlate with halo and black hole mass. Overall, SAMs do not reproduce the observed passive fractions as they fail to model the coupling between the heating and cooling of gas due to AGN feedback. We also extract and compile a multi-band photometric and environmental catalogue for ∼8000 MaNGA galaxies. The deep surface brightness profiles are extracted in a non-parametric fashion from the automated software AUTOPROFand reach depths of $28.5\,\mathrm{g}-\mathrm{mag\,arcsec^{-2}}$, $27.8\,\mathrm{r}-\mathrm{mag\,arcsec^{-2}}$ and $26.7\,\mathrm{z}-\mathrm{mag\,arcsec^{-2}}$. Non-parametric surface brightness profiles are shown to be more robust and reproducible relative to model (Sérsic or Sérsic + Exponential) dependent surface brightness profiles. As a complement to the photometric catalog,

[1]All acronyms are defined in the glossary.

rotation curves and a dynamical catalogue are also presented and used to construct multiple observed scaling relations. The latter are compared to similar scaling relations from the high-resolution NIHAO zoom-in simulations. NIHAO galaxies broadly agree with 12 observed scaling relations which the exception of those involved central surface densities (measured via Σ_1). Finally, we have also compared simulated field and LG dwarf galaxies to highlight similarities and differences. Present-day LG dwarfs show similar stellar properties to field galaxies but very different gas properties, particularly hot gas metallicities. The difference in gas metal content is the result of interactions amongst LG dwarfs which live in a higher density environment than the field. The high quality data reductions presented in this thesis will lead to further refinement of the cosmological simulations.

Acknowledgments

I believe that no achievement can occur in solitude; indeed, that is the case with the work presented here. Everything that I have accomplished in the last six years, including this document, is a result of the encouragement, inspiration, and support of many people. Firstly and most importantly, none of this would be possible without the opportunities, guidance, support, and teaching provided by my supervisor, Prof. Stéphane Courteau. It has been a pleasure to work with you and going on this journey to understand our magnificent Universe. Even though I will cherish the last six years forever, I am thrilled with the thought of being your long-term scientific collaborator and a friend.

I would also like to express my deepest gratitude towards many collaborators; Prof. Andrea Macció (my future boss), Tobias Buck, Mike Smith, Tom Jarrett, Matteo Fossati, David Wilman, Dave Hanes, Aaron Dutton, and Marvin Blank. Thank you for all providing me with valuable data, simulations, and answering my many questions. A special thanks to Prof. Sarah Sadavoy and Mark Richardson for the encouraging chats in Stirling and enthusiastic science communication; and to Prof. Philippe Di Stefano for sharing my love of soccer.

I am grateful to Queen's University and the McDonald Institute for all the resources provided to support my research. I would also like to thank Loanne Meldrum

for the random chats/helpful suggestions and being an amazing and most helpful graduate assistant. Thanks to Peggy Hauschild, Kyra Funk, Tammie Kerr, Julie McDonald, and Melissa Balson, for their assistance whenever I was lost and/or confused. You make the department work!

I am also grateful to so many friends without whom I would not have made it here. A special thank you to Dhruv Bisaria, Matt Frostt, Sean Begy, Zahra Basti, Ananthan Karunakaran, Nathalie Ouellette, Zac Kenny, Alexandra Pedersen, and Ben Tam for the countless chats, meals, drinks, and helpful career advice. Connor Stone, for being an amazing office mate (both in-person and virtual), I am really honoured to have shared this PhD experience with you. Thank you for being a valuable collaborator and an even more valuable friend. A huge thanks to my best friend, Christine Hall, for being there (through all the ups and downs) even though you were not in Kingston. A special mention to Alison and Peter Lubink (and baby Kiara) for the check-ins, walks/runs/bike rides, and really great conversations! I am extremely grateful for the friendship of Anne Fisher; thank you for daily chats, guidance, encouragements, and prayers. Thank you Akanksha Bij for making my final days in Kingston incredible! I will always remember and cherish sharing deep thoughts with you! Last, but certainly not the least, my beloved family in Kingston; Corina, Greg, and Owen MacLeod. Thank you for all the love you have shown me and being there for me. It is because of you that I will always call Kingston HOME!

יהוה יהוה אל רחום וחנון

ארך אפים

ורב הסד ואמת

Statement of Originality

Other than Chapter 2, the research presented in this thesis was completed under the supervision of Prof. Stéphane Courteau (Queen's University). Unless stated otherwise, the author (Nikhil Arora) performed all the analysis and data reduction, wrote the manuscript, and created all figures and tables. All observations and simulations were performed by others. Unless otherwise specified, co-authors provided meaningful insights into revisions of the associated manuscripts as their primary contribution.

Chapter 2 contains a version of the published paper titled *"On The Role of Supermassive Black Holes in Quenching Star Formation in Local Central Galaxies"* by Nikhil Arora, Matteo Fossati, Fabio Fontanot, Michaela Hirschmann, and David J. Wilman (Arora et al. 2019). Matteo Fossati generated the SDSS $z = 0$ data and the algorithm for selecting central galaxies. Present-day snapshots for SAGE were created with the Theoretical Astrophysical Observatory Mock Galaxy Factory[2].

Chapter 3 contains a version of the published paper titled *"MaNGA galaxy properties – I. An extensive optical, mid-infrared photometric, and environmental catalogue"* by Nikhil Arora, Connor Stone, Stéphane Courteau, and Thomas H. Jarrett (Arora et al. 2021). Connor Stone wrote the automated software AUTOPROFand Thomas H. Jarrett reduced the WISE mid-infrared data. All data products created for this

[2] https://tao.asvo.org.au/tao/mock_galaxy_factory/

project were publicly available.

Chapter 4 contains a manuscript of a paper to be submitted to the MNRAS titled *"MaNGA galaxy properties – II. A detailed comparison of observed and simulated spiral galaxy scaling relations"* by Nikhil Arora, Stéphane Courteau, Connor Stone, and Andrea V. Macció. Connor Stone helped with the algorithm for extracting rotation curves from the MaNGA velocity maps. All data from observations for this project will be publicly available through the publication.

Chapter 5 contains a version of the published paper on titled *"NIHAO-LG: The uniqueness of Local Group dwarf galaxies"* by Nikhil Arora, Andrea V. Macciò, Stéphane Courteau, Tobias Buck, Noam I. Libeskind, Jenny G. Sorce, Chris B. Brook, Yehuda Hoffman, Gustavo Yepes, Edoardo Carlesi, and Connor Stone (Arora et al. 2022). Andrea V. Macció and Aaron Dutton created the NIHAO-LG and NIHAO-LG(nmd) simulations.

Astronomy is useful because it elevates us above ourselves; it is useful because it is grand. It shows us how small is man's body, how great his mind, since his intelligence can embrace the whole of this dazzling immensity, where his body is only an obscure point, and enjoy its silent harmony.

- Henri Poincaré

Contents

List of Tables

List of Figures

Glossary

ΛCDM Cold Dark Matter Dark Energy paradigm.

μ_e The Surface Brightness (SB) of the isophote at Effective radius in units of mag arcsec^{-2}.

Σ_1^* Projected stellar mass surface density measured within a radius of 1kpc for the galaxy, in units of $M_\odot$kpc^{-2}.

AGN Active Galactic Nuclei.

AJ Astronomical Journal.

ApJ Astrophysical Journal.

AutoProf An automated software for the extraction of non-parametric surface brightness profiles from galaxy images.

Axis Ratio The ratio between the projected semi-major and minor axis of an astronomical object.

Blue Cloud Galaxy population which are actively forming stars; generally disky morphology and bluer optical colours.

CALIFA Calar Alto Legacy Integral Field spectroscopy Area.

CANDELS-GOODS-S Cosmic Assembly Near-infrared Deep Extragalactic Legacy Survey – The Great Observatories Origins Deep Survey – South.

COG Curve of Growth.

Colour The ratio of fluxes measured in two different wavebands. It is generally calculated as the difference in magnitude between filters of short a nd longer wavelengths.

DESI-LIS Dark Energy Sky Instrument Legacy Imaging Survey.

Dust Extinction The process of scattering or absorption of light from small organic particles in the galaxy. It results in loss of light along the line of sight during observation.

Dynamical Mass The total mass (baryon and dark matter) within a radius R for a galaxy. It is calculated using the virial theorem, $M(R) = V_{circ}^2 R/G$, where G is the gravitational constant and V_{circ} is the circular velocity.

Effective Radius The radius, R_e, in units of kpc, at which half the total light is enclosed.

ETG Early-Type Galaxies.

Faber-Jackson Relation An astronomical scaling relation connecting the luminosity/stellar mass and central velocity dispersion of elliptical galaxies.

Feedback The process of depositing energy into the surrounding areas due to Supermassive Black Hole (SMBH) or supernovae explosions.

Free-fall time The time taken by an object to collapse under its own gravitational attraction, given the absence of other forces.

Fundamental Plane A galaxy scaling relation that relates Effective radius, $\mu_{\rm e}$ and the velocity dispersion measure at Effective radius. This scaling relation is used for studying the evolution of elliptical galaxies.

Green Valley A transient galaxy population undergoing either quenching or re-ignition of star formation.

HI A 21 cm spectral feature created by a neutral hydrogen atom due to a spin flip of the electron; becoming anti-aligned with respect to the spin of the proton.

Hα The first Balmer emission of the Hydrogen atom, emitted at 656.281 nm. It is used to measuring galaxy Rotation Curve (RC) and Star Formation Rate (SFR).

IFU Integral Field Unit.

IMF Initial Mass Function.

Initial Mass Function An empirical formalism that describes the initial mass distribution for a population of stars.

Isophotal $\mathbf{R}_{23.5}$ A projected radius measured at a surface brightness level of 23.5 mag arcsec^{-2}.

Isophotal Radius The radius at which a threshold Surface Brightness is reached.

LG Local Group of Galaxies.

Local Group The set of galaxies which includes the Milky Way (MW), Andromeda Galaxy (M31) and approximately ∼100 dwarf galaxies.

LTG Late-Type Galaxies.

M31 Andremeda Galaxy.

MaNGA Mapping Nearby Galaxies at Apache Point.

Mass-to-Light Ratio A conversion factor that translates the amount of light coming from an object to the baryonic mass of that object. It is usually normalised to the mass-to-light ratio of the Sun.

Metallicity The abundance of elements heavier than hydrogen or helium present in an astronomical object.

MIR Mid-Infrared.

MLCR Mass-to-light Color Relation.

MNRAS Monthy Notices of the Royal Astronomical Society.

MW Milky Way Galaxy.

MZR Mass-Metallicity Relation.

NIHAO Numerical Investigation of a Hundred Astrophysical Objects.

NSA NASA-Sloan Atlas.

ODR Orthogonal Distance Regression.

Point Spread Function Mathematical characterization of the distribution of light from a point source over a large area at the detector due to blurring and atmospheric effects.

PSF Point Spread Function.

Quenching Astrophysical process whereby star formation in galaxies is terminated.

RAR Radial Acceleration Relation.

RC Rotation Curve.

Red Sequence Population of galaxies which are no longer forming stars; generally of elliptical type and with redder optical colours.

Rotation Curves A relation describing the circular velocity as a function of the projected or physical radius of the galaxy.

SAM Semi-Analytic Model.

SB Surface Brightness.

SDSS Sloan Digital Sky Survey.

SFH Star Formation History.

SFR Star Formation Rate.

SMBH Supermassive Black Hole.

SMFS Star Formation Main Sequence.

Softening Length A fix to prevent numerical divergence in the gravitational force between two particles by modifying the gravitational potential for a particle as $\Phi = -1/(r^2 + \epsilon^2)^{1/2}$ where ϵ is the softening length.

SPH Smoothed Particle Hydrodynamics.

Star Formation History A function the related the star formation rate and cosmological time for a galaxy.

Stellar Mass Function An empirical function that describes the number density of galaxies as a function of stellar mass.

STFR Stellar Tully-Fisher Relation.

Surface Brightness Profile Surface brightness (intensity per unit area) as function of galactocentric radius.

Surface Brightness The flux of light received per unit area, often measured as the magnitude received within an angular area. It has the units of $L_\odot$ kpc^{-2} or mag $arcsec^{-2}$.

Tully-Fisher Relation An astronomical scaling relation connecting the luminosity/stellar mass and the circular velocity of a galaxy.

VRM$_*$ Velocity-Radius-Stellar Mass scaling relations.

WISE Wide-field Infrared Survey Explorer.

WXSC WISE Large Galaxy Atlas and Extended Source Catalogue.

Chapter 1

Introduction

Galaxies, within the cosmological cold dark matter paradigm (ΛCDM; White and Rees 1978; White and Frenk 1991), are complex non-linear systems composed of stars, gas, dust, and supermassive black holes gravitationally bound in a halo of (putative) dark matter. These components interact with each other through a set of complex multi-scale physical processes such as star formation (Kennicutt 1998), baryonic feedback (Cattaneo 2019), adiabatic contraction (Blumenthal et al. 1984), halo expansion (Brook and Di Cintio 2015), spiral and bar formation (Sellwood and Masters 2021), and chemical evolution (Gallazzi et al. 2005). Studies of such astrophysical processes require high-quality multi-wavelength imaging and spectroscopy.

The advent of quantum efficient charged coupled devices (CCDs) has resulted in significant improvements in the measurement of fundamental properties of galaxies. Such technological advancements have paved the way for the compilation of large samples of galaxies over a wide range of stellar masses and environments. For instance, all-sky surveys such as the Sloan Digital Sky Survey (SDSS; Abdurro'uf et al. 2022), Dark Energy Sky Instrument-Legacy Imaging Survey (DESI; DESI Collaboration et al. 2016), and Wide-field Infrared Survey Explorer (WISE; Wright et al. 2010) have

yielded large multi-wavelength imaging catalogues which provide a wealth of local and global galaxy properties such as luminosity, colour, stellar mass, sizes, concentration. To complement these imaging surveys, large scale Integral Field Units (IFUs) such as Mapping Nearby Galaxies at Apache Point (MaNGA; Bundy et al. 2015), Calar Alto Legacy Integral Field spectroscopy Area (CALIFA; Walcher et al. 2014), and SAURON (Bacon et al. 2001) have also yielded spatially-resolved galaxy spectra which encode galaxy chemical and dynamical properties such as stellar ages, metallicities, dynamical mass, star formation rates.

The combination of such photometric and spectroscopic data has revealed essential information about galaxy formation and evolution theory. For example, in the parameter space of stellar mass versus star formation rates for the 500,000 observed SDSS galaxies (see Fig. 1.1), two separate populations defined by their star formation properties emerge; the blue cloud and the red sequence (Eales et al. 2018). The blue cloud, also known as the Star Formation Main Sequence (SFMS; Wuyts et al. 2013; Cano-Díaz et al. 2016; Hall et al. 2018), consists of galaxies which are actively forming stars; while the red sequence of galaxies consists of galaxies which are no longer undergoing star formation, these are fully quenched or often referred to as "red and dead" (Dressler 1980; Baldry et al. 2006). Furthermore, somewhere in the middle, the green valley is a transient population of galaxies in the process of halting star formation and terminally quenching (Schawinski et al. 2014; Salim 2014). Different astrophysical processes lead to these three galaxian populations.

The SFMS mainly consists of disky galaxies at all stellar masses residing in low density regions of the Universe. Blue cloud galaxies are gas rich, have younger stellar populations, and bluer optical colours. Feedback from star formation (Dekel and

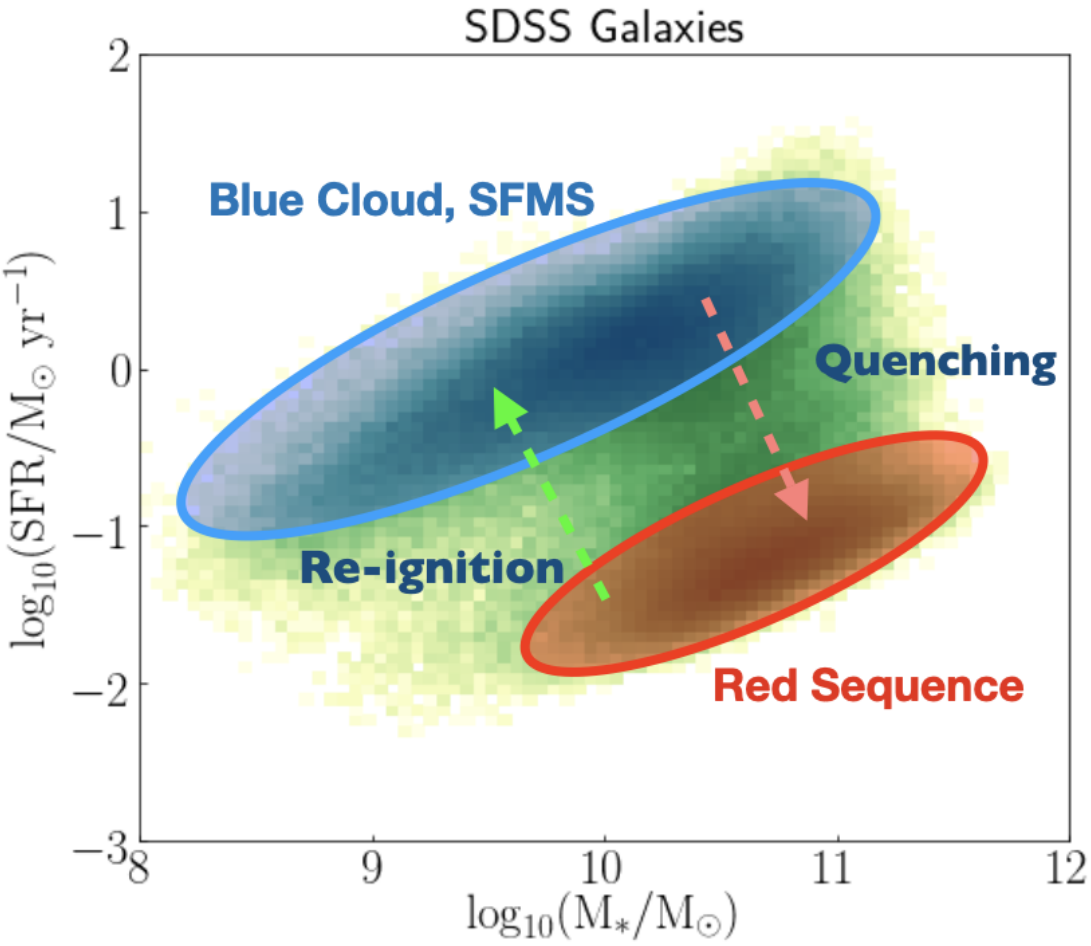

Figure 1.1: Star formation rate versus stellar mass for SDSS galaxies. The bimodal populations, blue cloud and red sequence are also visible. This figure is based on data from Wilman et al. (2010).

Silk 1986; Woods 2022) and supermassive black holes (SMBHs; Fabian 2012), plus removal of gas due to environment (Gunn and Gott 1972; Dekel et al. 2003), all lead to suppression of star formation and ultimately the red sequence of galaxies. Red sequence galaxies have elliptical morphologies, no gas, redder optical colors, and live in high density regions. Lastly, the green valley population contains galaxies "caught in the midst" of quenching (due to feedback or environment) or re-igniting

star formation (due to gas rich mergers and/or galaxy fly-bys).

Complementing such rich observations with numerical simulations of galaxies enables the refinement of our theories of cosmic structure formation. These simulations have shown that galaxies grow through hierarchical clustering, involving a multitude of physical processes over large range of physical scales within the Λ Cold Dark Matter (ΛCDM) paradigm (White and Frenk 1991; Springel et al. 2005). These processes include gravitational and hydrodynamic interactions, star formation, black hole growth and feedback processes (Somerville and Davé 2015; Vogelsberger et al. 2020). Numerical cosmological simulations can broadly be divided into two categories; the "dark-matter-only (DMO) simulations (Springel et al. 2008; Klypin et al. 2011) and the (full-blown) hydrodynamical simulations (e.g., Schaye et al. 2015; Wang et al. 2015). These simulations reproduce the co-evolution of dark matter and baryon over cosmic timescales in a comoving cosmological box resulting in a large number of galaxies at $z \sim 0$ (Pillepich et al. 2018; Davé et al. 2019; Habouzit et al. 2019). However, such cosmological simulations in a box also result in galaxies with limited mass and spatial resolution. To get high resolution galaxies, individual galaxies are selected and re-simulated with high mass and spatial resolutions to output cosmological zoom-in simulations (Wang et al. 2015; Sawala et al. 2016; Hopkins et al. 2018). These different types of cosmological simulations are presented in Fig. 1.2. Semi-Analytical Models (SAMs) also complement hydrodynamic simulations where the large-scale distribution of the Universe and baryonic properties are calculated using a set of coupled analytical differential equations (Somerville et al. 2008; Hirschmann et al. 2014; Henriques et al. 2015a; Somerville and Davé 2015; Guo et al. 2013a).

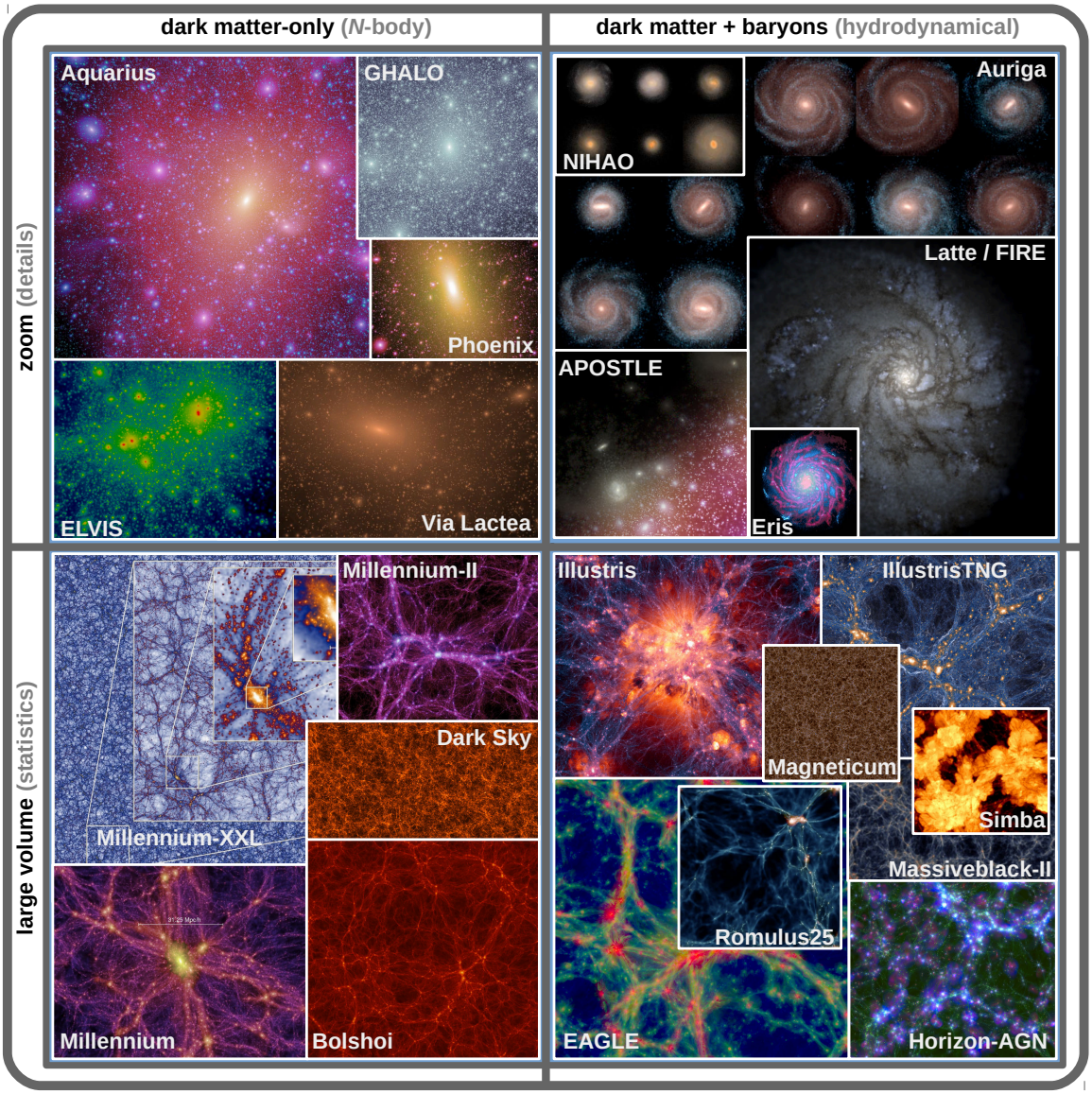

Figure 1.2: Summary of various types of cosmological simulations used for studying galaxy formation and evolution. Adapted from Vogelsberger et al. (2020)

.

Comparing observations and simulations of galaxies can reveal tantalizing information about their formation and evolution. In this thesis, we shall pay close attention to such comparisons between simulations and observations.

1.1 Comparing Observations and Theory

Various avenues can be taken to compare simulations of galaxies with observations where each path informs us about different aspects of our theory of galaxy formation and evolution. For instance, detailed comparisons involve the global and structural properties of the stellar component of galaxies ranging from early times at "cosmic noon" ($z \sim 2-3$) to the present day. One simple, yet powerful, comparison between data and models involves the distribution functions of global properties such as luminosity or stellar mass. Schechter (1976) showed that the galaxy stellar mass function can be parametrized with a simple mathematical function. At low redshifts, a double Schechter function provides a good match to the luminsoty and/or stellar mass distribution of galaxies (Baldry et al. 2006; Muzzin et al. 2013; Weigel et al. 2016). At higher redshifts, reproducing the galaxy stellar mass function through cosmological simulations is more challenging and requires processes at both the low and high mass ends preventing overcooling (which leads to unusually massive galaxies; see Croton et al. 2006). Despite these complications, large simulations broadly succeed in reproducing the stellar mass functions of galaxies at various redshifts (Schaye et al. 2015; Somerville and Davé 2015; Pillepich et al. 2018).

Another type of comparison between galaxy observations and simulations involves galaxy scaling relations which are tight correlations between key galaxy properties (Bender et al. 1992; Kennicutt 1998; Courteau et al. 2007; Hall et al. 2012; Lange

et al. 2015) such as size, luminosity and circular velocity. A wealth of information about these galaxy properties, their evolution and their physical underpinnings, can be gleaned from the slope, intercept, and scatter of those fundamental scaling relations. Some well-known galaxy scaling relations rooted in dynamics are the Faber-Jackson (FJ) and Tully-Fisher (TF) relations (Faber and Jackson 1976b; Tully and Fisher 1977b). In their original versions, they relate the total luminosity of a galaxy with a measure of internal dynamics such as either a nominal velocity dispersion or a maximum circular velocity. Modern FJ and TF representations involve the stellar (Dutton et al. 2010; Hall et al. 2012; Ouellette et al. 2017; Aquino-Ortíz et al. 2020a) and total mass of the galaxy (McGaugh 2005; Lapi et al. 2018; Stone et al. 2021a), instead of the luminosity and velocity, respectively. A complete understanding of FJ, TF, and stellar-to-total mass relations involves an intricate interplay between luminous (baryonic) and dark (non-baryonic) matter that has yet to be fully characterized (Dutton et al. 2007, 2011a; Brook et al. 2012; Macciò et al. 2012; Chan et al. 2015). More than 40 years since their inception, a detailed physical understanding of these relations still eludes us.

Another scaling relation of interest involves the galaxy colour and luminosity (Baldry et al. 2004; Peng et al. 2012). The hydrodynamical processes that regulate the formation of stars in a galaxy are imprinted in the colour-luminosity relation. While most semi-analytic and hydrodynamical simulations reproduce the star-forming part of the colour-luminosity relation rather successfully, the red sequence is either completely missed or the predicted galaxy population is much less pronounced than observations reveal (Nelson et al. 2018; Vogelsberger et al. 2020). The stellar-to-halo-mass relation as well as the colour-luminosity relation are but two of numerous galaxy

scaling relations whose fundamental understanding is ever more pressing and finally tractable with the advent of very large multi-band multi-epoch surveys of galaxies and similarly broad and more accurate cosmological simulations.

1.2 Local Group of Galaxies

Galaxy scaling relations can also be used to understand the various overall galaxy property distributions, such as the impact of environment. For instance, one wishes to know if galaxy properties, and thus scaling relations that are inferred from them, change as a function of time and environment. Cosmological simulations can help us address the latter question.

It is now well-known that galaxies in a dark matter, dark energy dominated Universe evolve through complex paths that involve hierarchical merging and secular evolution. As a result, galaxies often cluster in groups of different mass and size. This is indeed true of our "Local Group" of galaxies which consists of two massive galaxies, our Milky Way (MW) and Andromeda Galaxy (M31), along with a set of ~ 60 dwarf galaxies. Due to its proximity, our Local Group offers an ideal laboratory for testing out models of galaxy formation and evolution, especially at the low mass end of the stellar mass function. These dark-matter-dominated dwarf galaxies (McConnachie 2012) provide critical tests of the ΛCDM paradigm of galaxy formation and evolution and the particle nature of dark matter itself (Ackermann et al. 2015).

Observations of Local Group analogs of galaxies also show a diversity of star formation histories along with unique stellar kinematics, gas content, and stellar substructure (Dolphin et al. 2005; Spekkens et al. 2014; Gallart et al. 2015; Cicuéndez and Battaglia 2018). These results suggest a range of baryonic accretion modes for

the MW and M31 as well as pre-enrichment processes for dwarf galaxies. For instance, many simulations predict the existence of two distinct metallicity populations (Gottloeber et al. 2010b; El-Badry et al. 2016; Genina et al. 2019), however numerous physical explanations have been proposed to explain them. Of interest to us are the effects, if any, that the environment has in shaping the dwarf populations in the Universe. Along with comparing simulations and observations of galaxies, we must also compare simulated galaxies found in the field and in the Local Group. This experiment would highlight the similarities and differences created in dwarf galaxy properties as a result of the environment of the Local Group.

1.3 Goals of the Thesis

The goal of this thesis is to present various comparisons between simulations and observations of galaxies. To facilitate such comparisons, we present a new analysis of observed data from all-sky galaxy surveys which allows us to extract intrinsic galaxies properties. These latter can then be compared with similar properties extracted from cosmological simulations and semi-analytic models to refine our understanding of galaxy formation and evolution. In this thesis, these comparisons enable a better understanding of star formation quenching, galaxy structural properties (such as size, stellar mass, and velocity) and the role of environment.

1.4 Outline

This thesis, which includes various comparisons between numerical models and observations of galaxies to understand a range of astrophysical processes, is presented in the following way: in Chapter 2, we compare SDSS data with SAMs to explore

the effects of AGN feedback in massive central galaxies in the local Universe. This study highlights the importance of accurate implementation of the heating and cooling of gas within simulations. In Chapter 3, a multi-wavelength photometric and environmental catalogue is presented for the MaNGA galaxy survey. The optical *grz* imaging for the catalogue were obtained through the DESI legacy imaging while the mid-infrared imaging was retrieved using WISE. The photometry was performed using the automated non-parametric software AutoProf (Stone et al. 2021b). Chapter 4 complements the photometric catalogue for the MaNGA galaxies with rotation curves and dynamical catalogues extracted and compiled by us. In this chapter, the use of multiple global and spatially-resolved galaxy properties and scaling relations enables a unique comparison between observed MaNGA and simulated NIHAO galaxies. Chapter 5 comments on the uniqueness of the dwarf galaxies in the Local Group (LG) using the NIHAO simulation-suite. Field dwarfs from NIHAO projects are compared from new constrained LG simulated dwarfs to highlight the role that environment plays in shaping the dwarf population in the Universe. We conclude in Chapter 6 with a summary of our results and a discussion of future related investigations.

Chapter 2

Quenching of Central Galaxies in the Local Universe

2.1 Preamble

This chapter contains a version of a paper titled **"On The Role of Supermassive Black Holes in Quenching Star Formation in Local Central Galaxies"** (Arora et al. 2019). This project was initiated during the late stages of the author's Bachelor's degree. However, substantial changes were made between the original version and what appears herein. In this work, state-of-the-art semi-analytic models (SAMs) were compared with observed data to examine the role of black holes in the quenching of star formation in present-day central galaxies. It was found that SAMs fail to reproduce the observed fraction of passive central galaxies due to the inadequate (incomplete) modelling of the coupled heating and cooling processes of the interstellar gas.

2.2 Abstract

We analyse the role of AGN feedback in quenching star formation for massive, central galaxies in the local Universe. In particular, we compare the predictions of two semi-analytic models (L-GALAXIES and SAGE) featuring different schemes for AGN feedback, with the SDSS DR7 taking advantage of a novel technique for identifying central galaxies in an observational data set. This enables us to study the correlation between the model passive fractions, which is predicted to be suppressed by feedback from an AGN, and the observed passive fractions in an observationally motivated parameter space. While the passive fractions for observed central galaxies show a good correlation with stellar mass and bulge mass, passive fractions in L-GALAXIES correlate with the halo and black hole mass. For SAGE, the passive fraction correlates with the bulge mass as well. Among the two models, SAGE has a smaller scatter in the black hole–bulge mass ($M_{\rm BH} - M_{\rm Bulge}$) relation and a slope that agrees better with the most recent observations at $z \sim 0$. Despite the more realistic prescription of radio-mode feedback in SAGE, there are still tensions left with the observed passive fractions and the distribution of quenched galaxies. These tensions may be due to the treatment of galaxies living in non-resolved substructures and the resulting higher merger rates that could bring cold gas which is available for star formation.

2.3 Introduction

The interplay between gravitational and hydrodynamic processes dictates the formation and evolution of galaxies in the Universe. Large amounts of dark matter, through gravitational interactions, form haloes that provide a gravitational potential for the baryons (gas and stars) to fall towards their cores. This gas, through

its self-gravity and radiative processes, cools down to form compact clouds that lead to the formation of stars, forming extended structures called galaxies that evolve in time through gravitational and hydrodynamic interactions (White and Frenk 1991). It is now widely accepted that the formation of galaxies and clusters of galaxies occurs through hierarchical clustering of matter in the Λ Cold Dark Matter(ΛCDM) paradigm (White and Rees 1978; White and Frenk 1991). With respect to the hydrodynamic processes, galaxies can be broadly split into two categories; star-forming galaxies which appear blue in the sky and quiescent galaxies that are red and do not form stars at present times (Dressler 1980; Baldry et al. 2006). This bimodality in population is evident in a relation that connects the star formation rate (SFR) and the stellar mass of the galaxy (Whitaker et al. 2012; Cano-Díaz et al. 2016; Santini et al. 2017). The star-forming galaxies lie on a tight relation whereas the quiescent galaxies form a population below the relation.

'Quenching', i.e. the combination of physical and dynamical processes leading to the fast decrease of star formation activity in a galaxy and its removal from the SFR–stellar mass relation, as a function of various galaxy structural and dynamical parameters have been widely studied over the past few decades. Using Sloan Digital Sky Survey (SDSS) data, it has been demonstrated that the galaxy colour bimodality strongly depends on stellar mass and the environment (Baldry et al. 2006; Wilman et al. 2010; Peng et al. 2010, 2012). In particular Bluck et al. (2014b) show fraction of passive galaxies ($f_{passive}$) as a function of stellar mass with the bulge mass. Using the tight relation between the bulge mass and supermassive black hole (SMBH) mass reported in Häring and Rix (2004), Bluck et al. (2014a,b) argue that $f_{passive}$ should depend on the black hole mass and hence the active galactic nuclei (AGN) luminosity.

Whitaker et al. (2017), with 3D-HST data, studied the relationship between the SFR, galaxy sizes and central densities for high-redshift galaxies. They find that galaxies with high central densities are red and have lower specific star formation rate sSFR(= SFR/M_*) whereas galaxies with low surface central density are blue and have, on average, higher sSFR.

In theoretical models of galaxy formation within a ΛCDM Universe, massive galaxies reside the center of galaxy groups and clusters. At late times, such systems are supposed to grow in mass through accretion from cooling flows which fuels star formation. These cooling flows would lead to continuous growth, making central galaxies more massive and compact (high seŕsic indices) (Croton et al. 2006; Donzelli et al. 2011; Cooper et al. 2015). This is in contrast with the observed galaxy stellar mass function (SMF) and luminosity function which depicts a knee at the high mass end (Benson et al. 2003; van Daalen and White 2017). This cut-off at high mass suggests the presence of a mechanism that either removes the gas or prevents it from cooling down, making galaxies red and dead. A number of physical mechanisms have been proposed to explain how quenching of star formation is ensued and sustained in galaxies. At their core, these mechanism involve either heating, ionizing or stripping the gas from the galaxy (Gabor et al. 2010). For massive galaxies, called central galaxies, the SMBH plays a critical role in regulating/halting star formation. The energy created by the SMBH, referred to as AGN feedback, has the potential to heat, ionize or eject the cold gas from the galaxy (Somerville and Davé 2015; King and Pounds 2015).

The energy and momentum output from an SMBH, called AGN feedback, can

affect the gas in three ways; heating the gas (thermal feedback); ionizing or photo-dissociate the gas (radiative feedback); or ejecting the gas through the presence of hot gas bubbles, winds, or jets (mechanical feedback Somerville and Davé 2015). Di Matteo et al. (2005) and Springel (2005) carried out 3D simulations of AGN feedback and showed that depositing 5 per cent of the AGN bolometric luminosity in the surrounding gas particles can lead to very strong galactic outflows that halt the black hole growth and remove almost all gas from the galaxy, quenching star formation. These simulations lacked cosmological initial conditions and consider the sole case of a binary galactic merger of ideal disc galaxies with no hot gas haloes. However, these simulations still produce self-regulated Black Hole growth and tight $M_{BH} - \sigma$ relation, which matche observations (Tremaine et al. 2002; Beifiori et al. 2012).

Semi-analytic models (SAMs) have also developed schemes to apply separate prescriptions of radiative feedback through winds and radio-mode feedback through jets. In a landmark study, Croton et al. (2006) introduced two modes of AGN feedback: quasar mode where the accretion is comparable to the Eddington limit and radio-mode with radiatively inefficient accretion. The energy output from radio-mode feedback is then used to regulate BH growth and create a hot gas halo. Recipes for AGN feedback differ from model to model but Somerville and Davé (2015) identified some common features in AGN feedback schemes for different models. All BHs grow through cooling flows that results in accretion of hot and cold gas. BH accretion is simulated through instabilities created in the disc or due to mergers, where accretion is radiatively efficient. Radiatively inefficient accretion leads to low-energy jets. The energy output by these low-energy jets are proportional to the mass of the BH and is used to offset cooling flows and govern heating of the gas (Croton et al. 2006; Somerville

et al. 2008; Fontanot et al. 2006, 2011; Guo et al. 2013a; Hirschmann et al. 2014, 2016). The heating and cooling processes of the gas in these SAMs are calculated independently and hence are decoupled. Croton et al. (2016) proposed a coarse way to couple the above mentioned heating and cooling processes. They assume that cold gas is heated by the AGNs within a radius rheat which is proportional to the heating and cooling rates. The gas in that region never cools again.

Observational evidence for AGN feedback is still very weak. Brightest cluster galaxies (BCG) offer the best evidence for the presence of AGNs. Without feedback BCGs would go through more star formation events (Fabian 2012). X-ray observations of central cluster galaxies point to the presence of hot gas atmospheres that have very large cooling times which are associated with mechanical feedback from AGN activity (Fabian 1994; Hogan et al. 2017).

It is also possible to quench massive isolated galaxies due starvation of gas. Galaxies with $M_* > 10^{11}\,M_\odot$ seem to have lower fraction of neutral hydrogen, $f_{\rm HI} \equiv \log_{10}(M_{\rm HI}/M_*) < -2$ (Huang et al. 2012). These galaxies are expected to have low star formation activity. Furthermore, galaxies with massive bulges have discs which have a high Toomre Q parameter which prevents neutral gas collapse leading to morphological quenching (Kennicutt 1989; Martig et al. 2009). Bitsakis et al. (2019) used the CALIFA (Walcher et al. 2014) galaxies to show that systems with bulge-to- total luminosity ratios greater than 0.2 are predominantly found to be quenched.

The aim of this paper is to study how SMBH processes control quenching of star formation in central galaxies in the local Universe. For such a task, a pure and comparable selection of massive central galaxies from SAMs and observational data is of the utmost importance. To uniformly select central galaxies from both SAMs and

observational data, we apply a modified techniques developed in Fossati et al. (2015) of assigning stellar mass ranks within a cylindrical aperture. For these centrals, we calculate the fraction of quenched galaxies within a given bin. It has been reported that such quenched fractions depend very strongly on the stellar mass ($M_{\rm stellar}$) and the dark matter halo mass ($M_{\rm halo}$). However, due to the strong correlation between the two quantities (Matthee et al. 2017; Gu et al. 2016) and the complexities involved in calculating $M_{\rm halo}$ for observational galaxies, a new, more observationally motivated parameter is needed. The projected density (number of neighbours in a cylindrical aperture) can be calibrated easily and correlates strongly with the $M_{\rm halo}$ at fixed stellar mass (Hogg and SDSS Collaboration 2003; Kauffmann et al. 2004a; Croton et al. 2005; Wilman et al. 2010). Therefore, we will also test the trends of the passive fractions for central galaxies in a more observationally motivated parameter space which includes stellar mass and density of neighbours in a cylindrical aperture.

This chapter is structured in the following way. In Section 2.4, we describe the galaxy formation models we use accompanied with a detailed description of cooling modes and AGN feedback prescriptions which is followed by describing the observational data, the SDSS(DR7), section 2.5. In Section 2.6, we discuss the parameter space that can uniformly be used between observations and SAMs to study star formation quenching. We also describe the algorithm implemented to select massive central galaxies from both model and observed galaxies. Section 2.7 presents passive fraction in central galaxies and its correlation with various halo driven and baryonic driven galaxy properties. In Section 2.8, we discuss the black hole-bulge mass relation and star formation quenching in that parameter space. Finally, Section 2.9 presents the conclusions and the global interpretation of our results.

2.4 Galaxy Formation Models

For this study, we use the SAMs provided in (Henriques et al. 2015b, hereafter H15) and (Croton et al. 2016, hereafter C16). Both SAMs adopt an AGN feedback prescriptions that correspond to an improved version of Croton et al. (2006) model. In this section, we briefly describe the updates to the galaxy formation models and the radio-mode AGN feedback prescriptions.

2.4.1 L-GALAXIES

We start with the version of Munich SAM described in H15 which is an update of the model of Guo et al. (2013a). The galaxy formation model has been implemented on Millennium (Springel et al. 2005) and Millennium-II (Boylan-Kolchin et al. 2009) dark matter simulations to achieve a range of 5 order of magnitudes in stellar masses ($10^7 M_\odot < M_* < 10^{12} M_\odot$). Model galaxy outputs match the abundance of galaxies and their passive fraction from $z = 3$ to $z = 0$. H15 adopt the Planck Collaboration et al. (2014) cosmology; $\sigma_8 = 0.829$, $H_0 = 67.3$km s^{-1}, $\Omega_\Lambda = 0.685$, $\Omega_m = 0.315$, $\Omega_b = 0.0487$ ($f_b = 0.155$) and $n = 0.96$. The Munich SAM has updated treatment of the baryonic processes to address two problems; (1) very early formation and quenching of low-mass galaxies and (2) large fraction of massive galaxies still forming stars at low redshift. These problems are solved by delaying the reincorporation of the wind ejecta, lowering the threshold surface density of cold gas for star formation eliminating ram pressure stripping in haloes with mass less than $M \sim 10^{14} M_\odot$. Furthermore, H15 uses radio-mode AGN feedback scheme from Croton et al. (2006) to efficiently suppress gas cooling and star formation at lower redshift.

Radio-mode feedback

Previous versions of Munich SAMs used the same radio-mode feedback prescription as in Croton et al. (2006). However, the feedback model still results in a large amount of massive star-forming systems $z = 0$ (Henriques et al. 2013). In H15, the radio-mode feedback is modified to suppress cooling and star formation more efficiently at late times. The continual accretion of hot gas from the host galaxies is formulated to be

$$\dot{M}_{BH,R} = k_{AGN} \left(\frac{M_{hot}}{10^{11} M_{\odot}} \right) \left(\frac{M_{BH}}{10^{8} M_{\odot}} \right). \tag{2.1}$$

In Eq. 2.1, M_{hot} is the hot gas mass and M_{BH} is the mass of the black hole in the host galaxy, k_{AGN} is the normalization of the radio-mode feedback with a value of 5.3×10^{-3} $M_{\odot} yr^{-1}$ (see H15).

The accretion of material on to the SMBH results in energy injected into the halo in the form of jets. The energy in the jets is

$$\dot{E}_{radio} = \eta \dot{M}_{BH,R} c^2, \tag{2.2}$$

where $\eta = 0.1$ is efficiency parameter and c is the speed of light. The energy from the jet modifies the cooling rate of the gas disc by

$$\dot{M}_{cool,eff} = \max[\dot{M}_{cool} - 2\dot{E}_{radio}/V^2_{200c}, 0]. \tag{2.3}$$

These jets add hot gas to the surrounding suppressing cooling and therefore star formation. These massive systems use up all the available cold gas and then can no longer accrete cold gas, leading to quenching.

2.4.2 SAGE

C16 presented the Semi-Analytic Galaxy Evolution (or SAGE) model which is an update of the SAM presented in Croton et al. (2006). The galaxy formation model updates a number of physical prescriptions: gas accretion, ejection due to feedback, reincorporation via the galactic fountain, gas cooling-radio mode AGN heating cycle, quasar mode AGN feedback, treatment of gas in satellite galaxies, galaxy merger, and disruption and build-up of intra-cluster stars. For this study, we use a galaxy catalogue from the Theoretical Astrophysical Observatory (Bernyk et al. 2016)[1] where SAGE is applied to the Millennium simulation (Springel et al. 2005) with WMAP-1 cosmology (Spergel et al. 2003); $\sigma_8 = 0.9$, $H_0 = 73.0\text{km s}^{-1}$, $\Omega_\Lambda = 0.75$, $\Omega_m = 0.25$, $\Omega_b = 0.045$ ($f_b = 0.17$) and $n = 1.0$. The fiducial parameters are constrained primarily to the stellar mass function at $z = 0$ from Baldry et al. (2008). Furthermore, a secondary set of constraints are applied using the star formation rate density history (Somerville et al. 2001), the baryonic Tully-Fisher relation (Stark et al. 2009), the mass-metallicity relation (Tremonti et al. 2004) and the black hole-bulge mass relation (Scott et al. 2013).

Another important feature to note in SAGE is the treatment of galaxies whose parent dark matter substructures are lost below the mass resolution limit of the Millennium Simulation (i.e. the so-called orphan galaxies). SAGE does not follow the evolution of such a population, but it is assumed that these objects are instantaneously disrupted due to tidal interactions. The stellar mass from the disrupted galaxy is added to either the intra-cluster component or gets added to the central galaxy. This decision depends on duration of survival of the subhalo with respect to the average

[1] https://tao.asvo.org.au/tao/

for a subhalo of its general properties. Such a treatment can result in substantially altering the stellar masses of central galaxies and consequently the shape of the Stellar Mass Function (C16, Knebe et al. 2018). The reader is referred to C16 for further details.

Radio-mode feedback

Radio-mode feedback prescription in SAGE is an update from the model presented in Croton et al. (2006). The accretion rate of hot gas onto the SMBH follows a Bondi-Hoyle formulation (Bondi 1952) and is only a function of the local temperature and the mass of the SMBH:

$$\dot{\mathrm{M}}_{\mathrm{BH,R}} = \kappa_{\mathrm{R}} \frac{15}{16} \pi \mathrm{G}\ \overline{\mu} \mathrm{m_p} \frac{\mathrm{kT}}{\Lambda} \mathrm{M_{BH}}. \tag{2.4}$$

In Eq. 2.4, κ_{R} is the 'radio-mode efficiency' parameter with a value of, $\overline{\mu}\mathrm{m_p}$ is the mean particle mass, T is the local temperature and $\Lambda = \Lambda(\mathrm{T}, \mathrm{Z})$ is the gas cooling function that depends on the temperature and the metallicity. Using Eq. 2.2, we can use the accretion rate to calculate the luminosity of the SMBH. The accretion on to the black hole acts as a heating mechanism for the gas and the heating rate for the radio-mode feedback can be quantified as

$$\dot{\mathrm{M}}_{\mathrm{heat}} = \frac{\dot{\mathrm{E}}_{\mathrm{radio}}}{0.5 \mathrm{V}^2_{\mathrm{vir}}}, \tag{2.5}$$

where the numerator is the luminosity of the black hole given by Eq. 2.2 and the denominator represents the specific energy of the gas in the halo.

The biggest update on the SAM from Croton et al. (2006) is the coarse coupling of the heating and cooling mechanism of the halo gas. C16 defines a heating radius,

R_{heat}, inside which the gas never cools. At this radius, the energy injected by radio-mode feedback is equal to the energy the halo gas would loose to cool on to the galaxy disc. In this coupled heating-cooling cycle, the cooling rate of gas becomes

$$\dot{M}'_{cool} = \left(1 - \frac{R_{heat}}{R_{cool}}\right)\dot{M}_{cool}. \tag{2.6}$$

In Eq. 2.6, R_{cool} is the cooling radius such that

$$\dot{M}_{cool} = \frac{1}{2}\left(\frac{R_{cool}}{R_{vir}}\right)\left(\frac{M_{hot}}{t_{cool}}\right). \tag{2.7}$$

In this case, gas can only cool between R_{heat} and R_{cool} and if $R_{heat} > R_{cool}$, cooling of gas is quenched. The heating radius in the model is only allowed to increase in size in order to retain memory of previous heating episodes.

2.4.3 Choice of SAMs

The two SAMs we employ in this study are representative of the different codes used in the literature (see Knebe et al. 2018 for a comparison between different SAMs) and their predictions are easily available through web interface. Moreover, these two SAMs are well suited for our purposes, i.e. quantifying the impact of radio-mode AGN feedback on the onset of the passive fraction of observed galaxies.

These two codes, although both starting from the original Croton et al. (2006), represent quite different approaches to the implementation of radio-mode AGN feedback. On the one hand, L-GALAXIES still employs a phenomenological prescription whose main aim is to reproduce the high-mass end of the SMF by quenching the cooling flows expected at the centre of massive dark matter haloes. In H15, there is no attempt to model the details of the gas accretion on to the central SMBH, but the

main dependencies of radio-mode luminosities as a function of macroscopic quantities such as the hot gas and/or the SMBH mass. A number of different SAM codes share the same approach (like Bower et al. 2006, De Lucia and Blaizot 2007 and Guo et al. 2011).

On the other hand, SAGE employs a more physical approach to gas accretion, trying to account for the detailed physics of the coupled gas cooling-heating cycle. The C16 model is representative of an approach that has been considered (although in different frameworks and with different levels of sophistication) also by Monaco et al. (2007), Somerville et al. (2008) and Fanidakis et al. (2011).

Therefore, the comparison between these two models provides us with valuable insights on the effect of these two approaches on the overall galaxy population, while keeping the number of models to a manageable number.

2.5 Observational Data

For comparison to our galaxy formation models, we use a SDSS-DR7 (Abazajian et al. 2009) data set. The observed data is built with a modified catalogue from Wilman et al. (2010) which is drawn from the SDSS-DR7 sample. The data sets provide the number of neighbours for every primary galaxy in a cylindrical aperture of different projected radii ranging between 0.1–3.0 Mpc. To ensure that the sample is volume complete, we limit the data set to r-band absolute magnitude of $M_r \leq -20$ and a depth of $z \leq 0.08$. Furthermore, in order to account for the 'missing galaxies' due to Malmquist bias, each galaxy is assigned a weight that is the ratio between the maximum volume in which these galaxies could be observed over the volume of the whole sample. Using these weights, we calculate the passive fraction within a bin as

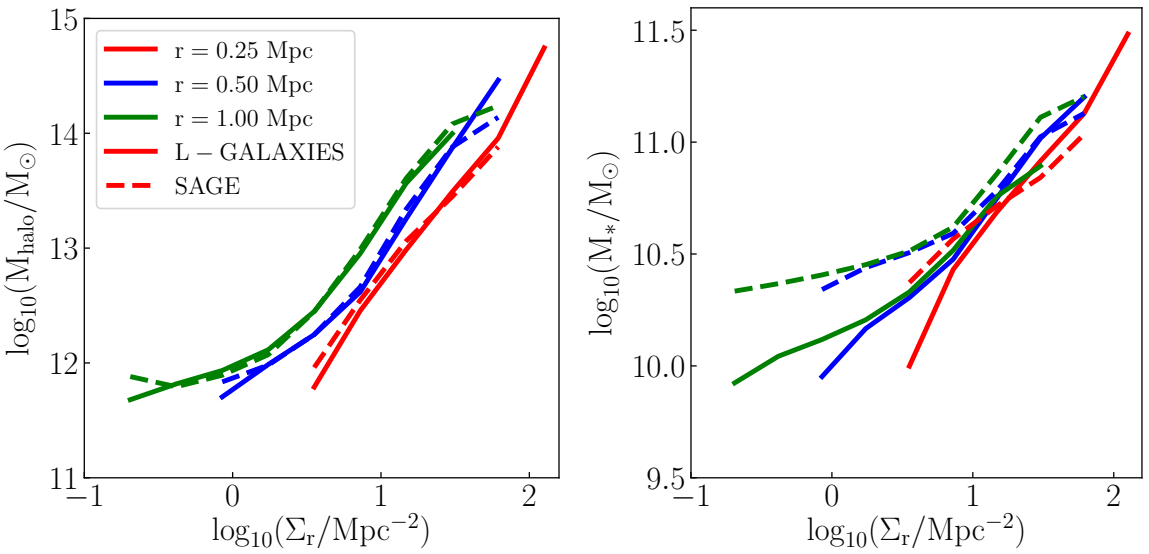

Figure 2.1: Median dark matter halo mass (left-hand panel) and stellar mass (right-hand panel) as a function of neighbour density for various aperture sizes (different colours) at $z = 0.0$. The solid lines show central galaxies from L-GALAXIES and dashed lines show central galaxies from SAGE.

$$f_{pass} = \frac{\Sigma w_{pass}}{\Sigma w_{all}}. \tag{2.8}$$

In order to select passive galaxies, we use specific star formation rates defined as $sSFR = SFR/M_*$. A system is defined to be passive if $sSFR < 0.3t_{hubble}^{-1} \approx 10^{-11} yr^{-1}$ (Franx et al. 2008; Hirschmann et al. 2014). The stellar masses and star formation rates are obtained by cross-correlating the sample with the MPA-JHU catalogue (Kauffmann et al. 2003; Brinchmann et al. 2004).

2.6 Selection of the Parameter Space and Central Galaxies

For a fair comparison between the observed and simulated galaxies, with respect to the star formation suppression, an observationally motivated parameter space is

critical. In the ideal case, star formation quenching should be studied in the stellar mass–halo mass parameter space. Properties such as star formation rates, optical sizes of galaxies are sensitive to their own growth history and therefore correlate strongly with stellar mass. Similarly, dynamic properties such as maximum circular velocity, virial velocity scale with the dark matter halo mass. However, using the stellar mass - halo mass parameter space comes with two disadvantages. Firstly, the strong degeneracy between stellar mass and halo mass (Yang et al. 2008) making it difficult to decide which parameter dominates passive fractions. Furthermore, estimating the dark matter halo mass for a large number of galaxies can only be done indirectly and is accompanied by large uncertainties.

Both obstacles can be avoided by using a parameter that is observationally motivated and correlated with halo mass. For this study, we analyse the passive fractions in an observationally motivated parameter space of stellar mass–neighbour density. The neighbour density is a measure of the local environment and correlates strongly with halo mass. We calculate the neighbour density for our model galaxies in a similar fashion to Wilman et al. (2010) and Fossati et al. (2015). This allows us to study the impact of environment on various galaxy properties. For a galaxy, the neighbour density is calculated to be

$$\Sigma_R = \frac{N_R}{\pi R^2}. \tag{2.9}$$

These densities are calculated within a projected aperture at various radii, R, ranging from $0.1 - 3.0$Mpc. Galaxies are counted as neighbours if they fall within the said aperture and their Hubble flow velocities are within a velocity width of $dv = \pm 1500$ km s^{-1}. In this framework, galaxies with $N_R = 0$ are considered isolated

systems. Isolated systems are given an arbitrary value that is equal to the half the minimum density for galaxies that have neighbours; to ensure they are represented on a logarithmic scale.

Fig. 2.1 shows the median halo mass (left-hand panel) as a function of the density in apertures of various projected radii (various colours) for central galaxies as defined from the simulation. The two different galaxy formation models are shown using different line styles. The strong correlation between environment and halo mass is seen for both SAMs which is due to the fact that both were run using the millennium simulations. Lower density environment trace lower halo masses. This is expected as higher mass create a deeper gravitational potential which leads to a denser environment. In the local Universe, halo mass as a function of environment is independent of the aperture size.

The right-hand panel in figure Fig. 2.1 shows the median stellar mass of central galaxies as a function neighbour density for various aperture radii. Like with halo mass, we notice a strong correlation between stellar mass and density. Galaxies with large stellar masses live in dense environment. At low densities, SAGE produces higher stellar mass galaxies than L-GALAXIES by ~ 0.3 dex even though the median halo mass is comparable. The reason for this higher stellar mass is suspected to be the merger rate and the treatment of the orphan galaxies discussed in Section 2.4.2. Another reason for the disagreement might be a weak stellar feedback prescription allowing for the gas to cool down in low-density environment to form stars. However, a complete analysis of this problem is out of the scope of this study.

For selecting central galaxies from both models and observations, we use a modified scheme of mass ranks within a cylindrical aperture presented in Fossati et al. (2015).

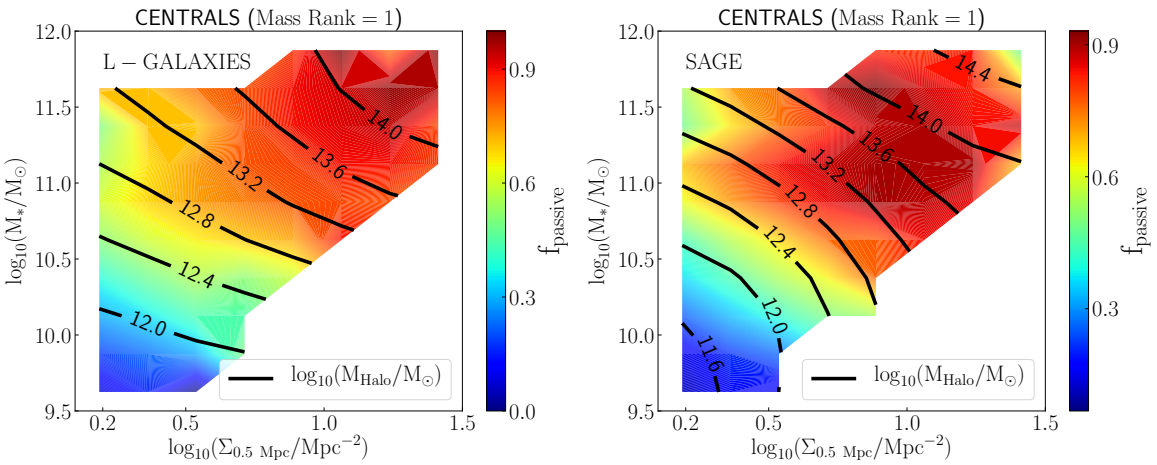

Figure 2.2: Passive fractions in the $M_* - \Sigma_r$ parameter space for L-GALAXIES (left-hand panel) and SAGE (right-hand panel). We use 0.5 Mpc aperture for calculating the neighbour density for model galaxies. The passive fractions are shown for central galaxies that are selected by assigning mass ranks using the adaptive aperture $r(8, 2.5, 2000)$. The contours presented on both panels represent the median halo mass in each bin in log space.

We refer the interested readers to the Appendix 2.10 for more details in the adopted scheme and its differences with respect to Fossati et al. (2015). The depth of the cylinder is selected in velocity space and the radius in calculated using Eq. 2.10. For both SAMs and observations, we use the adaptive aperture with $n = 8$, $r_{\rm max} = 2.5$ Mpc and $v_{\rm depth} = 2000$km s^{-1} to select central galaxies for the rest of the study. The choice of these parameters provide a balance between the completeness of the selections and its purity.

2.7 Passive Fractions in Galaxies

2.7.1 Dependence on Halo Mass

We start with a discussion about the behaviour of passive fractions for central galaxies as a function of stellar mass, halo mass and galaxy density (Fig. 2.2). We see that most

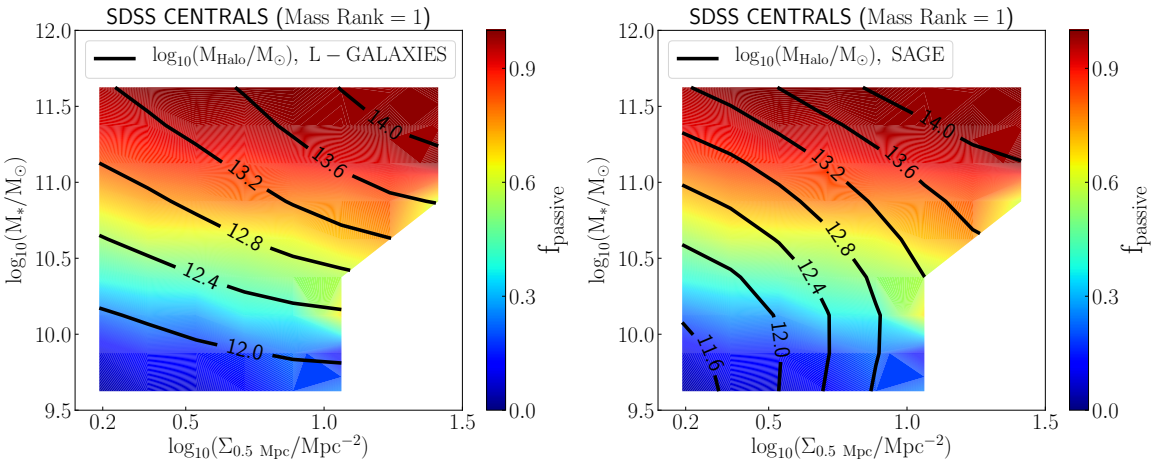

Figure 2.3: Passive fractions in the $M_* - \Sigma_r$ parameter space for SDSS central galaxies selected using mass ranks assigned by the adaptive aperture. We use 0.5 Mpc aperture for calculating the neighbour density around central galaxies. The contours show the median halo mass for the two SAMs, L-GALAXIES (left-hand panel) and SAGE (right-hand panel).

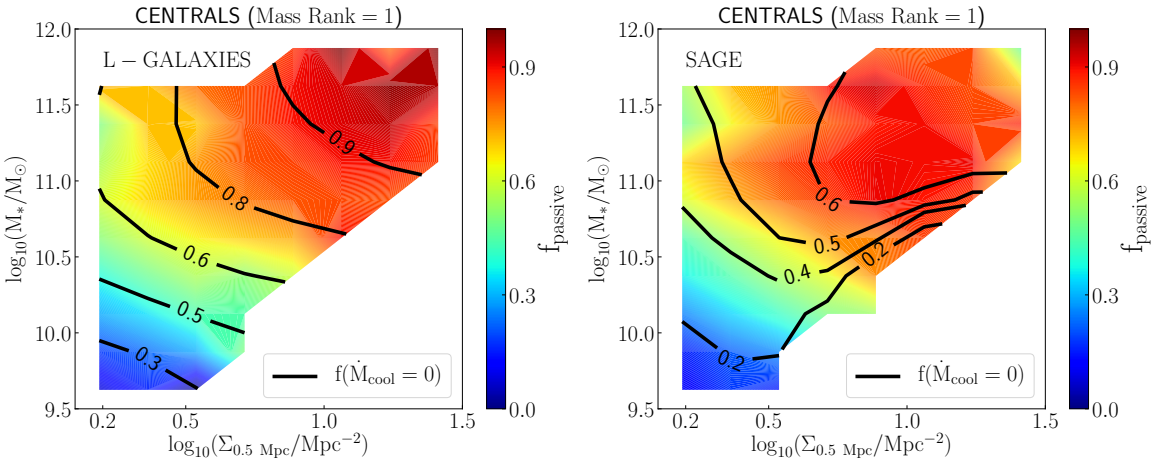

Figure 2.4: Passive fractions in the $M_* - \Sigma_r$ parameter space for L-GALAXIES (left-hand panel) and SAGE (right-hand panel). We use 0.5 Mpc aperture for calculating the neighbour density for model galaxies. The passive fractions are shown for central galaxies that are selected by assigning mass ranks using the adaptive aperture $r(8, 2.5, 2000)$. The contours on top show the fraction of galaxies where the cooling of hot gas due to radio-mode AGN feedback is recorded to be zero.

star-forming galaxies reside in low-density environments and have lower stellar/halo masses. Similarly, most quenched galaxies live in high-density environment like groups or clusters and are typically very massive in stellar or halo mass. Furthermore, a relation between passive fraction and halo mass is also seen. Galaxies living in small haloes are actively star-forming whereas those living in massive haloes seem to be passive. Qualitatively, these trends are the same for both L-GALAXIES and SAGE galaxy formation models. An interesting feature of Fig. 2.2 is the lack galaxies in high density and low mass ($\log(M_*/M_\odot) < 10,\ \log(\Sigma_{0.5\mathrm{Mpc}}/\mathrm{Mpc}^{-2}) > 0.5$). Due to the low number of galaxies in this part of the parameter space, we choose to remove these systems, in order to avoid spurious conclusions due to low-number statistics. In order to prevent that, we considered bins of stellar mass and galaxy density with more than 30 objects in them.

We next superimpose the halo mass contours shown in Fig. 2.2 to the passive fraction from the observed SDSS data in Fig. 2.3. The left-hand panel represents the contours from L-GALAXIES while SAGE predictions are shown on the right. In the left-hand panel of Fig. 2.3, we notice that the observed star-forming central galaxies living in isolated environment are hosted in low halo masses. On the high mass, high-density region in the parameter space, trends similar to model passive fraction are observed. The most massive galaxies in the local Universe are quenched regardless of the environment that they live in. Star formation quenching for observed central galaxies appears to be mainly driven by a quantity that correlates with stellar masses. Although the contours do not match the SDSS data perfectly, L-GALAXIES seem to catch the dominant dependence of quenching on stellar mass while SAGE predicts a density/halo mass to play a significant role, bigger than what SDSS is telling us.

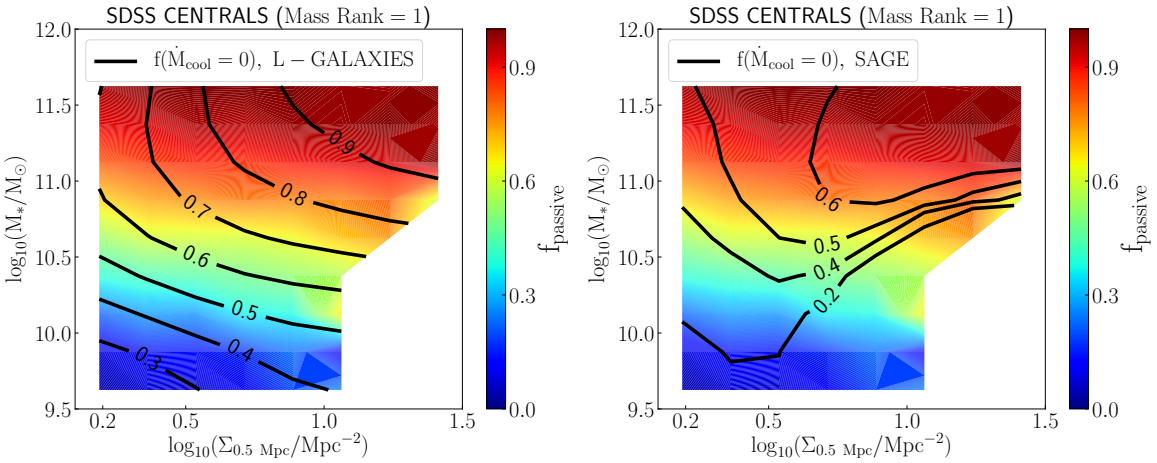

Figure 2.5: Passive fractions in the $M_* - \Sigma_r$ parameter space SDSS central galaxies selected using mass ranks assigned by the adaptive aperture. We use 0.5 Mpc aperture for calculating the neighbour density around central galaxies. The contours on top show the fraction of galaxies where the cooling of hot gas due to radio-mode AGN feedback is recorded to be zero, L-GALAXIES (left-hand panel) and SAGE (right-hand panel).

An interesting feature seen in Fig. 2.3 are the very massive quenched galaxies that live in low-density environment which are not reproduced by L-GALAXIES and SAGE galaxy formation models.

2.7.2 Dependence on AGN Heating

For central galaxies, radio-mode AGN feedback would inject energy into the galaxies heating the gas, ultimately preventing cooling and subsequent gravitational collapse and ceasing star formation. For both SAMs, we can calculate the rate of cooling of the hot gas in the presence of AGN radio-mode feedback (see equations Eq. 2.3 and 2.6). Fig. 2.4 presents the passive fraction for the two models in the $M_* - \Sigma_r$ parameter space with the contours representing the fraction of galaxies where gas cooling is prevented by feedback. With L-GALAXIES, the passive fraction corresponds closely to

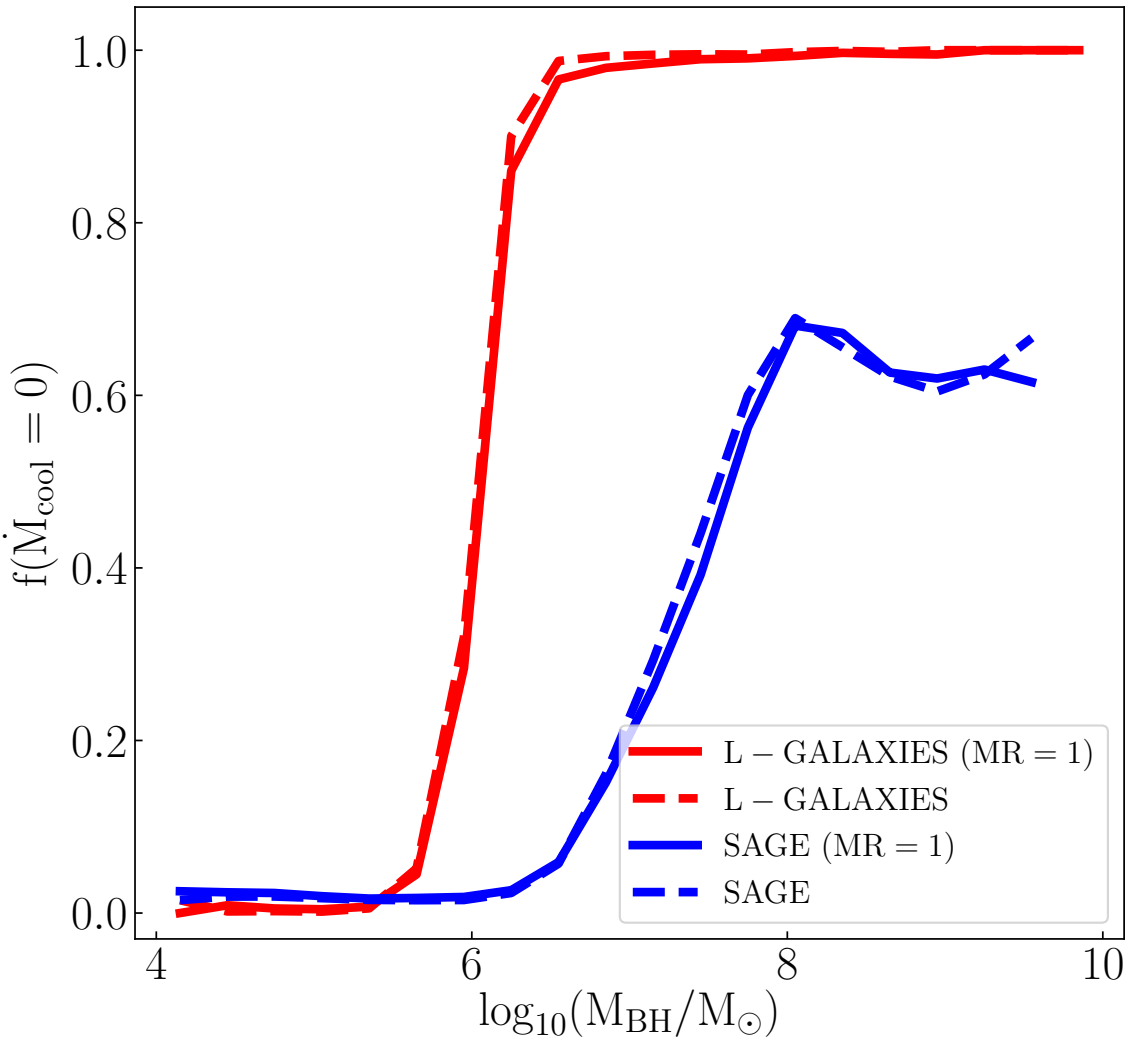

Figure 2.6: Fraction of galaxies with zero gas cooling rate as a function of black hole mass. The central galaxies selected using mass ranks assigned by the adaptive aperture are presented using solid lines and dashed lines show the central galaxies as defined by the SAMs. Red represents L-GALAXIES and blue represents SAGE galaxies. The central galaxies defined by the SAMs and using our algorithm have identical behaviour.

the fraction of galaxies with no cooling. The right-hand panel of Fig. 2.4 shows the same plot for SAGE. While the quenched region of the parameter space still corresponds to maximum $f(\dot{M}_{\rm cool} = 0)$, the fraction of galaxies with no cooling peaks at 60 per cent. The smaller value for $f(\dot{M}_{\rm cool} = 0)$ is suggestive of a competition between the radio-mode AGN feedback and formation of stars. Furthermore, even though both SAMs use the same equation for star formation, the efficiency of converting gas to stars has been tuned very differently.

In general, we can say that AGN feedback is dominant in quenching star formation in central galaxies. The region of high passive fraction in Fig. 2.4 corresponds to galaxies which have little no cooling of gas.

Fig. 2.5 represents the passive fractions for the observed SDSS sample, for central galaxies as a function of stellar mass and density on an aperture of 0.5 Mpc. The contours are the same as in Fig. 2.4 for both L-GALAXIES (left-hand panel) and SAGE (right-hand panel). We test the possibility that galaxies that are a part of massive haloes should be passive due to presence of SMBHs that injects enough energy into the galaxy to suppress cooling leading to quenching of star formation.

For L-GALAXIES the impact of AGN feedback is not very significant for less massive and fairly isolated systems, only 30 per cent of the galaxies have gas cooling completely suppressed due to radio-mode feedback. For low mass galaxies, the fraction of galaxies with no cooling agrees very well with the fraction of passive galaxies. With increasing stellar masses and galaxy density, the fraction of galaxies without gas cooling goes up to 90 per cent. However, observed massive central galaxies with low star formation rate have varying $f(\dot{M}_{cool} = 0) \simeq 0.7 - 0.9$. On the other hand, SAGE contours in the right-hand panel of Fig. 2.5 look more different that L-GALAXIES and diverge from the

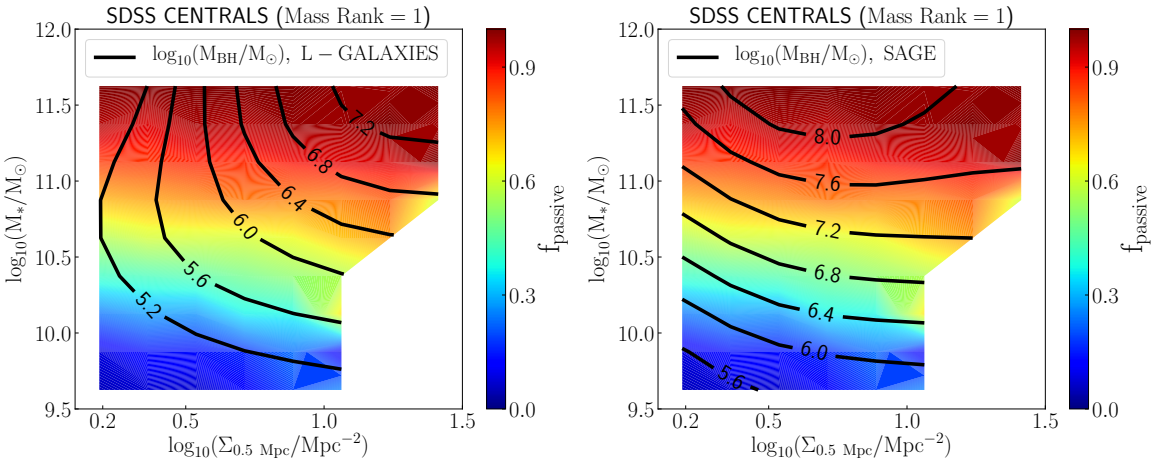

Figure 2.7: Passive fractions in the $M_* - \Sigma_r$ parameter space SDSS central galaxies selected using mass ranks assigned by the adaptive aperture. We use 0.5 Mpc aperture for calculating the neighbour density around central galaxies. The contours on top show the median black hole masses for L-GALAXIES (left-hand panel) and SAGE (right-hand panel).

observed passive fraction. Even with the more complex radio-mode AGN feedback, low $f(\dot{M}_{\rm cool} = 0)$ in the passive region of the observed parameter space presents a challenge for SAGE.

2.7.3 Dependence on Black Hole Mass

If the central black hole is responsible for quenching central galaxies at $z \sim 0$, then a relation between black hole mass and the lack of cooling of gas should be seen in the model. Fig. 2.6 shows $f(\dot{M}_{cool} = 0)$ as function of $M_{\rm BH}$ for central galaxies selected using the mass rank assigned by the adaptive aperture for both SAMs. AGN feedback in L-GALAXIES very strongly controls the cooling of gas. Nearly all central galaxies that host an SMBH with $\log_{10}[M_{\rm BH}/M_\odot] \geq 6.0$ are extremely inefficient at cooling gas. For SAGE, gas cooling only starts to become inefficient for central galaxies with more massive SMBH ($\log_{10}(M_{\rm BH}/M_\odot) \sim 8.0$) which corresponds to 60

per cent with no gas cooling. A central galaxies population with $\log_{10}(M_{\rm BH}/M_{\odot}) > 8.0$ contains a significant number of galaxies that are cooling gas that could be still forming stars. Cooling flows are expected to be the main fuel for star formation in these massive galaxies living in dense environments; however, gas rich mergers with gas-rich satellites can also provide cold gas and cause star formation.

Fig. 2.7 shows the observed passive fractions from Fig. 2.5 with overlying contours of median black hole mass for central galaxies in both SAMs. For both simulations, the most massive black holes correspond to the passive part of the observed parameter space. However, observed massive galaxies that live in isolated environments are passive correspond to low-mass SMBH from L-GALAXIES. The high passive fractions observed for the massive isolated galaxies represents a possible tension with the AGN feedback scheme adopted in L-GALAXIES, due to the predicted low mass of corresponding central SMBH. None the less, other causes, like the lack of cold gas, may explain star formation quenching in these objects. This tension suggests a possible problem for the growth of the SMBH residing in central galaxies, especially in isolated environments in SAMs.

Qualitatively, the contours for SMBH mass for SAGE show a better agreement with the observed passive fraction (see right-hand panel Fig. 2.7). Independent of the environment, massive centrals hosting massive SMBH correspond to massive observed passive galaxies. Despite the more massive SMBH, the fraction of centrals with suppressed gas cooling (see Fig. 2.5 and 2.6) seems to stay low, indicating inefficient heating.

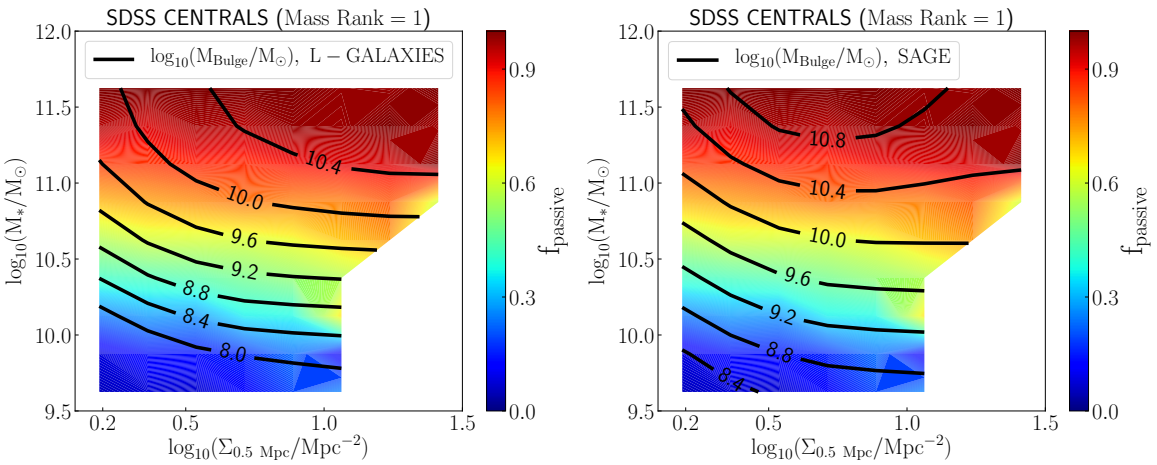

Figure 2.8: Passive fractions in the $M_* - \Sigma_r$ parameter space SDSS central galaxies selected using mass ranks assigned by the adaptive aperture. We use 0.5 Mpc aperture for calculating the neighbour density around central galaxies. The contours on top show the median bulge mass for L-GALAXIES (left-hand panel) and SAGE (right-hand panel).

2.7.4 Dependence on Bulge Mass

To explore star formation quenching for central galaxies, we next explore the role of bulge mass in SAMs. The left-hand panel in Fig. 2.8 shows the observed passive fractions with overlying contours presenting the bulge mass for central galaxies in L-GALAXIES. In general, the observed star-forming galaxies correspond to low bulge mass whereas passive observed galaxies host massive bulges.

The observed passive fraction agrees strongly with the model bulge masses for both SAMs. Active galaxies, independent of the environment, host smaller bulges. As the fraction of quenched galaxies increases in the parameter space, so does the model bulge mass. The disagreement between model and observed massive, quenched isolated galaxies could be studied using Fig. 2.8. The left-hand panel show the model bulge mass from L-GALAXIES. It is seen that observed massive, quenched isolated galaxies

correspond to massive bulge and low mass black hole. The reason for disagreement could be due to a large scatter in the $M_{\rm Bulge} - M_{\rm BH}$ relation.

Looking at Fig. 2.7 and 2.8, we notice that SAGE has more massive black hole and bulges that L-GALAXIES. Such a situation is a direct consequence of the higher merger rate of galaxies in SAGE than in L-GALAXIES. This implies that bulges grow much more efficiently and more mass is locked into bulges than is required (Knebe et al. 2018). This merger excess might also help in making the SMBH more massive and might result in a tighter $M_{\rm Bulge} - M_{\rm BH}$ relation (Jahnke and Macciò 2011). However, SAGE still shows some net cooling in these galaxies which could indicate that gas cooling in SAGE might be inconsistent with observations. Comparing the two SAMs, we can conclude that in L-GALAXIES quenching is mainly related to the halo and bulge mass and is more efficient. In SAGE, quenching is mainly related to the SMBH and bulge mass. Neither SAM is able to completely capture the whole complexity of the observed passive galaxy population.

2.8 Black Hole - Bulge Mass relation

In the previous sections, we have shown that star formation quenching seems to be driven either by the presence of an AGN or a massive bulge. Central galaxies from L-GALAXIES and SAGE show that the presence of massive SMBH can suppress the gas cooling and eventually cease star formation. In general, the star formation activity in central galaxies is driven by the coupling between the black hole and bulge mass and their growth mechanisms. Various studies, observational and theoretical, have reported a tight relationship between the mass of the central black hole and the mass of the bulge (Ferrarese and Merritt 2000; Häring and Rix 2004; Croton 2006; Beifiori

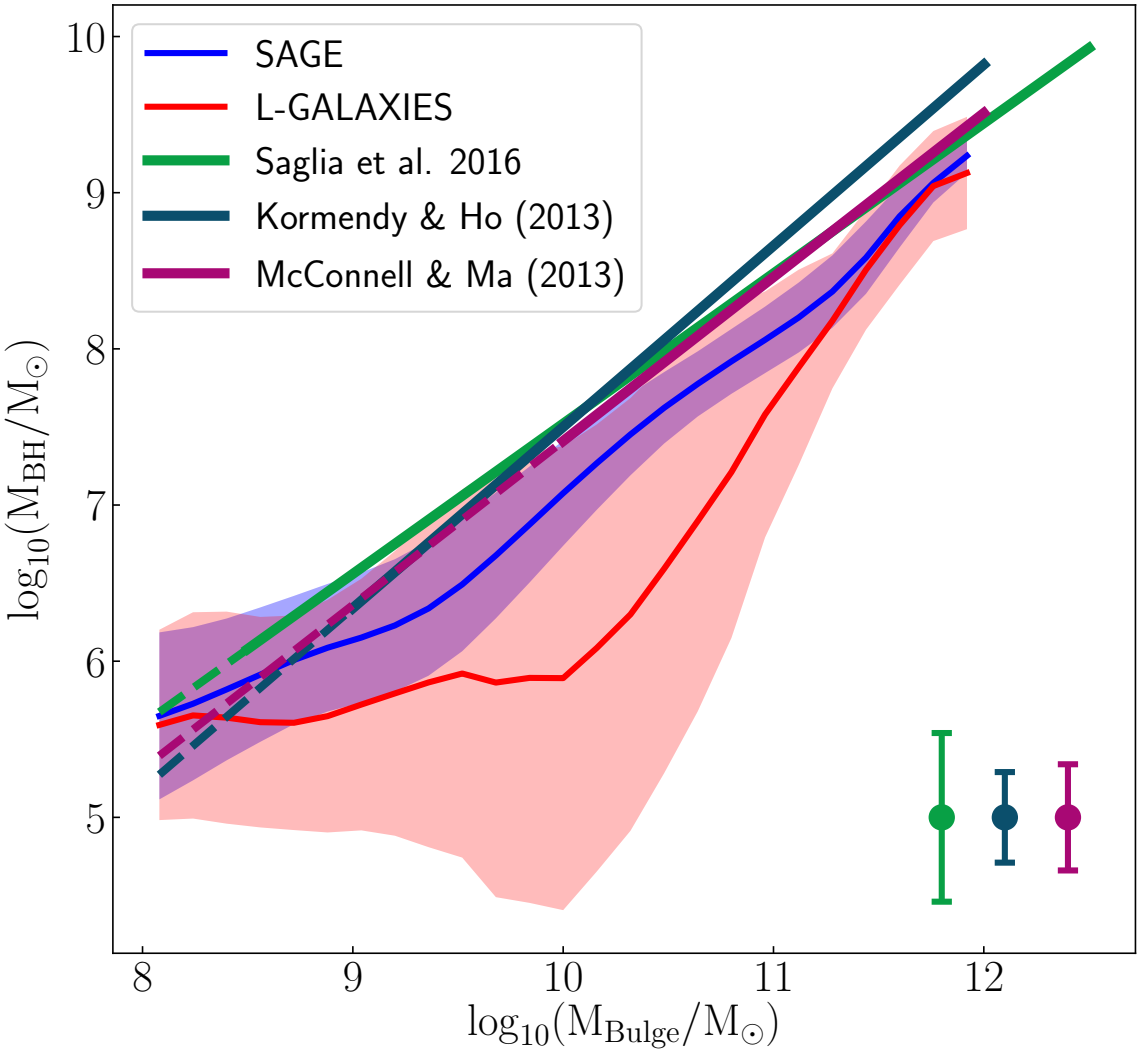

Figure 2.9: Black hole mass vs. bulge mass for the SAMs compared to various observed relations. For both SAMs, the line represents the mean calculated in a bulge mass bin of 0.16 dex and the shaded region shows the standard deviation within the same bin. The observed relations are best fit lines from Saglia et al. (2016), Kormendy and Ho (2013a) and McConnell and Ma (2013). The dashed lines for the observed relations show the extrapolation to a lower bulge mass range. The points shown on the lower right corner represent the scatter for the observed relations.

et al. 2012; Saglia et al. 2016). In this section, we discuss the black hole–bulge mass relation for the SAMs used in this study. Fig. 2.9 shows the $M_{\rm BH} - M_{\rm Bulge}$ relation for L-GALAXIES and SAGE centrals and comparisons with best-fitting power laws provided in Saglia et al. (2016), Kormendy and Ho (2013a) and McConnell and Ma (2013) (solid straight lines). The red and blue solid lines show the mean black hole mass for L-GALAXIES and SAGE respectively. The shaded region represents the standard deviation within the same bulge mass bin for the SAMs, while the points with error bars in the lower right corner show the typical scatter in the observed studies.

Fig. 2.9 shows the two models predict quite a different shape of $M_{\rm BH} - M_{\rm Bulge}$ relation. In general, both models predict SMBH masses at fixed $M_{\rm Bulge}$ that are lower than observational estimates, but that agree on a 1σ level. SAGE predicts an almost constant scatter with bulge mass, and much smaller than L-GALAXIES. On average the average standard deviation in L-GALAXIES is 0.56 dex higher than SAGE.

In detail, $\rm M_{BH}$ are always underpredicted in the range $8.5 \lesssim \log_{10}(\rm M_{Bulge}/M_{\odot}) \lesssim 11.0$, with better agreement at higher and lower bulge masses. SAGE predicts a slope for the $M_{\rm BH} - M_{\rm Bulge}$ relation that is closer to the observation estimate (due to the fact that the model has been explicitly calibrated to reproduce the constrains). On the other hand, L-GALAXIES strongly underpredicts $\rm M_{BH}$ at intermediate masses. Since the agreement with data at the high-mass end is satisfactory, this results in a different slope of the $M_{\rm BH} - M_{\rm Bulge}$ relation with respect to observations.

It is worth stressing that the overall shape of the $M_{\rm BH} - M_{\rm Bulge}$ relation depends on the whole accretion history of SMBHs. In particular, in L-GALAXIES, the main mechanism responsible for both SMBH and bulge growth are galaxy mergers (Kauffmann and Haehnelt 2000), i.e. the so-called QSO-mode of SMBH accretion. Marulli et al.

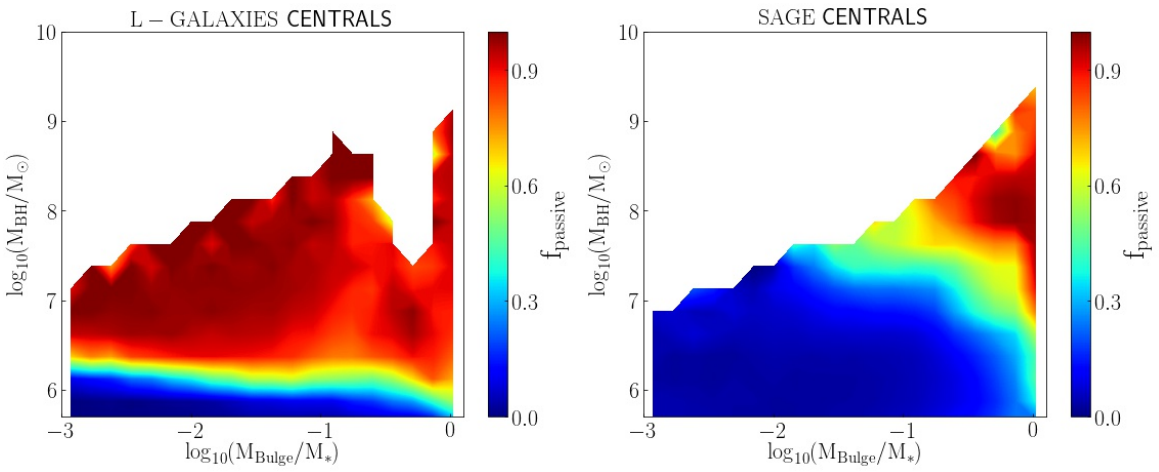

Figure 2.10: Passive fractions in the $M_{BH} - M_{Bulge}/M_*$ parameter space for central galaxies in L-GALAXIES (left-hand panel) and SAGE (right-hand panel).

(2008) already showed the limitation of the Kauffmann and Haehnelt (2000) model in reproducing the redshift evolution of the bright QSO population. In this scenario, the radio-mode feedback contributes marginally to the shape of the relation. We do not expect the tension between L-GALAXIES and observed $M_{BH} - M_{Bulge}$ relation to affect our conclusions much, given the simple scaling of radio-mode efficiency with M_{BH} in Eq. 2.1. This is especially true at the high-mass end of the SMF, where the radio-mode prescription has been calibrated against.

Moreover, it is also worth noticing that the exact shape and scatter in the $M_{Bulge} - M_{BH}$ relation have been revised by a number of works (Graham and Scott 2013, Fontanot et al. 2015 and Shankar et al. 2016), highlighting possible selection biases, that make the exact comparison between model predictions and data outside the aims of the present work.

2.8.1 Impact on SFR Quenching

Our analysis shows that the lack of star formation activity in observed central galaxies correlates with observed stellar mass and the presence of a massive bulge component. Fig. 2.10 shows the behaviour of passive fractions for model central galaxies in $M_{BH} - M_{Bulge}/M_*$ parameter space. In the left-hand panel we present the passive fraction for central galaxies in L-GALAXIES. Quenching in central galaxies is dominated by the presence of a massive black hole, independent of baryonic properties such as stellar mass. As soon as the black hole mass reaches a certain threshold ($\log_{10}(M_{BH}/M_\odot) \sim 6.0$), quenching of star formation seems to onset.

In the right-hand panel, the passive fraction for SAGE central galaxies is presented. In general, the passive fraction seem to be driven by the presence of massive black holes and a significant central bulge. Star forming central galaxies in SAGE have relative small black holes and small bulges. It is only when both the black hole and bulge become gravitationally significant, the onset of quenching occurs. However due to lack of statistical samples in observed SMBH masses, Fig. 2.10 can only be presented for SAMs and therefore, remains a prediction.

2.9 Conclusion

In this work, we have presented how star formation quenching depends on various galaxy properties and their environment for two SAMs and an observed sample. Theoretically, most massive galaxies reside in the deepest part of the gravitational potential well which corresponds to the centre of the dark matter halo. In such cases, one should expect that these systems accrete most of the gas through cooling flows from the hot gas reservoir and hence go through a continuous star formation activity.

Massive galaxies also host massive central black holes that inject energy in the system through radio-mode AGN feedback. In most cases, this energy will be enough to completely suppress the cooling flow resulting in star formation quenching.

The radio-mode AGN feedback is an empirical prescription embedded in SAMs to deposit energy into the galaxy halo (see equations Eq. 2.1 and 2.4). L-GALAXIES and SAGE implement radio-mode AGN feedback that offsets the gas cooling in massive central galaxies that live in dense environment quenching them (see Fig. 2.4). In order to study the impact of radio-mode feedback, global properties such as halo mass and stellar mass are of great importance. The known stellar–halo mass relation implies that massive galaxies reside in massive haloes and observationally have low star formation activity (Conroy and Wechsler 2009; Behroozi et al. 2013; Kravtsov et al. 2018). But due to the strong correlation between the stellar mass and halo mass of central galaxies, it becomes difficult to decide whether it is the halo mass or stellar mass that dominates quenching of star formation. We then use an observationally motivated parameter, the environmental density in a cylindrical aperture introduced in Fossati et al. (2015), to study star formation quenching. Environmental density breaks the degeneracy between halo mass and stellar mass and can easily be implemented on both observed and model galaxies. We use the same cylindrical aperture to select central galaxies from the models and observations; we also assume an adaptive aperture to select a pure sample of central galaxies for the analysis.

The evidence that massive observed central galaxies are quenched suggest that presence of mechanisms that suppress gas cooling or eject gas to cease star formation. Both SAMs do not ideally match the observed passive fractions which correlate with the stellar mass and bulge mass. Central passive fractions in L-GALAXIES correlate

with model halo and bulge mass whereas for SAGE, passive fractions correlate with SMBH and bulge mass. Both SAMs predict star-forming massive isolated galaxies which is in contrast with observations. Furthermore, L-GALAXIES have problems with black hole growth in an isolated environment; massive field galaxies seem to have SMBH 2 orders of magnitudes smaller than SAGE. Such a discrepancy is very evident in the intermediate mass range of the $M_{\rm BH} - M_{\rm Bulge}$ relation. In order to match the observations, we suspect that SMBHs in isolated massive centrals in L-GALAXIES should grow faster than their bulges.

Meanwhile, the suppression of cooling flows in SAGE via radio-mode feedback is less effective than the L-GALAXIES framework. In SAGE, massive central galaxies that live in dense environments are forming stars at higher rate compared to L-GALAXIES. This can be a result of higher merger rates that bring in a large amount of cold gas that is available for star formation. Furthermore, the high star formation rate is attributed to a higher star formation efficiency parameter in the Kennicutt-Schmidt relation (Kennicutt 1998).

While both SAMs have their strengths and weaknesses, the simple description of AGN feedback in L-GALAXIES seems to be performing as good as with respect to a more complex treatment in SAGE. However, a better treatment for SMBH growth is required for L-GALAXIES that can allow for a better agreements with the observed $M_{\rm BH} - M_{\rm Bulge}$ relation.

2.10 Appendix: Selection of Central Galaxies

Central galaxies are expected to be gravitationally dominant in the environment that they live in. Star formation quenching in central galaxies is mainly caused by the

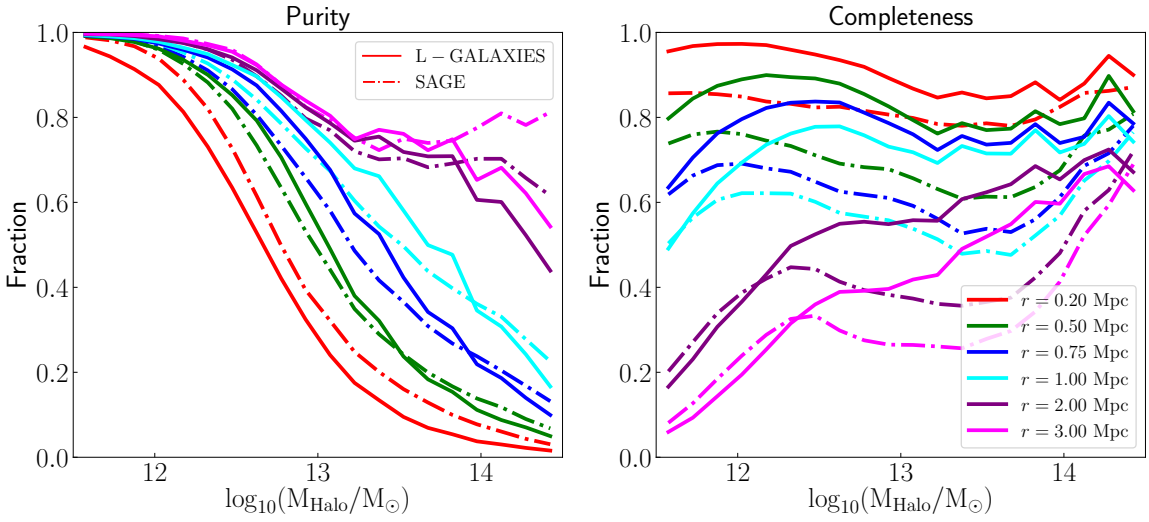

Figure 2.11: Purity and completeness as a function of halo mass for central galaxies (Mass Rank = 1). The different colours show various aperture radii where the velocity depth has been fixed to 1000 km s^{-1}. Solid lines show L-GALAXIES and dashed-dotted lines show central galaxies from SAGE.

energy outflows due the presence of an AGN (Silk and Mamon 2012). Therefore, an accurate selection of central galaxies is critical. Any contamination in the central galaxy selection can affect the trends seen in passive fractions and leads to inaccurate conclusions about the impact of AGN heating.

Before starting the discussion about the selection of central galaxies, we define two metrics that characterize a statistical sample: purity and completeness. The purity is defined as the ratio of the number of correctly identified centrals and the total number of identified centrals; the completeness is the ratio of identified centrals and the total number of central galaxies. Maximizing both quantities is desired, however a trade-off between the two needs to be found for selecting central galaxies (Fossati et al. 2015).

The galaxy formation models provided the information about a galaxy being central or satellite. For observed systems, we can use observed parameters to investigate it's gravitational dominance. To select central galaxies, we place a cylindrical aperture with radius in physical space and the height in velocity space. Each galaxy in this cylinder is assigned a rank based on its stellar mass. If a galaxy achieves a mass rank of 1, it is classified as a central galaxy. The radius of the cylinder is either fixed or adaptive aperture, as defined in Eq. 2.10 where $r_{\rm max}$ is the maximum radius the adaptive aperture can have, α and β are parameters relate the virial radius of the halo to the stellar mass. The parameter n is defined as the isolation criterion and plays the role of preventing small apertures that might lead to a decrease in purity.

$$\mathrm{r(n, r_{max}, v_{depth}) = min(r_{max}, n \cdot 10^{\alpha \log M_* + \beta})\ [Mpc]} \tag{2.10}$$

We start with the discussion of selecting central galaxies while having the radius and velocity of the projected cylinder fixed. Fig. 2.11 describes the purity (left) and completeness (right) for selecting central galaxies (MassRank = 1) as a function of halo mass for the two simulations (solid: L-GALAXIES and dashed-dotted: SAGE). The colours show the various radii of the projected aperture while the velocity depth is kept constant at 1000 km s^{-1}.

A small aperture results in most galaxies being classified as central galaxy which, of course, is incorrect. The smaller aperture is unreliable at high halo masses where central galaxies should live in dense environments, i.e. high number of satellite galaxies. With bigger apertures the purity at high halo mass increases as satellites are correctly identified. Completeness as a function of halo mass, for small radius, decreases on slightly. As we increase the aperture size, the completeness at low halo

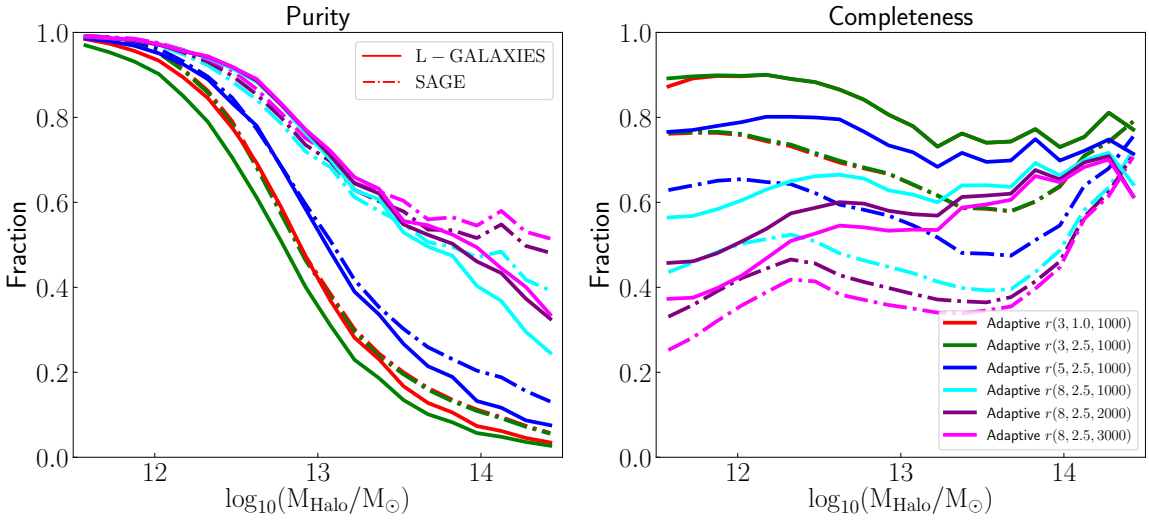

Figure 2.12: Purity and completeness as a function of halo mass for central galaxies (Mass Rank $= 1$). The different colours show various adaptive apertures represented using Eq. 2.10. Solid lines show L-GALAXIES and dashed-dotted lines show central galaxies from SAGE.

masses decreases faster than at high halo masses. The completeness of our algorithm never reaches 1.0 because the most massive galaxies in halos might not be the central galaxy (Skibba et al. 2011). In general as the size of the aperture increases, the purity increases and completeness decreases for both SAMs. Our results are consistent with that of Fossati et al. (2015) which used a galaxy formation model from Guo et al. (2011). With fixed aperture, finding a balance between reasonable purity and completeness seems to be a difficult task.

In order to find an optimal balance between the purity and completeness, we make use of the adaptive aperture. The adaptive aperture exploits the strong correlation between the stellar mass and the size of the dark matter halo for central galaxies. Fig. 2.12 depicts the various configurations of the adaptive apertures that are tested.

Similar trends are seen for the purity and completeness in the various adaptive apertures as compared to the fixed aperture. Fig. 2.12 tells us that an increase in the value of n improves the purity of the selection at high halo masses. On the other hand, a sharp decrease in completeness is seen for the central sample at low halo masses. Independent of n, the velocity depth does not show any impact on the purity and completeness of the sample. While we put more emphasis on the purity of the sample, a certain balance between purity and completeness is desired. Therefore for both our simulations, we use the adaptive aperture with $n = 8$, $r_{\rm max} = 2.5$ Mpc and $v_{\rm depth} = 2000\,{\rm km\ s^{-1}}$ to select central galaxies for the rest of the study.

As the input parameters for selecting central galaxies can be easily measured observationally, this technique can be implemented on both model and observed galaxies. The uniform comparison of model and observed galaxies is a great advantage of this technique. However, not all central galaxies are the most massive which results in some satellites being defined as centrals. For example, in small galaxy groups where the central and satellite galaxy have similar stellar masses, our definition of central galaxy might not be accurate (Fossati et al. 2017). For further details about the shortcomings of our techniques, the reader is referred to Fossati et al. (2015).

Chapter 3

MaNGA Photometric Catalog

3.1 Preamble

This chapter contains a version of the paper on **"MaNGA galaxy properties – I. An extensive optical, mid-infrared photometric, and environmental catalogue"** (Arora et al. 2021). In this study, a large extensive photometric and environmental catalogue for the MaNGA galaxy survey is presented. The catalogue includes optical and mid-infrared photometry and made use of novel automated software, AUTOPROF, for the extraction of surface brightness profiles. The catalogue compiled in this study is publicly available.

3.2 Abstract

We present an extensive catalogue of non-parametric structural properties derived from optical and mid-infrared imaging for 4585 galaxies from the MaNGA survey. DESI and Wide-field Infrared Survey (WISE) imaging are used to extract surface brightness profiles in the g, r, z, $W1, W2$ photometric bands. Our optical photometry takes advantage of the automated algorithm AUTOPROFand probes surface brightnesses

that typically reach below 29 mag arcsec^{-2} in the r band, while our WISE photometry achieves 28 mag arcsec^{-2} in the *W1* band. Neighbour density measures and central/satellite classifications are also provided for a large subsample of the MaNGA galaxies. Highlights of our analysis of galaxy light profiles include (i) an extensive comparison of galaxian structural properties that illustrates the robustness of non-parametric extraction of light profiles over parametric methods; (ii) the ubiquity of bimodal structural properties, suggesting the existence of galaxy families in multiple dimensions; and (iii) an appreciation that structural properties measured relative to total light, regardless of the fractional level, are uncertain. We study galaxy scaling relations based on photometric parameters, and present detailed comparisons with literature and theory. Salient features of this analysis include the near-constancy of the slope and scatter of the size–luminosity and size–stellar mass relations for late-type galaxies with wavelength, and the saturation of the central surface density, measured within 1 kpc, for elliptical galaxies with $M_* > 10.7\,M_\odot$ (corresponding to $\Sigma_1 \simeq 10^{10}\,M_\odot\,\mathrm{kpc}^{-2}$). The multiband photometry, environmental parameters, and structural scaling relations presented are useful constraints for stellar population and galaxy formation models.

3.3 Introduction

A comprehensive picture of galaxy formation and evolution, as well as reliable data-model comparisons, requires access to large homogeneous photometric and spectroscopic samples of galaxies covering a broad range of morphologies, stellar and dynamical masses, star formation histories, environmental conditions, and more. Previously, such measurements have been extracted from large imaging and spectroscopic

wide-field surveys such as 2MASS (Jarrett et al. 2000), SDSS (York et al. 2000), GAMA (Driver et al. 2009), and others. More recently, large-scale acquisition of spatially resolved structural properties of galaxies has been achieved with integral-field spectroscopy. The latter is especially valuable in this context since it allows the synchronous collection of global and spatially resolved chemical and dynamical properties such as stellar mass surface density, age, metallicities, star formation rates, circular velocity, velocity dispersion and more, across a broad wavelength range. Pioneering integral-field spectroscopy surveys of galaxies such as SAURON (Bacon et al. 2001), ATLAS^{3D} (Cappellari et al. 2011), CALIFA (Walcher et al. 2014), and SAMI (Allen et al. 2015), provide such properties, although for relatively small samples.

With its spatially resolved optical spectroscopic data for ∼10000 nearby galaxies (z∼0.15), the SDSS-IV survey "Mapping Nearby Galaxy at Apache point observatory" (MaNGA; Bundy et al. 2015; Wake et al. 2017) has heralded a new era of large-scale galaxy studies with integral field units (IFUs)[1]. MaNGA uses a 127-fiber IFU to provide high-quality spatially resolved kinematic and chemical information for galaxies by collecting spectra at each pixel out to a maximum of 1.5/2.5 effective radii ($R_{\rm eff}$) for 85/15 percent of the MaNGA sample (Cano-Díaz et al. 2016; Sánchez et al. 2016, 2018; Graham et al. 2018; Méndez-Abreu et al. 2018). The MaNGA galaxies were selected from the NSA[2] catalogue with no inclination or size selection cuts. For more details about the MaNGA sample, see Bundy et al. (2015) and Wake et al. (2017).

Large-scale IFU surveys, such as MaNGA and CALIFA (Walcher et al. 2014), open an avenue for the exploration of spatially resolved counterparts to global structural

[1]While the MaNGA target sample includes ∼10,000 objects, 4585 of them are publicly available at the time of writing.

[2]NASA Sloan Atlas, Blanton et al. (2011)

drivers and scaling relations in galaxies. For instance, the MaNGA survey has already yielded new insights about evolutionary mechanisms such as star formation quenching; finding it to be regulated on global galaxy scales while star formation density is controlled locally (Bluck et al. 2020). Using the Pipe3D (Sánchez et al. 2018) output for MaNGA, Sánchez-Menguiano et al. (2020) have also explored the relation between the average stellar age and gas-phase metallicity for star-forming systems. While this relation had been observed globally (Lian et al. 2015), the spatially resolved nature of the MaNGA data also revealed a local correlation.

In addition to the published spatially resolved spectroscopic MaNGA data, a comprehensive understanding of MaNGA galaxies requires a full suite of structural and environmental galaxy properties. A catalogue of model-dependent MaNGA galaxy structural parameters (effective sizes, total magnitudes, Sérsic indices, ellipticities, position angles) already exists (Fischer et al. 2019, hereafter F19). The MaNGA PYMORPHPhotometric Value Added Catalogue (MPP-VAC) provides structural parameters for MaNGA galaxies extracted through Sérsic and Sérsic+Exponential fits to 2D surface brightness profiles. However, model-dependent assumptions about the light distribution of galaxies severely bias and limit any investigations of galaxy structure and evolution, as shown below. Providing galaxy structural parameters in *non-parametric* fashion is the main goal of this study.

In this paper, we present an extensive compilation of *model-independent* galaxian structural parameters based on optical and mid-infrared (MIR) imaging of all MaNGA galaxies extracted respectively from the Dark Energy Sky Instrument Legacy Imaging Survey (DESI Collaboration et al. 2016; Dey et al. 2019)[3] and Wide-field Infrared

[3]In what follows, the acronym DESI is meant to represent the Dark Energy Sky Instrument Legacy Imaging Survey.

Survey Explorer (*WISE*) surveys. The combination of optical and MIR bands is especially sensitive to the evolved stellar population, sites of star formation, and distribution of dust within galaxies. Broader multiband coverage for MaNGA galaxies is also being developed elsewhere; major imaging campaigns of MaNGA galaxies at radio (Masters et al. 2019) and ultraviolet wavelengths (Molina et al. 2020) are either in place or in progress. These will expand our understanding of MaNGA galaxies with clearer views of processes such as star formation on small spatial/time scales and the distribution of neutral hydrogen within galaxies, the fuel for star formation.

The surface brightness (SB) profiles extracted from the DESI and WISE imaging surveys for the MaNGA galaxies allow us to extract numerous non-parametric structural properties representing various measures of galaxy size, surface brightness, luminosity, stellar mass, and stellar mass surface density. Along with the structural parameters for MaNGA galaxies, environmental demographics are also provided below. Our compilation supplements fifth nearest-neighbour density measurements for MaNGA galaxies (see Argudo-Fernández et al. 2015; Etherington and Thomas 2015, for details), with important information about the gravitational dominance of a galaxy (i.e. central and satellite designation) within its own halo. These considerations motivate the assembly of a catalogue of environmental properties for a large subsample of MaNGA galaxies, in addition to the photometric catalogues. The environmental catalogue that we present below includes measures of neighbour densities and classification of these galaxies as a central or satellite.

A natural outcome of such an extensive data compilation is the construction and study of galaxy scaling relations. The slope, zero-point, and scatter of such empirical scaling relations present evidence of the underlying physics that dictates structure

formation and evolution of galaxies (Mo et al. 1998; Courteau et al. 2007; Dutton et al. 2007; Brook et al. 2012; Hall et al. 2012; Lange et al. 2015). The MaNGA non-parametric data sets produced in this study allow for an analysis of various galaxy scaling relations in different photometric bands. Among others, the size–stellar mass ($R-M_*$) relation and the stellar surface density (Σ_1 measured within 1 kpc) - stellar mass relations ($\Sigma_1 - M_*$) are presented. As discussed below, these relations enable constraints of the gas accretion and merger history as well as quenching and feedback models in galaxies (Chiosi and Carraro 2002; Shen et al. 2003; Franx et al. 2008; Saglia et al. 2010; Fang et al. 2013; Woo and Ellison 2019).

This chapter is organized as follows: in Section 3.4, we describe the procedures used to extract surface brightness profiles in optical and MIR bands. The extraction and correction of non-parametric galaxy structural properties are also discussed and presented in tabular format. The environmental catalogue is presented in Section 3.4.2. With our catalogue in place, we provide in Section 3.5 a broad overview of the DESI and WISE parameters for our MaNGA Public sample. Unimodal and bimodal structural distributions are also highlighted. In Section 3.6, we compare our model-independent structural parameters for MaNGA galaxies, such as size, apparent magnitude, and stellar mass, with literature values. Our MIR photometry and derived structural properties are compared to optical structural properties in Section 3.7. With our optical and MIR photometry validated, we combine these data sets in Section 3.8 to infer structural galaxy scaling relations of MaNGA galaxies with a focus on the size–stellar mass, $R-M_*$, relation in Section 3.8.1, and the central surface density–stellar mass, $\Sigma_1 - M_*$, relation in Section 3.8.3. We conclude in Section 3.9.

3.4 Light Profile Extraction

Our galaxy sample consists of 4585 galaxies from the public release of the MaNGA survey. The full MaNGA galaxy survey will yield ∼10 000 objects with a uniform distribution of stellar mass $M_* > 10^9 M_\odot$, with no inclination or size selections.

For our optical photometry, we have cross-correlated the public MaNGA data release with the DESI [4] (DESI Collaboration et al. 2016) and extracted 10×10 arcmin^2 images in the *g, r,* and *z* bands for 4585 matching galaxies. The large galaxy images ensure that the background sky level can be robustly characterized and subtracted. We use our fully automated 'AUTOPROF' code (Section 3.4.1) to extract azimuthally averaged surface brightness profiles from DESI *g-,r-* and *z-* band images, with the solution fit to the *r* band for its minimal dust extinction and high signal-to-noise ratio (S/N; and for consistency with the parallel Photometry and Rotation Curve Observations from Extragalactic Surveys, or "PROBES", investigation by Stone and Courteau 2019 and Stone et al. 2021a). The *r*-band isophotal solution is applied to the *g* and *z* images for uniformity of the position angles, ellipticities, fluxes and color gradients. Unless otherwise stated, all band-dependent structural parameters refer to the *z* band photometry. The automation of AUTOPROFis well suited to large surveys like DESI, where interactive surface brightness extraction methods, such as those based on the XVISTA data reduction package[5], become prohibitive (see Courteau 1996; McDonald et al. 2011; Hall et al. 2012; Gilhuly and Courteau 2018, for more details).

Our MIR surface brightness profiles are derived from the WISE Large Galaxy Atlas

[4] https://www.legacysurvey.org
[5] http://ganymede.nmsu.edu/holtz/xvista/

and the Extended Source catalogue (WXSC; Jarrett et al. 2019)[6], which features custom image mosaic construction to produce native angular resolution products that include both WISE and NEOWISE imaging[7]to improve the sensitivity; complete details of image construction are provided in Jarrett et al. (2012). Here we use the *W1* (3.4μm) and *W2* (4.6μm) mosaics with 5.9$''$ and 6.5$''$ spatial resolution, respectively. These bands are sensitive to the evolved stellar populations (Jarrett et al. 2013), and hence the stellar mass content and distribution for the target galaxies. We have extracted from the WISE surface brightness profiles the same structural properties as those measured from the DESI optical photometry, except for the stellar surface density within 1 kpc which is not resolved for many WISE profiles. The robustness of our WISE derived structural properties is demonstrated in Section 3.7. Among others, the *W1* and *W2* band passes are especially sensitive to older, more mass dominant stellar populations resulting in robust stellar mass measurements. The comparison of stellar masses from our DESI and WISE photometry is presented in Section 3.7. In what follows, all surface brightnesses used and reported are in the AB magnitude system.

In Appendix 3.10, we provide Tables 3.8 and 3.9 to present the output format of the public multiband surface brightness profiles.

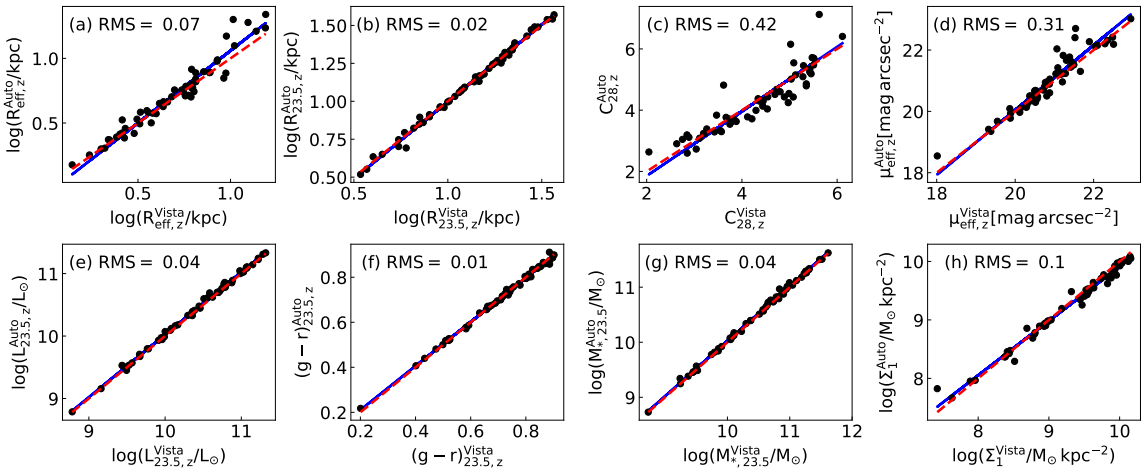

Figure 3.1: Comparison of photometrically derived non-parametric quantities from XVISTA interactive routines and AUTOPROFwith: (panel a) effective radius [$R_{\rm eff}$], (panel b) isophotal radius [$R_{23.5}$], (panel c) concentration index [C_{28}], (panel d) effective surface brightness [$\mu_{\rm eff}$], (panel e) luminosity within $R_{23.5}$ [$L_{23.5}$], (panel f) colour within $R_{23.5}$ [$(g-r)_{23.5}$], (panel g) stellar mass within $R_{23.5}$ [M_*], and (panel h) stellar mass surface density within 1 kpc [Σ_1]. The blue solid line shows the best orthogonal linear fit and the red dashed line shows the one-to-one line. All measurements are from DESI z-band photometry. The text in the top left-hand panel presents root mean square (rms) of the residuals for the one-to-one line.

3.4.1 AUTOPROF

The automated surface brightness profile extraction algorithm, "AUTOPROF" works on a combination of standard and machine learning based numerical techniques. A complete description of the AUTOPROFpipeline is presented in Stone et al. (in preparation). What follows is a brief outline.

The AUTOPROFpipeline first computes basic image parameters such as the background sky level, PSF, and galaxy centre. The background is determined as the mode of the pixel flux distribution. The PSF is determined uniquely for each image

[6]In what follows, WISE and the WISE Large Galaxy Atlas and the Extended Source catalogue are taken as synonymous (Jarrett et al. 2019).

[7](NEO)WISE data imaging and catalogueues can be retrieved from https://irsa.ipac.caltech.edu/

with circular apertures placed on a set of 50 non-saturated stars found using an edge detection convolutional filter. The galaxy centre is found by starting at the centre of the image and iteratively moving to brighter regions until a peak is found. The centre finding iterative step works by following the direction of increasing brightness as determined by the first FFT coefficient phase (FFT: Cooley and Tukey 1965) of the flux values around a circular aperture. On the sky subtracted and centred image, a global position angle and ellipticity is fit to the galaxy at the outer region of the galaxy (at approximately 3σ above the sky noise). The global fit is performed by minimizing the power in the second FFT coefficient of the flux values along the isophote. An elliptical isophote solution is fit to the sky-subtracted and centred image by simultaneously minimizing the second Fourier coefficient and a regularization term (Shalev-Shwartz and Ben-David 2014). The regularization term is the l_1 norm of the difference in ellipticity and position angle between adjacent isophotes. The use of a regularization term is borrowed from machine learning; other automated surface brightness profile extraction techniques take advantage of machine learning for all steps (Tuccillo et al. 2018; Smith et al. 2021).

A surface brightness profile is extracted at incremental radii corresponding to the median flux along each isophote. For isophotes at larger radii, AUTOPROFextracts a non-overlapping "band" of pixel flux values from the image, thus yielding a higher S/N for each isophote. A curve of growth is then calculated by integrating the surface brightness profile appropriately. The surface brightness uncertainty is computed from the 68.3% quartile range of the sampled flux along each isophote; this uncertainty is also propagated to the curve of growth.

Other surface brightness profile extraction techniques exist, such as the interactive

package PROFILE in XVISTA (Courteau 1996; McDonald et al. 2011; Hall et al. 2012; Gilhuly and Courteau 2018). Fig. 3.1 shows a comparison of several (uncorrected) structural properties defined in Section 3.4.2 for ∼50 MaNGA galaxies extracted using XVISTA and AUTOPROF. A good match between the two methods is found for $R_{23.5}$, $L_{23.5}$, $g-r$, and M_*. Other quantities in Fig. 3.1, such as $R_{\rm eff}$, C_{28} (see equation 3.1), and $\mu_{\rm eff}$ (measured at $R_{\rm eff}$), do not match as well. The effective radius comparison has a scatter of 0.07 dex, which matches the $R_{\rm eff}$ comparison of SDSS imaging parameters in Gilhuly and Courteau (2018, hereafter GC18) (0.06 dex) with the photometry of Walcher et al. (2014) for CALIFA galaxies. An equally poor match for $R_{\rm eff}$ relative to SDSS Petrosian radii is shown in fig. 9 of Hall et al. (2012). We also find a large rms of 0.42 dex comparing C_{28} estimates which reflects the large uncertainties involved in measuring outer radii based on total light (Graham et al. 2001; Trujillo et al. 2001). Likewise, a large rms of 0.42 dex is found for comparisons of C_{28} estimates, reflecting the large uncertainties involved in measuring outer radii based on total light (Graham et al. 2001; Trujillo et al. 2001). We argue in Section 3.6 that the poor reproducibility of $\mu_{\rm eff}$, $R_{\rm eff}$, and C_{28}, results largely from the ambiguous definition of total integrated luminosity in a photometric band, which these quantities all depend on. Still, we include these quantities in our tables for comparison with the literature.

Fig. 3.2 offers a visualization of the greater depth of the DESI imaging (coloured contours) relative to SDSS (black dots for the g and r bands). The photometric depth is chosen as the point at which a profile reaches a surface brightness error threshold of 0.22 mag arcsec^{-2} . As a result, the surface brightness levels are typically ∼2 mag arcsec^{-2} deeper where ∼1.5 mag arcsec^{-2} is attributed to the deeper DESI imaging (over SDSS) and ∼0.5 mag arcsec^{-2} is attributed to the isophote sampling

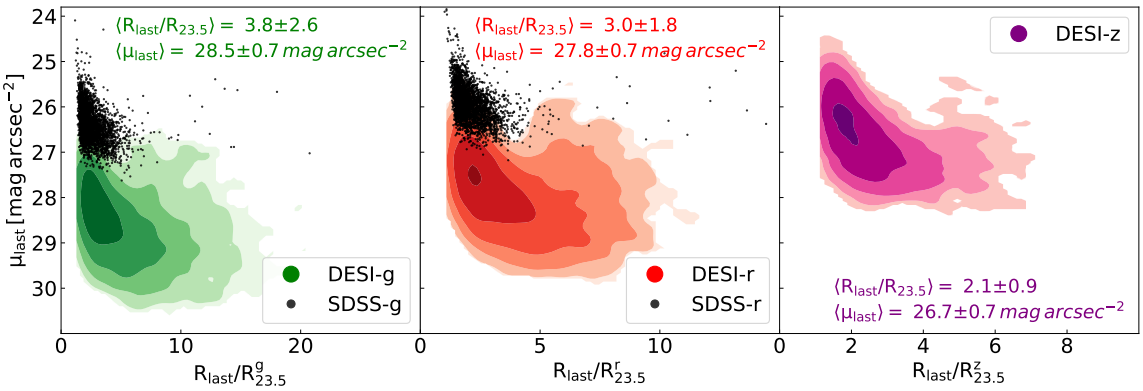

Figure 3.2: Lowest surface brightness levels and maximal radial extents of DESI surface brightness profiles in the g (left-hand panel), r (center panel) and z-bands (right-hand panel) with coloured contours in log density versus similar quantities for SDSS surface brightness profiles (black dots in the g and r bands; the z band is unavailable) for the same MaNGA galaxies. The radial axis shows the extent of the last point in each surface brightness profile scaled in units of $R_{23.5}$. The text within each panel indicates the average depth of our DESI photometry in the radius and surface brightness.

method in AUTOPROF(over XVISTA[8])

The coloured contours show the surface brightness levels and radial extents at which the surface brightness truncation occurs in the three DESI-grz bands. On average, the DESI photometric solutions extend radially beyond $2(z)-3.8(g)$ $R_{23.5}$ (greater radial extent at bluer wavelengths) and can reach surface brightness levels as low as $26.7(z)$ to $28.5(g)$ mag arcsec^{-2}, with some profiles going down to 30 mag arcsec^{-2} . Comparison with the SDSS data (extracted by ourselves using XVISTA procedures) shows that the combination of DESI images and the AUTOPROFsurface brightness extraction yields profiles that reach typically $\sim$2 mag arcsec^{-2} deeper than SDSS analysed with XVISTA given the same surface brightness uncertainty.

[8]The error threshold adopted by Gilhuly and Courteau (2018) for SDSS surface brightness profiles of CALIFA galaxies at g, r, and i bands is 0.15 mag arcsec^{-2}. A typographical error in that paper incorrectly lists that threshold as 1.5 mag arcsec^{-2} (sic) in their Section 3.

3.4.2 Parameter Extraction

We briefly describe the parameters inferred from optical and MIR imaging presented in the photometric and environment catalogues. A complete listing of our extracted parameters and their units is given in Tables 3.1 and 3.2.

Sizes

Some galaxy sizes are calculated relative to total light or measured at different isophotal levels. Relative sizes are calculated at 20, 50, and 80 per cent of the total light. The errors on these sizes are calculated by standard error propagation from the curve of growth (COG). Isophotal sizes are measured at the 22.5, 23.5 and 25 mag arcsec^{-2} isophotes from the surface brightness profiles in their respective band. Errors on isophotal sizes are calculated by standard error propagation from the surface brightness profile. While surface brightness errors tend to be larger than COG errors, the relative slope of the profiles results in larger errors for the sizes based on the COG.

The projected sizes (R) extracted from our photometry can be transformed into 3D physical radii (r), i.e., $r(R)$, by modelling projection effects. For flat discy stellar systems, the physical and projected radii are interchangeable (e.g. $r(R) \approx R$). For trixial systems, models suggest that $r(R) \approx (4/3)R$ (Hernquist 1990; Ciotti 1991; Ouellette et al. 2017). In Section 3.8, we review the impact of this transformation on galaxy scaling relations such as the size–mass relation.

Brightness, luminosities, and colours

Total apparent magnitudes and total luminosities enclosed within the $R_{23.5}$ and R_{25} radii are presented. The colour terms $g-r$, $g-z$ and $r-z$ are evaluated at $R_{23.5}$

Column name	Description	Unit	Data ype
MANGA-ID	MaNGA Identification	–	string
PlateIFU	MaNGA Plate-IFU	–	string
ObjID	SDSS-DR15 photometric identification number	–	long int
RA	Object Right Ascension (J2000)	°	float
DEC	Object Declination (J2000)	°	float
Z	NSA or SDSS redshift	–	float
TTYPE	Morphological T-Type (from MDLM-VAC)	–	float
GAL_EXTINCTION	Galactic extinction (DESI *grz* only)	mag	float
KCORRECTION	Cosmological *K-Corrections* (DESI *grz* only)	mag	float
R20	Radius where 20 per cent of the total light is integrated	arcsec	float
R20_E	Error in R20	arcsec	float
Reff	Effective radius	arcsec	float
Reff_E	Error in effective radius	arcsec	float
R80	Radius where 80 per cent of the total light is integrated	arcsec	float
R80_E	Error in R80	arcsec	float
R22.5	Isophotal radius calculated at 22.5 mag arcsec^{-2}	arcsec	float
R22.5_E	Error in R22.5	arcsec	float
R22.5_FLAG	Method of calculation: interpolation (0) and extrapolation (1)	boolean	int
R23.5	Isophotal radius calculated at 23.5 mag arcsec^{-2}	arcsec	float
R23.5_E	Error in R23.5	arcsec	float
R23.5_FLAG	Method of calculation: interpolation (0) and extrapolation (1)	boolean	int
R25	Isophotal radius calculated at 25 mag arcsec^{-2}	arcsec	float
R25_E	Error in R25	arcsec	float
R25_FLAG	Method of calculation: interpolation (0) and extrapolation (1)	boolean	int
C25	Concentration index measured using R20 and Reff	–	float
C28	Concentration index measured using R20 and R80	–	float
MU_20	Surface brightness at R20	mag arcsec^{-2}	float
MU_20_E	Error in Mu_20	mag arcsec^{-2}	float
MU_20_FLAG	Method of calculation: interpolation (0) and extrapolation (1)	boolean	int
MU_EFF	Surface brightness at the effective radius	mag arcsec^{-2}	float
MU_EFF_E	Error in effective surface brightness	mag arcsec^{-2}	float
Mu_EFF_FLAG	Method of calculation: interpolation (0) and extrapolation (1)	boolean	int
MU_80	Surface brightness at R80	mag arcsec^{-2}	float
MU_80_FLAG	Error in Mu_80	mag arcsec^{-2}	float
MU_80_FLAG	Method of calculation: interpolation (0) and extrapolation (1)	boolean	int
MAG23.5	Total apparent magnitude within R23.5	mag	float
MAG23.5_E	Error in total apparent magnitude within R23.5	mag	float
MAG23.5_FLAG	Method of calculation: interpolation (0) and extrapolation (1)	boolean	int
MAG25	Total apparent magnitude within R25	mag	float
MAG25_E	Error in total apparent magnitude within R25	mag	float
MAG25_FLAG	Method of calculation: interpolation (0) and extrapolation (1)	boolean	int
L23.5	Total luminosity within R23.5	$L_\odot$	float
L25	Total luminosity within R25	$L_\odot$	float
ELLIPTICITY	Ellipticity of the last isophote; $1-(b/a)$	–	float
PA	Position angle of the last isophote measured from north to east (DESI *grz* only)	°	float
MSTAR_235	Stellar mass measured at the *z*-band $R_{23.5}$ (*z* & *W*1 band only)	$M_\odot$	float
MSTAR_235_E	Error in stellar mass estimates measured at *z* band $R_{23.5}$ (*z* band only)	$M_\odot$	float
MSTAR_25	Stellar Mass measured at the *z*-band R_{25} (z band only)	$M_\odot$	float
MSTAR_25_E	Error in stellar mass estimates measured at *z*-band R_{25} (*z* band only)	$M_\odot$	float
SIGMA1	Stellar mass surface density within 1 kpc (z band only)	$M_\odot\,kpc^{-2}$	float
SIGMA1_E	Error in SIGMA1 (z band only)	$M_\odot\,kpc^{-2}$	float
SIGMA_EFF	Stellar mass surface density within R_{eff} (z band only)	$M_\odot\,kpc^{-2}$	float
SIGMA1_EFF_E	Error in SIGMA_EFF (z band only)	$M_\odot\,kpc^{-2}$	float
COLOR	$g-r$ and $g-z$ measured at z-band $R_{23.5}$ and R_{25} (z band only)	mag	float

Table 3.1: Photometric quantities for the MaNGA DESI photometric catalogue. The table includes calculated parameters along with the units and the data types. All parameters presented are uncorrected for Galactic extinction, inclination and cosmology. These parameters are available in three separate files for the DESI *grz* bands.

Column Name	Description	Unit	Data type
MANGA-ID	MaNGA Identification	–	string
PlateIFU	MaNGA Plate-IFU	–	string
ObjID	SDSS-DR15 photometric identification number	–	long int
RA	Object Right Ascension (J2000)	°	float
DEC	Object Declination (J2000)	°	float
Z	NSA or SDSS redshift	count	float
Dens_01	Number of neighbours within a 0.1-Mpc aperture	count	int
Dens_02	Number of neighbours within a 0.2-Mpc aperture	count	int
Dens_05	Number of neighbours within a 0.5-Mpc aperture	count	int
Dens_1	Number of neighbours within a 1-Mpc aperture	count	int
Dens_2	Number of neighbours within a 2-Mpc aperture	count	int
Dens_3	Number of neighbours within a 3-Mpc aperture	count	int
Mrank_AA	Identification of central or satellite galaxy; central (1) and satellite (>1)	rank	int
P_CEN	Probability of the galaxy being the central member in the halo	rank	float
P_SAT	Probability of the galaxy being a satellite in the halo	–	float

Table 3.2: Environmental properties for the MaNGA galaxies. The table includes each parameter along with the units and data types.

and R_{25} in the z band.

The ellipticity of the last measured isophote of a galaxy is used as the representative ellipticity of that galaxy on the sky.

These quantities are all calculated using linear interpolations of consecutive surface brightness profile or curve of growth data. If an interpolation is not possible, the last 25 percent of the profile is used to extrapolate up to that point using a linear fit. A flag for each structural parameter indicates an interpolation or extrapolation.

Concentration

The concentration of light, C_{28}, is a ratio of radii that enclose 20 per cent and 80 per cent of the total light:

$$C_{28} = 5\log(R_{80}/R_{20}). \tag{3.1}$$

A second measure of concentration, C_{25}, is also presented. Its use of R_{20} and R_{50} is operationally similar to Eq. 3.1. R_{50} is the effective radius, equivalent to $R_{\rm eff}$.

Stellar mass and surface stellar density

Stellar masses can be inferred from observed colours using stellar mass-to-light colour relations (MLCRs;Courteau et al. 2014). We use five different stellar mass estimates from the MLCRs presented in Roediger and Courteau (2015, hereafter RC15), Zhang et al. (2017, hereafter Z17), and García-Benito et al. (2019, hereafter B19). These MLCRs differ in their choice of stellar population synthesis model, adopted galactic extinctions, and input data used to calibrate the MLCR (global vs. resolved SED fits). Our stellar mass estimates use $g-r$ and $g-z$ colours measured at $R_{23.5}$ in the DESI-z band. The use of multiple colours yields better constraints on mass-to-light ratios (RC15, Z17, Gilhuly and Courteau 2018). The mass-to-light ratios (Υ_*) calculated from these colours are multiplied by the luminosity in the g, r, and z bands measured at $R_{23.5}$, which itself is inferred in the DESI-z band. This results in 30 stellar mass estimates that are averaged to provide a stellar mass estimate used throughout this study. The error in the stellar mass is the standard deviation of the 30 stellar mass measurements. MLCRs in RC15 and Z17 have only been calibrated for late-type systems and are exclusively applied to those systems. The stellar mass measurements for ETGs are thus measured using the MLCR presented in B19.

The stellar Υ_* enable the direct conversion of COGs into stellar surface density profiles. We calculate the stellar surface density within 1 kpc ($\Sigma_1 = M_{*,1\mathrm{kpc}}/\pi$) and the effective radius ($\Sigma_{\mathrm{eff}} = M_*/\pi R_{\mathrm{eff}}^2$) where M_* is the total stellar mass of the galaxy and $M_{*,1\mathrm{kpc}}$ is the stellar mass within the 1 kpc aperture.

The MIR stellar masses derived from $W1-W2$ colours and the MLCR of Cluver

et al. (2014) are shown as follows:

$$\log(M_*/L_{W1}) = -0.17 - 2.54 \times (W1 - W2), \tag{3.2}$$

where $L_{W1} = 10^{-0.4(M_{W1} - M_{\odot,W1})}$ is the luminosity, M_{W1} is the absolute magnitude in the $W1$ filter, and $M_{\odot,W1} = 3.24$ is the absolute magnitude of the Sun in $W1$ band. The same expression is used to get the luminosity for the WISE $W2$ photometric band, except that $M_{\odot,W2} = 3.27$.

These MLCRs use a Chabrier IMF, star formation and AGN activity, dust content, old stellar content, along with detailed stellar mass calibrations (Taylor et al. 2011). The colour in Eq. 3.2 is limited to the range $-0.05 \leq (W1 - W2) \leq 0.2$ as redder (bluer) sources may be contaminated by AGN or starburst activity (Jarrett et al. 2013).

Environmental parameters

Various environmental properties for 3207 MaNGA galaxies are presented in Table 3.2. The number of neighbours is extracted from the modified catalogue of Wilman et al. (2010) based on SDSS-DR7 (Abazajian et al. 2009). Galaxies are counted as neighbours if they fall within projected circular apertures of varying radii (0.25-3.0 Mpc) and their heliocentric Hubble flow velocities are within $\pm$1500 km s^{-1} of each other.

Central and satellite galaxies are identified via a stellar mass rank with a cylindrical aperture. The radius of the cylindrical aperture depends on the stellar mass of the galaxy and the depth of the cylinder is taken to be $\pm$ 2000 km s^{-1}. A galaxy with a stellar mass rank of 1 is identified as a central galaxy, whereas a mass rank greater than 1 is associated with a satellite galaxy. See Fossati et al. (2015) and Arora et al.

(2019) for a description of the stellar mass rank scheme to identify centrals and satellites. We have also cross-correlated the SDSS and MaNGA catalogues to compute the probability a galaxy being central or satellite according to the scheme of Fossati et al. (2017).

3.4.3 Parameter corrections

Our apparent magnitudes are corrected for Galactic extinction ($A_{\rm g}$), geometric projections (γ), internal extinction ($A_{\rm i}$), and k-correction ($A_{\rm k}$). Using the following transformation in each band:

$$m_{{\rm corr},\lambda} = m_{{\rm obs},\lambda} - A_{{\rm g},\lambda} - A_{\gamma,\lambda} - A_{{\rm k},\lambda}, \tag{3.3}$$

the Galactic extinction ($A_{\rm g}$) is obtained from the NSA-Sloan Atlas[9] (NSA; Blanton et al. 2011), which are themselves taken from Schlegel et al. (1998). The cosmological k-correction ($A_{\rm k}$) uses the template from Blanton and Roweis (2007).

Correcting for internal extinction and geometric projections is more challenging, and depends on morphological type. Note that the discussion below applies to late-type galaxies (LTGs); ETGs are assumed dust-free and trixial and no such corrections are applied. MaNGA LTGs are identified via the MaNGA Deep Learning Morphological VAC (MDLM-VAC; Domínguez Sánchez et al. 2018). The effects of projection on the sky bias the measurement of intrinsic properties, hence our attempt to recover face-on equivalent measures with a simple model (Holmberg 1958; Stone et al. 2021a). A common correction for the deprojection of structural parameters involves a linear fit between the desired projected variable and the log of the cosine of the

[9] http://www.nsatlas.org/

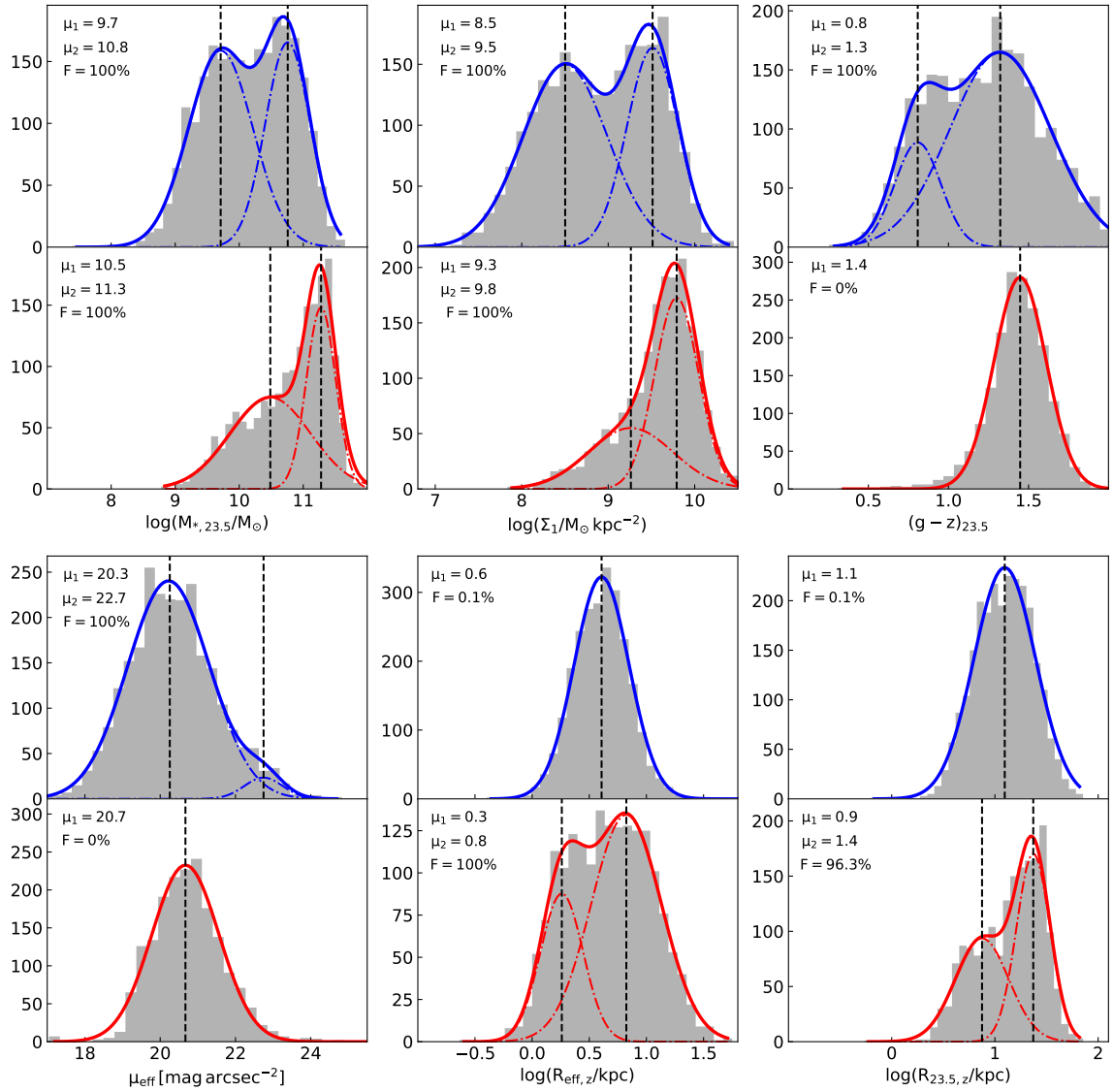

Figure 3.3: Distribution of MaNGA galaxy properties separated by galaxy morphology; LTGs in blue and ETGs in red. Shown are the stellar mass ($M_{*,23.5}$), stellar mass surface density within 1 kpc (Σ_1), colour measured within $R_{23.5}$ ($(g-z)_{23.5}$), effective surface brightness ($\mu_{\rm eff}$), effective radius ($R_{\rm eff}$), and isophotal radius at 23.5 mag arcsec^{-2} ($R_{23.5}$). The grey histogram in each panel shows the underlying data distribution. Each LTG/ETG property is fit with a double or single Gaussian; the optimal distribution is determined via the F-test (see the text for details). The data in each panel give the Gaussian mean(s) of the unimodal (bimodal) distributions and the F-test confidence for a single vs. double Gaussian distribution.

T-Type	N	$R_{23.5,g}$	$R_{23.5,r}$	$R_{23.5,z}$	$L_{23.5,g}$	$L_{23.5,r}$	$L_{23.5,z}$	$(g-r)_{23.5}$	$(g-z)_{23.5}$	$\log \Sigma_1$
(1)	(2)	(3)	(4)	(5)	(6)	(7)	(8)	(9)	(10)	(11)
0–10	1907	0.28 ± 0.03	0.25 ± 0.03	0.23 ± 0.03	-0.34 ± 0.08	-0.24 ± 0.09	-0.12 ± 0.09	0.22 ± 0.02	0.51 ± 0.04	0.01 ± 0.08
0–3	829	0.38 ± 0.05	0.37 ± 0.05	0.35 ± 0.05	-0.05 ± 0.11	0.10 ± 0.12	0.25 ± 0.12	0.34 ± 0.03	0.72 ± 0.04	0.43 ± 0.11
4–5	958	0.21 ± 0.04	0.19 ± 0.04	0.18 ± 0.04	-0.42 ± 0.11	-0.28 ± 0.11	-0.15 ± 0.11	0.26 ± 0.02	0.62 ± 0.04	0.05 ± 0.11
6–10	164	0.31 ± 0.08	0.26 ± 0.08	0.22 ± 0.08	-0.28 ± 0.23	-0.28 ± 0.24	-0.08 ± 0.24	0.01 ± 0.03	0.09 ± 0.08	-0.25 ± 0.18

Table 3.3: Inclination correction terms, γ, for various galaxy structural parameters in different photometry bands. Column (1) shows the T-Type bins used for the correction; column (2) presents the number of data points used for the fitting; and columns (3)–(11) show the correction factors for different structural properties. The first row gives γ for all galaxies; the next three rows give γ for specific morphological bins.

inclination (Giovanelli et al. 1994). This method is expressed in Eq. 3.4:

$$\log X_0 = \log X_i + \gamma \log(\cos(i)), \tag{3.4}$$

where X_0 is the variable corrected to face-on, X_i is the observed measurement, i is the inclination of the galaxy on the sky corrected for the stellar disc thickness and calculated using Eq. 3.5, and γ is the fitted correction factor:

$$\cos^2 i = \frac{(b/a)^2 - q_0^2}{1 - q_0^2}; \quad (q_0 = 0.13). \tag{3.5}$$

These corrections can be performed on a complete sample (Masters et al. 2010) or applied to subsamples based on galaxy properties for which inclination corrections are robust and known such as HI line widths (Tully et al. 1998), galaxy morphology (Maller et al. 2009; Masters et al. 2010), or total infrared luminosity (Devour and Bell 2019). The correction factor, γ, encompasses effects due to geometry (line-of-sight projection), stellar populations, and dust extinction as a function of inclination.

We solve Eq. 3.4 for γ with a forward least-squares fit between the desired variable and $\cos(i)$ in log space. For the fitting, we restrict the sample to an inclination range of

Scaling relation	Uncorrected		Corrected T–Types 1-10		Corrected 3 T-Type bins	
	m	σ	m	σ	m	σ
(1)	(2)	(3)	(4)	(5)	(6)	(7)
Σ_1–$M_{*,23.5}$	0.96 ± 0.01	0.24 ± 0.01	0.96 ± 0.01	0.23 ± 0.01	0.96 ± 0.01	0.23 ± 0.01
$R_{23.5,z}$–$M_{*,23.5}$	0.34 ± 0.01	0.11 ± 0.01	0.34 ± 0.01	0.11 ± 0.01	0.35 ± 0.01	0.10 ± 0.01
$R_{23.5,z}$–Σ_1	0.30 ± 0.01	0.17 ± 0.01	0.29 ± 0.01	0.16 ± 0.01	0.30 ± 0.01	0.17 ± 0.01
$R_{23.5,z}$–$L_{23.5,z}$	0.41 ± 0.01	0.08 ± 0.01	0.41 ± 0.01	0.09 ± 0.01	0.41 ± 0.01	0.09 ± 0.01
Σ_1–$L_{23.5,z}$	0.94 ± 0.01	0.30 ± 0.01	0.95 ± 0.01	0.30 ± 0.01	0.93 ± 0.01	0.29 ± 0.01
$(g-z)_{23.5}$–$L_{23.5,z}$	0.24 ± 0.01	0.24 ± 0.01	0.25 ± 0.01	0.22 ± 0.01	0.22 ± 0.01	0.21 ± 0.01

Table 3.4: Variation of slopes and scatters of galaxy structural scaling relations due to inclination corrections. Column (1) indicates the scaling relation; columns (2) and (3) give the uncorrected slope and scatter; columns (4) and (5) give the slope and scatter with a single full-sample correction (all T-Types); columns (6) and (7) give the slopes and scatter with corrections applied to three morphological bins.

$30° < i < 80°$ and assume an intrinsic thickness of $q_0 = 0.13$ to convert the ellipticity to inclination (Hall et al. 2012; Ouellette et al. 2017). Errors on γ are calculated using bootstrap sampling. Table 3.3 tabulates the correction factor, γ, for various galaxy structural properties of the MaNGA LTG sample in the *grz* bands. We present γ for the full sample (first row of Table 3.3) and split into three morphological bins done using the MLDM-VAC (last three rows of Table 3.3).

The absolute value of these correction factors differ from those presented in Masters et al. (2010) and Stone et al. (2021a). However, in all cases, the correction factors are small. For example, the correction factor for an isophotal radius in the transparent case is $\gamma \approx 2.3$ (Giovanelli et al. 1994), compared to our correction factor of $\sim 0.25 \pm 0.02$.

Ideally, an accurate inclination correction model should yield a reduction of the observed scatter in various galaxy scaling relations. This concept is tested in Table 3.4, which presents the variation of the slopes and scatter for a suite of structural galaxy scaling relations with inclination corrections. The slopes and scatter are found to

be robust against inclination corrections for nearly all scaling relations presented. A significant variation in the scatter of the $(g-z)_{23.5} - L_{23.5,z}$ relation is found for both inclination correction models, with or without binning by morphology. In light of the null variation in the slopes and scatter of galaxy scaling relations, we apply inclination corrections to our photometry without reducing our sample into various morphological bins.

3.5 Parameter Distributions

This section provides an overview of some important MaNGA galaxy properties and their range. Figure 3.3 offers a broad appreciation of the distribution of structural properties for galaxies in the MaNGA public release. For instance, if dwarf galaxies are defined as having a stellar mass $\log(M_*/M_\odot) \leq 9.5$ (Woo et al. 2008; Ouellette et al. 2017), only 11 percent of our galaxies are dwarfs. Our results in this section clearly highlight the presence of distinct populations in each of the LTG and ETG categories. The latter is made clear through the unimodal and bimodal trends displayed by some structural and dynamical parameters (Tully and Verheijen 1997; McDonald et al. 2009; Sorce et al. 2013; Ouellette et al. 2017). We define a unimodal distribution as one described by a normal distribution. The figure of merit to distinguish a bimodal from a unimodal distribution is the F-test that gives the probability that the observed distributions originate from two distinct Gaussian populations rather than a single one. These populations are represented by single or double Gaussian fits in Figure 3.3. F-test confidence results for a double vs a single Gaussian distribution and the fitted means for the double/single population(s) are indicated in each panel. Unimodal distributions are found for LTG sizes (effective and isophotal) and ETG

effective surface brightnesses and colour.

The following properties for LTGs show bimodal signatures; stellar mass (top left-hand panel), stellar surface density with 1 kpc (middle panel), effective surface brightness (bottom left-hand) and colour (top right-hand) measured at 23.5 mag arcsec^{-2} . The notion of surface brightness bimodalities has been addressed at some length in (Ouellette et al. 2017, and references therein). Surface brightness bimodalities in LTGs are especially conspicuous at dust-insensitive wavelengths such as the z band (Sorce et al. 2013).

For ETGs, stellar mass, stellar surface density within 1 kpc, isophotal radius at 23.5 mag arcsec^{-2} , and effective radius show bimodal signatures. A bimodality in the galaxian properties shown here reflects environmental influences, varying merger and star formation histories, and different radial dark matter fractions, which all play a key role in galaxy evolution. The coupling of these structural bimodalities with bimodal dynamical properties (if any) would greatly enhance galaxy formation scenarios.

The detailed investigation of bimodal trends in scaling relations, and the identification of galaxy subclasses, will be presented elsewhere. For now, we appreciate the need to consider one or two populations in fitting scaling relations over a range of galaxian properties.

3.6 Literature Comparisons

The following section presents comparisons of our galaxy structural parameters with similar values found in the literature. We first present a multifaceted comparison of the 1D surface brightness profiles generated using model-independent (e.g. AUTOPROF,

XVISTA) and model-dependent (e.g. GALFIT, PYMORPH) methods. Effective (half-light), isophotal radii and apparent magnitudes from the MPP-VAC of F19 are also compared with our photometry. This comparison recognizes that the MPP-VAC reports parameters from circularized light profiles. We caution that this operation is especially uncertain in light of unknown dust distributions, non-axisymmetric features and disc thicknesses, and the vagaries of 2D image decompositions (Gilhuly and Courteau 2018). Total magnitudes, and effective radii, should be the least model-biased parameters from F19, and hence our comparison below. Stellar masses are also compared with a PCA-based stellar mass estimation technique from Pace et al. (2019, hereafter P19). For the sake of comparison, parameters presented in this section are not corrected for Galactic extinction, inclination, and cosmology.

3.6.1 Surface brightness profile comparisons

Figure 3.4 compares 1D r-band surface brightness profiles extracted from DESI images (black points) by us and from SDSS images by GC18 (red points). The excellent agreement between those profiles results from quality DESI/SDSS imaging and the robust non-parametric surface brightness profile extraction with XVISTA and AUTOPROF. Figs. 3.1 and 3.4 compare various global properties between XVISTA and AUTOPROF, showing that both codes reproduce local variations in 1D surface brightness profiles with high fidelity.

Our catalogue also overlaps with F19 and GC18. The latter two studies used the 2D image fitting algorithm GALFIT to obtain Bulge-Disc decompositions for their samples based on the MaNGA and CALIFA samples, respectively. A total of 16 galaxies overlap between the MaNGA (us and F19) and CALIFA (GC18) samples.

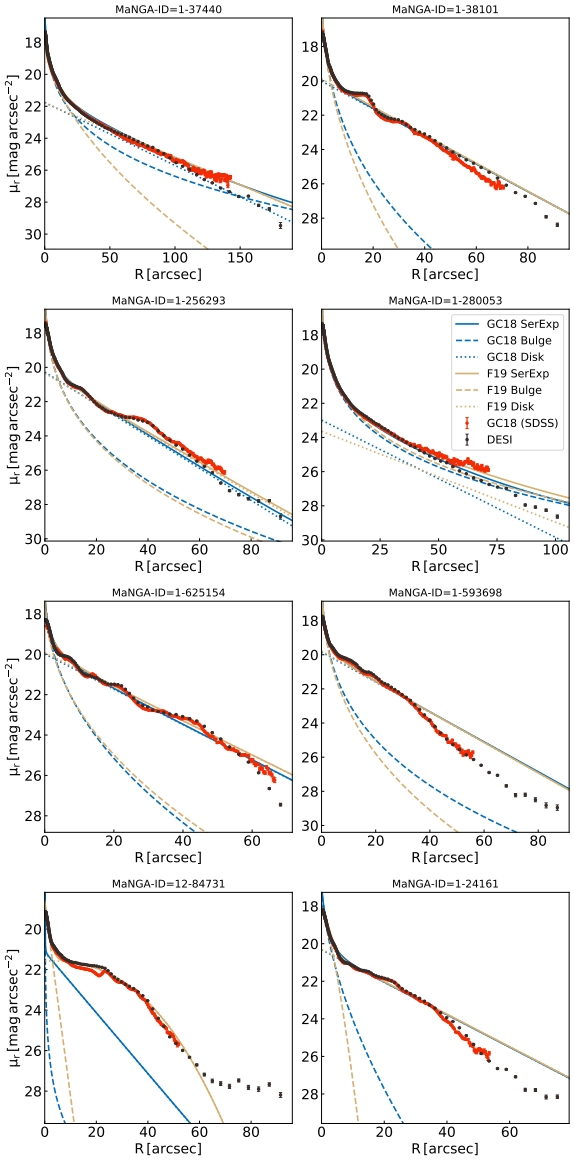

Figure 3.4: Comparison of our DESI-based 1D *r*-band surface brightness profile (black dots) with the SDSS-based surface brightness profile (red dot) of GC18. Also compared are the 2D Sérsic + Exponential decompositions using GALFIT by GC18 (cyan solid lines) and F19 (gold solid line). The Sérsic + Exponential decompositions are separated by their respective bulge (dashed line) and disc (solid line) contributions. Missing coloured lines represent failed fits by the original authors.

These overlapping galaxies enable a comparison of our independent results.

In Figure 3.4, the blue and gold solid line show the Sérsic + Exponential decompositions by GC18 and F19 respectively, for eight galaxies using GALFIT. We caution that the MPP-VAC (F19) present total apparent magnitudes in the circularized plane of the galaxy, i.e. corrected to face-on based on the simplest assumptions of a dust-free, infinitesimally-thin disc. The recovery of total apparent magnitudes (m) from the MPP-VAC in the plane of the sky must therefore be made with the equation $m'_r = m_r + 2.5\log(b/a)$ for the bulge and disc components, where b/a is the axis ratio of the galaxy.

The appreciation of more complex disc systems, with their triaxial bulges, thicker mid-planes, and sporadic dust extinction, calls for a more extensive modelling. Stone et al. (2021a) performed an extensive analysis of inclination corrections for disc galaxies. While some correction models showed a scatter reduction of various galaxy scaling relations, little agreement between different correction models was found.

For six out of the eight galaxies, the two independent GALFIT decompositions return Sérsic + Exponential models that can differ by as much as $\sim$0.4 mag arcsec^{-2}, demonstrating the great subjectivity between these model-dependent solutions while our non-parametric comparison only show differences on the order of $\sim$0.09 mag arcsec^{-2}. In some cases, only one user can find a valid solution for the GALFIT decomposition. Where both fits converge, they often find different bulge to disc ratios with a difference of $\sim$0.3 dex. Similar caveats for Bulge-Disc decompositions for the same galaxies using two different image fitters (GALFIT and IMFIT Erwin 2015) by GC18 showed discrepant results as well.

The large variations between the solutions of GC18 and F19, as well as the analysis

presented in GC18, remind us that generic parametric solutions are especially fragile and inconclusive. For these reasons, an analysis of galaxy structure or scaling relation should rely on the non-parametric characterization of surface brightness profiles.

3.6.2 Effective sizes

Fig. 3.5 compares our non-parametric $R_{\rm eff}$, measured in the DESI r band, with those found in F19 for a single Sérsic fit with PYMORPH. We have used the MDLM-VAC to divide our sample into LTG and ETG categories. Size measurements are taken in the r-band to enable a direct comparison with PYMORPHresults. PYMORPHand AUTOPROFagree well at small radii; at larger radii AUTOPROFyields smaller sizes than PYMORPH.

This behaviour is expected as a single Sérsic fit does not capture all the light from the outer regions of a galaxy, with low S/N, yielding a larger estimate for $R_{\rm eff}$. The effect is amplified for larger PYMORPH$R_{\rm eff}$ and for the ETG sample due to their higher light concentration relative to LTGs. For the complete population, a single Sérsic fit from F19 results in larger effective radii by 0.21 dex compared to our results.

The agreement between our methods improves with the two-component fits from F19. Fig. 3.6 shows a comparison between our non-parametric effective radii and those extracted from two-component Sérsic exponential fits. Both ETGs and LTGs are in agreement, though at large radii the scatter increases.

While the PYMORPHtwo-component fit improves the overall agreement with AUTOPROF, there remains significant random variations, especially with quantities determined relative to the total light of the galaxy, like the effective radius, $R_{\rm eff}$. The latter

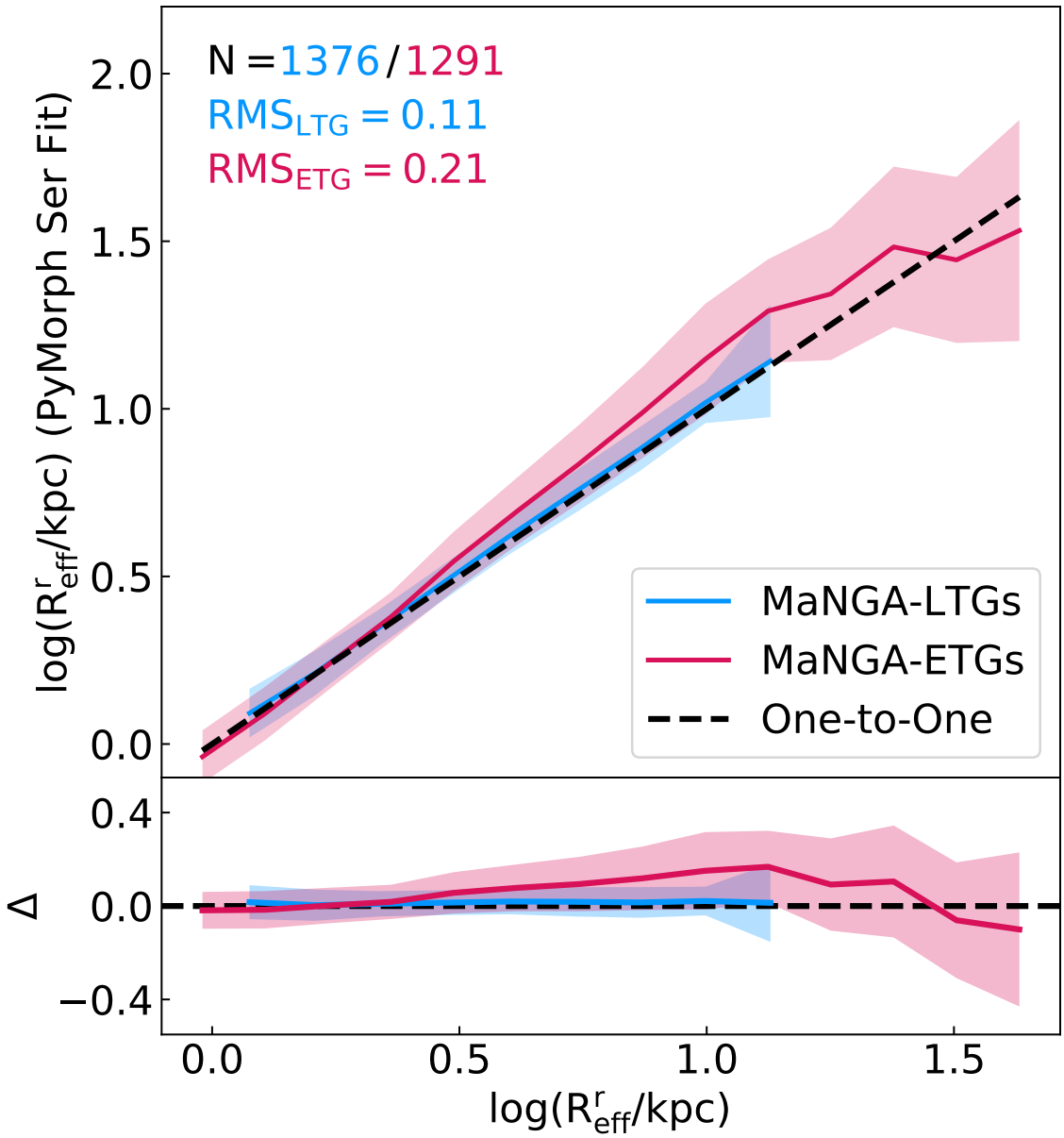

Figure 3.5: Comparison of our model-independent effective radii from DESI r-band surface brightness profiles with those from a single Sérsic fit from F19. The solid lines show the median for MaNGA-LTGs (blue) and MaNGA-ETGs (red) and the shaded region shows the scatter within a bin of size 0.12 dex. The dashed line shows the one-to-one line. The inset text shows the number of data points and root mean square (rms) for the LTG and ETG populations. The bottom panel shows the residual $\Delta = \log(R^r_{\rm eff}[PYMORPH]/R^r_{\rm eff})$.

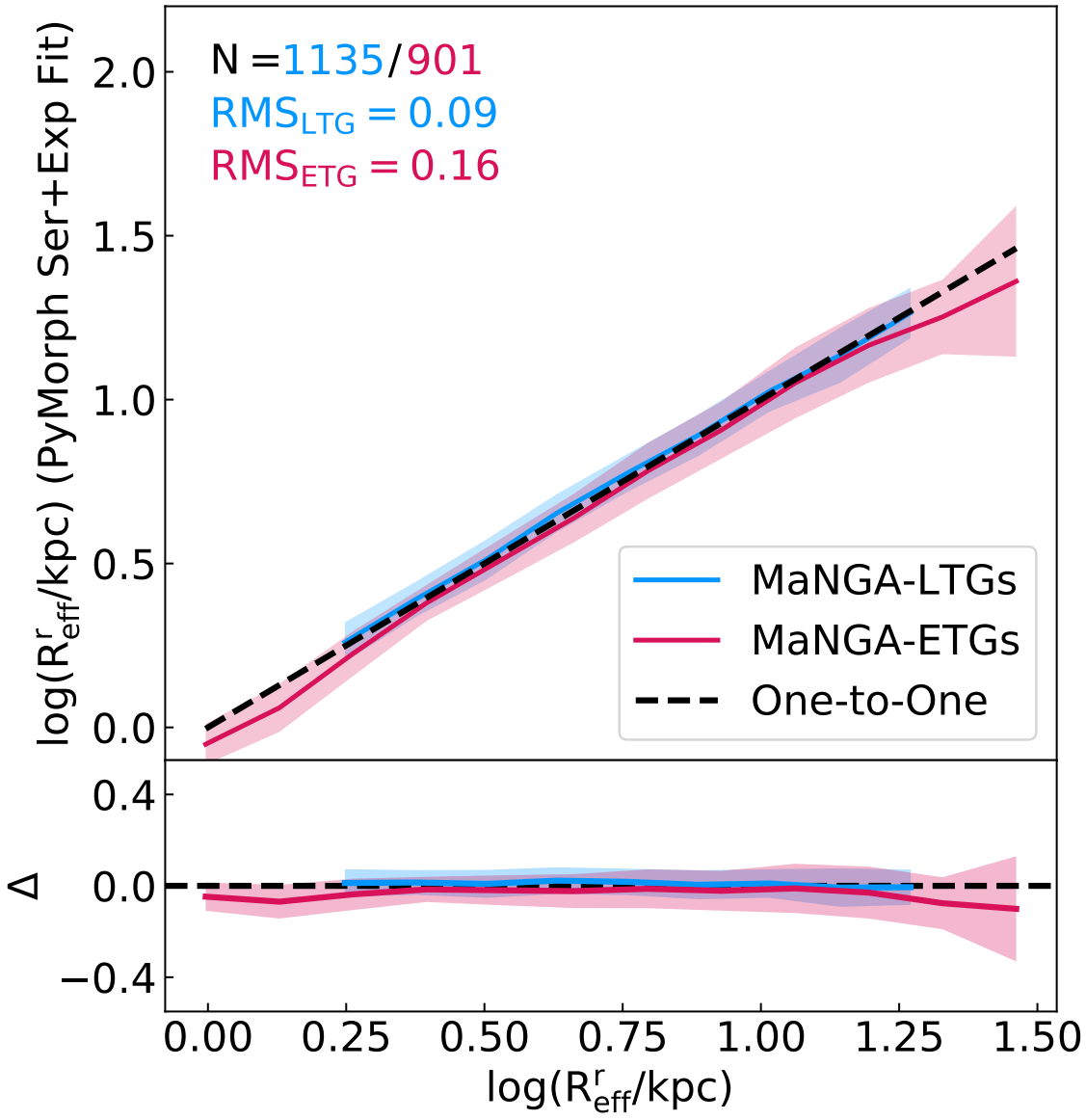

Figure 3.6: Same as Fig. 3.5 but the y-axis uses effective radii from Sérsic + Exponential fits by F19.

suffered from poor reproducibility, largely due to the uncertain definition of total apparent magnitude of a galaxy. In a similar vein, Hall et al. (2012) found that the scatter of velocity–radius–luminosity (VRL) scaling relations is reduced with isophotal radii and Trujillo et al. (2020) found that a stellar mass density radius reduces scatter in the size–mass relation. Similar impressions were echoed by GC18 who found differences as large as 0.16 dex (45%) between non-parametric and model-dependent measures of $R_{\rm eff}$ for CALIFA galaxies (Walcher et al. 2014). González-Samaniego et al. (2017) also used the FIRE simulations to point out the same pathology about $R_{\rm eff}$. For the size-dependent analyses that follow (Section 3.8), we limit our use of effective radii and pay special attention to isophotal size metrics. The scatter in the size–mass relation is discussed in Section 3.8.

3.6.3 Isophotal sizes

The parameters from the MPP-VAC can be used to construct de-projected surface brightness profiles in order to infer the isophotal radii measured at 23.5 mag arcsec^{-2}. These are compared with matching size measurements from the DESI photometry in Figure 3.7. Disagreements in isophotal sizes are larger for galaxies with preferred Sérsic model ($\sim$0.05 dex) compared to galaxies with preferred Sérsic+Exponential model ($\sim$0.04 dex). This reaffirms the results from Section 3.6.2 that simple Sérsic models cannot account for all of the galaxy light.

The comparison of model-independent isophotal radii measured with XVISTA and AUTOPROFin Figure 3.1 showed more consistency (0.02 dex), indicating that non-parametric modelling of galaxies is more reproducible. The larger rms ($\sim$0.05 dex) is explained by the vagaries in parametric modelling from GALFIT. Comparing Figs.

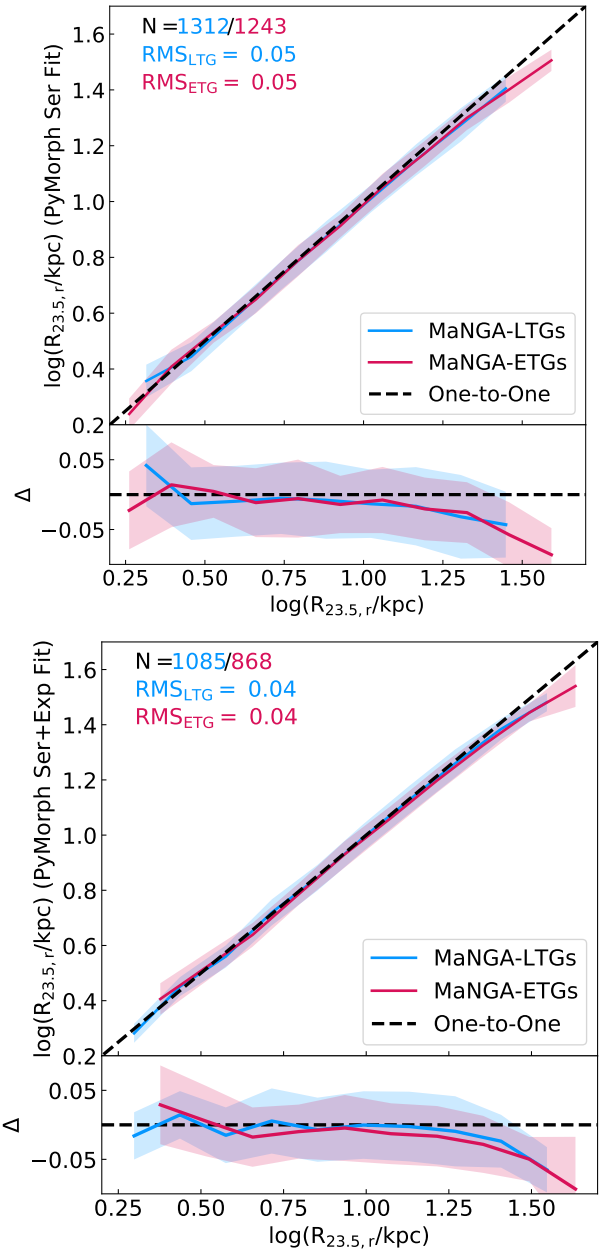

Figure 3.7: Comparison of our model-independent isophotal radius measured at 23.5 mag arcsec^{-2} from DESI r-band surface brightness profiles with model-dependent PYMORPHdecomposition from F19. The solid lines show the median for MaNGA-LTGs (blue) and MaNGA-ETGs (red), and the shaded region shows the scatter in a bin of width 0.12 dex. The dashed line is the one-to-one line. The legend shows the number of data points and rms for the LTG and ETG populations. The top and bottom panels show the Sérsic and Sérsic + Exponential fits, respectively. The bottom panels show the residual $\Delta = \log(R^r_{23.5}[PYMORPH]/R^r_{23.5})$.

3.7 and 3.6 demonstrates that isophotal sizes ($R_{23.5}$) are more consistent than sizes based on fraction of total light even while comparing non-parametric with model-dependent sizes.

3.6.4 Apparent magnitudes

Next, total apparent magnitudes extracted from DESI photometry are compared with MPP-VAC magnitudes from F19. The total apparent magnitudes are both calculated within 25 mag arcsec^{-2} and are not corrected for cosmology, Galactic and inclination extinctions. While total magnitudes are here mostly reported at the 23.5 mag arcsec^{-2} levels to maximize comparisons with literature values, the current comparisons (Figure 3.8 and 3.9) at the 25 mag arcsec^{-2} isophotal level takes advantage of the superior DESI imaging depth. Once again, the F19 total apparent magnitudes are deprojected according to the expression, $m' = m + 2.5\log(b/a)$. Fig. 3.8 compares apparent r-band magnitudes from our DESI surface brightness profiles with Sérsic fit magnitudes from F19, in various galaxy morphological bins. The rms values are given in dex (magnitude divided by 2.5). For both ETGs and LTGs, the DESI surface brightness profiles from AUTOPROFare ~ 0.10 dex brighter than those from PYMORPHwith a Sérsic fit. This further highlights that a single Sérsic fit fails to capture all the light from the object, leading to disagreements in effective galaxy sizes (Section 3.6.2).

Surprisingly, the addition of a second, exponential, component in PYMORPHfor MaNGA galaxies results in poorer fits (Figure 3.9). While random variations between PYMORPHand AUTOPROFfor LTGs are reduced with an additional component,

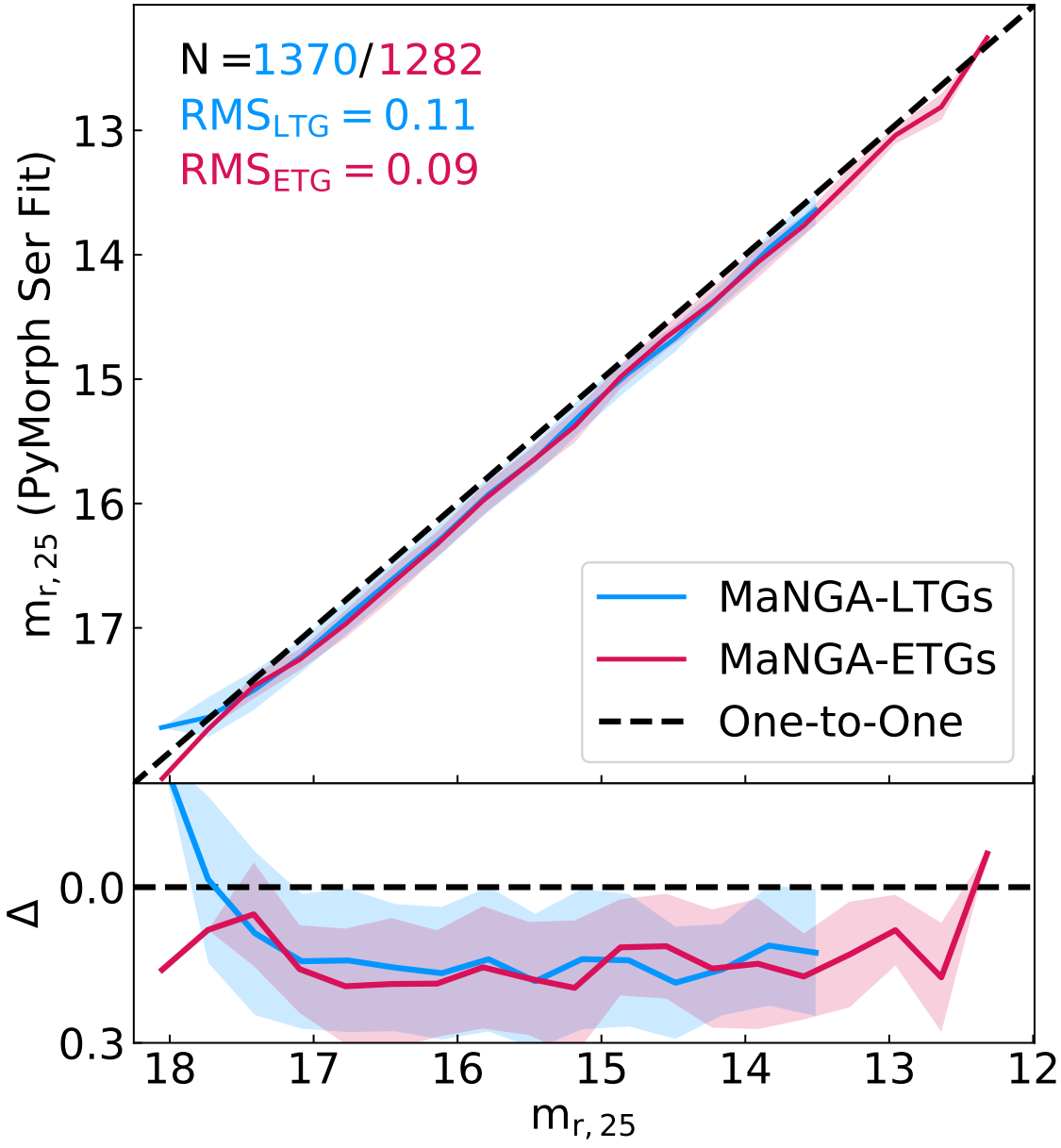

Figure 3.8: Comparison of our model-independent apparent magnitudes from DESI r-band surface brightness profiles with those from a single Sérsic fit from F19. For both methods, the total apparent magnitude is measured within the 25 mag arcsec^{-2} isophote. The bottom panel shows the residual.

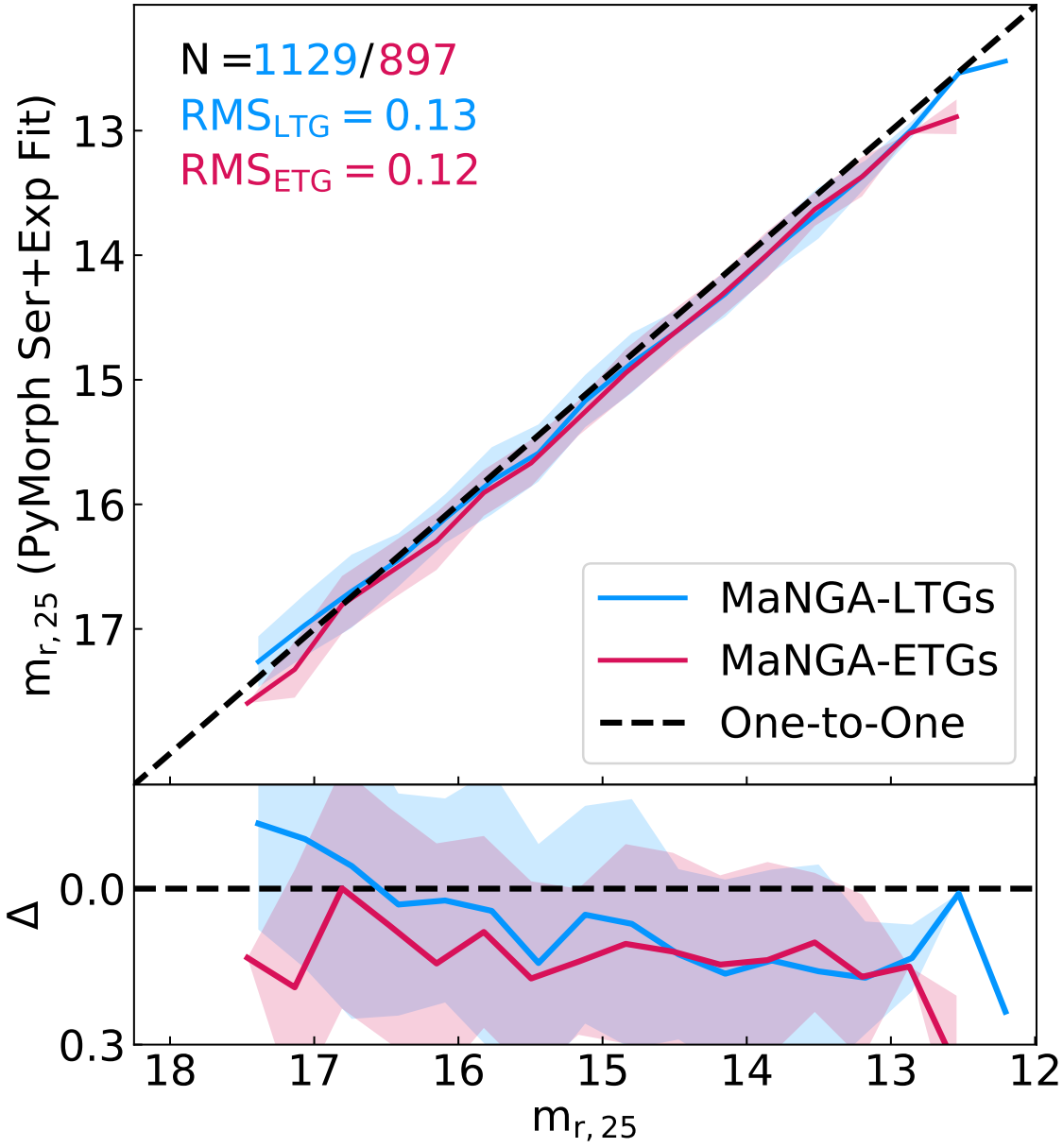

Figure 3.9: Same as Fig. 3.8 with apparent magnitude on the y-axis for a double Sérsic and exponential fit from F19.

.

PYMORPHstill underestimates the total light (calculated using the analytic Sérsic function) relative to our analysis. The shaded regions for both LTGs and ETGs in Figure 3.9 represent the inter-quartile range of the residuals. With our large sample, we can estimate the random error (as $1/\sqrt{N} \sim 0.03\,\mathrm{dex}$) to be very small, and the rms errors are thus largely systematic. Indeed, disagreements with our apparent magnitudes emerge largely from the model-dependent nature of the F19 photometric analysis that do not account for non-axisymmetric features such as bars, rings and spiral arms. Features unaccounted for by PYMORPHwill systematically yield fainter total magnitudes relative to non-parametric estimates. Along with the surface brightness profile comparison in Section 3.6.1, the size and apparent magnitude comparisons further reinforce the benefits of using model-independent technique for measuring galaxy structural properties.

3.6.5 Stellar masses

Figure 3.10 presents a comparison of our stellar mass estimates on the x-axis versus various literature sources on the y-axis. Our stellar masses are an amalgam of 30 variants derived from optical MLCRs (RC15; Z17; B19). These MLCRs use stellar population synthesis (SPS) models from Bruzual and Charlot (2003, hereafter BC03) and Conroy and Gunn (2010). The MLCRs presented in B19 apply to all galaxy morphologies, while RC15 and Z17 were only calibrated for LTGs and are here only used for those systems. The stellar masses from P19 in panel (a) were derived using Υ_* ratios calculated with a principal component analysis (PCA) that finds the best-fitting synthetic spectra for each MaNGA spaxel observation. Our stellar masses are measured within $R_{23.5}$ in the z band, while those from P19 are calculated using the

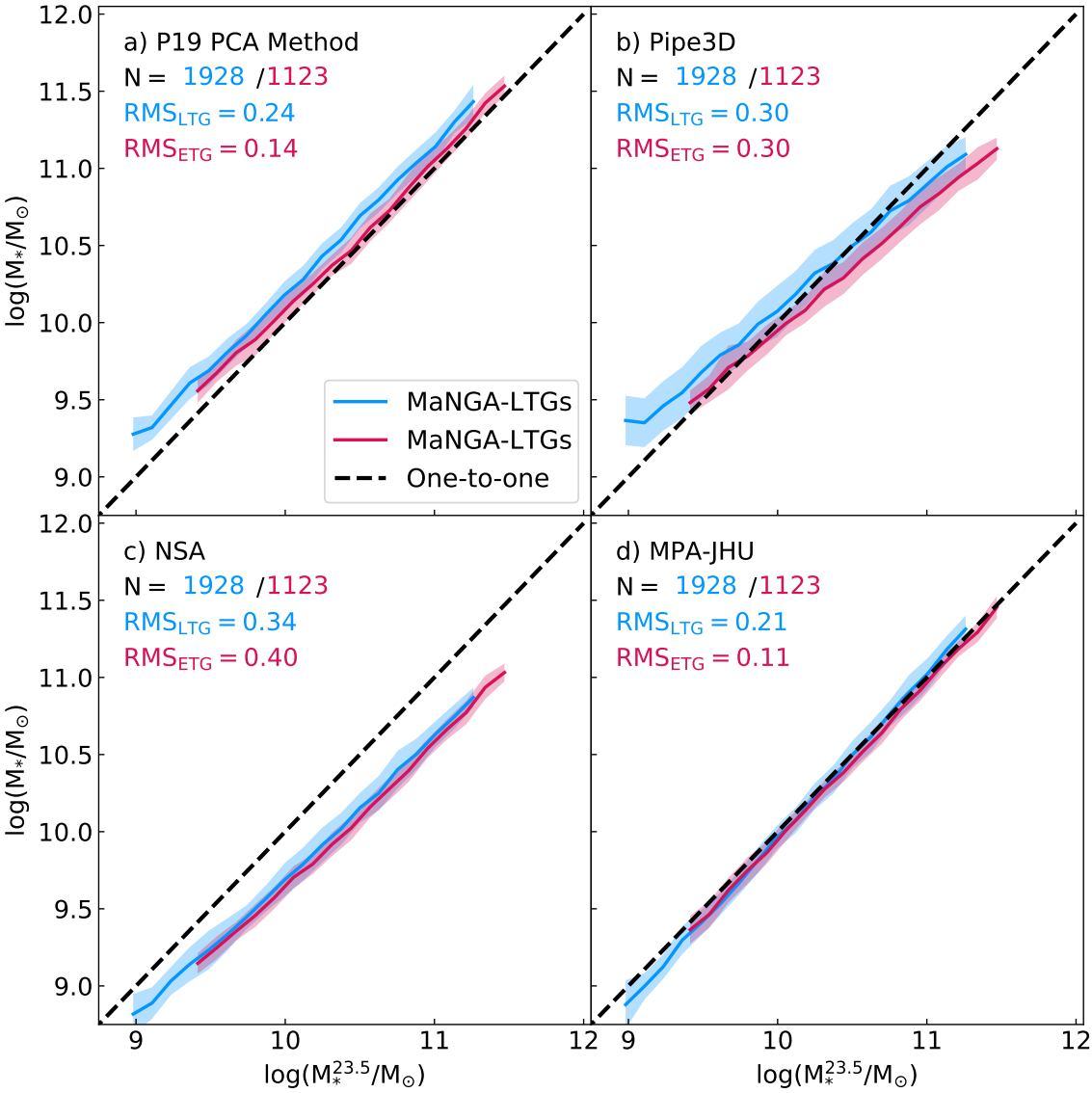

Figure 3.10: Comparisons of our stellar mass estimates from DESI photometry measured within $R_{23.5,z}$ shown on the x-axis versus those from various literature sources. The y-axes compare stellar mass estimates from panel (a): P19; panel (b): Pipe3D (Sánchez et al. 2016); panel (c): NSA photometry (Blanton and Roweis 2007); and panel (d) the MPA-JHU catalogue (Kauffmann et al. 2003; Brinchmann et al. 2004). The colour scheme matches that of Fig. 3.5. The solid line shows the median trends and the shaded regions represent the scatter within a bin. The top left inset gives the number of LTG (blue) and ETG (red) galaxies, as well as the rms for the respective stellar mass differences.

footprint of the MaNGA IFU with aperture correction performed using NSA excess fluxes.

The aperture-corrected stellar masses from P19 appear to be systematically larger than our estimates, especially for MaNGA LTGs (panel a of Figure 3.10). The comparison yields an rms offset of 0.25 (0.14) dex and a scatter of 0.09 (0.08) for the LTG (ETG) populations. These systematic differences are likely due to the adopted star formation histories (SFHs). P19 adopted smooth SFH templates; the omission of bursts in SFHs can bias the Υ_* high (RC15), resulting in larger stellar mass estimates. These systematic effects are more pronounced for LTGs as these systems have more bursty and active star formation histories. However, the reported rms offsets for this comparison are well within the systematic errors expected for MLCRs. Panel (b) compares our stellar masses against those calculated from Pipe3D (Sánchez et al. 2016); these are integrated within the FOV of the MaNGA IFU. We find an even larger rms offset and scatter range than our comparison with P19. The Pipe3D comparison shows a large rms difference of 0.30 dex and a scatter of 0.16 (0.1) dex for the LTGs (ETGs). For both LTGs/ETGs, our stellar mass estimates at the low (high) mass end are smaller (larger) than Pipe3D. The difference between our respective stellar mass estimates may arise from Υ_* calculation, which is done pixel by pixel for Pipe3D whereas our Υ_* is calculated using a global colour.

Panel (c) in Figure 3.10 compares stellar mass estimates inferred via K-corrected elliptical Petrosian photometry from the NSA (Blanton and Roweis 2007). In our stellar mass comparisons, NSA estimates present the largest discrepancy with the our photometry. Sources for this offset include (i) missing flux in the NSA photometry, (ii) adoption of simple stellar populations (SSPs) for the Υ_* conversions, and/or (iii)

the use of Petrosian magnitudes. The NSA elliptical-Petrosian photometry has been shown to yield bluer colors ($\Delta(g-r) = 0.046 \pm 0.008$) that the SDSS photometry for the complete MaNGA sample P19, thus causing systematic differences in stellar mass estimates.

Finally, Panel (d) compares our stellar mass estimates with those from the MPA-JHU catalogue (Brinchmann et al. 2004). Their stellar mass estimates are calculated using the z-band stellar Υ_* ratio obtained using the SDSS spectra that best model the H δ and D4000 absorption features applied to z band luminosities. The comparison in Panel (d) shows a superb match between the MPA-JHU and our photometry with a median across all bins lying close to the 1:1 line and an rms of 0.23 (0.12) dex for the LTGs (ETGs). Comparing all stellar mass estimates presented in Figure 3.10, MPA-JHU has the best agreement for both morphological types.

3.7 MIR Structural Parameters

This section presents a comparison of galaxy structural parameters extracted from our optical and MIR photometry. We first caution that surface brightnesses sampled with different pixel resolutions, as is the case here with the DESI and WISE data, cannot be compared directly unless profiles are all sampled (degraded) to the lowest resolution. Therefore, only integrated quantities between DESI and WISE data are compared below.

Fig. 3.11 shows the *W1* and DESI z-band luminosities measured at $R_{23.5,z}$. For the complete sample, *W1* luminosities are typically larger than z-band luminosities by $\sim$0.3 dex, as a result of a greater sensitivity of the *W1* bandpass to the dominant low mass (older) stellar population and lesser dust extinction in the *W1* band.

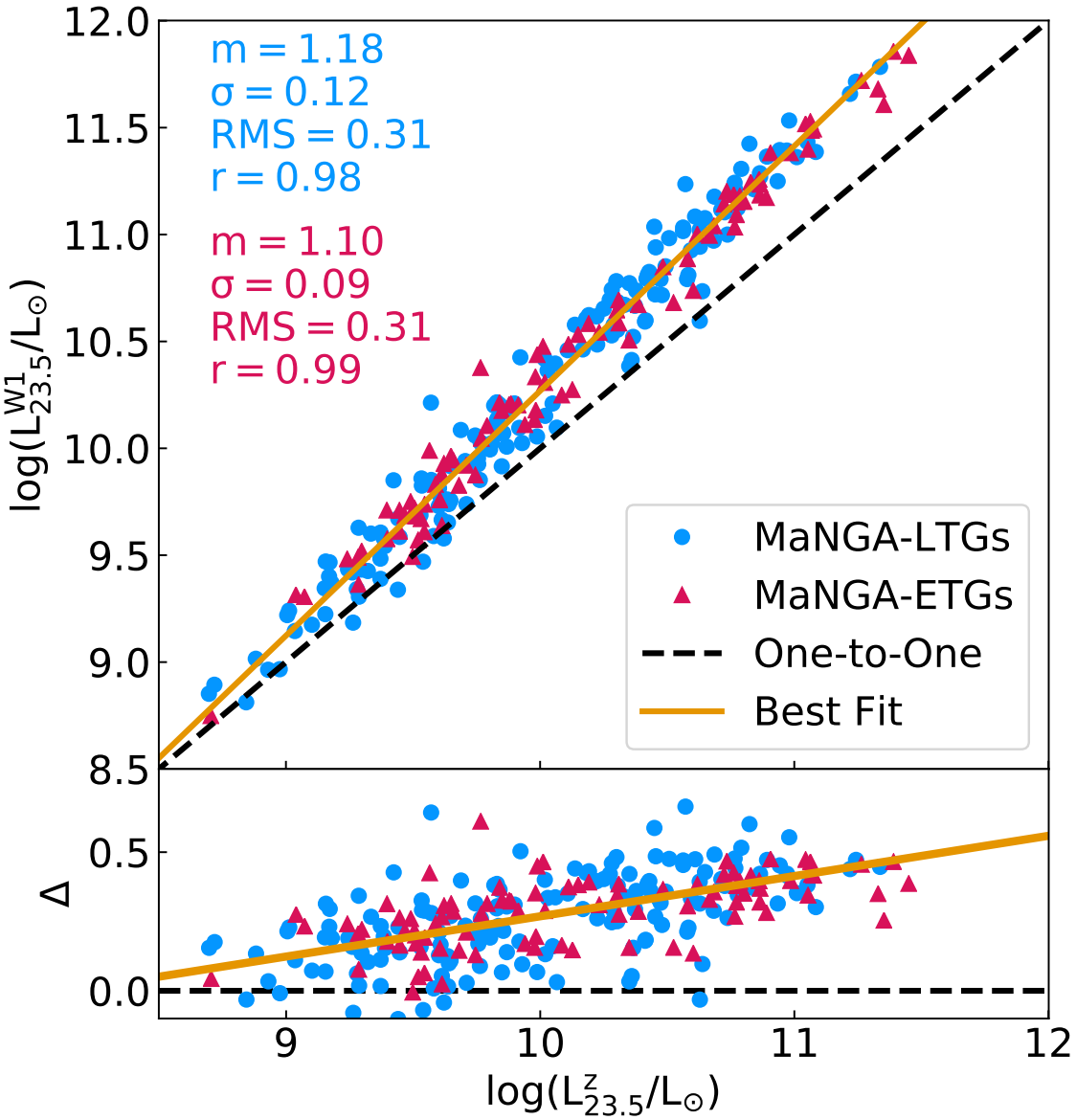

Figure 3.11: Comparison of total integrated luminosity inferred from DESI and *W1* images measured at $R_{23.5,z}$. The blue circles present the MaNGA-LTGs, and red triangles present MaNGA-ETGs. The orange line shows the best fit for the complete population and inset text presents statistics for the two populations.

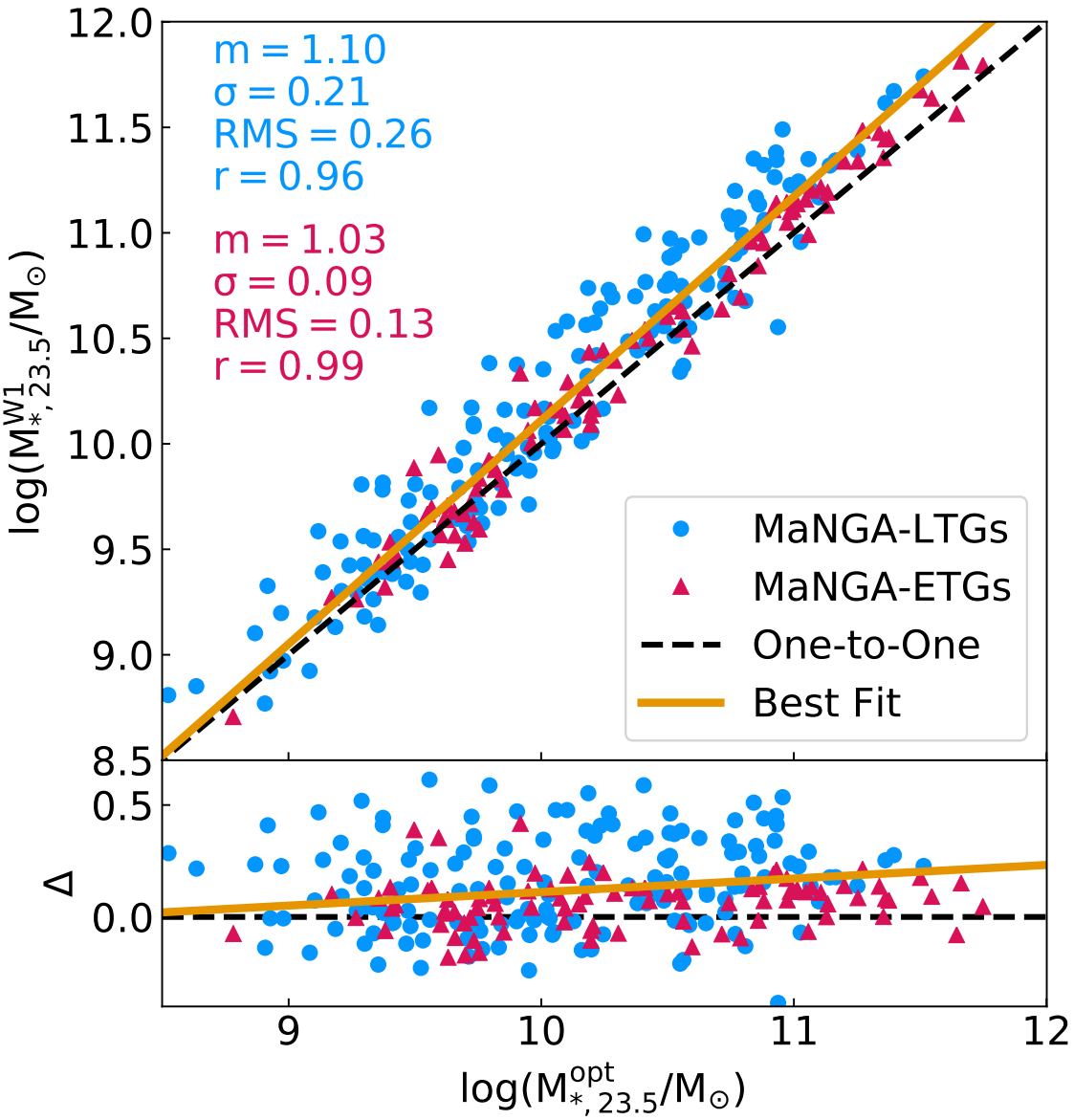

Figure 3.12: Comparison of stellar masses inferred from DESI and *W1* images measured at $R_{23.5,z}$. The format is the same as Figure 3.11. For LTGs, "opt" stellar masses are an average of five MLCRs presented in Section 3.4.2. For ETGs, "opt" stellar masses are measured using the MLCR of B19.

Furthermore, the *W1*-z colour term grows significantly with luminosity, as seen in the residual panel of Fig. 3.11. The scatter between DESI z and *W1* luminosities is tighter for the MaNGA-ETGs (than LTGs) largely due to their star formation activity being quenched (Cluver et al. 2014). The larger scatter for the LTG population is also indicative of a more diverse stellar population and larger dust content.

Finally, Fig. 3.12 compares stellar masses inferred from optical and MIR photometry measured at $R_{23.5,z}$. As discussed in Section 3.4.2, we used the average of five different MLCRs with $g-r$ and $g-z$ colours to calculate optical stellar masses. Mass estimates of a stellar population should not depend on the flux tracer, however dust extinction in optical bands could lead to systematic offsets, especially in late-type systems. While a systematic offset of 0.21 dex is detected in Figure 3.12, with *W1* stellar masses being larger than optical, the latter is within the bounds of typical MLCRs systematic variations of 0.2-0.3 dex (Taylor et al. 2011; Courteau et al. 2014; Roediger and Courteau 2015). Our optical and MIR stellar mass measurements are thus in good agreement with RC15. This reaffirms the conclusion that optical colours are robust tracers of the stellar mass (Taylor et al. 2011).

The differences in luminosity, and stellar mass (Figs. 3.11 and 3.12 respectively) at different wavelengths can serve as calibrators for stellar population models and numerical models of galaxy formation (MacArthur et al. 2004; Renzini 2006; Zheng et al. 2020).

3.8 Galaxy Scaling Relations

In the previous sections, we have demonstrated the robustness of our optical and MIR photometry. We have also shown that our DESI optical photometry is ∼1.5

mag arcsec^{-2} deeper than nominal SDSS imaging, and we have used the MLDM-VAC to define our MaNGA LTG and ETG subsamples.

We now present, in Table 3.5, a variety of scaling relations in DESI (*g, r, z*) and WISE (*W1, W2*) band passes for our MaNGA data. The scaling relations are all presented as orthogonal linear regressions (Virtanen et al. 2020, SCIPY). This treatment facilitates comparisons with matching studies in the literature, though we note that subtle differences in choice of fitting method and parameter definition can affect the final scaling relation parameters (see Table 3.6). As discussed in Section 3.5 and Figure 3.3 some distributions may call for more complex modelling, such as that characterized by a slowly varying slope or a piece-wise function. We revisit these complexities below.

Below we focus on two popular scaling relations drawn from our DESI and WISE photometric investigations of MaNGA LTGs and ETGs, namely the size–stellar mass ($R - M_*$) and Σ_1–stellar mass (Σ_1-M$_*$) relations. In the following sections, all structural parameters are measured at R$_{23.5}$ in the z band unless otherwise stated.

3.8.1 Size–stellar mass ($R - M_*$) relation

Fig. 3.13 shows the $R - M_*$ relation for LTG and ETG populations measured from our DESI and WISE photometry. The parameter distributions are shown as density contours, while the cyan (red) lines represent the orthogonal best fits to the LTG (ETG) data. The pink solid line shows the best-fitting relation from Stone et al. (2021a) who used a compilation of LTG surveys with DESI imaging for ∼1100 spiral galaxies. The photometric analyses for our MaNGA and PROBES samples use the same methods (DESI photometry, AUTOPROF, surface brightness profile treatments,

Scaling relation (1)	Band (2)	y (3)	x (4)	Type (5)	Slope (6)	Zero-point (7)	Scatter (8)	N (9)
Projected size–luminosity	g	$\log R^{g}_{23.5}$	$\log L^{g}_{23.5}$	LTGs	0.44 ± 0.01	-3.55 ± 0.03	0.08 ± 0.01	2411
				ETGs	0.49 ± 0.01	-4.05 ± 0.04	0.06 ± 0.01	1796
				All	0.42 ± 0.01	-3.32 ± 0.03	0.10 ± 0.01	4215
Projected size–luminosity	r	$\log R^{r}_{23.5}$	$\log L^{r}_{23.5}$	LTGs	0.43 ± 0.01	-3.40 ± 0.03	0.08 ± 0.01	2426
				ETGs	0.52 ± 0.01	-4.37 ± 0.04	0.06 ± 0.01	1801
				All	0.44 ± 0.01	-3.40 ± 0.03	0.10 ± 0.01	4236
Projected size–luminosity	z	$\log R^{z}_{23.5}$	$\log L^{z}_{23.5}$	LTGs	0.41 ± 0.01	-3.21 ± 0.03	0.08 ± 0.01	2456
				ETGs	0.54 ± 0.01	-4.56 ± 0.05	0.07 ± 0.01	1790
				All	0.44 ± 0.01	-3.41 ± 0.03	0.10 ± 0.01	4254
Projected size–luminosity	*W1*	$\log R^{W1}_{23.5}$	$\log L^{W1}_{23.5}$	LTGs	0.36 ± 0.01	-2.49 ± 0.12	0.10 ± 0.01	168
				ETGs	0.46 ± 0.02	-3.59 ± 0.17	0.09 ± 0.01	97
				All	0.40 ± 0.01	-2.98 ± 0.11	0.11 ± 0.01	265
Projected size–luminosity	*W2*	$\log R^{W2}_{23.5}$	$\log L^{W2}_{23.5}$	LTGs	0.34 ± 0.02	-2.32 ± 0.22	0.10 ± 0.02	67
				ETGs	0.42 ± 0.03	-3.19 ± 0.32	0.08 ± 0.02	32
				All	0.37 ± 0.02	-2.63 ± 0.17	0.10 ± 0.01	99
Projected size–stellar mass	g	$\log R^{g}_{23.5}$	$\log M_{*,23.5}$	LTGs	0.34 ± 0.01	-2.61 ± 0.03	0.12 ± 0.01	2408
				ETGs	0.40 ± 0.01	-3.39 ± 0.04	0.07 ± 0.01	1790
				All	0.30 ± 0.01	-2.22 ± 0.03	0.14 ± 0.01	4206
Projected size–stellar mass	r	$\log R^{r}_{23.5}$	$\log M_{*,23.5}$	LTGs	0.34 ± 0.01	-2.57 ± 0.03	0.10 ± 0.01	2408
				ETGs	0.46 ± 0.01	-3.88 ± 0.04	0.07 ± 0.01	1790
				All	0.34 ± 0.01	-2.53 ± 0.03	0.12 ± 0.01	4206
Projected size–stellar mass	z	$\log R^{z}_{23.5}$	$\log M_{*,23.5}$	LTGs	0.35 ± 0.01	-2.57 ± 0.03	0.10 ± 0.01	2408
				ETGs	0.49 ± 0.01	-4.17 ± 0.05	0.07 ± 0.01	1790
				All	0.37 ± 0.01	-2.73 ± 0.03	0.12 ± 0.01	4206
Projected size–stellar mass	*W1*	$\log R_{23.5}$	$\log M_{*,23.5}$	LTGs	0.34 ± 0.01	-2.51 ± 0.13	0.11 ± 0.01	168
				ETGs	0.46 ± 0.02	-3.59 ± 0.16	0.10 ± 0.01	97
				All	0.41 ± 0.01	-2.98 ± 0.11	0.12 ± 0.01	265
Projected size–stellar mass	*W2*	$\log R_{23.5}$	$\log M_{*,23.5}$	LTGs	0.40 ± 0.02	-2.80 ± 0.21	0.10 ± 0.01	67
				ETGs	0.44 ± 0.02	-3.38 ± 0.35	0.10 ± 0.02	32
				All	0.42 ± 0.02	-3.04 ± 0.19	0.11 ± 0.01	99
Physical size–stellar mass	z	$\log r_{23.5}$	$\log M_{*,23.5}$	LTGs	0.36 ± 0.01	-2.83 ± 0.04	0.11 ± 0.01	2433
				ETGs	0.50 ± 0.01	-4.07 ± 0.03	0.07 ± 0.01	1839
				All	0.42 ± 0.01	-3.26 ± 0.03	0.10 ± 0.01	4274
Physical size–stellar mass	*W1*	$\log r_{23.5}$	$\log M_{*,23.5}$	LTGs	0.36 ± 0.01	-2.51 ± 0.12	0.11 ± 0.01	168
				ETGs	0.46 ± 0.02	-3.45 ± 0.16	0.10 ± 0.01	97
				All	0.41 ± 0.01	-3.02 ± 0.12	0.12 ± 0.01	265
Σ_1–stellar mass	*grz*	$\log \Sigma_1$	$\log M_{*,23.5}$	LTGs	0.96 ± 0.01	-0.86 ± 0.08	0.24 ± 0.01	2408
				ETGs	0.66 ± 0.01	2.43 ± 0.11	0.26 ± 0.01	1790
				All	0.91 ± 0.01	-0.31 ± 0.07	0.29 ± 0.01	4206
$\Sigma_{\rm eff}$-stellar mass	*grz*	$\log \Sigma_{\rm eff}$	$\log M_{*,23.5}$	LTGs	0.70 ± 0.01	1.16 ± 0.13	0.36 ± 0.01	2408
				ETGs	-0.01 ± 0.03	8.85 ± 0.29	0.33 ± 0.01	1790
				All	0.62 ± 0.01	2.06 ± 0.12	0.43 ± 0.01	4206

Table 3.5: MaNGA Photometric Galaxy Scaling Relations in the g, r, z, *W1*, and W2 bands, with orthogonal linear fit results. Columns (1) and (2) give the scaling relation and the relevant photometric band(s); columns (3) and (4) give the variables on the y and x axis coordinates for the scaling relation; column (5) gives the morphological type used for the fit; columns (6)–(8) give the slope (m), zero-point (zp), and scatter (σ) for our linear orthogonal distance regression; and column (9) gives the number of data points used in each fit.

Scaling relation (1)	Source (2)	Sample (3)	Type (4)	Band (5)	N (6)	Slope (7)	Scatter (8)	Size metric (9)
$R - M_*$	This Work	MaNGA	LTGs	z	2408	0.35 ± 0.01	0.10 ± 0.01	$R_{23.5}$
	Shen et al. (2003)	SDSS	LTGs	z	99 786	0.40	0.15	$R_{\rm eff}$
	Pizagno et al. (2005)	SDSS	LTGs	i	81	0.242 ± 0.030	n/a	$R_{\rm d}$
	Lange et al. (2015)	GAMA	LTGs	z	6151	0.21 ± 0.02	n/a	$R_{\rm eff}$
	Ouellette et al. (2017)	SHIVir	LTGs	i	69	0.34 ± 0.02	0.15	$R_{23.5}$
	Stone et al. (2021a)	PROBES	LTGs	z	1152	$0.334^{0.009}_{0.004}$	$0.099^{0.002}_{0.003}$	$R_{23.5}$
	Trujillo et al. (2020)	IAC Stripe82	LTGs	i	464	0.318 ± 0.014	0.087 ± 0.05	$R_{23.5}$
$R - M_*$	This Work	MaNGA	ETGs	z	1790	0.49 ± 0.01	0.07 ± 0.01	$R_{23.5}$
	Shen et al. (2003)	SDSS	ETGs	z	99 786	0.56	0.15	$R_{\rm eff}$
	Lange et al. (2015)	SDSS	ETGs	z	2248	0.46 ± 0.02	n/a	$R_{\rm eff}$
	Ouellette et al. (2017)	SHIVir	ETGs	i	121	0.35 ± 0.04	0.12	$R_{23.5}$
	Trujillo et al. (2020)	IAC Stripe82	ETGs	i	279	0.453 ± 0.011	0.042 ± 0.004	$R_{23.5}$
$\Sigma_1 - M_*$	This Work	MaNGA	LTGs	grz	2408	0.96 ± 0.01	0.24 ± 0.01	$R_{23.5}$
	Barro et al. (2017)	CANDELS	LTGs	–	1328	0.89 ± 0.03	0.25	n/a
	Woo and Ellison (2019)	MaNGA	LTGs	i	∼41 000	0.86	0.24	n/a
	Stone et al. (2021a)	PROBES	LTGs	z	1152	$1.004^{0.021}_{0.035}$	$0.231^{0.005}_{0.006}$	$R_{23.5}$
$\Sigma_1 - M_*$	This Work	MaNGA	ETGs	grz	1790	0.66 ± 0.01	0.25 ± 0.01	$R_{23.5}$
	Barro et al. (2017)	CANDELS	ETGs	–	151	0.65	0.14	n/a
	Woo and Ellison (2019)	MaNGA	ETGs	i	∼15 000	0.75	0.17	n/a
	Fang et al. (2013)	GALEX/SDSS	ETGs	i	1247	0.64	0.16	n/a

Table 3.6: Literature comparisons for scaling relation from our photometry. Column (1) shows the scaling relation; column (2) presents the literature source; column (3) shows the sample used for the scaling relation; column(4) presents the morphological type; column (5) lists the photometric band used for the analysis; columns (6), (7) and (8) present the number of data points, slope and scatter for the best fit line; finally column (9) presents the size metric used for constructing the scaling relation. "n/a" are shown where the data are not available.

photometric band). It is therefore not surprising that our linear regression should match the PROBES fit so well. Stone et al. (2021a) also report a scatter of $0.099^{+0.002}_{-0.003}$ which is in perfect agreement with the observed scatter of our MaNGA galaxies. Overall, the MaNGA and PROBES LTGs have matching $R-M_*$ properties measured from a distinct sample of galaxies (though matching analysis routines).

The left-hand panel of Figure 3.13 (blue solid line) also presents a comparison with the linear $R - M_*$ relation from Trujillo et al. (2020) who reported a slope of 0.318 ± 0.014 and a scatter of 0.087 ± 0.005, based on SDSS-i band imaging and using isophotal sizes at 23.5 mag arcsec^{-2} . The different photometric band used in

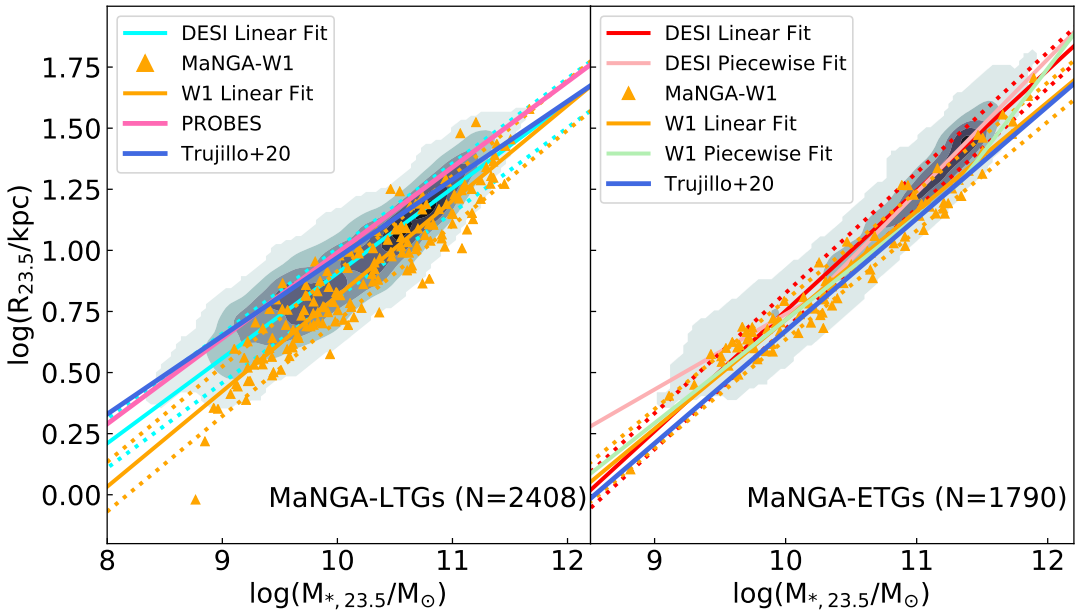

Figure 3.13: Size–stellar mass relation for LTGs (left-hand panel) and ETGs (right-hand panel). In each panel, grey filled contours represent the distribution of our DESI photometric data; the cyan (LTGs) and red (ETGs) lines are the orthogonal best fit for the corresponding populations. The orange triangles and solid line represent the same structural parameters measured with the WISE (*W1*) data. The dotted lines in each panel correspond to the 1σ scatter about the best-fitting line. In the left-hand panel, the $R - M_*$ relation for ∼1100 PROBES galaxies is presented as a pink line (Stone et al. 2021a). Both panels show the $R - M_*$ relation of Trujillo et al. (2020) based on ∼1000 galaxies. Piece-wise linear fits to the DESI and WISE data are also shown for the ETGs (see the text for details.)

our respective analysis may explain the slight slope and scatter mismatch for our respective $R - M_*$ relations.

For LTGs, the slope of the $R - M_*$ relation is independent of wavelength (Table 3.5). This agrees with Lange et al. (2015) who showed minimal variations in the slope of the $R - M_*$ relation for 8400 GAMA galaxies (Driver et al. 2009) across the *ugrizZYJHK* photometric bands modulo random variations (see Table 3.6). The actual value of our respective slopes differ on account of our respective size metric

choices (effective vs. isophotal radius).

The density map and the red solid line in the right-hand panel of Figure 3.13 represent the $R-M_*$ relation for our ETG sample. The single linear $R-M_*$ relation for ETGs is steeper (larger slope) and tighter (smaller scatter) than for LTGs. The slope and scatter of the ETGs $R-M_*$ relation is likely controlled by their formation via repeated mergers on high impact parameter orbits (Shen et al. 2003). Dry (gas-less) mergers are the most plausible explanation for the steep size growth of the ETGs From $z\sim1$ to now (Huertas-Company et al. 2013).

Our linear $R-M_*$ relation is in general agreement with (Trujillo et al. 2020), who found a slope of 0.453 ± 0.011 and an observed scatter of 0.042 ± 0.004 for 280 galaxies. The differences in best-fitting parameters are a result of the choice photometric band (SDSS-i) and least-square linear regression. Lange et al. (2015) found a range of $R-M_*$ relation slopes of $0.46-0.56$ (scatter not reported) for GAMA galaxies (Driver et al. 2009) in the SDSS-z band. They also used effective radii as the size metric making comparisons challenging. The exact value of the slope in Lange et al. (2015) depends largely on their morphological assignments of ETGs as guided by Seŕsic index, dust-corrected optical colour, and visual classification. We find a general trend that the $R-M_*$ relation for ETGs is steeper (shallower) if effective (isophotal) radii are used.

Figure 3.13 also presents the linear $R-M_*$ relation for our WISE *W1* photometry with the orange line and triangles for the LTGs/ETGs in the left-/right-hand panels. This relation (slope and scatter) is essentially the same as that inferred from DESI z-band images for our LTGs, further highlighting our conclusions in Table 3.5 that the slope and scatter for LTG $R-M_*$ relation is independent of the wavelength. The

Band	N	M_* limit	Piece-wise fits
(1)	(2)	(3)	(4)
DESI-z	1854	$\log M_* \leq 10.20$	$0.31(\log M_* - 10.20) + 0.80$
		$\log M_* > 10.20$	$0.55(\log M_* - 10.20) + 0.80$
W1	97	$\log M_* \leq 10.81$	$0.41(\log M_* - 10.81) + 1.05$
		$\log M_* > 10.81$	$0.52(\log M_* - 10.81) + 1.05$

Table 3.7: Linear piece-wise $R - M_*$ relations for MaNGA-ETGs. columns (1) and (2) give the photometric band and number of data points used for the fit; column (3) shows the stellar mass limit for the change in slope; and column (4) presents the piece-wise fits.

scatter and slope of the ETG WISE $R - M_*$ relation differ slightly from their z-band counterpart. This result is similar to that of Lange et al. (2015), who found large random variations in the slope of $R - M_*$ relation for ETGs.

Along with the projected $R-M_*$ relation (Table 3.5), we can calculate this relation with physical radii (see Section 3.4.2). Table 3.5 presents the physical $r_{23.5} - M_*$ relation for the DESI z and *W1* photometric bands. The projected and physical $r-M_*$ relations for LTGs are equal by definition. For ETGs physical sizes increase by 4/3 relative to projected values (Hernquist 1990; Chiosi and Carraro 2002), resulting in a predictable change in zero-points (by 0.125 dex) of the best-fitting relation. The best linear fits to physical relations are presented in Table 3.5.

Given the bimodalities in stellar mass and sizes for ETGs seen in Figure 3.3, we also model the $R - M_*$ relation based on DESI and WISE imaging with a double piece-wise linear fit (see Table 3.7). It is found that the slopes of our $R-M_*$ relations for LTGs and ETGs based on DESI and WISE data agree closely with the theoretical expectations. For LTGs, it can be shown that $R_{opt} \propto M_*^{0.33}$ for virialized galaxy discs

and assuming constant Υ_* per galaxy (Courteau et al. 2007). Various scaling arguments connecting structure formation to primordial density fluctuations (Blumenthal et al. 1984) also suggest that massive ETGs ($\log(M_*/M_\odot) \geq 10$) have $R \propto M_*^{0.53}$ (Burstein et al. 1997; Chiosi and Carraro 2002; D'Onofrio et al. 2020). The slope for lower mass ETGs is predicted to be shallower with $R \propto M_*^{0.33}$; closer to that of LTGs in the same mass range (Chiosi and Carraro 2002; Woo et al. 2008). The piecewise linear fit slopes for ETGs (Table 3.7), with a low and high mass transition at $\log(M_*/M_\odot) \sim 10.2$ matches theoretical expectations (0.33/0.53) in the same stellar mass bins quite closely (Blumenthal et al. 1984; Chiosi and Carraro 2002). The same statement holds for the WISE data with stellar mass transition being larger than the optical data. However, this larger stellar mass transition could be attributed to small statistics for low-mass WISE ETGs.

The agreement between the observed and predicted $R - M_*$ slopes is certainly encouraging. However, a complete data-model investigation should also match the zero-points, and scatters of observed scaling relations. Our MaNGA data base serves as a stepping stone for such a comparison with theoretical and numerical models of galaxy formation and structure.

In the next section, we explore other size metrics and their effects on slopes and scatters of the $R - M_*$ relation.

3.8.2 Slope and scatter variations of the $R - M_*$ relation

The spatially-resolved nature of our photometric solutions enables a detailed study of the $R - M_*$ relation with a suite of size metrics for both LTGs and ETGs, as shown in Fig. 3.14.

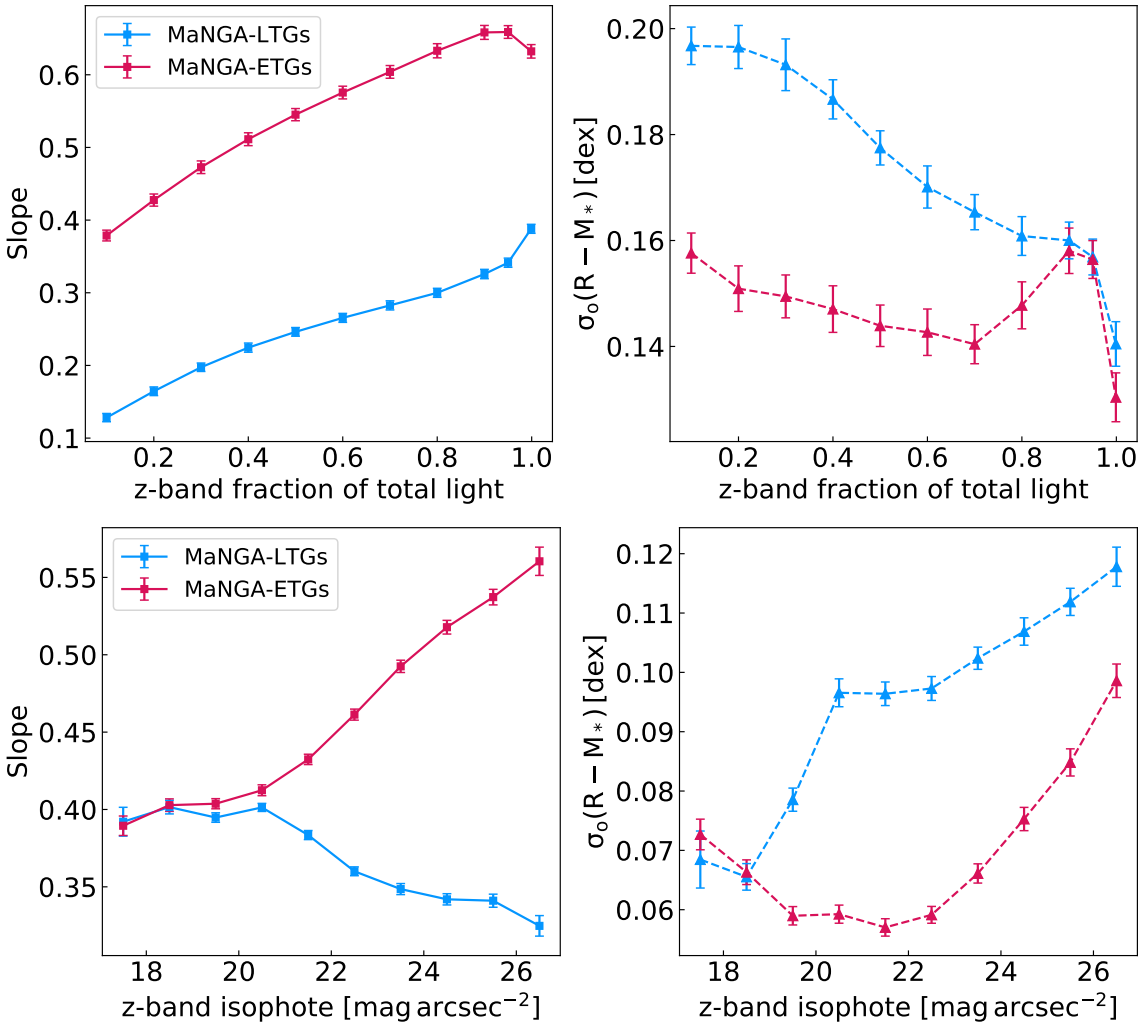

Figure 3.14: Variations of the slope and orthogonal scatter of the $R - M_*$ relation of LTGs (blue) and ETGs (red) for different size measurements. The top panels show size measurements at various fractions of total light. Isophotal size measurements are presented in the bottom panels. $R - M_*$ slopes are presented in the left-hand panels with connected squares. Observed orthogonal scatter measurements are presented in the right-hand panels with connected triangles. The error bars on all points correspond to bootstrap uncertainties.

Slope variations of the $R - M_*$ relation

The left-hand panels of Fig. 3.14 show variations of the slope of the $R - M_*$ relation with size metrics measured relative to the total light (top panels) and isophotal levels (bottom panels). For both morphologies, the slope of the $R - M_*$ relation increases linearly with light fraction. However, the $R-M_*$ slopes for LTGs and ETGs with sizes measured at different isophotal levels have nearly opposite behaviours, as seen in the bottom left-hand panel of Figure 3.14. The $R-M_*$ relation slope for LTGs settles to the theoretical value of 0.33 (Courteau et al. 2007) between 23 and 26 z-mag arcsec^{-2} . The slope for the ETGs grows steadily before flattening to a value of $\sim$0.53 at or beyond 26 z-mag arcsec^{-2} . The value where the slope flattens agrees with the theoretical prediction found in Burstein et al. (1997) and Chiosi and Carraro (2002). The exact nature of the slope of the $R - M_*$ relation as a function of size metric can be related to the interplay between the relative slopes of the surface brightness profiles and COG.

For LTGs, $R - M_*$ slopes range from 0.13 to 0.39 (fractional) or 0.39 to 0.33 (isophotal); the slopes are always smaller if measured relative to the total light, and the trends are opposite. For ETGs, $R-M_*$ slopes range from 0.42 to 0.62 (fractional) or 0.39 to 0.63 (isophotal). The steeper $R - M_*$ slope for ETGs (see Section 3.8.1) is expected from a high occurrence of dry mergers and feedback from stars and supermassive black holes (Shen et al. 2003; Huertas-Company et al. 2013). The use of $R_{\rm eff}$ also yields a closer match to theoretical predictions of the $R - M_*$ slope. The theoretical prediction can also be matched with isophotal radii by binning galaxies in stellar mass (similar to Chiosi et al. 2020).

Scatter variations of the $R - M_*$ relation

The right-hand panels of Fig. 3.14 show variations in the orthogonal scatter of the $R-M_*$ relation with size metrics measured relative to the total light (top panels) and isophotal levels (bottom panels). For both morphologies, the $R - M_*$ scatter profiles (top right-hand panel of Figure 3.14) show different behaviours. The scatter for LTGs decreases monotonically from 0.20 to 0.15 dex with increasing total light fraction. The tightest $R - M_*$ relation is found when all the light from our photometry is taken into account. For ETGs, the scatter of the $R-M_*$ relation is mostly constant around $\sim$0.14 dex for all size metrics.

Trends with isophotal sizes differ: smallest orthogonal scatter for the $R - M_*$ relation is found at 18.5 (21.6) z-mag arcsec^{-2} for LTG (ETG) populations. Our conclusions remain the same if forward scatter was used instead of orthogonal. This result comes as a surprise in light of the current literature that points to the isophotal radius of 23.5 mag arcsec^{-2} that minimizes the scatter of VRL scaling relations (Courteau 1996; Hall et al. 2012). More recently, Trujillo et al. (2020) found the radius corresponding to a stellar surface density of 1 $M_\odot$ pc^{-2} also shows a tight $R-M_*$ relation along with the added benefit of definition motivated by the physics of star formation in galaxies. This radius corresponds to a fainter isophote ($\sim$26 mag arcsec^{-2}) which is larger than the isophotal radius of 23.5 mag arcsec^{-2} . Our findings contradict this as the radius giving the tightest $R - M_*$ relation is found to be at 18.5 (21.5) z mag arcsec^{-2} for LTGs (ETGs). Sánchez Almeida (2020) performed a similar exercise and found the isophotal radius of 24.7 ± 0.5 r-mag arcsec^{-2} minimizes the scatter. The difference between our results is related to the definition of scatter of a linear relation (half of inter-quartile range vs. rms) and the choice of the photometric

band (DESI-z vs. SDSS-r).

Scatter values are also always smaller for isophotal sizes than light fraction sizes. This occurs because light fraction sizes encompass multiple surface brightness levels, thus enhancing the mix of stellar populations at any radius and yielding larger $R-M_*$ scatter values (see e.g. Trujillo et al. 2020). The results in this section are further corroborated with our MIR photometry that show similar trends [minimum scatter on 17.5(20) mag arcsec^{-2} for ETGs(LTGs)]. These are not shown in Figure 3.14 for simplicity. It has been noted the the isophotal level of 23.5 i-mag arcsec^{-2} minimizes scatter of the TFR (Giovanelli et al. 1994; Hall et al. 2012). In an upcoming publication, we investigate the radius, if any, that minimizes the scatter of the VRL scaling relations simultaneously.

3.8.3 Σ_1-stellar mass (Σ_1–M_*) relation

The $\Sigma_1 - M_*$ relation reveals information about the star formation and merger histories of galaxies (Barro et al. 2017) and the physical/time evolution of their central components of galaxies (Woo and Ellison 2019; Chen et al. 2020a,b). While the calculation of the stellar surface density at 1 kpc can be challenging given large distance errors and saturation issues, Σ_1 traces properties the bulge component with the added advantage of being model-independent. Fig. 3.15 shows the $\Sigma_1 - M_*$ relation for MaNGA LTGs and ETGs based on our DESI optical photometry. Because the WISE data cannot resolve 1-kpc regions for MaNGA galaxies, this section on Σ_1 only uses our optical photometry.

Our orthogonal fit parameters for the $\Sigma_1 - M_*$ relation are presented in the bottom row of Table 3.5. Stone et al. (2021a) found a similar $\Sigma_1 - M_*$ relation with a slope

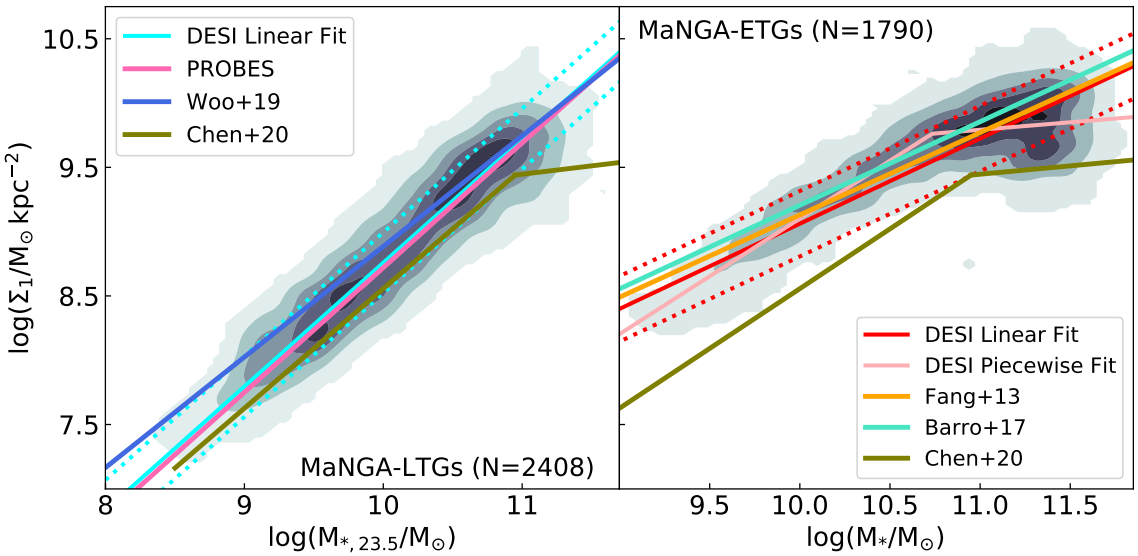

Figure 3.15: Σ_1 - stellar mass relation for the LTGs (left-hand panel) and ETGs (right-hand panel) using our optical DESI photometry. The density maps in grey show the data distribution. Orthogonal best fits are represented by solid cyan (LTGs) and red (ETGs) lines; the dotted lines show $1\,\sigma$ scatter for the best-fitting relations. For LTGs, the stellar masses are measured as the average of five MLCRs presented in Section 3.4.2. For ETGs, the stellar masses are measured using the MLCR of B19. We compare our LTG relation with Woo and Ellison (2019) and Stone et al. (2021a), and our ETG relation with Fang et al. (2013) and Barro et al. (2017) (see the text for the redshift range). Both panels show the $\Sigma_1 - M_*$ relation of Chen et al. (2020a) which fits all morphological types. A piece-wise linear fit to the DESI data is also shown for the ETGs (see the text for details).

of $1.005^{0.021}_{0.035}$ and a scatter of 0.23 ± 0.01 dex for their PROBES sample.

This relation is also fit by Woo and Ellison (2019) who found a $\Sigma_1 - M_*$ slope of 0.86 and a scatter of 0.24 dex using ∼2100 MaNGA galaxies with SDSS photometry and MPA-JHU stellar masses (Brinchmann et al. 2004; Kauffmann et al. 2004b). Their different slope may be explained by their use of the SDSS i band, a different definition of stellar mass and a least-square linear fit. Their fit is not a good match to our relation (Fig. 3.15).

Our $\Sigma_1 - M_*$ slope for ETGs matches closely to that of Fang et al. (2013) whose

study of ∼1300 quenched galaxies selected from the SDSS with $z < 0.075$ yielded a slope of $0.64^{+0.23}_{-0.20}$. However, their reported scatter of 0.16 dex is significantly smaller than ours. This disagreement could be due to sample selection, choice of MLCRs to calculate stellar masses and the assumptions about the IMF. The conversion of light into stellar mass is also inherently uncertain. While our study targets morphologically selected ETGs, Fang et al. (2013) selected green valley galaxies that are quenched. Even though there is overlap in these samples, an ETG sample and green valley/quenched sample are different. For instance, green valley galaxies can exhibit a range of morphologies (Mendez et al. 2011) and ETGs can show large range in star formation histories. In principle, Σ_1 should be more sensitive to the star formation history than visual morphologies explaining our larger scatter for the relation.

The right-hand panel of Figure 3.15 also shows the $\Sigma_1 - M_*$ relation of Barro et al. (2017) for CANDELS GOODS-S galaxies at $0.5 < z < 1.0$ (Guo et al. 2013b) who reported a slope of 0.65 ± 0.03 and a zero-point of 2.71 ± 0.05. For quiescent galaxies, Barro et al. (2017) found that the slope of the $\Sigma_1 - M_*$ relation remains constant as a function of redshift; only the zero-point evolves with time. For a fixed stellar mass bin, Σ_1 should decrease over time (Barro et al. 2017). Our similar slopes and smaller zero-point strengthen this assertion as our local universe MaNGA ETGs ($z < 0.15$) achieve the same slope and a smaller zero point.

An interesting feature of the $\Sigma_1 - M_*$ relation for ETGs is its flattening for $\log(M_*/M_\odot) \geq 10.7$. As a result of this feature, and as stated for the $R - M_*$ relation of ETGs Section 3.8.1, caution should be taken while fitting a linear relation to the ETG $\Sigma_1 - M_*$ relation (see the right-hand panel of Figure 3.15). Along with the linear regression, we fit piece-wise linear function to the data distribution, with $\log \Sigma_1 =$

$0.90(\log M_* - 10.73) + 9.76$ for $\log M_* \leq 10.73$, and $\log \Sigma_1 = 0.12(\log M_* - 10.73) + 9.76$ for $\log M_* > 10.73$. We note that the transition in stellar mass at $\log M_* \sim 10.7$ in this piece-wise fit is mirrored in the bimodal distribution of stellar masses for ETGs seen in Figure 3.3. However, the stellar mass transition in the $R - M_*$ relation of ETGs is found at $\log \mathrm{M}_* \sim 10.2$. We are reminded that the bivariate distributions are controlled by two random variables.

Chen et al. (2020a) also used a piece-wise function to describe the $\Sigma_1 - M_*$ relation for the complete MaNGA sample calculated to be: $\log \Sigma_1 = 0.93(\log M_* - 10.95) + 9.44$ for $\log M_* \leq 10.95$, and $\log \Sigma_1 = 0.13(\log M_* - 10.95) + 9.44$ for $\log M_* > 10.95$. Their piece-wise linear fit is shown in the left- and right-hand panels of Figure 3.15. Their slopes for the low- and high-mass ends of the fit match ours quite well. However, the disagreement in our respective zero-points is significant and may result from our respective stellar mass calculations and different samples. Chen et al. (2020a) used stellar masses provided by the NSA (Blanton et al. 2011); our procedure is described in Section 3.4.2. Indeed, a large difference is found between the stellar masses by NSA and in this study; our photometry results in larger stellar masses by 0.34 (0.40) dex for LTGs (ETGs) that could be due to the systematic offsets of the MLCRs (see Figure 3.10). Chen et al. (2020a) fit a linear piece-wise function to the full MaNGA sample while our fit is restricted to ETGs. Both of these effects could cause the observed zero point difference, although it is surprising that the slopes remain unaffected.

For LTGs and low-mass ETGs, the slope of the $\Sigma_1 - M_*$ relation near unity (0.96 and 0.90) is suggestive of a co-evolution of the inner and outer regions through star

formation and environmental interactions. Indeed, these galaxies may have an enhanced $sSFR(= SFR/M_*)$ which builds up stellar mass in their inner regions (Woo and Ellison 2019). The shallower $\Sigma_1 - M_*$ slope (0.13) at the high-mass end for ETGs likely applies to galaxies with little star formation but ongoing overall accretion, leading to a flattening of the $\Sigma_1 - M_*$ relation at $\Sigma_1 \sim 10^{10}\,\mathrm{M_\odot kpc^{-2}}$. A complimentary explanation for the saturation of Σ_1 in high mass ETGs involves partially depleted central cores due to coalescing black holes at high redshifts (King and Minkowski 1966; Ferrarese et al. 1994; Lauer et al. 1995; Gebhardt et al. 1996; Graham and Guzmán 2003). A proper appreciation of the saturation of Σ_1 in galaxies will require additional data, such as SFRs, maps of neutral and molecular gas reservoirs, environmental parameters to characterize interactions and gas infall. While some of these data still exist, a detailed investigations of the shallower slope at the high-mass end is beyond the scope of this study. We also caution that Σ_1 may be sensitive to projection, dust extinction, and stellar population effects.

3.9 Summary and Future Work

We have presented high-quality optical and MIR surface brightness profiles and environmental properties for the MaNGA galaxy survey. We made use of DESI imaging and our software (AUTOPROF; Stone et al. 2021a) to extract azimuthally averaged optical surface brightness profiles. On average, the DESI photometry reaches $\sim$2 mag arcsec^{-2} deeper than the SDSS photometry in the *gr* photometric bands which arises from a combination of deeper DESI imaging and our novel technique, AUTOPROF. The WISE profiles are extracted from the WXSC (Jarrett et al. 2019) which uses deconvolution techniques to achieve a higher resolution than the native WISE

imaging. 70 per cent (33 per cent) of the WISE *W1* (W2) surface brightness profiles are as deep in radial extent as the DESI photometry and can be used to compute scaling relations at the fiducial isophotal radius $R_{23.5,z}$.

Excellent agreement is found between most model-independent structural parameters from AUTOPROFand those obtained with well-tested surface photometry routines based on the XVISTA software package for astronomical image processing (Courteau 1996). Disagreements between AUTOPROF, XVISTA and the literature, are largely found for parameters that scale with total light such as effective radii, effective surface brightness, and concentration indices. The bimodal nature in the distribution of some structural parameters is also suggestive of distinct galaxy populations in the Universe.

Detailed comparisons of our surface brightness profiles and structural parameters with other studies were presented. The non-parametric surface brightness profiles from AUTOPROF(DESI) and GC18 (SDSS) agree well, even reproducing small local variations. However, the reconstructed surface brightness profiles from the bulge-to-disc decompositions of GC18 and F19 exhibit large differences ($\sim 0.4\,\mathrm{mag\ arcsec^{-2}}$) demonstrating the challenges involved in such parametric modelling. Moreover, similar disagreements are found between our model-independent surface brightness profiles and the parametric decompositions of both GC18 and F19, highlighting once again the fragile nature of parametric modelling.

Our comparisons of effective radii and apparent magnitudes with PYMORPHof F19 have also revealed disagreements for $R_{\rm eff}$, especially for ETGs ($rms \sim 0.2$)dex. Better comparisons are found for isophotal radii ($rms \sim 0.05$)dex, demonstrating the superior reproducibility of isophotal sizes over those measured relative to total light

fractions. Our apparent magnitudes are also typically brighter than those of F19 by ∼0.1 dex. This is expected as, unlike parametric models, our non-parametric surface brightness extraction captures all the light. The GALFIT implementations of GC18 and F19 preferentially favor high S/N regions and systematically predict fainter magnitudes for low S/N. These systematic effects average out to fainter total integrated light, relative to our non-parametric results.

Our stellar mass estimates, measured at $M_*(R^z_{23.5})$ and obtained from multiband photometry and various MLCRs, compare favorably with those found in the literature, such as MPA-JHU catalogue (Kauffmann et al. 2003), NSA photometry (Blanton and Roweis 2007), Pipe3D (Sánchez et al. 2016), and P19. Our stellar masses for LTGs, based on the average of multiple MLCRs from RC15, Z17, and B19, are 0.24 dex smaller than those of P19. This offset is explained by the modelling of SFHs by P19 that systematically biases Υ_* high. Our stellar masses for ETGs, based on the MLCR from B19, are 0.11 dex smaller than those of P19. The largest stellar mass differences, found for the NSA stellar mass estimates with an rms of 0.34 (0.40) dex for LTGs (ETGs), may stem from uncertainties in the NSA elliptical-Petrosian photometry. The best match with our stellar mass estimates is found for the MPA-JHU catalogue, with an rms of 0.21 (0.11) dex for LTGs (ETGs).

We also present WISE photometry for a subset of ∼ 300 MaNGA galaxies. It provides an independent measure of stellar masses, which agree with our optical estimates within 0.21 dex (see also Taylor et al. 2011). Dust extinction may explain the small systematic differences in the stellar mass estimates of LTGs. In addition to providing accurate stellar masses, spatially-resolved MIR fluxes are most valuable for studies of the star formation main-sequence, SFR$-M_*$ (Cluver et al. 2017; Hall et al.

2018) stellar population properties (Cluver et al. 2014, 2020).

The slope and scatter of the $R - L_*$ and $R - M_*$ relations for LTGs are found to be independent of bandpass (from g to *W2* Table 3.5). For ETGs, slope variations for the $R - M_*$ relation from bluer to redder bands can be linked to varying stellar populations over a range of stellar masses (Lange et al. 2015). The $R-L_*$ and $R-M_*$ slopes and scatters for LTGs and ETGs also agree well, within $1\,\sigma$, with published values (see Figures 3.13 and 3.15).

We have examined the variations of the slope and scatter of the $R - M_*$ relation for a range of size metrics. The slopes of the $R - M_*$ relations for LTGs and ETGs with size metrics measured relative to total light grow linearly with fraction of total light. Conversely, slopes calculated using isophotal sizes decrease (increase) for LTGs (ETGs) from brighter to fainter regions. These trends are dictated by the relative slope variations in the surface brightness profiles and curves of growth.

Isophotal sizes also yield tighter $R - M_*$ relations (smaller scatter) than sizes measured at relative fractions of total light. The isophotal radius measured at 18.5 (21.5) mag arcsec^{-2} also yields the tightest $R - M_*$ relation for the LTG (ETG) population by orthogonal scatter. Our orthogonal linear fits result in slopes for the LTGs abs ETGs that match theoretical predictions of the $R - M_*$ relations.

The $\Sigma_1 - M_*$ relation is also presented for both MaNGA LTGs and ETGs and an excellent agreement is found with the literature. For LTGs, the slope of the $\Sigma_1 - M_*$ relation is near unity, indicating a co-evolution of stellar mass and Σ_1 that is driven by enhanced star formation and environmental effects. For ETGs, a near constant Σ_1 is found for $M_* > 10.5$. A piecewise linear function was adopted to better match the $\Sigma_1 - M_*$ distribution. The saturation of Σ_1 at high stellar mass could be related

to SFRs, environment, neutral/molecular gas distribution, etc.

The multiband photometry, environmental parameters, and structural scaling relations presented in our study may be used to constrain stellar populations models, test semi-analytic or numerical models of galaxy formation, and test their subgrid physics prescriptions (Dutton and van den Bosch 2009; Brook et al. 2012; Henriques et al. 2015a). While extensive, the photometry and scaling relations studied here only inform us about baryonic properties of galaxies. An essential aspect of galaxy formation and evolution is understanding the co-evolution of baryons and dark matter through a simultaneous study of photometric and kinematic properties of galaxies (Courteau et al. 2007; Hall et al. 2012; Ouellette et al. 2017). The MaNGA survey includes dynamical information for all observed galaxies, making this an exciting avenue for related investigations.

3.10 Appendix: Surface Brightness Profiles

This Appendix shows the output format of the DESI-*grz* and WISE *W1, W2* surface brightness profiles that are provided as supplementary material. The DESI and WISE surface brightness profiles are provided in the AB and Vega magnitude systems, respectively. The conversions from Vega to AB magnitudes in the *W1* and *W2* bands are given by (Jarrett et al. 2013):

$$\mathrm{m}_{\mathrm{AB}}^{W1} = \mathrm{m}_{\mathrm{Vega}}^{W1} + 2.683, \tag{3.6}$$

$$\mathrm{m}_{\mathrm{AB}}^{\mathrm{W2}} = \mathrm{m}_{\mathrm{Vega}}^{\mathrm{W2}} + 3.319. \tag{3.7}$$

Column (1)	Unit (2)	Description (3)
R	arcsec	Semimajor axis length of the isophote
SB	mag arcsec^{-2}	Median surface brightness in the AB magnitude system
SB_E	mag arcsec^{-2}	Error on the surface brightness
MAG	mag	Total magnitude within the isophote, computed by integrating the surface brightness profile
MAG_E	mag	Error on the total magnitude within the isophote
ELLIP	–	Ellipticity of the isophote; $\epsilon = 1 - b/a$, where b is the semi-minor axis length of the isophote, and $a = R$.
ELLIP_E	–	Error on the ellipticity, computed by analysing the local variability within 1 PSF
PA	°	Position angle of isophote measured from north to east
PA_E	°	Error on the position angle, computed by analysing the local variability within 1 PSF
MAG_DIRECT	mag	Total magnitude within the isophote computed by flux summation
SB_FIX	mag arcsec^{-2}	Average surface brightness in the AB magnitude system along isophote with ellipticity and position angle set to global values
SB_FIX_E	mag arcsec^{-2}	Error on SB_FIX
MAG_FIX	mag	Total magnitude enclosed within the isophote. Computed by integrating SB_FIX profile
MAG_FIX_E	mag	Error on MAG_FIX

Table 3.8: Output format of the DESI *grz* surface brightness profiles provided as supplementary material. Column (1) refers to the column names in each galaxy surface brightness profile; Column (2) shows the units for each parameter; Column (3) describes each profile entry. All DESI-*grz* surface brightness profiles are named with the MaNGA-ID followed with the extension "_AP.prof"

Column (1)	Unit (2)	Description (3)
radius	arcsec	Semimajor axis length of the isophote
SBpix	–	Surface brightness in digital number along the isophote
SBmag	mag arcsec^{-2}	Surface brightness in mag arcsec^{-2} along the isophote in the Vega magnitude system
SBerr	mag arcsec^{-2}	Error on surface brightness in the Vega magnitude system
SBtotmod	mag arcsec^{-2}	Total surface brightness for the bulge+disc model in the Vega magnitude system (Jarrett et al. 2019)
SBbulge	mag arcsec^{-2}	Surface brightness of the bulge component in the Vega magnitude system (Jarrett et al. 2019)
SBdisk	mag arcsec^{-2}	Surface brightness of the disc component in the Vega magnitude system (Jarrett et al. 2019)

Table 3.9: Output format of the WISE *W1, W2* surface brightness profiles provided as supplementary material. Column (1) refers to the column names in each galaxy surface brightness profile; Column (2) shows the units for the parameter; Column (3) describes each profile entry. All WISE *W1, W2* surface brightness profiles are named with the WISE catalogue name followed with the extension ".profile.w1/w2.txt". A separate file named "DESI-WISE-index.tbl" provides a conversion table between the MaNGA-ID and WISE-NAME.

Chapter 4

Observations and Simulation Comparison

4.1 Preamble

This chapter contains the draft of a paper titled **"MaNGA galaxy properties – II. A detailed comparison of observed and simulations spiral galaxy scaling relations"** to be submitted to the MNRAS.

4.2 Abstract

We present a catalogue of dynamical properties for 2368 late-type galaxies from the MaNGA survey. The latter complements the catalogue of photometric properties for the same MaNGA galaxies based on deep optical DESI photometry (Arora et al. 2021). Rotation curves (RCs), extracted by model fitting Hα velocity maps from the MaNGA Data Analysis Pipeline, extend out to 1.4 (1.9) R_e for the primary (secondary) MaNGA samples. The RCs and ancillary MaNGA Pipe3D data products were used to construct various fundamental galaxy scaling relations that are compared uniformly with similar relations from NIHAO zoom-in simulations. Simulated

NIHAO galaxies are found to broadly reproduce the observed MaNGA galaxy population for $\log M_* < 9\,\mathrm{M}_\odot$. However, massive galaxies with large sizes, high velocities, and high star formation rates as seen in nature are missing from the NIHAO simulations. Moreover, NIHAO galaxies have higher than observed densities at high stellar masses and lower than observed densities for low stellar masses as a result of over-efficient feedback in NIHAO. We also present the spatially-resolved scatter for the VRM_* structural relations using MaNGA. We find that scatter in the galaxian interiors is a consequence of the diversity of inner RC shapes, while scatter in the outskirts is dictated by the great range of stellar surface densities which itself is controlled by sporadic star formation. The presentation of the detailed spatially-resolved scatter brings together the complex connections between local and global astrophysical processes.

4.3 Introduction

Given their importance for constraining galaxy formation and evolution models, studies of galaxy scaling relations enjoy a rich history (Faber and Jackson 1976a; Tully and Fisher 1977a; Bender et al. 1992; Mo et al. 1998; Steinmetz and Navarro 1999; Courteau et al. 2007; Mo et al. 2010; Kormendy and Ho 2013b; Lelli et al. 2017; Stone et al. 2021a; D'Onofrio et al. 2021). The slope, zero-point, and scatter of scaling relations (Courteau et al. 2007; Kormendy and Ho 2013b; Lange et al. 2015) encode critical information about the structure of galaxies and provide stringent constraints to galaxy formation models (Dutton et al. 2007; Brook et al. 2012; Koch et al. 2017; Dutton et al. 2017; van de Sande et al. 2019; Starkenburg et al. 2019). Such data-model comparisons require large unbiased multi-band observed galaxy data (Jarrett

et al. 2000; York et al. 2000; Driver et al. 2009) and modern state-of-the-art galaxy formation simulations (see Vogelsberger et al. 2020, for a review).

The advent of galaxy surveys with large scale integral field spectroscopy such as MaNGA (Bundy et al. 2015; Wake et al. 2017), ATLAS^{3D} (Cappellari et al. 2011) and CALIFA (Walcher et al. 2014) has opened up new areas of investigations with high quality spatially-resolved dynamical and chemical properties of galaxies. The coupling of IFU data with deep multi-band photometric observations (Courteau 1996; Hall et al. 2012; Gilhuly and Courteau 2018; Ouellette et al. 2017; Arora et al. 2021, hereafter A21) allows detailed studies of different astrophysical processes such as star formation (Pandya et al. 2017), baryonic feedback, dynamics, interactions between baryon and dark matter (Dutton et al. 2011a), impact of environment (Peng et al. 2012), chemical evolution (Gallazzi et al. 2005; Sánchez-Menguiano et al. 2020), angular momentum distributions (Romanowsky and Fall 2012; Obreschkow and Glazebrook 2014), and so on. On the theoretical front, modern state-of-the-art cosmological simulations in a cosmological cold dark matter paradigm allow tracking of the co-evolution of baryons and dark matter (Wang et al. 2015; Crain et al. 2015; Remus et al. 2017; Pillepich et al. 2018; Hopkins et al. 2018; Habouzit et al. 2019). While the distribution (but not the nature!) of dark matter in the Universe is fairly well understood, especially on large-scales, modelling stars, their formation, and gas distributions within galaxies remains a most unconstrained aspect of galaxy formation and evolution theories (Avila-Reese et al. 2011; Sawala et al. 2011; Weinmann et al. 2012; Agertz and Kravtsov 2015). Modern large-scale surveys such as the ones mentioned above provide rich and versatile data that can be used to constrain the distribution of various baryonic properties in cosmological simulations.

Providing the most recent, up-to date and uniform comparison between simulations and observations of galaxies is the motivation for this study. Such comparisons highlight not only benchmarks for our current understanding of galaxy formation and evolution but they also identify specific areas of improvement for galaxy formation models. Two separate approaches can be taken to enable uniformly data-model comparisons of galaxies. One can use cosmological simulations and post-process the data products to generate mock images and spectra of galaxies that include observational characteristics such as atmosphere blur, background sky noise, photometric bandpasses, etc (Torrey et al. 2015; Bottrell et al. 2017; Elagali et al. 2018; Deeley et al. 2021; Bottrell and Hani 2022; Camps et al. 2022). The comparison of such mock data products with real observations can then highlight similarities and differences. Alternatively, one can remove all possible biases and errors from observations (such as extragalactic and galactic dust extinction, photometric band effects, inclination effects, sky noise, sample completion, etc.) and produce data products that can directly be compared to simulated galaxies (Arora et al. 2019; Frosst et al. 2022). Our approach for a robust data-model comparison is the latter.

Combining the MaNGA photometric catalogue (A21) and auxiliary data from Pipe3D (Sánchez et al. 2018) with robust rotation curves creates an extensive observed catalogue which is ideal for comparison with galaxy formation models. Along with the MaNGA survey, we take advantage of the Numerical Investigation of a Hundred Astrophysical Object (NIHAO) project which provides ∼60 zoom-in late-type galaxy simulations. Generally, most data-model comparisons of galaxies focus on a few informative properties of galaxies such as star formation rates (Starkenburg et al. 2019), galaxy sizes (de Graaff et al. 2022), shapes of rotation curves (Santos-Santos

et al. 2018), black hole scaling laws (Çatmabacak et al. 2022), etc. With the substantial MaNGA data presented in A21 and here, we can create 12 galaxy scaling relations out of 7 galaxy structural parameters. The usage of multiple scaling relations (Dutton et al. 2011b; Trujillo-Gomez et al. 2011; Brook et al. 2012) allows for a multi-dimensional data-model comparison that identifies specific parameters which simulations struggle to reproduce. Another important aspect of observation-simulation comparisons is the quantification of fit parameters of scaling relations, especially slope and scatter. While slope comparisons between simulations and observations are relatively trivial, scatter comparisons require the removal of observed biases (distance uncertainty, disk thickness, inclination, mass-to-light conversions, etc.). A common approach to handling such biases consists of removing observational errors in quadrature to retrieve the intrinsic scatter of galaxy scaling relations (Strauss and Willick 1995; Saintonge and Spekkens 2011; Hall et al. 2012; Lelli et al. 2017). However, such a method ignores the correlations between the different biases leading to an underestimation of intrinsic scatter. A Bayesian formalism to calculate intrinsic scatter (Stone et al. 2021a) takes correlated observed errors into account and returns robust estimates of intrinsic scatter. The Bayesian intrinsic scatters for scaling relations determined here can serve as an accurate robust test for galaxy formation simulations.

Furthermore, a great advantage of modern deep multi-band imaging and large IFU surveys is to allow analyses of spatially-resolved scaling relations (e.g., Radial Acceleration Relation, Lelli et al. 2017; Stone and Courteau 2019; Star Formation Main Sequence, Cano-Díaz et al. 2016; Hall et al. 2018). Recent studies of spatially-resolved scaling relations have already revealed new aspects of galaxy formation and

evolution. For example, the presence of a tight spatially-resolved star formation main sequence relation (SFMS) is comparable to the global SFMS (Wuyts et al. 2013; González Delgado et al. 2016; Wang et al. 2017; Hall et al. 2018; Ellison et al. 2018). The presence of a spatially-resolved star formation law is strongly dependent on small-scale local gas and stellar surface density. Spatially-resolved scaling relations based on a wide array of structural parameters are still largely lacking. The variations of scatter as a function of galactocentric radius for scaling relations (such as size-mass, size-velocity, and Tully-Fisher relations) can be a powerful tool in identifying the drivers of diversity in galaxy structure. Spatially-resolved scatter diagnostics can simultaneously constrain the overall distribution of galaxy properties as well as astrophysics on sub-galactic scales (for eg. the spatially-resolved Star Formation Main Sequence and the Radial Acceleration Relation). Comparisons of spatially-resolved scaling relations can also inform more advanced tests for cosmological simulations. With our deep photometric and dynamical data, for the first time, we study the variations and drivers of scatter as a function of location in observed and simulated galaxies.

This chapter is organized as follows: in Section 4.4, we describe the photometry and rotation curves (RCs) from the MaNGA galaxy survey and the process of extracting and correcting various galaxy properties. All of our processed data, including the observed light profiles and RCs, are made public. In Section 4.4, we compare our RCs against other observed rotation curves and scaling relations. Section 4.5 gives a brief description of the NIHAO galaxy formation simulations that are compared against observations. In Section 4.6, we present a simultaneous comparison of 12 galaxy scaling relations between MaNGA, with their observed Bayesian

intrinsic scatter, and NIHAO. In Section 4.7, we examine the radial variations of the spatially-resolved scatters for structural galaxy scaling relations for MaNGA and NIHAO. Concluding remarks are offered in Section 4.8, with en eye towards improving numerical simulations of galaxy formation and evolution.

4.4 Observational Data

In this section, we briefly describe our extraction of photometric properties for the MaNGA galaxies using deep imaging. A detailed description of the extensive imaging catalogue is found in A21. RCs rotation curves and dynamical properties are also derived below, and compared against other published rotation curves and scaling relations.

4.4.1 Photometry

In order to lay the foundations for our study of the photometric and dynamical properties of MaNGA galaxies, we first take advantage of the extensive catalogue of non-parametric multi-band photometric and environmental properties for ∼4500 MaNGA galaxies, as presented in A21. This photometric catalogue relied on the deep optical *grz*-band imaging from the Dark Energy Sky Instrument Legacy Imaging Survey [1] (DESI Collaboration et al. 2016; Dey et al. 2019, hereafter DESI) and the WISE Large Galaxy Atlas and the Extended Source catalogue (WXSC; Jarrett et al. 2019). Non-parametric azimuthally-averaged surface brightness (SB) profiles were extracted using the automated astronomical image analysis tool, AUTOPROF (Stone et al. 2021b). AUTOPROF performs a robust background subtraction and finds an

[1] https://www.legacysurvey.org

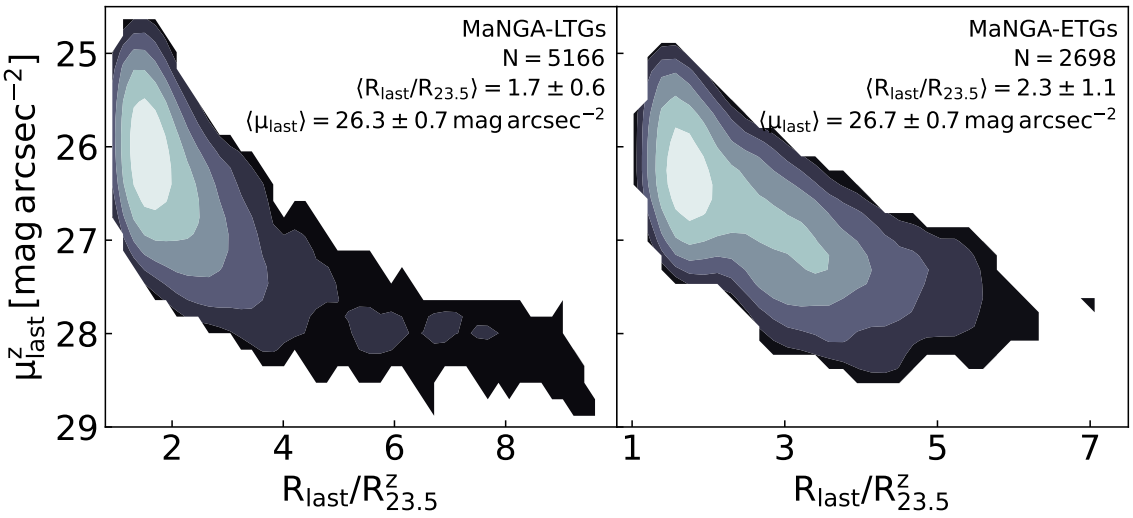

Figure 4.1: Surface brightness depth versus maximal spatial extent (in units of $R_{23.5}$) for MaNGA galaxies. The surface brightness profiles for LTG (left) and ETGs (right) were extracted through AUTOPROF in the z-band. The text insets give the number of galaxies, mean maximal spatial extent, and mean surface brightness depth in the z-band.

accurate galaxian center for each galaxy image before fitting elliptical isophotes.

The center, position angle (PA), and ellipticities of each isophote is fit to the DESI r-band images for MaNGA galaxies. The r-band imaging is chosen for the extraction of isophotal profiles due to its high signal-to-noise ratio and low dust extinction relative to the other bands (A21). To obtain multi-band photometry, the r-band isophotes are applied to the other gz-band images via forced photometry, resulting in complimentary grz surface brightness profiles. The "forced photometry" component of AUTOPROF ensures uniformity in measurement of surface brightness, ellipticities, fluxes, and color gradients. For a more comprehensive description of the AUTOPROF software package and its capabilities, the reader is referred to Stone et al. (2021b).

Because of their lowest sensitivity to dust extinction, all photometric properties

were calculated using the DESI z-band surface brightness profiles. This also ensures uniformity with other studies (Stone et al. 2021a; Arora et al. 2021; Frosst et al. 2022).

While the photometric data presented in A21 were based on the galaxies selected using the public SDSS-DR16 catalogue (Ahumada et al. 2020), the MaNGA photometric data used in this study are based on the SDSS-DR17 (Abdurro'uf et al. 2022). The cross-correlation between the MaNGA data release from SDSS-DR17 and the DESI sky survey yielded 7864 galaxies; 5166 of which were classified as LTGs (Domínguez Sánchez et al. 2018), and used in our comparison between simulations and observations. Fig. 4.1 presents the maximal SB depth in the z-band of our photometric LTG (left) and ETG (right) samples. Thanks to the deep DESI imaging and the versatility of AUTOPROF, we can probe SBs down to (on average) $\sim$26.3 mag arcsec^{-2} and $\sim$2 R/R$^{z}_{23.5}$ for MaNGA LTGs. Our robust non-parametric photometry through DESI imaging and AUTOPROF results in gathering 0.1 dex more light and 0.3 dex more stellar masses for the same galaxies than presented in the NSA catalogue (Blanton and Roweis 2007).

4.4.2 Rotation Curves

A key aspect of this study is coupling of kinematic data presented here with the photometric information from A21 for the same galaxies. Our spectroscopic analysis takes advantage of the Hα emission line-of-sight (LOS) velocity maps (hereafter Hα velocity maps) provided through the MaNGA Data Analysis Pipeline (MaNGA-DAP; Westfall et al. 2019; Belfiore et al. 2018) and accessed via the "Marvin" toolkit (Cherinka et al. 2019).

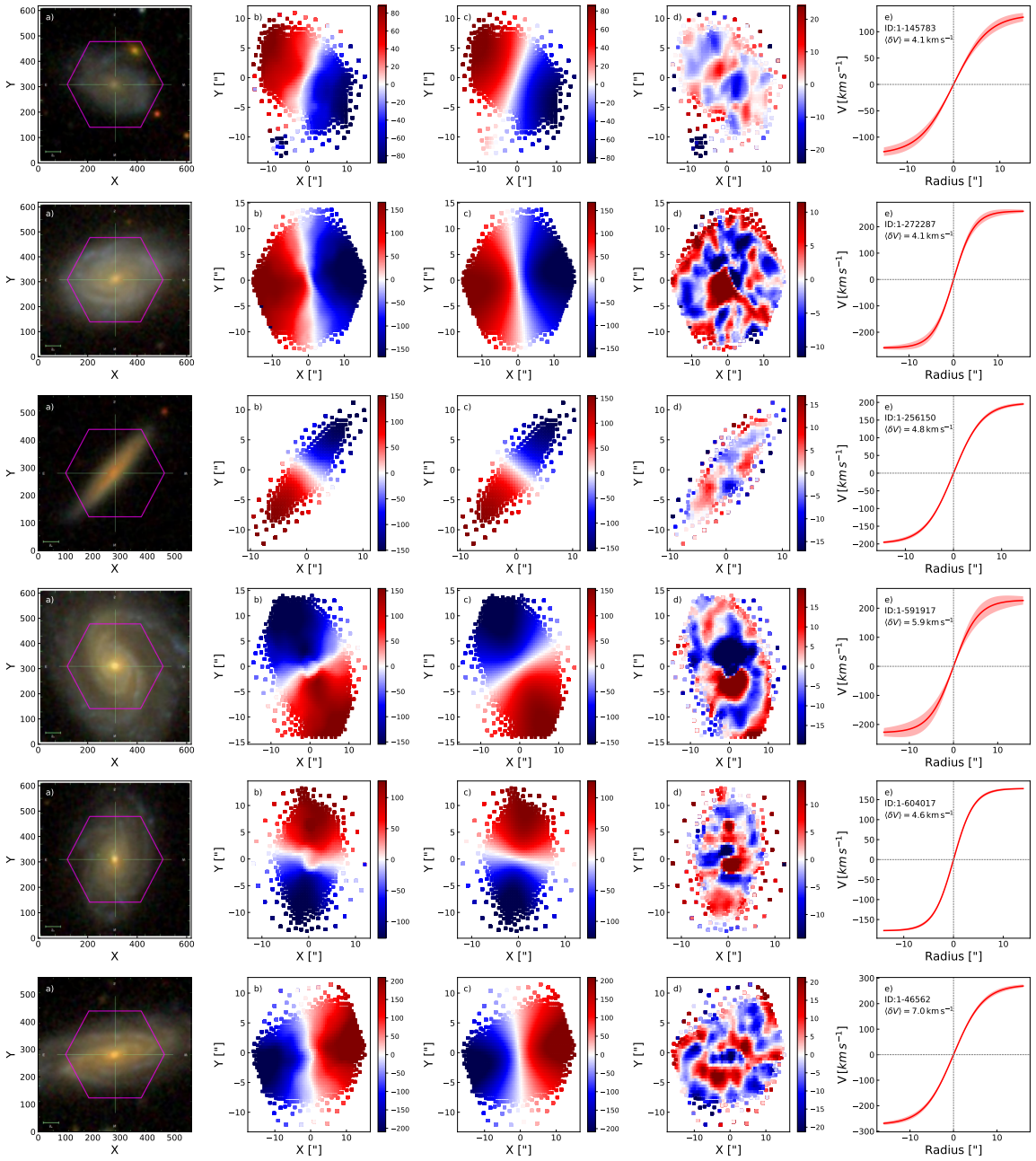

Figure 4.2: MaNGA Hα velocity maps and extracted RCs. For each row, corresponding to a different MaNGA target, panel a) shows the composite SDSS-*gri* image with the MaNGA IFU footprint (in magenta); panel b) shows the matching Hα velocity map from the MaNGA IFU; and panels c), d) and e) present the tanh model velocity maps, residual maps ($V_{\rm obs} - V_{\rm model}$), and the corresponding rotation curve. The inset in panel e) also gives the MaNGA-ID and average data-model residual $\langle \delta V \rangle = \langle (V_{\rm obs} - V_{\rm model}) \rangle$.

Velocity model

RCs were obtained by fitting the following model to the Hα velocity map

$$V_{\rm LOS}(R,\theta) = V_{\rm sys} + V(R)\cos(\theta)\sin(i), \tag{4.1}$$

where $V_{\rm LOS}(R)$ is the observed LOS velocity at radius R, $V_{\rm sys}$ is the systematic (heliocentric) velocity, θ is the azimuthal angle, i is the inclination of the galaxy on the sky, and $V(R)$ is the adopted rotational velocity model. In Eq. 4.1, $R = \sqrt{x_{\rm g}^2 + y_{\rm g}^2}$ and $\theta = \tan^{-1}(y_{\rm g}/x_{\rm g})$ are calculated using Cartesian coordinates within the disk of the galaxy. These are defined as:

$$x_{\rm g} = x'_{\rm s}\cos(-{\rm PA}) + y'_{\rm s}\sin(-{\rm PA}), \tag{4.2}$$

and

$$y_{\rm g} = \frac{y'_{\rm s}\cos(-{\rm PA}) - x'_{\rm s}\sin(-{\rm PA})}{\cos(i)}, \tag{4.3}$$

where $x'_{\rm s} = x_{\rm s} - x_{\rm c}$ and $y'_{\rm s} = y_{\rm s} - y_{\rm c}$ are centred projected coordinates on the sky with the observed galaxy center given by $(x_{\rm c}, y_{\rm c})$, and PA is the observed position angle. For this study, and for uniformity with other studies (Courteau 1997; Aquino-Ortíz et al. 2020b; Brownson et al. 2022), we write:

$$V(R) = V_{\rm max} \times \tanh(R/R_{\rm t}), \tag{4.4}$$

for the rotational velocity model in Eq. 4.1, where $V_{\rm max}$ is the maximum velocity, and $R_{\rm t}$ is a turnover radius between the rising and flat portion of the RC. Therefore, the kinematic modeling of MaNGA galaxies requires fitting a dynamical model with seven

parameters; (x_c, y_c), i, PA, V_{sys}, V_{max}, and R_t. These fit parameters are described in Section 4.9.

For the fit initialization, (x_c, y_c), and V_{sys} are first set to zero, while the inclination and PA use values calculated through the DESI photometry (A21). V_{max}, and R_t are initialized by fitting Eq. 4.4 to a "mock rotation curve", calculated by interpolating observed Hα velocity map along to the photometric major axis. The quality of the dynamical model is evaluated as the "mean square error", $\langle \delta V^2 \rangle = \langle (V_{obs} - V_{model})^2 \rangle$. We calculate robust fit parameters of our dynamical model by running our fitting algorithm 20 times with initialization values randomly chosen within ± 50 per cent of the first fit evaluated with the initial values mentioned above. The final fit is calculated with the set of fit parameters which return the lowest $\langle \delta V^2 \rangle$ out of the random 20 runs. Fig. 4.2 shows the composite SDSS *gri* image, the corresponding Hα velocity map, the model velocity map, the residual and the rotation curves for six late-type MaNGA galaxies. The top row of Fig. 4.2 shows a galaxy with a foreground object; in general, we find that our fitting routine is robust against background/foreground objects observed within the MaNGA IFU.

Our dynamical models fit the observed MaNGA Hα velocity maps very well. The average $\langle \delta V \rangle$ for all the MaNGA galaxies is $7\,\mathrm{km\,s^{-1}}$ (see Fig. 4.3). However, the distribution of $\langle \delta V \rangle$ has a non-negligible tail at high $\langle \delta V \rangle$. Indeed, objects with $\langle \delta V \rangle \geq 10\,\mathrm{km\,s^{-1}}$ present signatures of non-circular motions (caused by bars and bulges) that are unaccounted for within our dynamical model. These non-circular motions (caused by bars and bulges) are mainly dominant in the central parts of galaxies and have an amplitude of $\sim$15 $\mathrm{km\,s^{-1}}$. Given the stellar mass distribution of MaNGA galaxies ($\log M_* > 9\,\mathrm{M_\odot}$); such non-circular motions would not make a large

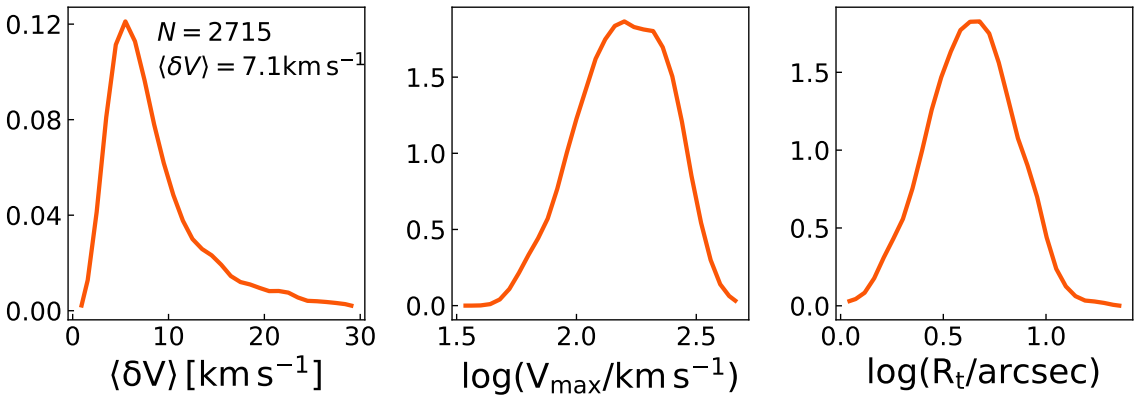

Figure 4.3: Distributions of the fit quality (evaluated as $\langle \delta V \rangle = \langle (V_{\rm obs} - V_{\rm model}) \rangle$), as well as the model maximum (asymptotic) velocity, $V_{\rm max}$, and turnover radius, $R_{\rm t}$.

impact on the results presented here. Given that the galaxy scaling relations that we study trace largely the outer galaxian regions, the central non-circular motions should be insignificant in our analysis (Sellwood et al. 2021).

The coupling of the MaNGA spectroscopic data with our photometry from A21 enables us to quantify the physical extent of the MaNGA spectral data. The MaNGA primary and color-enhanced samples (primary+) have indeed been claimed to probe regions out to 1.5R$_{\rm e}$, and the secondary sample would extend out to 2.5R$_{\rm e}$ (Bundy et al. 2015). The effective radii came from the NASA Sloan Atlas (NSA) catalog (Blanton and Roweis 2007). The distribution of the extent of the spectroscopic data scaled with various characteristic radii extracted from A21 is shown in Fig. 4.4. The extent of both primary+ and secondary sample is found to be lower than the nominal 1.5 and 2.5R$_{\rm e}$. This is because our non-parametric approach and more sensitive DESI imaging yield ∼0.3 mag more light for MaNGA-LTGs (A21) than conventional SDSS imaging. Indeed, A21's effective radii are larger than those from the NSA catalog. As a result, the MaNGA primary+ and secondary samples extend out to 1.43 ± 0.35 R$_{\rm e}$

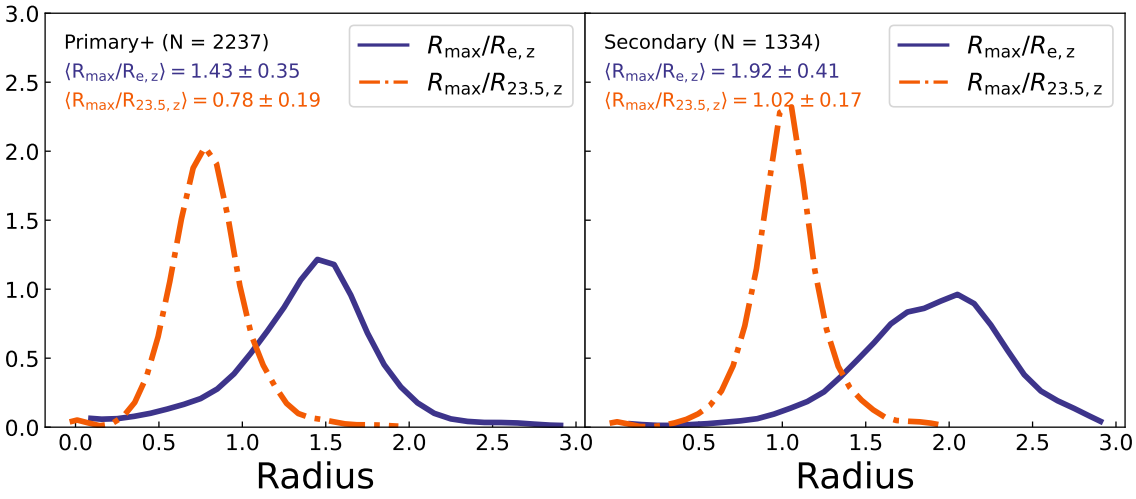

Figure 4.4: Distribution of the MaNGA RC extents in terms of different photometric radii. $R_{\rm max}$, $R_{\rm e,z}$, and $R_{23.5,\rm z}$ are the luminosity-weighted maximum radius (in arcsec) for the MaNGA IFU, the effective radius, and the isophotal radius measured at a surface brightness level of 23.5 mag arcsec^{-2}, all reported in the z-band. $R_{\rm e,z}$, and $R_{23.5,\rm z}$ were obtained from DESI photometry of MaNGA galaxies (A21). The left and right panels show primary (+color enhanced) and secondary samples, separately. The insets give the median RC extents with an error of 1σ.

and $1.92 \pm 0.41\,{\rm R_e}$, respectively.

Fig. 4.4 also shows the MaNGA RC extents scaled by isophotal radius. The isophotal (or mass density) measurements for galaxy sizes are more robust, accurate, and reproducible (Hall et al. 2012; Trujillo et al. 2020, A21). In term of isophotal size, measured at the 23.5 mag arcsec^{-2} isophote, the MaNGA spectroscopic data extends out to 0.78 ± 0.19 (1.02 ± 0.17) $\rm R_{23.5}$ for the primary+ (secondary) samples, respectively.

Error estimation

We use "Jackknife resampling" (Quenouille 1949) to estimate the fit parameter errors of our dynamical models (Eq. 4.1). A spaxel is randomly selected and all spaxels

within 2.5″ radius are removed to produce a new truncated velocity map. The new velocity map is then fit again with Eq. 4.1 to calculate truncated fit parameters. The Jackknife resampling process is repeated 100 times. The error on the fit parameters is the 16-84 per centile range for the 100 Jackknife runs. These errors are also reported in the catalogue of dynamical properties (Section 4.9).

Quality cuts

Our MaNGA LTG sample (Domínguez Sánchez et al. 2018) consists of 5166 galaxies for which DESI-*grz* imaging and robust photometry through AUTOPROFis available. To obtain RCs for MaNGA LTGs, we only use galaxies which achieve photometric inclinations between 30-80 degrees. This inclination cut ensures robust inclination corrections for the RC. For galaxies with DESI photometric data and favourable inclinations, we run our velocity model to extract RCs. For the galaxies with both photometry and RCs, we only use systems where the seven fits parameters for the velocity models have errors $< 20\%$. In the end, we are left for the remainder of this study with a final set of 2368 galaxies which have robust photometry and RCs.

4.4.3 Parameter Extraction and Correction

While the photometric (A21) and dynamical catalogues presented here are highly versatile, we are primarily concerned with the sizes, stellar mass, velocity metrics, dynamical masses, and stellar mass surface density within a physical radius (e.g., 1 kpc).

The photometric properties were extracted and corrected using methods described in A21. These are briefly described below; see A21 for more details.

Corrections

All SB profiles used in this study were corrected for Galactic and internal extinction, as well as for cosmological K-corrections. The Galactic extinction corrections were retrieved from the NSA catalogue (Blanton et al. 2011), originally taken from Schlegel et al. (1998). These corrections are available for the optical *grz* photometric bands. The cosmological K-corrections were calculated using templates from Blanton and Roweis (2007).

Our corrections for internal dust extinction and geometry/inclination were applied after extracting the structural parameters. The inclination corrections were calculated using a linear fit between each structural parameter and the log of the cosine of the inclination (Giovanelli et al. 1994). The inclination correction can be written as:

$$\log X_0 = \log_X i + \gamma \log(\cos i), \tag{4.5}$$

where X_0 is the galaxy property corrected to face-on view, X_i is the observed galaxy property, and i is the observed inclination of the galaxy disk on the sky. The photometric inclination, i, is related to the projected axis ratio (b/a) of the object as

$$\cos^2 i = \frac{(b/a)^2 - q_0^2}{1 - q_0^2}, \qquad (q_0 = 0.13) \tag{4.6}$$

where q_0 is the assumed stellar disk thickness (Hall et al. 2012). For more details about the various corrections to the MaNGA photometric data, see A21.

The RCs are also corrected for inclination by dividing the sin of the disk inclination (see Eq. 4.1). It should be noted that the kinematic inclinations are independent of the photometry as the former is a fit parameter in our dynamical model. The difference

between kinematic and photometric inclinations can reach $\sim 5 \pm 9^{\circ}$ (see Figure 4.5).

Parameter extraction

The sizes, stellar masses, and surface densities were estimated using the photometric data. For greater compatibility with simulations (which predict mass rather than light), we convert all of our light-weighted properties into mass-weighted properties. Stellar mass estimates for the MaNGA galaxies were calculated using various stellar mass-to-light color relations (MLCRs; Courteau et al. 2014). To achieve the maximum robustness for our stellar mass estimates, five different MLCRs were averaged from Roediger and Courteau (2015), Zhang et al. (2017), and García-Benito et al. (2019). The stellar mass estimates use $g-r$ and $g-z$ optical colours and luminosities from all three DESI bands. As a result, the stellar masses are calculated as the average of 30 different measurements and their standard deviation is taken as the error.

The physically-motivated galaxy sizes used in this study represent the semi-major axis of various isophotal levels, measured in $\mathrm{mag\,arcsec^{-2}}$ or $\mathrm{M_{\odot}\,pc^{-2}}$. As shown by Trujillo et al. (2020), such a representation of sizes yields a tighter scatter for the size–mass relation.

We use the quantity, $\Sigma_1 = M_{*,1\,\mathrm{kpc}}/\pi$ $[M_{\odot}\,\mathrm{pc}^{-2}]$, as a representation of stellar mass surface density within a projected radius; specifically 1 kpc.

Velocity metrics were calculated by interpolating the inclination-corrected RCs at various radii. Finally dynamical masses, $M_{\mathrm{dyn}}(R)$, are calculated using the velocity, $V(R)$, at projected radius, R, the gravitational constant, G, and assuming a spherical halo:

$$M_{\mathrm{dyn}}(R) = \sqrt{\frac{V^2(R)R}{G}}. \tag{4.7}$$

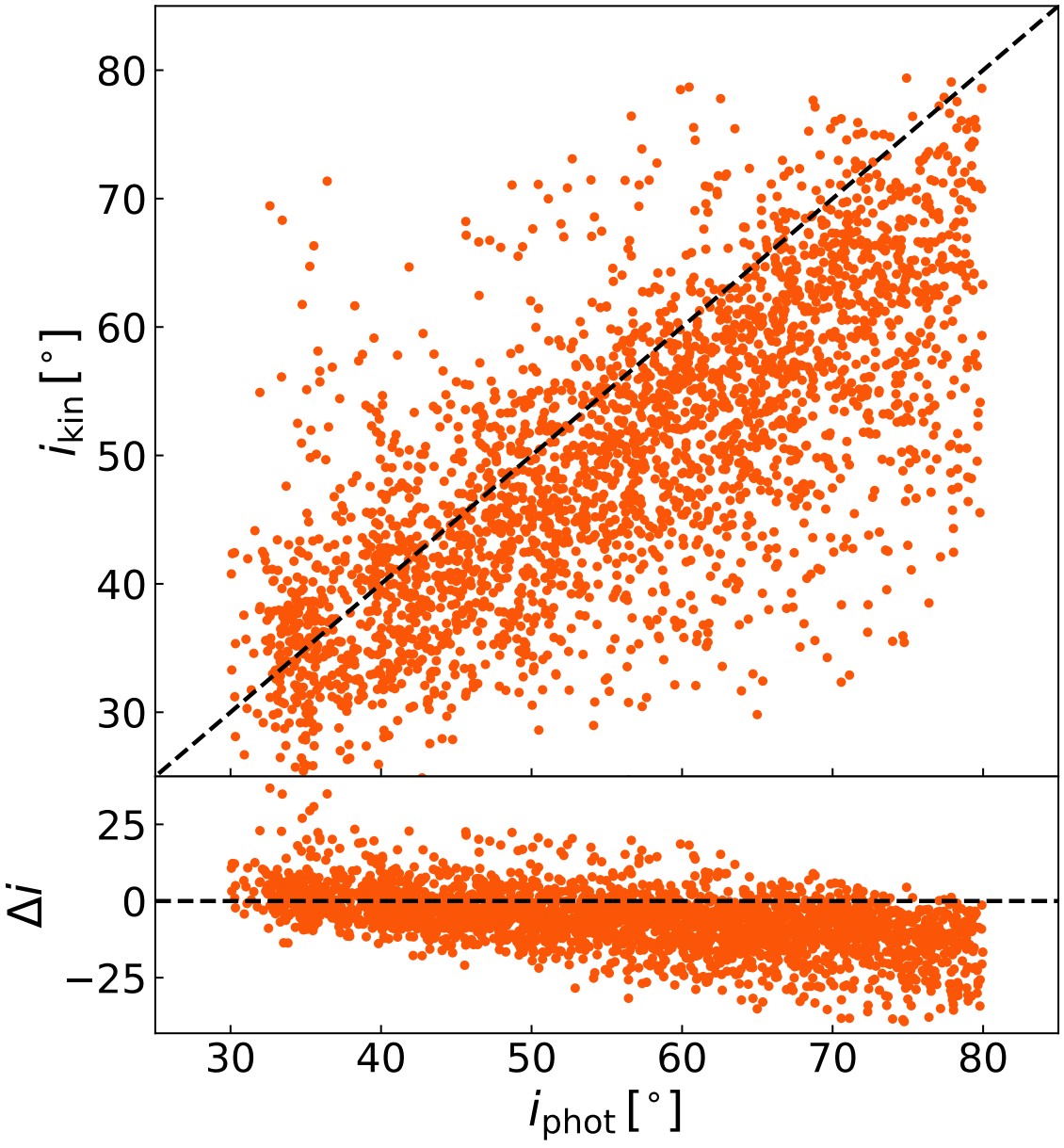

Figure 4.5: Comparison of photometry inclinations from AUTOPROFversus kinematic inclinations obtained from model velocity fitting. The dashed black line is the one-to-one relation.

The error in the dynamical mass at radius R is calculated as

$$\delta M_{\rm dyn}(R) = \left[\left(\frac{2V(R)R\delta V(R)}{G}\right)^2 + \left(\frac{V(R)^2\delta R}{G}\right)^2\right]^{1/2}. \quad (4.8)$$

In Eq. 4.8, $\delta V(R)$ and δR are the measured uncertainties.

4.4.4 Literature Comparisons

We confirm the validity of our MaNGA RCs by comparing them with similar independent observations for the same object. Fig. 4.6 shows such a comparison for the ten galaxies overlapping between MaNGA and the PROBES ("Photometry and Rotation Curve Observations from Extragalactic Surveys") sample (hereafter PROBES; Stone and Courteau 2019; Stone et al. 2021a). MaNGA's spectroscopic data were taken with an IFU, while most PROBES RCs were obtained via Hα long-slit spectra (except 1-135468 taken in HI). While the MaNGA RCs can be extrapolated to infinity (as a result of the tanh fit), the extent of the models shown in Fig. 4.6 is limited to the IFU spatial coverage. The pair of 10 RCs between PROBES and MaNGA trace each other quite well; on average the RCs from both samples differ by $\sim$24 km s^{-1} or $\sim$0.1 $V_{\rm max}$. The match is nearly perfect for galaxies (MaNGA-ID) 1-446131 and 1-605088. Galaxy (MaNGA-ID) 1-135468 shows a great match between the MaNGA IFU and HI observations (which naturally extend further). While PROBES RCs have typically greater spatial extent, MaNGA RCs sometimes provide better coverage in the central parts of disk galaxies.

The full catalogue enables us construct scaling relations which can also be compared with the literature. Fig. 4.7 presents the VRM$_*$ scaling relations for $\sim$2300 LTGs compared with other sources. The orthogonal distance regression (hereafter

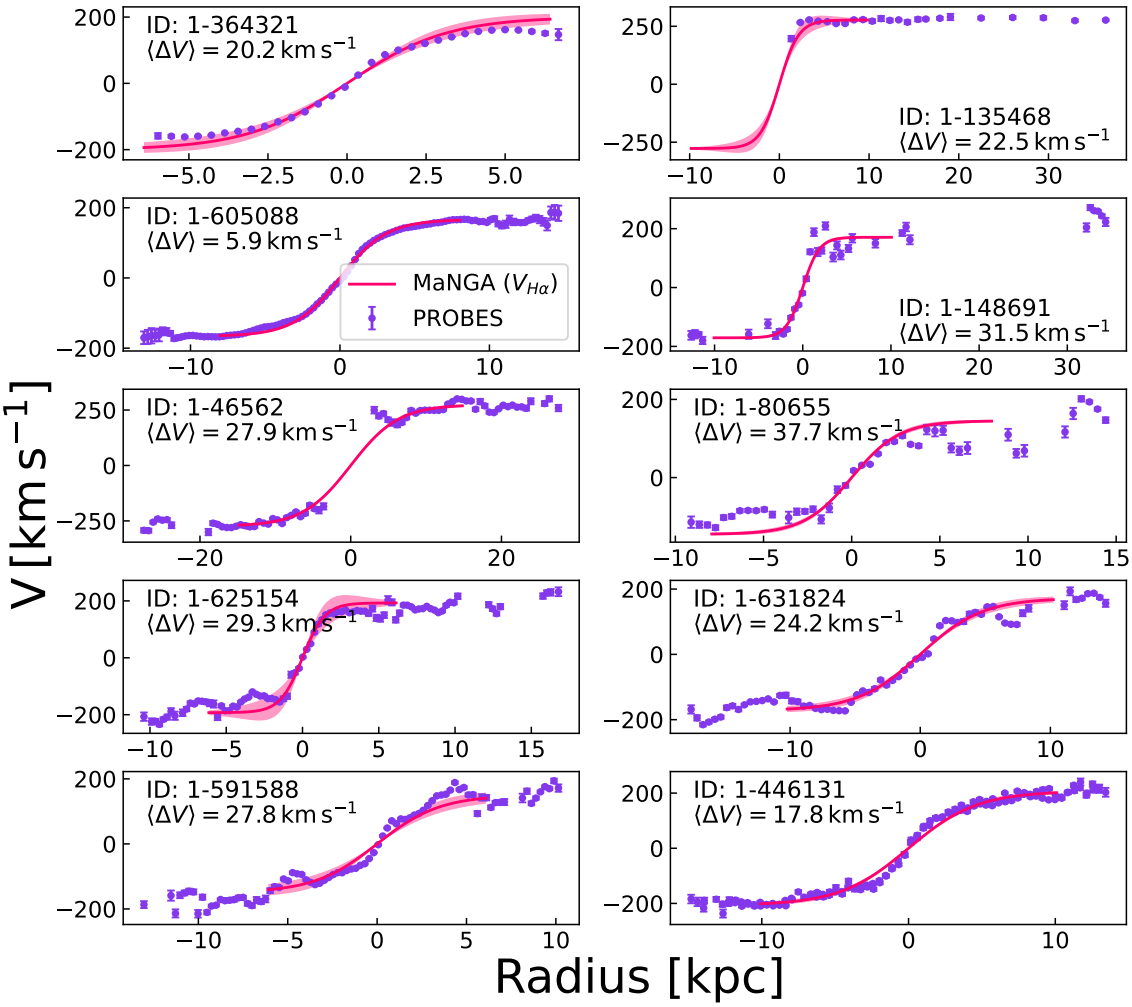

Figure 4.6: Comparison of inclination-corrected RCs for the ten galaxies between MaNGA and the PROBES sample (Stone et al. 2021a). Each panel compares the long slit Hα RC (purple points with error bars) from PROBES with the RC (pink solid lines with shaded regions) extracted from the MaNGA Hα velocity map. The inset text gives the MaNGA object ID and the RMS between the MaNGA/PROBES data sets.

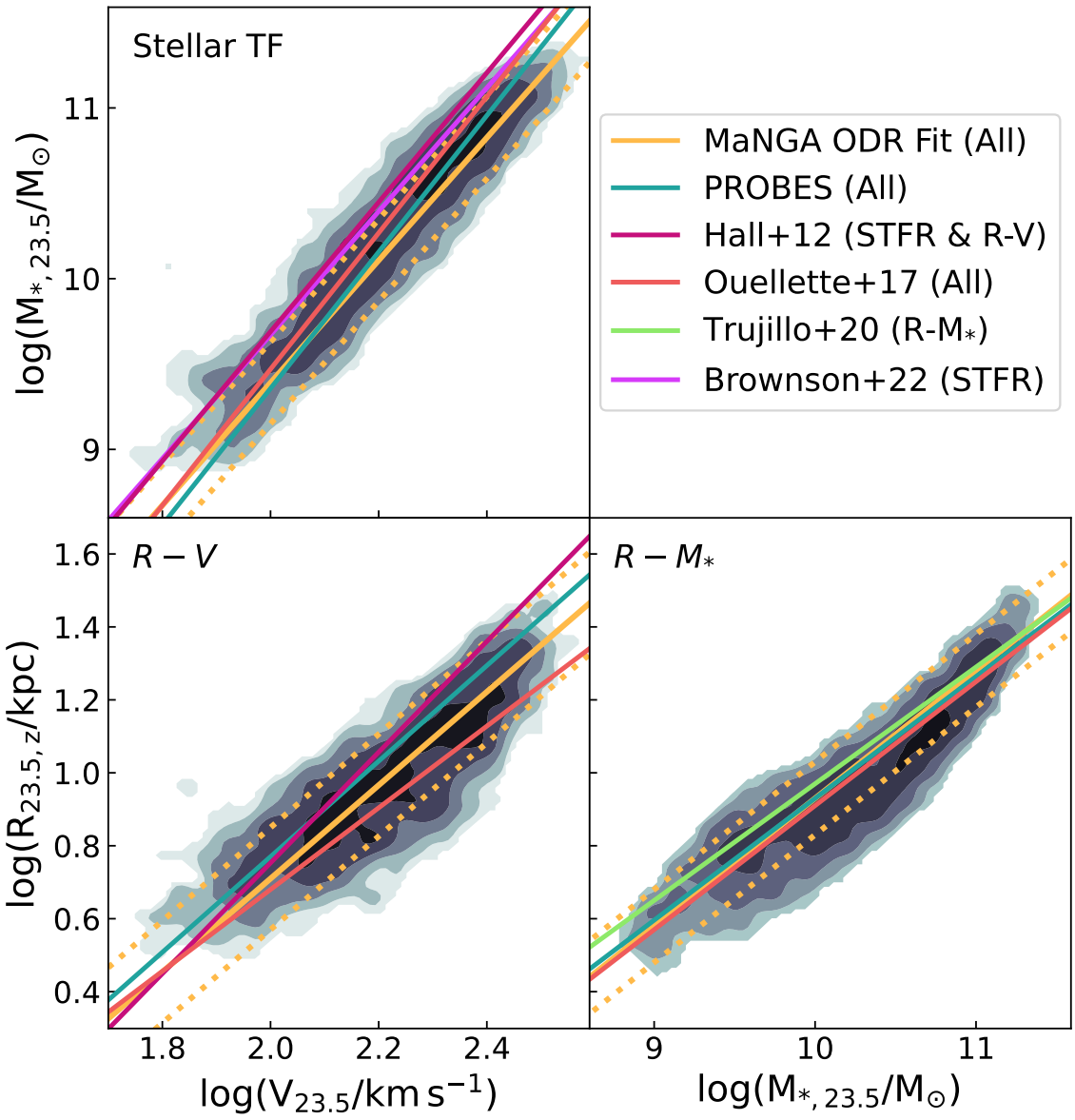

Figure 4.7: MaNGA VRM$_*$ scaling relations measured at an isophote of 23.5 mag arcsec^{-2} in the z-band. The three panels show the stellar TFR (top-left), R–V relation (bottom-left), and, the R–M$_*$ relation (bottom-right). In each panel, the density contours show the underlying MaNGA data fitted with a linear orthogonal distance regression (orange solid line; the 1σ scatter is shown as an orange dotted line). Each scaling relation is compared with various literature sources. The legend (top-right) highlights those sources with the relevant scaling relations in parenthesis.

Scaling Relation (1)	N (2)	y (3)	x (4)	α (5)	β (6)	$\sigma_{\rm obs}$ (7)	$\sigma_{\perp}$ (8)
Stellar Tully-Fisher	2368	$\log M_{*,23.5}$	$\log V_{23.5}$	3.59 ± 0.04	2.21 ± 0.08	0.24 ± 0.01	0.06 ± 0.01
Projected size–velocity	2368	$\log V_{23.5}$	$\log R_{23.5,z}$	1.28 ± 0.02	-1.85 ± 0.05	0.14 ± 0.01	0.09 ± 0.01
Projected size–stellar mass	2368	$\log R_{23.5,z}$	$\log M_{*,23.5}$	0.35 ± 0.01	-2.57 ± 0.03	0.10 ± 0.01	0.09 ± 0.01

Table 4.1: VRM$_*$ scaling relations for the 2368 MaNGA galaxies. Each scaling relation is modelled as $y = \alpha x + \beta$ through orthogonal distance regression. Column (1) gives the scaling relation, column (2) shows the number of points fit; columns (3-4) present the x and y variables for the fit; columns (5-6) show the slope (α), zero-point (β), and the observed scatter ($\sigma_{\rm obs}$), respectively; and, column (8) gives the orthogonal scatter ($\sigma_{\perp}$) for the scaling relation.

ODR) linear fits and scatters for each relation are given in Table 4.1. In general, our photometry and RC modelling yield scaling relations that match other studies. For the sake of uniformity and unless otherwise stated, the selected comparisons in Fig. 4.7 use isophotal radii measured at the 23.5 mag arcsec^{-2} isophote. In what follows, we briefly discuss and compare each scaling relation.

Projected size – stellar mass relation

The MaNGA size-mass (R – M$_*$) relation, shown in the bottom-right panel of Fig. 4.7, has an ODR slope of $\log R_{23.5,z} = (0.35 \pm 0.01) \log M_{*,23.5} + (-2.57 \pm 0.03)$ and an observed scatter of 0.10 ± 0.01 dex. That relation, the same as that presented in A21, can be compared with similar ones presented by Ouellette et al. (2017), Trujillo et al. (2020), and Stone et al. (2021a) for different samples. For instance, Ouellette et al. (2017) used SDSS i-band photometry for the SHIVir survey of Virgo cluster galaxies to derive a R – M$_*$ relation with a similar ODR slope of 0.34 ± 0.02, shown as the dark orange solid line, though with a larger scatter of 0.15 dex. That larger scatter is due to a much lower sample size (69 galaxies) in the SHIVir survey. Stone et al. (2021a) also

constructed a R – M_* relation for 1152 PROBES galaxies with structural parameters measured using similar methods as ours. Both analyses of the PROBES and MaNGA data sets used DESI imaging and SB profiles extracted through the AUTOPROF. It is therefore not surprising that their ODR slope of $0.334^{0.009}_{0.004}$ and scatter of $0.099^{0.002}_{0.003}$ should be so close to ours for MaNGA. Any (very small) difference ought to be explained by the use of two different samples.

Studying 464 LTGs from the SDSS IAC Stripe82 survey, Trujillo et al. (2020) found an isophotal ODR slope of 0.318 ± 0.014 (light green solid line) and a scatter of 0.087 ± 0.005. Isophotal sizes are sensitive to the choice of photometric bands; while we use z-band, Trujillo et al. (2020) used the SDSS-i band. The difference in the fit parameters are a result of choice of photometric band for our respective analysis.

Projected size – velocity relation

The size – velocity (RV) relation for MaNGA LTGs, shown in the bottom-left panel in Fig. 4.7, has an ODR fit of $\log R_{23.5,z} = (1.28 \pm 0.02) \log V_{23.5} + (-1.85 \pm 0.05)$ with an observed scatter of 0.14 ± 0.01. The PROBES galaxies also benefit from long-slit Hα RCs and yield an RV relation whose parameters are closely matched with MaNGA's; $\alpha = 1.325^{0.074}_{0.034}$ and $\sigma_{\rm obs} = 0.128 \pm 0.004$. The RV relation for the SHIVir galaxies (Ouellette et al. 2017) has a much smaller slope of 1.1 ± 0.1. The difference could be due to environmental effects, or small number statistics. The latter actually thwarts a conclusive answer. Hall et al. (2012) used SDSS photometry and rotational velocities from integrated HI linewidths from Springob et al. (2005, 2007) to find a steeper RV slope of 1.518 ± 0.065 and an observed scatter of 0.152 dex. While our scatters agree within the error, the slopes for our respective RV relations differ significantly.

While integrated HI linewidths are often shown to reproduce various well-defined spatially-resolved rotational velocities (Courteau 1997), an exhaustive study should be conducted to characterize the spatial coverage of the HI linewidths used by Hall et al. (2012). The latter is beyond the scope of this paper.

Different velocity measurements can definitely result in different slopes for our respective R – V relation. Other sources of uncertainties include distance measurements and inclination corrections.

Stellar Tully – Fisher relation

The combination of our photometry (A21) and RC analysis yields a stellar Tully-Fisher (STFR), or M_*–V relation, which informs us about the cross-talk between the stellar and dark matter in MaNGA galaxies (Dutton et al. 2010; Hall et al. 2012; Ouellette et al. 2017; Stone et al. 2021a; Aquino-Ortíz et al. 2020b). The STFR for MaNGA LTGs, measured at $R_{23.5}$, shown in the top-left panel of Fig. 4.7, is described by $\log M_{*,23.5} = (3.59 \pm 0.04) \log V_{23.5} + (2.21 \pm 0.08)$ with an observed scatter of 0.24 ± 0.01 dex. This ODR fit slope agrees with theoretical derivations of $\alpha \sim 3 - 4$ (Courteau 1997). Moreover, of the three VRM scaling relations studied here, the STFR is the tightest with a small orthogonal scatter ($\sigma_\perp = \sigma_{\rm obs}/(1+m^2)^{0.5}$), as shown in Table 4.1. The study of 1152 PROBES galaxies by Stone et al. (2021a) yielded a STFR slope of $3.997^{0.144}_{0.039}$ and an observed scatter of $0.248^{0.009}_{0.007}$ dex. Similarly, Ouellette et al. (2017) found a STFR slope of 3.99 ± 0.18 for SHIVir galaxies. These two STFRs are actually steeper than the one found here for MaNGA galaxies. This discrepancy can be explained by the sample differences; SHIVir and PROBES sample consists of more dwarf galaxies than MaNGA. As is seen in the Baryonic Tully-Fisher

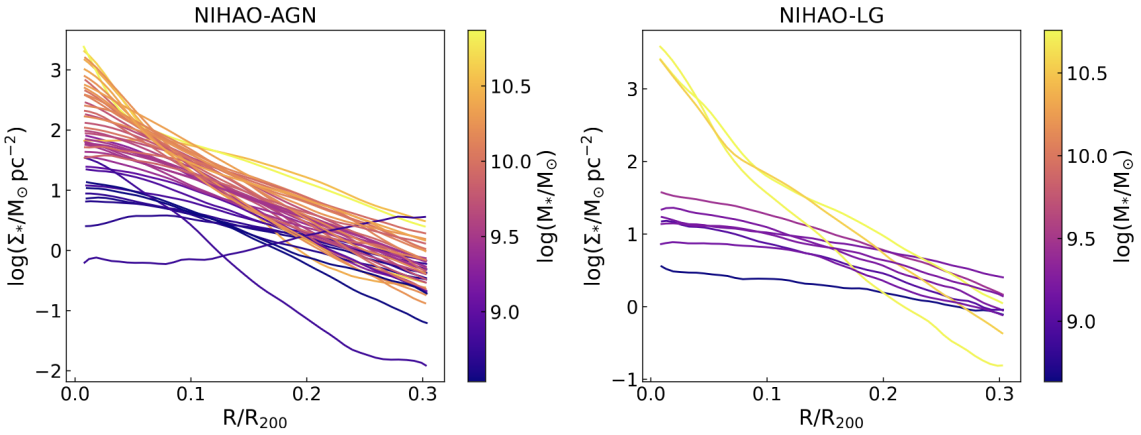

Figure 4.8: Stellar mass surface density profiles for NIHAO-AGN (left panel) and NIHAO-LG (right panel) galaxies. The colour of each line represents the stellar mass of each galaxy at $z = 0$. The radial axis is normalized by R_{200} ($= 600H_0^2/8\pi G$). The stellar mass density profiles are calculated for the halo aligned face-on.

relation, dwarfs have a different stellar TFR slope until corrected for gas mass.

Brownson et al. (2022) also studied the correlation between dynamical tracers and star formation quenching in galaxies with MaNGA galaxies. Their modelling of stellar velocities used a formalism similar to ours with Eq. 4.1, Brownson et al. (2022) yiedling a STFR slope of 3.62±0.13. The latter is certainly a closer match to our Hα velocity-based STFR slope than those measured by Ouellette et al. (2017) or Stone et al. (2021a). However, the scatters differ, 0.24 dex in this study versus 0.09 dex in Brownson et al. (2022), as a result of the definition of scatter interquartile range versus root mean square error. The zero-points also differ by ∼0.2 dex, due to the different stellar measurements and various assumptions such as the choice of IMFs and the location of stellar mass measurements.

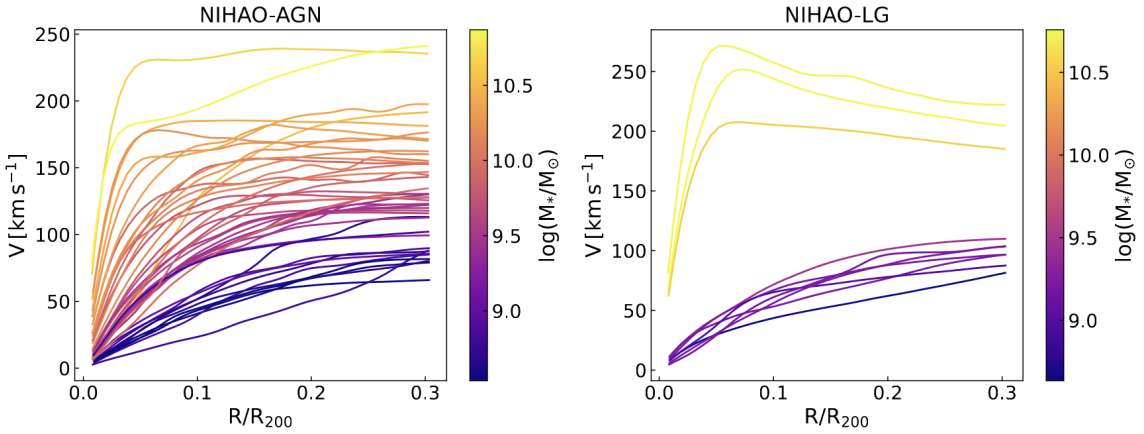

Figure 4.9: RCs for NIHAO-AGN (left panel) and NIHAO-LG (right panel) galaxies. The colour of each line represents the stellar mass of each galaxy. The radial axis is normalized by R_{200}. RCs are calculated for halos viewed edge-on.

4.5 NIHAO Galaxy Formation Simulations

Having established a solid baseline of observed disk galaxy scaling relations for MaNGA sample, we are now poised to make direct comparisons with numerical simulations of galaxy formation in order to tease out any differences that could either indicate limitations of our theoretical formalism or biases in the way that structural parameters are being measured. For the sake of this comparison, we use galaxies from the "Numerical Investigation of a Hundred Astrophysical Objects" (NIHAO) cosmological zoom-in simulations (Wang et al. 2015). The NIHAO simulations were run with a flat ΛCDM cosmology with parameters from the *Planck Satellite Investigation*: $H_0 = 100h\,km\,s^{-1}\,Mpc^{-1}$ with $h = 0.671$, $\Omega_m = 0.3175$, $\Omega_\Lambda = 0.6824$, $\Omega_b = 0.049$, $\sigma_8 = 0.8344$ and $n = 0.9624$ (Planck Collaboration et al. 2014). The hydrodynamics used an updated N-body SPH solver GASOLINE (Wadsley et al. 2017). All NIHAO galaxies were allowed to form stars following the Kennicutt-Schmidt law (Kennicutt 1998) with suitable density and temperature thresholds, $T < 15000\,K$ and

$n_{th} > 10.3\,cm^{-3}$. Energy is re-injected back into the interstellar medium (ISM) from stars through blast wave supernova feedback. Massive stars also ionize the ISM before their supernova explosion referred to as "early stellar feedback" (Stinson et al. 2006; Wang et al. 2015). The "early stellar feedback" (ESF) mode allows 13% of the total stellar flux to be injected into the ISM. This differs from the original prescription of Stinson et al. (2013) to account for increased mixing and match the abundance matching presented in Behroozi et al. (2013). For the supernova feedback, massive stars with $8\,M_\odot < M_* < 40\,M_\odot$ inject energy and metals into the the ISM. The energy is injected into high density gas and is radiated away due to efficient cooling. For gas particles inside the blast radius, cooling is delayed by $30\,Myr$ (Stinson et al. 2013).

Supermassive black holes (SMBH) and their associated feedback are also included in the latest version of the NIHAO simulation (Blank et al. 2019). All NIHAO galaxies with halo mass $M_{200} > 5 \times 10^{10} M_\odot$ were seeded with a SMBH with mass $10^5 M_\odot$. SMBH accretion in NIHAO galaxies follows the Bondi-Hoyle-Lyttleton parametrization where the accretion is limited by the Eddington rate (Bondi 1952). The feedback from SMBH is a result of the accretion where 15 per cent of the generated luminosity is deposited into the nearby gas thermal energy. Simulated NIHAO galaxies have been shown to match various observed galaxy properties and scaling relations (Macciò et al. 2016; Obreja et al. 2016; Buck et al. 2017; Dutton et al. 2017). However, our detailed analysis below will shed some contrasting light on these assertions. Some genuine challenges, such as matching the galaxy population diversity, do indeed exist (Frosst et al. 2022).

For the present analysis, we use all NIHAO galaxies with AGN feedback, which are centrals, and that have $\log M_* > 8.5\,M_\odot$. The latter stellar mass restriction is made to

match the MaNGA stellar mass distribution. Out of the 91 galaxies from the NIHAO project, 45 NIHAO objects satisfy the stellar mass criteria. All NIHAO-AGN galaxies were simulated with a dark matter particle mass $1.38 \times 10^7\,\mathrm{M}_\odot$ with a softening of 1.86 kpc and gas softening of 782 pc. To further increase the size of our simulated sample, we use massive galaxies from the NIHAO-LG simulations performed with the same hydrodynamics (no AGN feedback) but constrained to reproduce the Local Group environment (Arora et al. 2022). For the NIHAO-LG simulations, we also utilize all galaxies with $\log M_* > 8.5\,\mathrm{M}_\odot$. NIHAO-LG galaxies were run with a dark matter particle mass of $1.62 \times 10^6\,\mathrm{M}_\odot$ with a softening length of 860.3 pc and a gas softening length of 487 pc. Figs. 4.8 and 4.9 show the individual stellar mass surface density profile and rotation curves for NIHAO-AGN and NIHAO-LG galaxies. Both NIHAO simulations span a large range of stellar mass surface densities and velocities, similar to the MaNGA observations.

4.6 Galaxy Scaling Relations

With our observed and simulated galaxy samples in place, we can now construct multiple galaxy scaling relations to establish detailed comparisons. The latter can capture the multi-faceted nature of galaxy formation and avenues of progress for hydrodynamical simulations. To uniformly compare simulated and observed galaxies, we measure all galaxian structural properties at a physically-motivated radius defined by a stellar mass surface density (rather than isophotal levels, which are ill-defined for numerical simulations). Through the MaNGA photometry, we find that $\mathrm{R}_{23.5,z}$ corresponds to a median $\Sigma_* \sim 13\,\mathrm{M}_\odot\,\mathrm{pc}^{-2}$ with 16-84 per cent quartile range of 9.5-$16.7\,\mathrm{M}_\odot\,\mathrm{pc}^{-2}$. Therefore, for our comparison with simulations, all galaxian structural

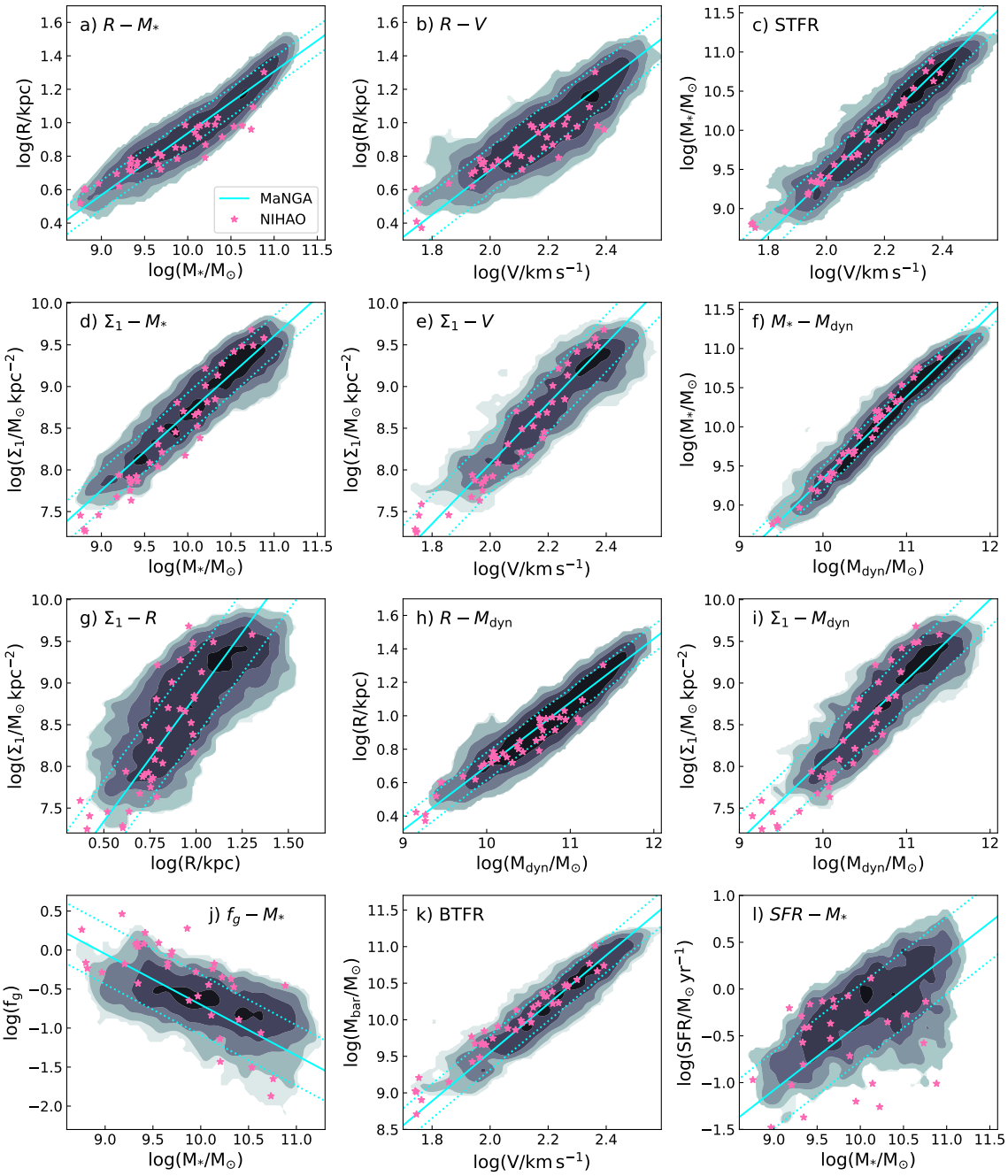

Figure 4.10: Comparison of 12 scaling relations between MaNGA and simulated NIHAO galaxies. The density contours match the underlying MaNGA observations; the cyan solid and dotted lines present the ODR best fit and scatter respectively. The pink stars represent the simulated NIHAO galaxies. All properties for both observed and simulated galaxies are calculated at a radius which corresponds to a stellar surface density of $10\,M_\odot\,pc^{-2}$ (with the exception of the gas mass (Panel j) and SFR (Panel l) which are obtained using Pipe3D). The inset label identifies the scaling relation.

properties are measured at a radius corresponding to $\Sigma_* = 10\,\mathrm{M}_\odot\,\mathrm{pc}^{-2}$.

Fig. 4.10 presents a qualitative comparison of various structural scaling relations between MaNGA and NIHAO. The corresponding fitting parameters are reported in Table 4.2 below. The top row of Fig. 4.10 shows the structural VRM_* scaling relations; size-stellar mass, size-velocity, and STFR. Overall, the simulated NIHAO galaxies follow similar relations as the observed galaxies, as the pink stars scatter more or less evenly about the best fit cyan line, but some differences exist. Most conspicuously, it is seen that simulated disk galaxies, with large sizes, high stellar masses and circular velocities, are underrepresented. This is primarily due to NIHAO's selection function; such massive systems were excluded from the simulations, and so this is expected. For the parameter space where NIHAO galaxies exist, both $R - M_*$ and $R - V$ relations show simulations are consistent with the size distribution of MaNGA galaxies. This is further evident in STFR, BTFR, $M_* - M_{\mathrm{dyn}}$, and $R - M_{\mathrm{dyn}}$ relations as well; while all NIHAO galaxies scatter within observed 1σ region, the massive end of the observed relations are free of simulated objects.

The comparison of scaling relations involving Σ_1 also shows that NIHAO galaxies with high stellar mass ($M_* \gtrsim 10^{10}$) have higher central stellar densities than observed. All massive NIHAO galaxies consistently lie at or above the upper 1σ observed line. These high central stellar densities for massive spiral galaxies are indicative of the weaker baryonic feedback which fails to remove material to prevent over-cooling (see also McCarthy et al. 2012). At the low mass end, simulated NIHAO galaxies have slightly lower Σ_1 than the observed MaNGA sample (see Panels d, e, g, and i of Fig. 4.10). For low mass galaxies, the strong stellar feedback removes baryons perhaps too efficiently from the central parts to depress Σ_1 relative to observations. The strong

stellar feedback in NIHAO also leads to an overall expansion of the halo (Dutton et al. 2016) causing slightly larger sizes compared to MaNGA systems for low mass systems.

Finally, the bottom panel of Fig. 4.10 shows comparison of scaling relations for gas masses (Panel j) and star formation rates (SFRs; Panel l). Gas masses and SFRs were taken from the Pipe3D outputs for the MaNGA IFU data (Sánchez et al. 2016). The observed gas masses are estimated from the dust attenuation while taking the oxygen abundance into account, while SFRs are derived from Pipe3D's simple stellar population (SSP) template fitting for the last 100 Myr. For simulated NIHAO galaxies, gas mass estimates correspond to the total mass of gas particles within a radius where the stellar surface density is $10\,\mathrm{M}_{\odot}\,\mathrm{pc}^{-2}$. SFR estimates are an average SFR within the last 100 Myr. We note that the gas mass estimates between simulations and observations are not uniformly assessed, since Pipe3D uses MaNGA data that are limited to the extent of the IFU ($1.5/2.5\,\mathrm{R}_{e}$). Furthermore, the Pipe3D outputs do not provide errors for the gas mass and SFR estimates, and therefore intrinsic scatter for scaling relations involving these properties cannot be robustly calculated.

Panel j) in Fig. 4.10 shows the fraction of gas ($f_g \equiv M_g/M_*$) as a function of stellar mass for the MaNGA and NIHAO galaxies. As expected, low stellar mass galaxies have a larger fraction of gas relative to high stellar mass galaxies (Catinella et al. 2010; Cortese et al. 2011; Huang et al. 2012). In general, and especially for the lower mass systems, the NIHAO simulated galaxies retain more gas than observed MaNGA distributions; the opposite is true at higher masses. As stated above, the low and intermediate stellar mass NIHAO galaxies show signatures of over-cooling (as shown before in Arora et al. 2022). However, the excess gas could also be a result of the mis-match between the observed and simulated gas measurements. A few

massive NIHAO galaxies have reduced gas content, however consistent with MaNGA observations.

Panel k) of Fig. 4.10 shows the baryonic Tully-Fisher relation (BTFR) for MaNGA and NIHAO galaxies. Unlike the STFR, which showed a great simulation-observation match (Panel c), the simulated galaxies rotate too slow for a given baryonic mass. This is a systematic trend at most masses, but especially at the low mass end, possibly as a result of over-cooling and/or the measurement non-uniformity. The significant discrepancy at the low-mass end of the BTFR has also been observed in other simulation-observation comparisons (Brook et al. 2012; McQuinn et al. 2022).

Finally, panel l) features the SFR$-M_*$ relation for MaNGA and NIHAO. Along with the star formation main sequence (SFMS; Cano-Díaz et al. 2016; Hall et al. 2018), some of the MaNGA LTGs are also found in the "green valley" (Salim 2014). As with many other scaling relations presented here, NIHAO galaxies lie on the distribution of observed MaNGA galaxies. However, for a given mass, some NIHAO galaxies have much lower SFRs than observed. Again, this is likely cause by the strong stellar feedback within NIHAO galaxies, leading to lower SFRs than observations. Massive NIHAO galaxies with high star formation rates are also missing.

Overall, NIHAO galaxies reproduce the broad observed MaNGA spiral galaxy properties. However, some discrepancies remain. In the next section, we quantify our model-observation comparisons by measuring ODR slopes and Bayesian intrinsic scatters for the 12 scaling relations presented in Fig. 4.10.

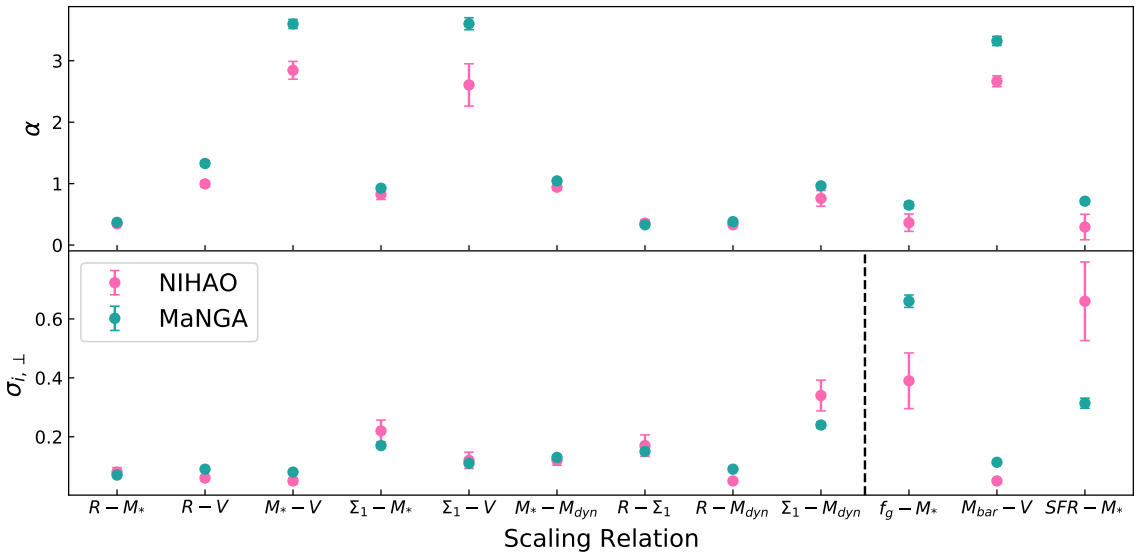

Figure 4.11: Comparison of the slopes and Bayesian intrinsic scatters for the MaNGA and NIHAO scaling relations presented in Fig. 4.10. The top panel shows the slopes, α, of the scaling relations, while the bottom panel gives the orthogonal Bayesian intrinsic scatters, $\sigma_{i,\perp}$. All properties for both observed and simulated galaxies are calculated at a radius which corresponds to a stellar surface density of $10\,\mathrm{M}_\odot\,\mathrm{pc}^{-2}$ (with the exception of the gas mass and SFR which are obtained using Pipe3D). The pink and teal dots represent simulated NIHAO and observed fits, respectively. The x-axis shows each scaling relation. All scaling relations to the right of the dashed vertical line (in the bottom panel) use the observed orthogonal scatter since the intrinsic scatter cannot be calculated. The error bars at each point are calculated using bootstrap resampling over 1000 runs.

4.6.1 Slope Intrinsic Scatter Comparison

We can now compare the ODR slopes and intrinsic scatters of the different scaling relations between MaNGA and NIHAO. The slope values along with bootstrap errors are tabulated in Table 4.2 and shown in the top panel of Fig. 4.11. There is generally decent, however differences exist, agreement between the derived slopes for various scaling relations (compare columns 4 and 7 of Table 4.2). The best matches are found for the $R - M_*$, $R - \Sigma_1$, and $R - M_{\mathrm{dyn}}$ relations. Sizes are a common denominator in

Sample			MaNGA			NIHAO		
Scaling Relation	y	x	α	$\sigma_{\rm obs}$	$\sigma_{i,\perp}$	α	σ_i	$\sigma_{i,\perp}$
(1)	(2)	(3)	(4)	(5)	(6)	(7)	(8)	(9)
Project size-stellar mass	$\log R$	$\log M_*$	0.37±0.01	0.09±0.01	0.07±0.01	0.35±0.01	0.08±0.01	0.08±0.01
Project size-velocity	$\log R$	$\log V$	1.33±0.02	0.14±0.01	0.09±0.01	0.99±0.05	0.08±0.01	0.06±0.01
Stellar Tully-Fisher	$\log M_*$	$\log V$	3.59±0.04	0.24±0.01	0.08±0.01	2.84±0.15	0.15±0.03	0.05±0.01
Σ_1-stellar mass	$\log \Sigma_1$	$\log M_*$	0.93±0.01	0.24±0.01	0.17±0.01	0.83±0.08	0.29±0.05	0.22±0.04
Σ_1-velocity	$\log \Sigma_1$	$\log V$	3.59±0.05	0.34±0.01	0.11±0.01	2.62±0.32	0.34±0.06	0.12±0.04
Stellar mass-halo mass	$\log M_*$	$\log M_{\rm dyn}$	1.05±0.01	0.16±0.01	0.13±0.01	0.94±0.05	0.16±0.02	0.12±0.02
Σ_1-size	$\log \Sigma_1$	$\log R$	0.33±0.01	0.16±0.01	0.15±0.01	0.36±0.06	0.18±0.04	0.17±0.04
Size-halo mass	$\log R$	$\log M_{\rm dyn}$	0.38±0.01	0.10±0.01	0.09±0.01	0.33±0.01	0.05±0.01	0.05±0.01
Σ_1-halo mass	$\log \Sigma_1$	$\log M_{\rm dyn}$	0.97±0.02	0.32±0.01	0.24±0.01	0.75±0.12	0.42±0.06	0.34±0.05
Gas mass-stellar mass*	$\log f_g$	$\log M_*$	-0.65±0.03	0.39±0.01	–	-0.37±0.14	0.42±0.11	0.39±0.13
Baryonic Tully Fisher*	$\log M_{\rm bar}$	$\log V$	3.32±0.04	0.24±0.01	–	2.65±0.08	0.13±0.02	0.05±0.01
Star formation main sequence*	$\log SFR$	$\log M_*$	0.72±0.02	0.41±0.02	–	0.26±0.22	0.68±0.14	0.66±0.14

Table 4.2: ODR linear fits for various scaling relations using MaNGA and NIHAO galaxies evaluated at the radius corresponding to a stellar surface density of $10\,{\rm M}_\odot\,{\rm pc}^{-2}$. Column (1) shows the scaling relation, and columns (2-3) give the variables for the corresponding relation. Columns (4-6) show the slope (α), observed scatter ($\sigma_{\rm obs}$), and orthogonal Bayesian intrinsic scatter ($\sigma_{i,\perp} = \sigma_i/\sqrt{1+\alpha^2}$) of each scaling relation for the observed MaNGA sample. Likewise, columns (7-9) give the slope, scatter (σ_i) and orthogonal scatter ($\sigma_{i,\perp}$) for the NIHAO galaxies. The errors in each fit parameters are calculated using 1000 bootstrap runs. The " – " indicate the scaling relations for which Bayesian intrinsic scatter could not be calculated.

these relations. However, significant disagreements between observations and simulations are found for relations involving velocity estimates (specifically $R-V$, STFR, $\Sigma_1 - V$, and BTFR), as well for the gas-stellar mass relation and SF main sequence.

For $R-V$, STFR, and BTFR, the NIHAO results are closer to theoretical predictions (Courteau et al. 2007), but they diverge from the observed slopes. The disagreements for scaling relations involving velocity metrics are also reflected in the simulation's inability to reproduce the diversity of observed RCs (Oman et al. 2015; Frosst et al. 2022). NIHAO galaxies undergo additional halo expansion due to over-efficient stellar feedback which results in lower simulated central densities and shallower RCs (Dutton et al. 2017; Frosst et al. 2022).

The gas-stellar mass relation and SF main sequence are also fully at odds. This

divergence between MaNGA and NIHAO is largely due to the difference in measurements of the parameters. With gas mass and SFR being retrieved from Pipe3D (Sánchez et al. 2018), these properties are measured at $1.5R_{\rm e}$ while all other properties are measured a radius corresponding to $10\,{\rm M}_{\odot}\,{\rm pc}^{-2}$. In general, NIHAO galaxies have been shown to qualitatively reproduce the slopes for the BTFR (Dutton et al. 2017; McQuinn et al. 2022) and SFMS (Blank et al. 2021) at $z = 0$.

Along with the slope, which defines the connection between two astrophysical parameters, the scatter of scaling relations informs us about the cosmic variations within the process of galaxy formation and evolution. Total scatter is composed of observational errors and intrinsic cosmic scatter. With the Bayesian prescription of Stone et al. (2021a), we are able to remove the covariant observational errors and infer the intrinsic scatter for scaling relations. The bottom panel of Fig. 4.11 shows the observational orthogonal intrinsic scatter ($\sigma_{i,\perp} = \sigma_i/\sqrt{1+\alpha^2}$) for the MaNGA sample. These observed orthogonal intrinsic scatters can be uniformly compared with matching NIHAO scaling relation scatters.

Analysing the observed intrinsic and simulated scatters (columns 6 and 9 of Table 4.2, the $R - M_*$, $\Sigma_1 - V$, $M_* - M_{\rm dyn}$, and $R - \Sigma_1$ relations give the best matches; while the largest discrepancies are found for the $\Sigma_1 - M_*$ and $\Sigma_1 - M_{\rm dyn}$ relations. Note that for scaling relations involving gas mass and SFRs, we are unable to calculate the observed intrinsic scatters as the errors on gas mass and SFRs are not available. Those values are indicated with "–" in Table 4.2. The source of the disagreements between NIHAO and MaNGA scatters is complex. We are comparing ∼2300 MaNGA galaxies versus only 60 NIHAO galaxies for the NIHAO scaling relations. This could be viewed as a source of scatter discrepancy but numerous relations listed above have

very similar intrinsic scatters. Thus Poisson statistics should only affect the uncertainty on the fit parameter and not the fit parameter themselves. The worst intrinsic scatter discrepancies also involve two relations with Σ_1 ($\Sigma_1 - M_*$ and $\Sigma_1 - M_{\rm dyn}$). Qualitatively, massive NIHAO galaxies are too concentrated in the central parts. This once again highlights simulations inability to reproduce the range of observed central stellar densities (McCarthy et al. 2012).

4.7 Spatially-Resolved Scatters

We now take advantage of our spatially-resolved data to address the novel notion of spatially-resolved scatter variations in the fundamental VRM$_*$ galaxy scaling relations. As mentioned above, the scatter of scaling relations, along with the observational errors, encapsulate fluctuations in the different processes that produce a distribution of galaxy properties. Of particular interest to us is the variation of scatter as a function of spatial position within galaxies as it holds the ability of the universe to create a uniform (or non-uniform) set of mass (baryon and dark matter) distributions. The variation of scatter as a function of spatial position within galaxies is a powerful tool to connect astrophysics at the different scale of galaxy formation. To understand the variation of the scatter for a scaling relation, we study the variation of the "normalized scatter" ($\sigma_\perp/\sigma_\parallel$) as a function of a physically-motivated size metric (measured here using the stellar mass surface densities). If a scaling relation is constructed using galaxy properties X and Y with a slope, α, and observed scatter, $\sigma_{\rm obs}$, then the orthogonal scatter, $\sigma_\perp = \sigma_{\rm obs}/\sqrt{1+m^2}$, informs us about the scatter normal to that scaling relation. The choice of orthogonal scatter enables a uniform comparison of spatially-resolved scatters while taking into account the variations in the slope

as well. $\sigma_{\parallel}$ represents the scatter parallel to a scaling relation; in other words, it corresponds to the dynamical range of a scaling relation in a two-dimensional space. Mathematically, the parallel scatter is the standard deviation calculated as:

$$\sigma_{\parallel} = std\left[\frac{-X}{\sqrt{\alpha^2+1}} + \frac{-\alpha Y}{\sqrt{\alpha^2+1}}\right]. \tag{4.9}$$

The ratio, $\sigma_{\perp}/\sigma_{\parallel}$, is therefore, able to provide information about the relative galaxy diversity for a given scaling relation at different radii.

In this section, we wish to study the variations of the curve formed by the scatter (normalized and orthogonal) as a function of the radial metric. Ideally, one would calculate Bayesian intrinsic scatters to analyse the amplitude of such a curve. For the computation of Bayesian intrinsic scatters, the variation of each parameter and its associated error with galactocentric radius must be known (Stone and Courteau 2019; Stone et al. 2021a). Major sources of error on most structural parameters, and their corresponding scaling relations, include mass-to-light ratios, distance, and intrinsic disk thickness. Some of these vary with radius (e.g., M*/L, disk thickness), others do not (distance). However, in all cases, we assume the error profile to be constant with galactocentric radius. As a result, the presentation of intrinsic scatter would only alter the amplitude of the function and not the shape (which is of interest to here).

Fig. 4.12 shows variations of the scatter metric as a function of stellar mass surface density for the VRM_* scaling relations for MaNGA and NIHAO galaxies. The green vertical line represents the normalized and orthogonal scatter calculated for a stellar surface density range of $9.5 - 16.7\,\mathrm{M}_{\odot}\,\mathrm{pc}^{-2}$, which itself corresponds to an isophotal level of $23.5\,\mathrm{mag\,arcsec}^{-2}$ in the z-band for MaNGA LTGs. Independent of the scatter metric, the VRM_* scaling relations show a significant variation of $\sim$0.2 dex for

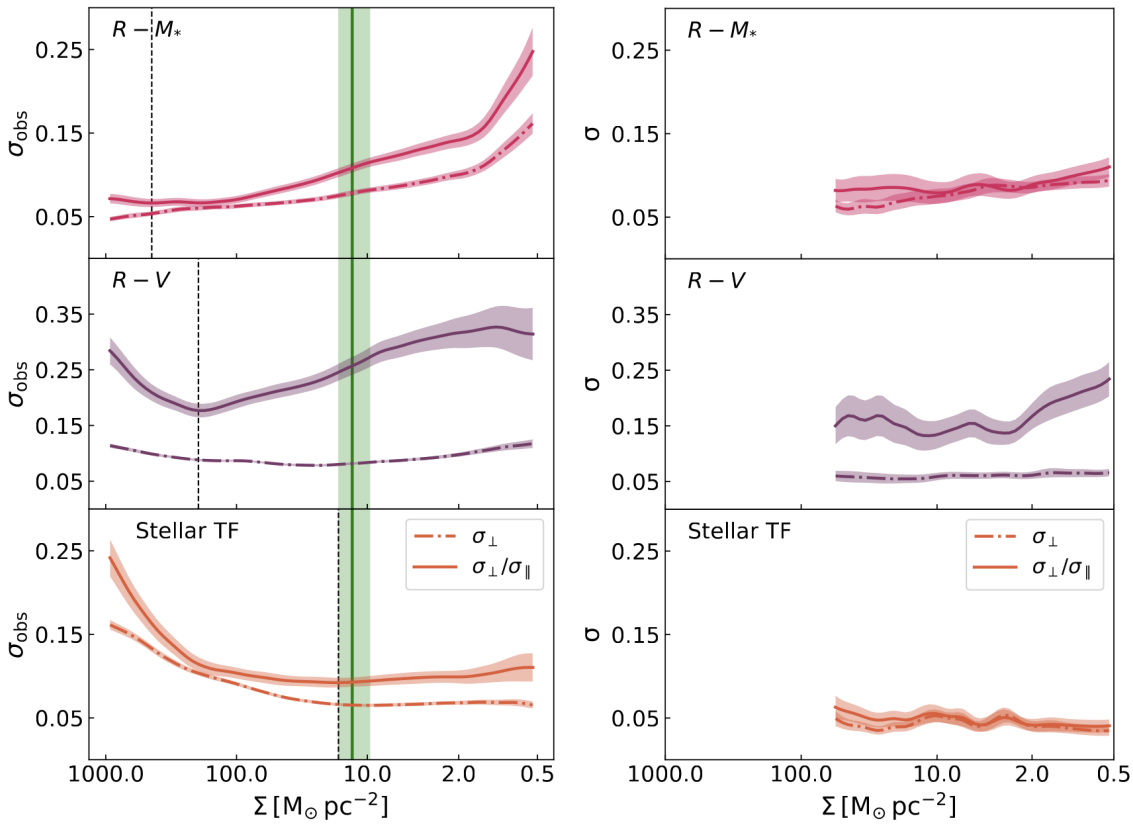

Figure 4.12: Variation of the scatter as a function of stellar surface density for the VRM$_*$ scaling relations. The dashed-dotted and solid lines represent the orthogonal scatter ($\sigma_\perp$)and the normalized scatter ($\sigma_\perp/\sigma_\parallel$), respectively. The shaded regions show the error calculated for the scatter using 1000 bootstrap runs. For clarity, the shaded region represents twice the error. The left-hand windows show the observational MaNGA data while the right-hand windows show the simulated NIHAO data. For the left column (all three windows), the dashed black vertical line shows the isophotal radius where $\sigma_\perp/\sigma_\parallel$ is minimized. The green vertical line and shaded regions correspond to an isophotal level of 23.5 mag arcsec^{-2} in the z-band for the MaNGA sample. The x-axis baseline is the same in all windows to facilitate a direct comparison.

different sub-galactic regions within the MaNGA sample. Thus, regardless of the size metric, the scatter variations of VRM$_*$ scaling relations can inform us about the radial dependence of processes controlling the evolution of galaxy structures. Analysing spatially-resolved scatter for scaling relations (as has been done for the radial acceleration relation (Stone and Courteau 2019) and the SFMS (Wuyts et al. 2013; Cano-Díaz et al. 2016; González Delgado et al. 2016; Wang et al. 2017; Hall et al. 2018; Ellison et al. 2018)) provides a more complete understanding of the physics shaping galaxy properties in the Universe. As with the spatially resolved SFMS, this spatially resolved scatter can allow us to connect the physics on the local scale to the global astrophysics.

The top panel in the left-hand column of Fig. 4.12 shows variations of the scatter metrics for the size-mass relation. The dashed vertical black line represents the density where the lowest normalized scatter is recorded. The minimized normalized scatter shows the region where a particular scaling relation provides the most information; this is a region where the dynamic range ($\sigma_{\parallel}$) is maximized and the orthogonal scatter ($\sigma_{\perp}$) is minimized. For the $R-M_*$ relation, the minimum normalized scatter is found at $\Sigma_* \sim 444\,\mathrm{M}_\odot\,\mathrm{pc}^{-2}$ or $19.6\pm0.3\,\mathrm{mag\,arcsec}^{-2}$ in the z-band. The minimum density and SB level are found in the inner parts of the LTGs where the bulge component dominates the light and mass budget. From this analysis, it is evident that the stellar contents of galaxy bulges are quite uniform while disk components show greater diversity. The orthogonal scatter (dashed-dotted line) for the $R-M_*$ relation decreases with increasing stellar surface densities. The larger stellar surface densities probe inner/bulge dominated regions within LTGs; these regions behave similarly to

the tighter (smaller scatter) size-mass projections for ETGs (Lange et al. 2015; Trujillo et al. 2020; Arora et al. 2021). The smaller scatter is the result of bulge growth via repeated wet/dry mergers (Shen et al. 2003; Huertas-Company et al. 2013).

The correlation between galaxy size and velocity informs us about the growth of angular momentum in galaxies, via the connection between luminous and dark content in galaxies. The lowest normalized scatter in the $R-V$ relation is found at $\Sigma_* \sim 196\,\mathrm{M}_\odot\,\mathrm{pc}^{-2}$. This corresponds to a z-band isophotal level of $20.4\pm0.04\,\mathrm{mag\,arcsec}^{-2}$, which is typically found in the inner parts of LTGs. The larger normalized scatter for higher stellar surface densities results from the wide variations in the rising parts of LTG RCs (Oman et al. 2015, 2019; Frosst et al. 2022).

We contrast the diversity of inner RCs with the scatter of the size-velocity and stellar TFR. The larger scatter of the low stellar surface density ($\Sigma_* < 196\,\mathrm{M}_\odot\,\mathrm{pc}^{-2}$) is the result of a broader distribution of galaxy sizes at a particular stellar surface density. The quartile range of isophotal radius increases as lower stellar surface density are examined. This behaviour is similar to the $R-M_*$ relation where larger normalized scatters are obtained in the disk-dominated regions of LTGs. The larger scatters on both sides of the minimum density are indeed a result of the parameter diversities for LTGs. In the inner parts of galaxies, velocity metrics show significant diversity (Oman et al. 2015, 2019; Frosst et al. 2022), while physically-motivated galaxy sizes (corresponding to stellar mass surface densities) show larger diversities in the galaxies outskirts. Such diversity in physically-motivated galaxy sizes are a result sporadic star formation in the outer regions of galaxies (Rodríguez-Baras et al. 2018).

The combination of $R-M_*$ and $R-V$ relations also yields the STFR which directly

relates the luminous and dark matter content in galaxies. The minimum scatter of the STFR is found at $\Sigma_* \sim 17 M_\odot\,pc^{-2}$, which corresponds to an isophotal level of 23.2 ± 0.7 mag arcsec^{-2} (in the z-band). This result agrees with other findings that the Tully-Fisher relation has its scatter minimized at an isophotal size of 23.5 mag arcsec^{-2} (in the i-band) (Giovanelli et al. 1994; Courteau 1996; Hall et al. 2012). Slight differences between specific isophotal levels emerge from our measure of scatter based on normalized scatter. The larger scatters for ($\Sigma_* > 17\,M_\odot\,pc^{-2}$) are due to the inner shapes of the stellar mass and velocity profiles. The larger diversity in the shapes of the stellar mass and velocity profiles leads to a large inner normalized and orthogonal scatter. The smaller, near constant, normalized and orthogonal scatter are a result of the flat nature of stellar mass profiles and rotation curves in the outer/disk dominated regions of the MaNGA galaxies.

In summary, the study of spatially-resolved scatters (normalized and orthogonal) has shown that the inner scatters of the combined VRM$_*$ scaling relations are dominated the great diversity of galaxy RCs. Conversely, scaling relations built on parameters measured in the galaxy's outskirts are controlled by the non-uniformity in stellar surface density, likely driven by stochastic star formation and feedback. It is evident from the left-hand panel of Fig. 4.12 that the scatter varies significantly (78%) as a function of radius. Therefore, for a more complete understanding of the physics of galaxy scaling relations, we caution against the use of scatter based on a single radial metric. Given the availability of IFUs (such as MaNGA, CALIFA, and SAMI) and deep imaging (such as DESI, LSST), spatially-resolved scaling relations must be investigated in order to achieve a global understanding of structure evolution on local and global scales.

Before we compare spatially-resolved scatter with NIHAO, we caution the readers about the use of spatially resolved scatter for VRM$_*$ scaling relations. The shape of the curves in Fig. 4.12 depend very much on sample definition and size. We would expect those curves to be different if, for example, only dwarf galaxies were included. With MaNGA's target selection restricted to $\log(M_*/M_\odot) > 9$, our conclusions apply to massive LTGs. While this section provides a proof-of-concept and demonstrates the usefulness of spatially-resolved scatters, we will use in a future study a larger and more morphologically diverse observed sample.

The right-hand column in Fig. 4.12 shows spatially-resolved scatters for the VRM$_*$ scaling relations using the NIHAO galaxies. Given the (small) central densities observed in Fig. 4.8 for NIHAO galaxies, we cannot achieve the large stellar surface densities seen for MaNGA galaxies in Fig. 4.12. We can only study resolved scatters for $\Sigma_* < 50\,\mathrm{M}_\odot\,\mathrm{pc}^{-2}$ using NIHAO galaxies. The x-axis baseline for the left and right panels in Fig. 4.12 were made equal to enable uniform model-observation comparisons. The lower number of zoom-in simulations increases the random error within our fits for the VRM $_*$ relations.

The size-mass relation for NIHAO behaves very similarly to the scatters observed for the MaNGA galaxies. The calculated orthogonal scatter for the $R - M_*$ relation using the NIHAO systems shows a decrease with increasing stellar surface density. The same is broadly true for normalized scatter using NIHAO LTGs which also decreases towards the central galaxian regions. For $\Sigma_* > 5\,\mathrm{M}_\odot\,\mathrm{pc}^{-2}$, the normalized scatter for the $R - M_*$ relation is then mostly consistent with a constant behaviour. In general, NIHAO galaxies produce a roughly similarly diverse size and stellar mass profile distributions as seen for observed MaNGA galaxies. This is also true for the

$R-V$ and STFR. The orthogonal scatter for the $R-V$ relation is somewhat constant as a function of stellar mass surface density. While, both normalized and orthogonal scatter for the STFR show much more fluctuations, they are consistent with an average $\sigma \sim 0.08$.

4.8 Conclusions

This paper has presented a dynamical catalogue of galaxy RCs for MaNGA LTGs, as a complement to the extensive photometric and environmental catalogue of A21. Based on these data and the NIHAO numerical simulations, an extensive comparison between galaxy observations and simulations of galaxies could be established. Some successes and failures of the simulations were noted.

The MaNGA Hα velocity maps were fitted with an inclined rotating disk model assuming a hyperbolic tangent model for the circular velocities as a function galactocentric radius. The fitting procedure allowed us to extract inclination-corrected RCs for MaNGA galaxies which provided us with accurate dynamical properties. The tanh velocities fit the MaNGA Hα velocity cubes very well, with an average error of $\sim$7 km s^{-1}. However, errors as high as $\sim$15-20 km s^{-1} were recorded due to non-circular flows in the galaxy's central parts. While non-circular motions affect our study only weakly, their investigations would greatly benefit the comprehensive and rigorous analysis of galaxy velocity fields.

The combination of RCs with robust photometry for the MaNGA galaxy reveals the full extent of the MaNGA spectral data. With robust photometry based on deep imaging ($\mu_z \sim$26 mag arcsec^{-2}), we establish that the primary+ (secondary) MaNGA samples extend out to 1.4 ± 0.4 (1.9 ± 0.4) R_e. In general, our DESI photometry

collects 0.3 mag more light than the NSA SDSS photometry which explains the lesser extent of the MaNGA velocity fields in units of effective radii. On the other hand, the use of isophotal radii is independent of total light and provides a more accurate extent for the MaNGA IFU. In units of $R_{23.5}$ (z-band), the primary+ (secondary) MaNGA spectroscopic data extend out to 0.8 ± 0.2 (1.0 ± 0.2).

The ten RCs overlapping the MaNGA and PROBES surveys (the former using Hα velocity maps, the latter long-slit Hα RCs) show excellent agreement, with average differences no greater than $\sim$20 km s^{-1}. MaNGA velocity maps and extracted RCs are indeed well suited for analyzing the dynamics of a galaxy's interiors. The RCs for MaNGA allow for the construction of spatially-resolved structural scaling relations. ODR fit parameters for the VRM_* scaling relations (measured at isophotal levels) are provided in Table 4.1 and Fig. 4.7. The VRM_* scaling relations from MaNGA agree well with other similar relations presented in the literature (see Stone et al. 2021a, for more comparisons), including studies using MaNGA galaxies.

For uniform comparisons between simulations and observations, the metric at which structural parameters are measured is no longer isophotal but rather corresponding to a stellar mass surface density threshold. A stellar mass density of $10\,M_\odot\,pc^{-2}$ was chosen for this comparison as it closely relates to the common isophotal $R_{23.5}$. The versatility and richness of the MaNGA data enable comparisons of observations and simulations through multiple scaling relations. Using dynamical information, DESI photometry (A21), gas and SF properties, we construct 12 galaxy scaling relations to compare observed MaNGA and simulated NIHAO galaxies. NIHAO simulations broadly reproduce the observed LTG populations ($\log M_* > 9\,M_\odot$)

seen in the MaNGA data. Qualitatively, most NIHAO galaxies lie within the observed 1σ region (see Fig. 4.10). Good matches are indeed found for the $R - M_*$, $M_* - M_{\rm dyn}$ and $R - M_{\rm dyn}$ relations. The simultaneous comparison using multiple scaling relations is beneficial in constraining various astrophysical phenomena (star formations, dynamics, stellar populations, etc.)

However, as a result of their complex selection function, NIHAO simulations also lack galaxies with high stellar mass, circular velocity, and star formation rates. The largest discrepancies between NIHAO and MaNGA are found for scaling relations involving velocity metrics and Σ_1. Both of these are controlled by the feedback prescription and halo response to feedback (McCarthy et al. 2012; Dutton et al. 2016). For scaling relations involving gas masses, NIHAO galaxies produce a larger gas fraction than observed in low stellar mass galaxies ($\sim$0.3 dex) due to over-cooling. However, part of that discrepancy may be due heterogeneous measurements for gas masses. Any excess gas does not result in high SFR for NIHAO galaxies; rather, the NIHAO SFMS show broad agreement with the observed one (see also Blank et al. 2021).

The spatially-resolved scatter for VRM$_*$ scaling relations for MaNGA and NIHAO systems is also studied. The scatter of scaling relations encodes astrophysical processes that cause cosmic variation in galaxy formation and evolution. We study the variations of the normalized scatter, which provides information about the orthogonal dispersion as well as the dynamical range of a scaling relation, as a function of stellar mass surface densities. In the inner parts, the larger scatter of the $R - V$ and STFR are dominated by the diversity of galaxy RCs (Frosst et al. 2022). Conversely, for the $R - M_*$ relation, the normalized scatter in the inner regions remains low due to

well-mixed bulge populations. The scatter for the VRM_* scaling relations at large galactocentric radii is dominated by the diverse stellar mass surface densities. The effect of the diverse stellar mass surface density is most evident in the $R - M_*$ relation where the scatters, both orthogonal and normalized, continue to increase with decreasing stellar surface density. The larger scatter in stellar mass surface density could result from sporadic star formation at larger galactic radii due to mergers and interactions.

We also compare the spatially-resolved scatters of observed MaNGA and simulated NIHAO galaxies. For the surface densities available in NIHAO, the simulated $R-M_*$ relation is broadly consistent with MaNGA data. Furthermore, both the $R - V$ and STFR relations are broadly consistent with a constant scatter as a function of stellar surface density, albeit for lower surface stellar density. The reproduction of the spatially-resolved scatters by simulations is significant as these scatters connect the global property distribution to the small-scatter astrophysical process. Most conspicuously, NIHAO simulations do not produce the high stellar masses and central densities that are seen in MaNGA data.

While NIHAO is broadly able to reproduce properties of the observed LTG galaxy population, areas of discrepancies remain, such as those pertaining to central stellar densities and the diversity of RCs due to AGN feedback. With the spatially-resolved data presented here, we may now constrain simulations at all possible physically-motivated radii which represent different sub-galactic environments. Not only should simulations be able to reproduce basic galaxy scaling relations (size-mass, SFMS, TFR), they should also match the observed spatially-resolved properties and relations (such as the diversity of inner RC slopes, spatially-resolved SFMS, RAR, metallicity

gradients, etc.) These detailed comparisons bring together the complex connections between local and global astrophysical processes.

4.9 Appendix: The Kinematic Catalogue

This section presents the headers for the kinematic catalogue based on the 2368 MaNGA LTGs used in the study (Table 4.3). In this supplementary material, we provide the extracted fit parameters for our velocity model along with velocity and dynamical masses measured at $R_{23.5,z}$. The MaNGA RCs are also provided as supplementary material and the file format is described in Table 4.4.

Column Name (1)	Description (2)	Unit (3)	Data Type (4)
MaNGA-ID	MaNGA Identification	—	string
RA	Right Ascension of the object (J2000)	°	float
DEC	Declination of the object (J2000)	°	float
Z	NSA or SDSS redshift	—	float
XC	X coordinate for the centre of the observed galaxy	arcsec	float
dXC	Error in XC	arcsec	float
YC	Y coordinate for the centre of the observed galaxy	arcsec	float
dYC	Error in YC	arcsec	float
Vsys	Systemic (heliocentric) velocity of the object	$\mathrm{km\,s^{-1}}$	float
dVsys	Error in V_sys	$\mathrm{km\,s^{-1}}$	float
PA	Fit position angle	°	float
dPA	Error in PA	°	float
I	Fit inclination	°	float
dI	Error in inclination	°	float
Vm	Fit V_{max} for the tanh function (Eq. 4.4)	$\mathrm{km\,s^{-1}}$	float
dVm	Error in Vm	$\mathrm{km\,s^{-1}}$	float
Rt	Fit R_t for the tanh function (Eq. 4.4)	arcsec	float
dRt	Error in rt	arcsec	float
V235	Velocity measured at $R_{23.5,z}$ using the tanh function	$\mathrm{km\,s^{-1}}$	float
dV235	Error in V235	$\mathrm{km\,s^{-1}}$	float
Md235	Dynamical mass measured at $R_{23.5,z}$ (Eq. 4.7)	$M_\odot$	float
dMd235	Error in Md_235 (Eq. 4.8)	$M_\odot$	float

Table 4.3: Kinematic quantities for the MaNGA galaxies. Column (1) presents the column name described in column (2). The units and data for each property are presented in columns (3) and (4). The table is made available in the supplementary material in a comma separated values file format.

Column Name (1)	Description (2)	Unit (3)
Rad_arc	Projected galactocentric radius	arcsec
Rad_phy	Physical galactocentric radius	kpc
Vel	Circular velocity	$\mathrm{km\,s^{-1}}$
dVel	Error in circular velocity	$\mathrm{km\,s^{-1}}$

Table 4.4: A description of the file format of the rotation curves provided as supplementary material. Column (1) provides the column name described column (2), and with units given in column (3). All rotation curves are presented in a comma separated file format.

Chapter 5

Dwarf Galaxies in the Local Group

5.1 Preamble

This chapter contains a version of the paper on **"NIHAO-LG: The uniqueness of Local Group dwarf galaxies"** by Nikhil Arora, Andrea V. Macciò, Stéphane Courteau, Tobias Buck, Noam I. Libeskind, Jenny G. Sorce, Chris B. Brook, Yehuda Hoffman, Gustavo Yepes, Edoardo Carlesi, and Connor Stone (Arora et al. 2022). In this study, environmentally-constrained Local Group simulations from the NIHAO project were presented. The simulated Local Group dwarf galaxies were compared with simulated field dwarfs to show that the differences between the two populations are amplified for the gas properties of the Local Group dwarf galaxies. This is a result of the interactions of the Local Group dwarfs with each other leading to the sharing of high metallicity gas. The impact of the Milky Way and Andromeda galaxies on the evolution of the Local Group Dwarfs was found to be minimal.

5.2 Abstract

Recent observational and theoretical studies of the Local Group (LG) dwarf galaxies have highlighted their unique star-formation history, stellar metallicity, gas content, and kinematics. We investigate the commonality of these features by comparing constrained LG and field central dwarf halo simulations in the Numerical Investigation of a Hundred Astrophysical Objects (NIHAO) project. Our simulations, performed with NIHAO-like hydrodynamics which track the evolution of the Milky Way (MW) and M31 along with ∼100 dwarfs in the LG, reveal the total gas mass and stellar properties (velocity dispersion, evolution history, etc.) of present-day LG dwarfs to be similar to field systems. However, relative to field galaxies, LG dwarfs have more cold gas in their central parts and more metal-rich gas in the halo stemming from interactions with other dwarfs living in a high-density environment like the LG. Interestingly, the direct impact of massive MW/M31 analogues on the metallicity evolution of LG dwarfs is minimal; LG dwarfs accrete high-metallicity gas mostly from other dwarfs at late times. We have also tested for the impact of metal diffusion on the chemical evolution of LG dwarfs, and found that it does not affect the stellar or gaseous content of LG dwarfs. Our simulations suggest that the stellar components of LG dwarfs offer a unique and unbiased local laboratory for galaxy-formation tests and comparisons, especially against the overall dwarf population in the Universe.

5.3 Introduction

In the Λ cold dark matter (ΛCDM) paradigm, galaxy growth occurs through hierarchical assembly and secular evolution (White and Rees 1978; White and Frenk 1991; Kormendy and Sanders 1992). As a result, galaxies are dynamic entities that form

and assemble into groups and clusters. This holds for our Milky Way (MW) and the Andromeda galaxy (M31) which, along with numerous dwarf galaxies, form the Local Group (LG) of galaxies (Mateo 1998; McConnachie 2012; Kirby et al. 2013).

LG dwarf galaxies offer a superb laboratory to study the physics of galaxy formation and evolution. Indeed, numerous observational, theoretical, and numerical studies of the very nearby dwarf galaxies have been conducted (Mateo 1998; McConnachie 2012; Kirby et al. 2013; Benítez-Llambay et al. 2015, 2016; Libeskind et al. 2020, to name a few). A fundamental question arises regarding LG dwarfs as representative of the general dwarf galaxy population in the Universe. Alternatively one can ask whether the study of the LG dwarfs teaches us about galaxy formation at large, in the field. One might think that tidal interactions between dwarf galaxies and MW/M31 could lead to formation of streams and eventual phase mixing into the stellar haloes of MW/M31. These interactions can also transfer pristine gas from MW/M31 to surrounding dwarfs which may induce star formation and evolution of metals in dwarf galaxies (Buck 2020). Such interactions could also lead to the stripping of gas leading to a "freeze out" of the stellar population in LG dwarfs. Could such environmental interactions distinguish the LG dwarfs from the general population of dwarfs in the Universe? What are the cosmological ramifications of such differences? This Copernican question has directly motivated the present paper.

The stellar assembly of dwarf galaxies in the LG is sensitive to internal (feedback and winds) and environmental (ram pressure and tidal stripping) processes, as well as the reionization of gas due to the ultraviolet (UV) background at early times. As a result, the star-formation histories (SFHs) of many LG dwarfs have been extensively studied to better understand the influence of these internal and external processes.

Some of these dwarfs form a large fraction of their stars at early times and are quenched after reionization (Sand et al. 2010; Brown et al. 2012; Okamoto et al. 2012), while others show moderate and continuous star formation to the present day (Weisz et al. 2014; Gallart et al. 2015). Overall, SFHs of dwarf galaxies are the product of reionization and the environment in which they are formed. Gallart et al. (2015) have also shown that dwarfs with no current star formation could form in dense, cluster/group-like environments. Dwarfs that form in low-density environments could thus retain their gas reservoir to fuel continuous star formation and younger stellar populations.

The presence of MW/M31 is likely to influence the gas, and therefore the stellar, content of LG dwarfs. Indeed, the fraction of neutral hydrogen in LG dwarf galaxies increases with distance from the MW (Spekkens et al. 2014; Putman et al. 2021). Dwarfs within the virial radius of the MW are especially deficient in cold gas while, in comparison, systems outside the virial radius have 100 times higher neutral gas fractions (Einasto et al. 1974; Grcevich and Putman 2009; McConnachie 2012; Spekkens et al. 2014). Gas-poor systems result largely from interactions with the hot halo of the MW typically due to ram pressure stripping, viscous stripping, and starvation (Gunn and Gott 1972; Hester 2006; Kawata and Mulchaey 2008; Fillingham et al. 2016).

While the evolution of dwarf galaxies seems broadly understood, a key question remains: Are the observed features of LG dwarfs unique or do field dwarfs show similar evolutionary tracks? A robust answer to this question must rest on two pillars. One is our ability to simulate the formation of the LG and its nearby neighbourhood in way that reproduces the main features of the LG. Namely, simulations that are constrained

to emulate the formation and evolution of the LG dwarfs within the 'context' of the actual observed LG. The other pillar consists of a detailed census of LG and field dwarfs in the local Universe. Depending on the choice of Stellar Mass − Halo Mass relation (SHMR), especially for the low-mass end, about $0.3 - 0.4$ deg^{-2} of field dwarfs with surface brightness of $\sim$30 mag arcsec^{-2} are expected in the local volume, with distances between 3 and 10 Mpc from us (Danieli et al. 2018). Indeed the LG includes approximately 100 dwarf galaxies with a magnitude range $-17 \geq M_{\rm V} \geq -7$ within a volume of 3 Mpc (McConnachie 2012). Until the advent of deep large sky surveys, such as those provided by the Rubin Observatory with a limiting magnitude of 32 mag arcsec^{-2}, comparisons with a complete census of field dwarfs is beyond reach. While the presence (or lack) of unique aspects of the LG cannot currently be characterized with observed galaxies, high-resolution simulations may provide much valuable insight.

Identifying differences between LG and field dwarf galaxies can help in better isolating the role of environment in shaping the galaxy properties in the local Universe. In the context of other groups and clusters, galaxy properties like mean stellar age (Thomas et al. 2005; Clemens et al. 2006), morphology (Blanton and Moustakas 2009, and references therein), colour (Wilman et al. 2010; Cluver et al. 2020) and star formation rates (SFR; Fossati et al. 2015) have been shown to depend strongly on environment. Similar conclusions have been drawn about the influence of MW/M31 on LG satellite dwarfs (e.g., Gottloeber et al. 2010a; Benítez-Llambay et al. 2015, 2016; Buck et al. 2019; Genina et al. 2019; Libeskind et al. 2020; Di Cintio et al. 2021). However, if similarities exist between LG and field dwarfs, nearby populations of dwarf galaxies (which are more easily accessible) can be used as a proxy for distant

systems.

This paper presents such a comparison between the dwarf populations found in the LG and in the field through high-resolution simulations in order to highlight any similarities and/or differences. To this end, we take advantage of the Numerical Investigation of a Hundred Astrophysical Objects (NIHAO) simulations which trace the evolution of individual dark matter haloes and their baryonic components for the complete history of the Universe (Wang et al. 2015). The NIHAO simulations have already proven to be successful in matching various observations aspects of galaxy formation and evolution (Macciò et al. 2016, 2017; Obreja et al. 2019; Buck et al. 2020; Blank et al. 2021, and references therein). More details about these simulations are provided in Section 5.4.1.

Our field dwarf sample uses NIHAO haloes as presented in Wang et al. (2015). The LG dwarf sample is comprised of two constrained LG simulations with initial conditions provided from the CLUES collaboration (Gottloeber et al. 2010a), presented here for the first time, and performed with the exact same code and galaxy formation model used for the NIHAO project. The constrained LG simulation allowed for the evolution of LG environment containing the MW- and M31-like haloes and their associated dwarfs. Our comparisons rely mostly on common galaxy scaling relations such as the stellar mass−metallicity relation (hereafter MZR; Gallazzi et al. 2005; McConnachie 2012; Kirby et al. 2013), stellar mass–gas mass relation (Peeples et al. 2014), and the SHMR (Behroozi et al. 2013; Moster et al. 2014).

Because the formation and evolution of dwarfs in high-resolution simulations is sensitive to the implemented subgrid prescriptions such as feedback, chemical enrichment, and metal diffusion, we have also compared the subgrid physics formalism that

may drive the pre-enrichment of LG dwarfs; namely metal diffusion. The impact of metal diffusion on the stellar assembly, SFRs, and chemical evolution of dwarf galaxies remains unclear. For instance, while Su et al. (2017) used the FIRE (Feedback In Realistic Environment; Hopkins et al. 2018) simulations to show that the subgrid metal diffusion does not impact SFRs on the galactic scales, Pilkington et al. (2012) and Williamson et al. (2016) found opposite results for the abundance of low-metallicity stars in dwarf galaxies (see also Kawata et al. 2014 and Escala et al. 2018). Given the current muddled picture about the evolution and abundance of metals in LG and field dwarfs, we present results from two constrained LG simulations; with and without metal diffusion.

This chapter is organised as follows: Section 5.4 outlines the NIHAO galaxy formation simulation which provides the field galaxy sample for this study, and presents the two constrained LG simulations. Section 5.5 highlights the similarities and differences between the constrained LG dwarf galaxies and the NIHAO dwarf galaxies at z $\sim$ 0. A multifaceted analysis of the dwarf galaxies using various galaxy scaling relations is also presented. The evolution of galaxy properties for the NIHAO and NIHAO-LG simulations to better understand the differences seen at $z = 0$ is addressed in Section 5.6, and conclusions are presented in Section 5.7 as we ponder the uniqueness (or lack thereof) of LG dwarfs and its implications.

5.4 Simulations

5.4.1 NIHAO galaxy formation simulations

Our field central galaxy sample relies on the NIHAO cosmological zoom-in simulations presented in Wang et al. (2015). The simulations were run with a flat ΛCDM

cosmology with parameters from the *Planck satellite*: $H_0 = 100h\,\mathrm{km\,s^{-1}\,Mpc^{-1}}$ with $h = 0.671$, $\Omega_\mathrm{m} = 0.3175$, $\Omega_\Lambda = 0.6824$, $\Omega_\mathrm{b} = 0.049$, $\sigma_8 = 0.8344$ and $n = 0.9624$ (Planck Collaboration et al. 2014). The hydrodynamics were performed with the updated N-body SPH solver GASOLINE2 (Wadsley et al. 2017) which includes the treatment of P/ρ^2 proposed by Ritchie and Thomas (2001). Gas cooling was performed through hydrogen, helium and various metal-lines in a uniform UV ionizing background. Photoionization and heating of the gas also occur via UV background and Compton cooling with temperatures from 10 to 10^9 K (Shen et al. 2010).

All NIHAO galaxies were allowed to form stars provided that the gas follows the Kennicutt-Schmidt law (Kennicutt 1998) with suitable density and temperature thresholds, $\mathrm{T} < 15000\,\mathrm{K}$ and $\mathrm{n_{th}} > 10.3\,\mathrm{cm^{-3}}$. Energy is re-injected back into the interstellar medium (ISM) from stars through stellar and blast wave supernova feedback. Massive stars also ionize the ISM prior to their supernova explosion; this is referred to as "early stellar feedback" (ESF Stinson et al. 2006; Wang et al. 2015) where 13 per cent of the total stellar flux of $2 \times 10^{50}\mathrm{erg\,M_\odot^{-1}}$ is injected into the ISM. This differs from the original prescription presented in Stinson et al. (2013) in order to account for the increased mixing of gas and aligns with the abundance matching results on MW scale (Behroozi et al. 2013). For supernova feedback, massive stars with $8\,\mathrm{M_\odot} < M_* < 40\,\mathrm{M_\odot}$ inject energy of 10^{51}erg and metals into the the ISM. Because the energy is injected into high density gas, it radiates away via efficient cooling on short time-scales. Therefore, for gas particles inside the blast radius, cooling is delayed by 30 Myr (Stinson et al. 2013) to prevent immediate radiation from high density gas particles (Stinson et al. 2006). The spiral and dwarf galaxies generated

Simulation	Box Size [Mpc h^{-1}]	m_{dark} [$M_\odot$]	ϵ_{dark} [pc]	ϵ_{gas} [pc]	N_{haloes}	N_{dwarfs}	Metal Diffusion?	Environment
NIHAO	60.1	1.74×10^6	931.5	398.0	91	37	Yes	Field
NIHAO-LG	100.0	1.62×10^6	860.3	487.7	104	64	Yes	Local Group
NIHAO-LG (nmd)	100.0	1.62×10^6	860.3	487.7	115	73	No	Local Group

Table 5.1: Various properties of our three NIHAO simulations. Columns give the box size, mass resolution of the DM particles, softening length of the dark and gas particles, number of haloes at redshift $z = 0$, usage of metal diffusion, and the simulated environment.

by NIHAO simulations have been shown to match numerous observed galaxy properties and scaling relations (Macciò et al. 2016; Obreja et al. 2016; Buck et al. 2017; Dutton et al. 2017). The NIHAO galaxy simulations result in numerically converged galaxies as shown by the ultra high-definition NIHAO runs (Buck et al. 2020).

5.4.2 NIHAO Local Group simulations

Our sample of dwarf galaxies in a LG environment was created with initial conditions from the Constrained Local UniversE Simulations (CLUES) project[1] (Gottloeber et al. 2010a; Carlesi et al. 2016; Sorce et al. 2016; Libeskind et al. 2020). Constrained simulations allowed us to track the position and environment of the MW, M31-like galaxies and their associated dwarfs. The haloes were identified and tracked in a cosmological box of 100 Mpc h^{-1} on a side, and constrained by observational data of the nearby Universe. This resulted in a high-resolution simulated spherical region of approximately 5 Mpc in radius. The initial conditions for the simulation box relied on the Wiener filter (WF, Hoffman and Ribak 1991; Hoffman 2009), a Bayesian linear algorithm, and constrained realizations of the Gaussian matter density field from observations of the local Universe and an assumed prior model (Zaroubi et al. 1995). The WF allowed for the construction of the cosmic displacement field needed

[1] http://www.clues-project.org.

to robustly model particle positions as a function of time for the constrained objects. The cosmic displacement field was created via a peculiar velocity field of the local Universe using the CosmicFlows-2 (CF2) catalogue of galaxy redshift and direct distances (Tully et al. 2013). Malmquist biases and lognormal errors in the CF2 data set are corrected using the bias minimization technique described in Sorce (2015). To correct for such displacements due to cosmic evolution and to calculate the positions of the galaxies progenitors, the reverse Zel'dovich approximation was applied (Doumler et al. 2013; Sorce et al. 2014). Finally, renormalization of the velocity field was performed to get particles with initial velocity values of the particles in the simulation box. A more detailed description of the CLUES initial conditions is found in Carlesi et al. (2016); Sorce et al. (2016); Sorce (2018) and Libeskind et al. (2020).

The initial conditions from CLUES simulations with the cosmology of NIHAO and hydrodynamics from ESF-GASOLINE2 lead to the constrained NIHAO-LG simulations. Along with the effect of environment (field vs. LG), we also monitored the variations in galaxy properties due to changes in subgrid physics implementations; especially the chemical evolution in dwarfs. To that end, we created two sets of constrained LG simulations: (i) NIHAO-LG: full NIHAO cosmology and hydrodynamics included along with metal diffusion from Wadsley et al. (2008), and (ii) NIHAO-LG(nmd): full NIHAO cosmology and hydrodynamics with no metal diffusion. We used the Chabrier initial mass function (Chabrier 2003) for stellar sampling in the simulation. As we sought differences between field central dwarfs and LG dwarfs, the variation of chemical evolution was an obvious implementation to modulate. Table 5.1 summarizes the basic properties of the three NIHAO simulations used in this study.

Dwarfs in the LG simulations

From the constrained LG simulations, we selected all haloes with 100 per cent high-resolution DM particles (i.e., no pollution from low-resolution particles), having at least 1000 particles (baryon and DM) and at least 100 stellar particles. Our dwarf galaxies are defined as central systems at $z = 0$ with $7.0 \leq \log(M_*/M_\odot) \leq 9.5$ from all pure haloes in the constrained LG simulations. Unless stated otherwise, all quantities (stellar mass, cold gas mass, etc.) were measured within $0.2R_{200}$; where R_{200} is the radius within the average density is 200 times the critical matter density of the Universe; $\rho_{\rm crit,0} = 3H_0^2/8\pi G$. We expect numerical resolution and convergence to only play a small role in the results presented here. The hydrodynamics, performed with GASOLINE2, as is the case for NIHAO and the constrained LG simulations, were stable with respect to resolution (Macciò et al. 2017, 2019). Galaxy properties in the NIHAO simulations have also been shown to converge despite the varying spatial and mass resolution over a large range of halo masses. The highest resolution NIHAO dwarf galaxies presented in Macciò et al. (2017) yielded galaxy properties in broad agreement with the general NIHAO-simulated galaxy population (Wang et al. 2015).

The distribution of our LG simulations (with and without metal diffusion) is presented in Fig. 5.1 through face-on and edge-on views centred on the respective MW analogue. MW and M31 analogues for both constrained LG simulations are shown as a pink star and a blue square respectively. The size of the dwarf galaxies (shown as circles) scales with their respective stellar masses at $z = 0$. Both LG simulations, NIHAO-LG and NIHAO-LG(nmd), resulted in similar spatial distributions of the central dwarf systems extending out to $\sim$5 Mpc. In each constrained LG simulation, two massive haloes were found with a total mass $M_{200} \sim 10^{12}\,{\rm M}_\odot$, a ratio of

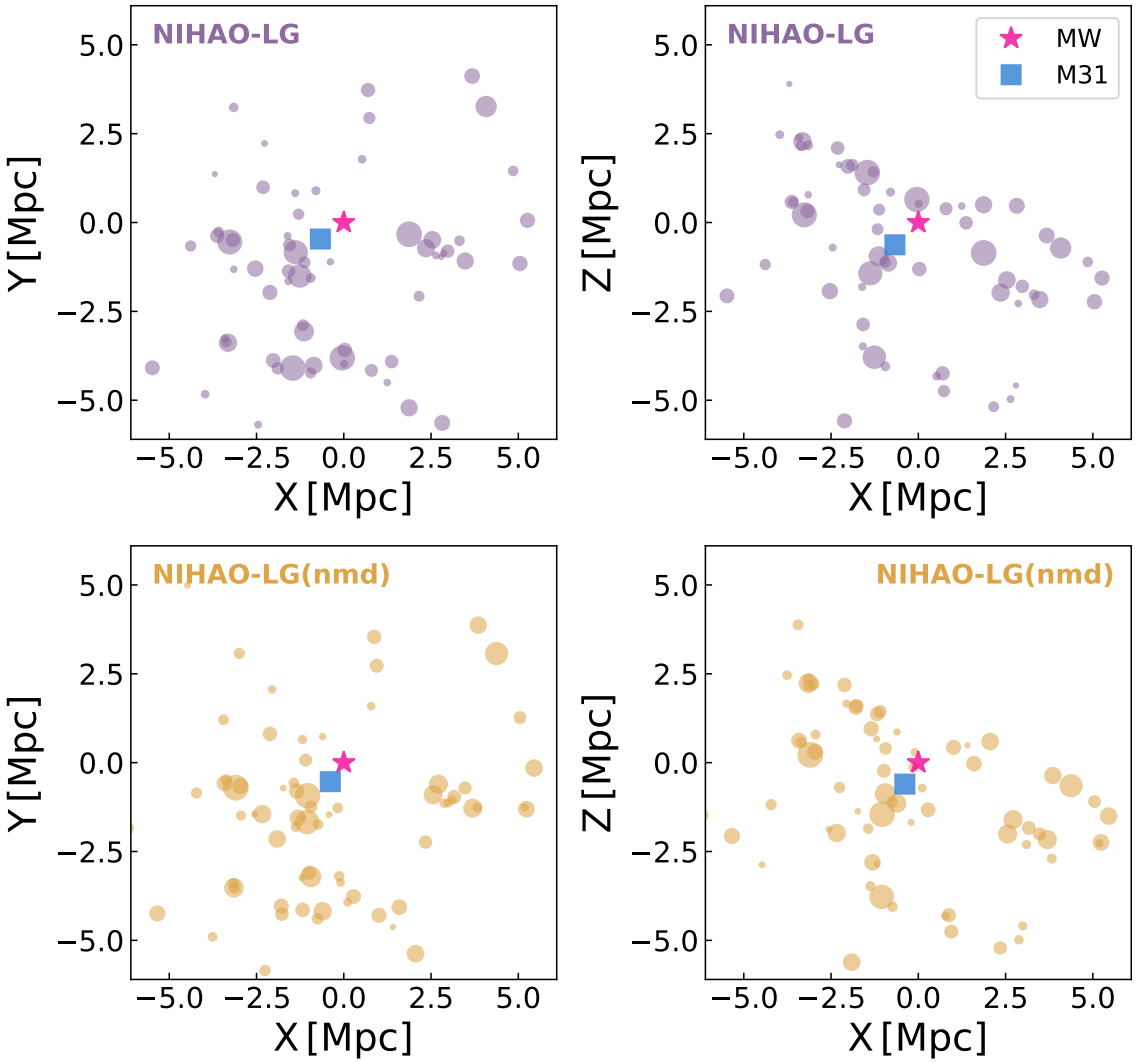

Figure 5.1: Distribution of dwarf galaxies ($7.0 \leq \log(M_*/M_\odot) \leq 9.5$) within our constrained LG simulations at $z = 0$. The top and bottom panels represent NIHAO-LG and NIHAO-LG(nmd), while the left- and right-hand panels show the face-on and edge-on orientations. Both LG simulations are centered centred on the MW (pink star) and M31 (blue square) analogues. In all panels, the dwarf systems are shown as circles whose sizes scale with stellar mass at $z = 0$.

stellar masses for the massive haloes of $M_*^{\rm MW}/M_*^{\rm M31} \sim 1.05$, and circular velocities of $\sim$230 km s^{-1}. Both massive haloes have virial radii of $\sim$ 200 kpc and are separated by $\sim$ 1 Mpc. Altogether, both NIHAO-LG simulations yielded similar stellar and cold gas distribution for the dwarfs halos selected for this study.

We also investigated NIHAO-LG and NIHAO-LG(nmd) for any "backsplash" dwarf halos; i.e., whether LG dwarfs were ever a satellite of the MW and/or M31 analogues (Buck et al. 2019). However, within the stellar mass range of $7.0 \geq \log(M_*/M_\odot) \geq 9.5$, no backsplash haloes were found in our constrained LG simulations. Only a few of backsplash haloes exist for central LG dwarfs with stellar mass of $\log(M_*/M_\odot) < 7.0$. The differences between LG and field central dwarf galaxy properties, discussed later in this paper, are attributed mainly to the global LG environment with possible relatively negligible contributions from the two massive haloes, MW/M31.

Observational comparisons

Fig. 5.2 shows the SHMR at $z = 0$ for the NIHAO and constrained NIHAO-LG simulations. For comparison, the halo abundance matching relations from Moster et al. (2014), Behroozi et al. (2013), and Kravtsov et al. (2018) are also shown. The inset panel in Fig. 5.2 features the NIHAO field and constrained LG analogues for the MW and M31 along with observed measurements. The simulated stellar and halo masses for the MW/M31 agree with current estimates of the observed stellar and halo masses for MW (Bland-Hawthorn and Gerhard 2016) and M31 (Yin et al. 2009; Sofue 2015). As stated in Wang et al. (2015), the NIHAO galaxies, which serve as our field galaxy sample, also agree well with halo abundance matching results (Kravtsov et al.

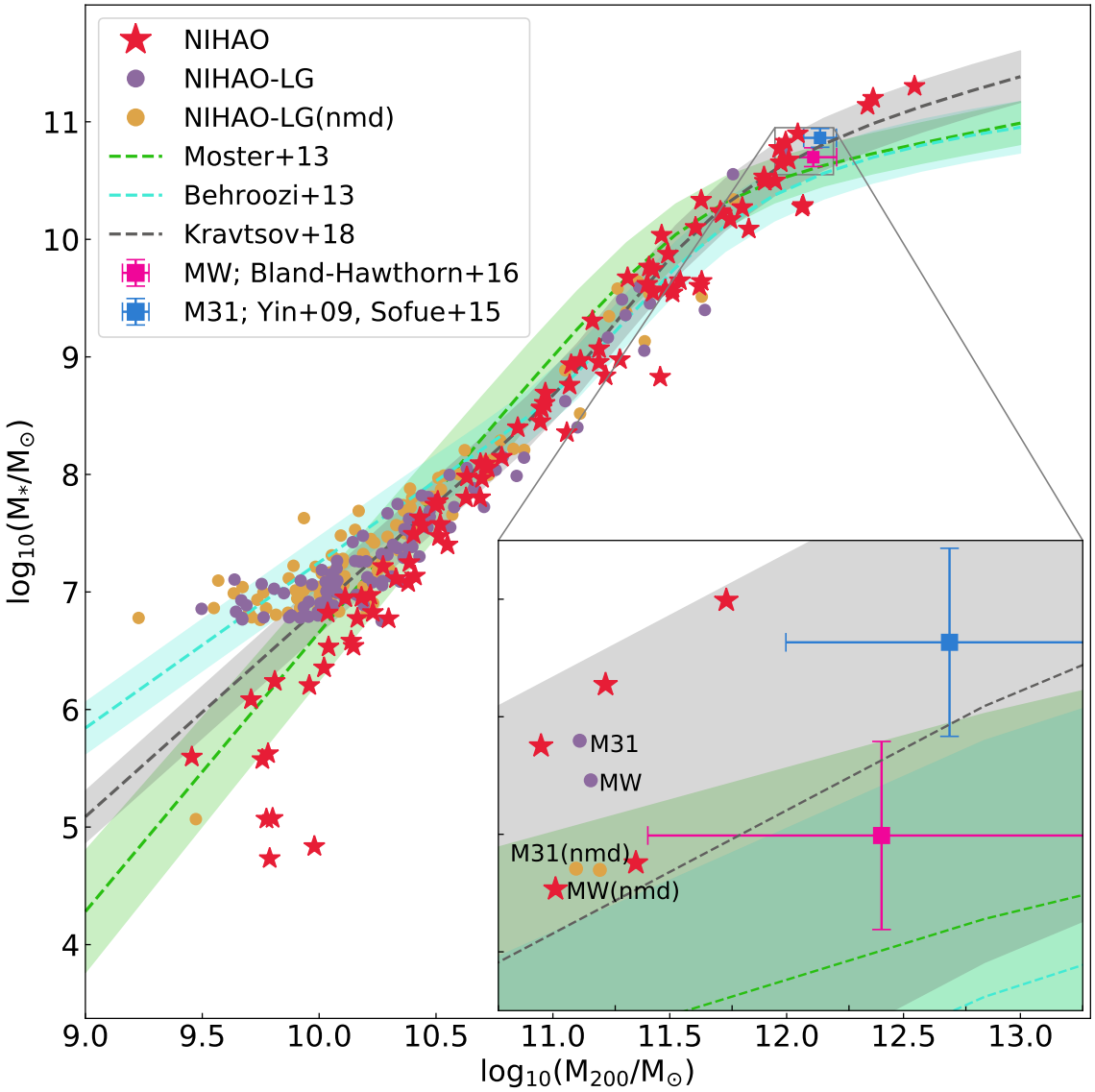

Figure 5.2: SHMR at redshift $z = 0$ for NIHAO (red stars) and two constrained LG simulations with (purple circles) and without (gold circles) metal diffusion. The dashed lines and shaded regions depict popular abundance matching relations from Moster et al. (2014), Behroozi et al. (2013) and Kravtsov et al. (2018). The zoomed inset panel show MW and M31 analogues and comparisons with massive NIHAO spirals. The observed stellar and halo masses for the MW (Bland-Hawthorn and Gerhard 2016), pink square, and M31 (stellar mass; Yin et al. 2009 and halo mass; Sofue 2015), blue square, are also presented.

2018). The dwarf galaxies ($\log(M_{200}/M_{\odot}) \leq 10.5$) in the constrained LG simulations also match the abundance matching relation from Behroozi et al. (2013). Likewise, the galaxies from the constrained LG simulations with $\log(M_{200}/M_{\odot}) \geq 10.5$ match the SHMR of NIHAO field centrals and the relation presented in Kravtsov et al. (2018). However, dwarfs in both LG simulations have stellar masses that exceed their NIHAO field counterparts by $0.2 - 0.3$ dex.

The shallow potential of LG dwarf galaxies is insufficient to retain high-metallicity gas due to strong supernova feedback and stellar winds (Dekel and Silk 1986). The LG dwarfs may also have lower DM fraction for the same stellar mass relative to field systems as a result of interaction episodes with host halos and other systems (Buck et al. 2019).

We further tested the validity of NIHAO and NIHAO-LG simulations by comparing various observational scaling relations. The left-hand panel of Fig. 5.3 shows the cold gas ($T < 20000$ K) content versus stellar mass in the NIHAO-LG simulations at redshift $z = 0$ within $0.2\,R_{200}$. This choice of radius isolates the central parts of haloes as ∼90 per cent of the atomic and molecular gas resides within $0.2\,R_{200}$ of both the field galaxies and LG dwarfs. Two observed cold gas mass-stellar mass relations from Peeples et al. (2014) and Bradford et al. (2015) are also presented. The green squares represent the median cold gas mass-stellar mass relation in Peeples et al. (2014) using the observed data from McGaugh (2005, 2012), Leroy et al. (2008), and Saintonge and Spekkens (2011). The error bars represent the 16 per cent−84 per cent percentile range of the observed data. The cyan line and shaded region, taken from Bradford et al. (2015), delineate the distribution of atomic gas mass for low mass galaxies ($\log M_{*} \leq 8.6$) in the Sloan Digital Sky Survey (SDSS; Aihara et al. 2011)

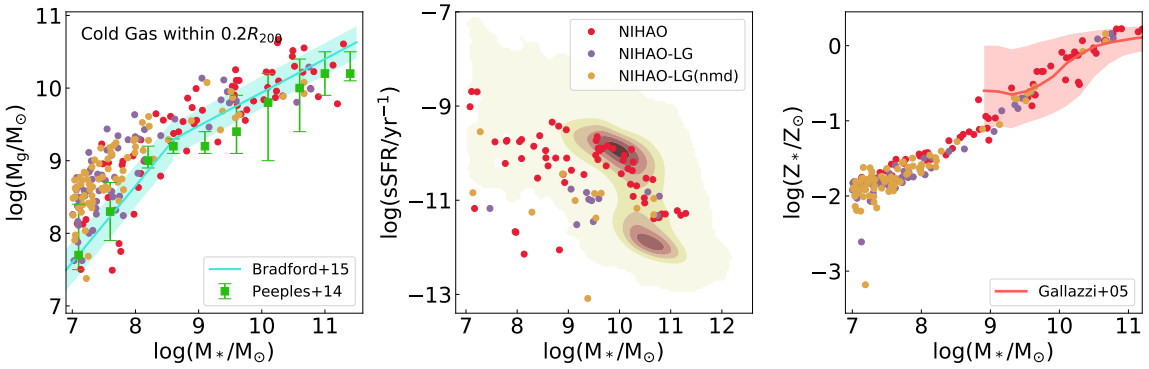

Figure 5.3: Various baryonic scaling relations at present day ($z = 0$) for NIHAO-LG simulations and comparisons with observations. Left-hand panel: Cold gas mass ($T < 20000\,\mathrm{K}$) vesus stellar mass at $z = 0$ for NIHAO, NIHAO-LG, and NIHAO-LG(nmd) simulated galaxies presented as red, purple, and gold circles. Observed cold gas mass-stellar mass relations from Peeples et al. (2014) and Bradford et al. (2015) are also presented. Center panel: Specific star formation rate, sSFR(= SFR/M_*), versus stellar mass, M_*, for the NIHAO (red circles) and NIHAO-LG simulations (purple and gold circles). The underlying number density distribution of SFR and M_* measurements for MPA-JHU SDSS galaxies (Kauffmann et al. 2003; Brinchmann et al. 2004) are shown. Right-hand panel: MZR for the NIHAO (red circles) and NIHAO-LG simulations (purple and gold circles). Also presented is the observed relation from Gallazzi et al. (2005).

and ALFALFA (Haynes et al. 2011). While the ALFALFA survey only detected HI gas content, the total (atomic) gas content is calculated as $M_{\rm g} = 1.4 M_{HI}$ (Oh et al. 2015).

The high stellar mass galaxies ($\log M_* \geq 8.5$) within the NIHAO and NIHAO-LG simulations agree well with observed cold gas content, while the cold gas content in dwarfs from NIHAO and both NIHAO-LG simulations is higher than the observed relations of Peeples et al. (2014) and Bradford et al. (2015). The larger gas content in the simulated galaxies (field and LG) is due to the overcooling of gas. However, given the large error bars (presenting the 16 per cent−84 per cent percentile range) at the low-mass end for Peeples et al. (2014), a fraction of the simulated LG dwarfs agree

with the observations.

We also compared the sSFR–M_* relation in the central panel of Fig. 5.3 with observations. The specific star formation rate, sSFR = SFR/M_*, is the ratio of the average SFR within the last 100 Myr and the enclosed stellar mass within $0.2R_{200}$, M_*. In general, NIHAO and both NIHAO-LG simulations match the distribution of SDSS galaxies, albeit with simulated dwarfs falling in the outskirts of the observed distribution. Given the uneven selection function of the simulated NIHAO systems and the different methods for measuring the observed quantities in Fig. 5.3, comparing NIHAO galaxies with large-scale surveys is a non-trivial task. However, even with this caveat, the overall agreement between NIHAO, NIHAO-LG and the SDSS is comforting.

The MZR relation of dwarf galaxies at redshift $z = 0$ can inform us about chemical evolution of the galaxies. Most of the metals were formed within stars and are distributed into the galaxy via stellar feedback. A comparison of the MZR between NIHAO and NIHAO-LG simulations and SDSS observations from Gallazzi et al. (2005) is presented in the right-hand panel of Fig. 5.3. While the observed data were only available for relatively massive systems ($\log(M_*/M_\odot) \gtrsim 9.0$), both NIHAO and NIHAO-LG-simulated systems match observations well. The MW and M31 analogues from both NIHAO-LG simulations also fall within the observed relation of Gallazzi et al. (2005). Small differences between simulations and observations slope measurements are expected from the sample sizes of our respective studies (Sorce and Guo 2016).

A key feature of this study is to highlight the similarities and differences between the simulated NIHAO field systems and NIHAO-LG dwarfs. Due to the near-identical

dwarf galaxy properties in NIHAO-LG and NIHAO-LG(nmd) galaxies in Figs. 5.1, 5.2 and 5.3; we only used dwarf galaxies from NIHAO-LG to compare with NIHAO field galaxies herein. For general interest, the comparison of different properties between NIHAO field and NIHAO-LG(nmd) at redshift $z = 0$ is presented in Appendix 5.8.

5.5 Field and LG comparisons

Below, we highlight similarities and differences between the NIHAO field and the NIHAO-LG dwarf samples. We begin with comparisons of the gas properties, specifically mass and metal content, followed by the metal content in stars of the simulated field and LG dwarfs. Each comparison contains the calculation of the average difference between the NIHAO field and NIHAO-LG dwarfs. The average difference between the two NIHAO field and NIHAO-LG dwarfs is defined as:

$$\langle \Delta(y_{\rm LG}|M_*)\rangle_{\rm LG} = \langle y_{\rm LG} - (\alpha_{\rm N} M_{*,\rm LG} + c_{\rm N})\rangle, \tag{5.1}$$

where $y_{\rm LG}$ is a galaxy property (gas mass, average stellar metallicity, etc.), $\alpha_{\rm N}$ and $c_{\rm N}$ are the slope and intercept of the fitted scaling relation from NIHAO field sample, and $M_{*,\rm LG}$ is the stellar mass of the NIHAO-LG systems. The variables on the right-hand side of Eq. 5.1 all yield the average difference, $\langle \Delta(y_{\rm LG}|M_*)\rangle_{\rm LG}$.

5.5.1 Gas mass

We start with a comparison of the gas content of dwarf galaxies in the LG and in the field. The left-hand panel of Fig. 5.4 shows total gas mass within $\rm R_{200}$ versus stellar mass (measured within $0.2R_{200}$) for the NIHAO field and NIHAO-LG dwarfs. The red line and shaded region are linear best fit and scatter for the M_g–M_* relation of

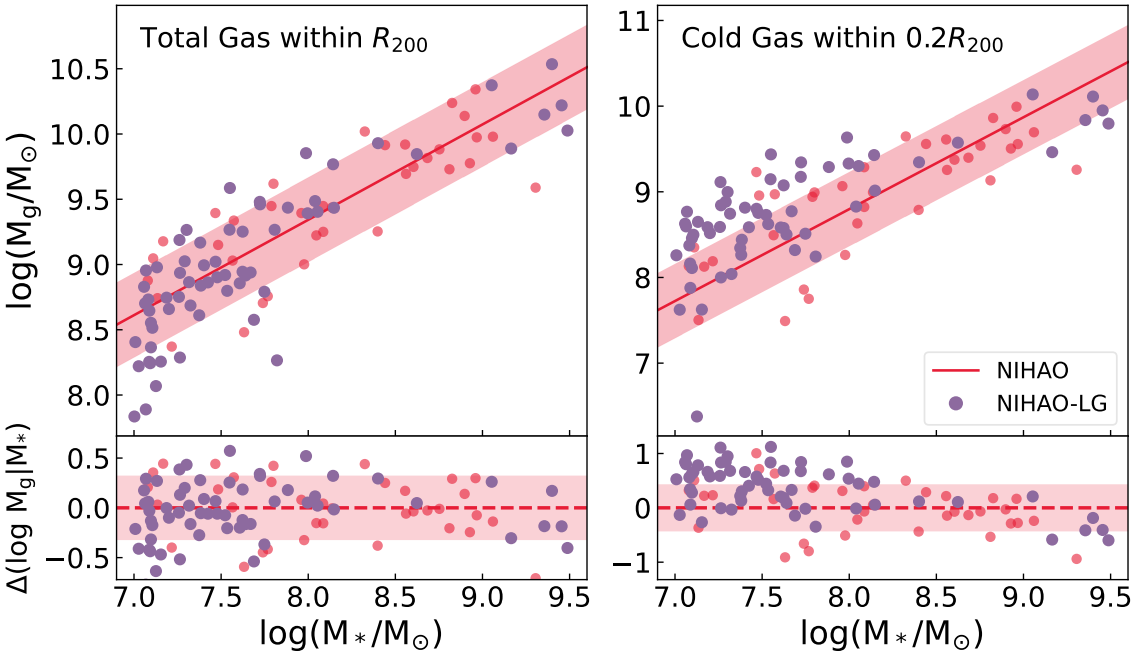

Figure 5.4: Total gas mass (left-hand panel) and cold gas mass ($T < 20000\,\mathrm{K}$; right-hand panel) versus stellar mass at $z = 0$ for NIHAO field (red circles) and NIHAO-LG (purple circles) dwarf galaxies. The solid red line and shaded region represent a best fit of the NIHAO field dwarf galaxies and 1σ scatter about that fit, respectively. Total gas masses are measured within $\mathrm{R_{200}}$ while cold gas and stellar masses are measured within $0.2\mathrm{R_{200}}$. The residuals with respect to the NIHAO field dwarf best fit are shown in both bottom panels.

the NIHAO field simulation. It is found that the total gas content of the NIHAO-LG dwarfs lies within the 1σ scatter (0.30 ± 0.06 dex) of the NIHAO field galaxies. A few LG dwarfs ($\log M_* \leq 7.8$) deviate from the observed trends for field dwarf systems which might be associated to random scatter about the NIHAO field galaxy relation. Most of these NIHAO-LG dwarfs with lower gas content exhibit older, metal-poor stellar content as 50 per cent of the stellar mass was formed within the first $\sim$5 Gyr of their formation.

The right-hand panel of Fig. 5.4 shows the cold gas ($\mathrm{T} < 20000\,\mathrm{K}$) content in the

field and LG dwarf systems at redshift $z = 0$ within $0.2\,R_{200}$. The 1σ scatter for the NIHAO field dwarf relation is 0.46 ± 0.10 dex, and the average difference with the NIHAO-LG dwarf population is calculated to be 0.41 ± 0.11 (Table 5.2). While the average difference for NIHAO-LG dwarfs, across the complete stellar mass range, is less than the scatter for the NIHAO field relation, LG dwarfs with $\log M_* \leq 8.0$ have a larger ($\sim$0.5 dex) central cold gas content compared to field galaxies. While the total gas distribution for field and LG are very similar; a larger fraction of the total gas within the NIHAO-LG dwarfs appears to be cold. The residuals for the NIHAO-LG dwarfs in comparison to NIHAO field systems, shown in the bottom-right panel in Fig. 5.4, present a systematic trend for NIHAO-LG systems with an excess cold gas at the low-stellar mass end and a dearth of cold gas at the high-stellar mass end.

In summary, we have found similar distributions for the total gas contents within the NIHAO field and NIHAO-LG dwarfs. However, a significant fraction of the gas content within NIHAO-LG dwarfs exists as cold gas in the central parts. The unique gas content for the NIHAO-LG dwarfs should be connected to metal content and its evolution. We explore the metal content of the NIHAO field and NIHAO-LG dwarfs next.

5.5.2 Gas metallicity

Fig. 5.5 shows a comparison of the gas metallicity between field NIHAO field and NIHAO-LG dwarf systems. The left- and right-hand panels show the mean gas metallicity for all the gas within the halo and the mean gas metallicity for the cold gas within $0.2\,R_{200}$ respectively. The field NIHAO systems have $Z_{\rm g} \propto M_*^{0.56\pm0.05}$ with a scatter of 0.12 ± 0.03 dex. The NIHAO-LG dwarfs, on the other hand, exhibit a bimodal

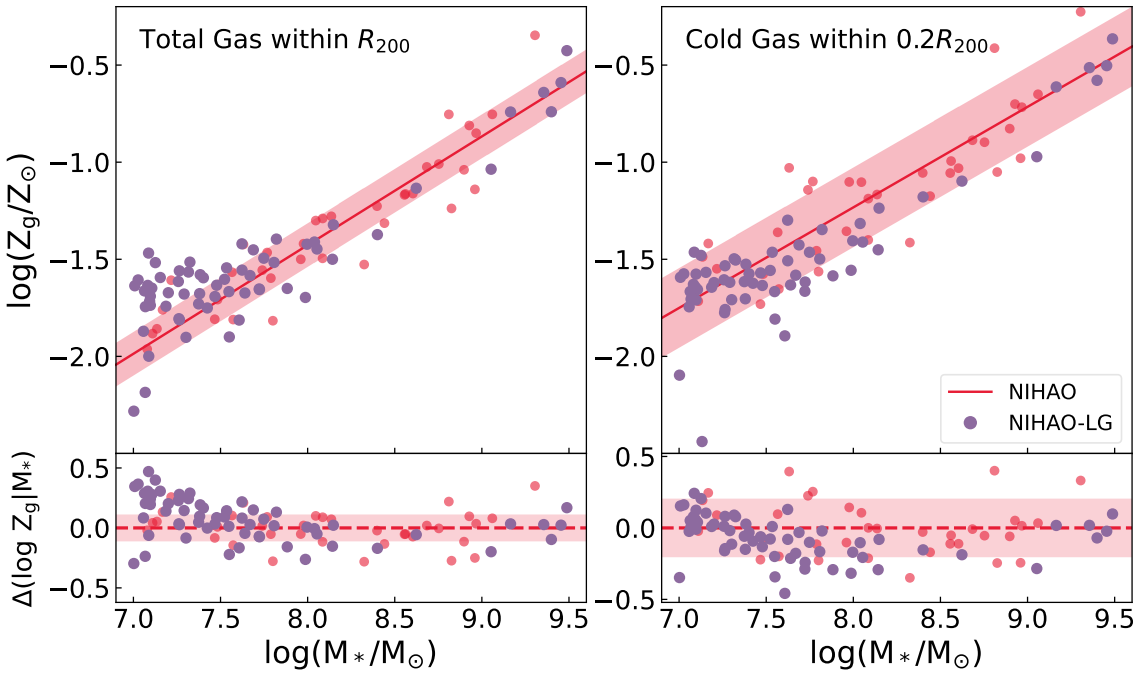

Figure 5.5: Average gas metallicity versus stellar mass for NIHAO field (red circles) and NIHAO-LG (purple circles) dwarf galaxies. The left- and right-hand panels show the metallicity of all the gas within R_{200} and the metallicity of the cold gas within $0.2R_{200}$, respectively. All other details are as in Fig. 5.4.

distribution in the $Z_{\rm g}$–M_*. Low stellar mass NIHAO-LG dwarfs ($\log(M_*/M_\odot) \leq 8.0$) have a higher, though approximately constant, gas metallicity than NIHAO field with $\log(Z_g/Z_\odot) \sim -1.6$. High-stellar mass NIHAO-LG dwarfs follow the same trend and scatter as the NIHAO field galaxies. The average difference between NIHAO field and NIHAO-LG systems of 0.18±0.06 for the $Z_{\rm g}$–M_* relation is larger than the 1σ scatter for the NIHAO field relation. This excess metallicity is addressed at greater length in Section 5.6.3.

The right-hand panel of Fig. 5.5 shows the cold gas metallicity versus stellar mass for NIHAO field and NIHAO-LG dwarfs. The field sample follows a similar relation to total gas content in the halo, with $Z_{\rm g} \propto M_*^{0.50\pm0.06}$ but with a larger scatter

of 0.19 ± 0.04 dex. The NIHAO-LG dwarf galaxies fall within the field relation, presenting no difference in the central cold gas metallicity. Indeed, the difference between NIHAO field and NIHAO-LG dwarfs is found to be negligible; equal to 0.00 ± 0.04 (Table 5.2). Comparing the left- and right-hand panels of Fig. 5.5, we can conclude that metal-rich gas in the NIHAO-LG systems is found outside the central parts of dwarf halos, at radii greater than $0.2R_{200}$. The source of the excess gas-phase metals could be indicative of recent inflowing metal-rich gas due to interactions in the LG which has yet to cool down, and/or the result of strong stellar feedback related outflows from the central regions of dwarf systems itself. To evaluate the dominant process, we compare field and LG dwarfs in the $M_{\rm g}$–M_* and $Z_{\rm g}$–M_* relations as a function of time in Section 5.6.

5.5.3 Stellar metallicities

Fig. 5.6 shows a comparison of stellar metallicity between NIHAO field and NIHAO-LG dwarf systems. NIHAO field dwarfs follow $Z_* \propto M_*^{0.47 \pm 0.04}$ with a scatter of 0.09 ± 0.02 dex. NIHAO-LG dwarfs differ mildly ($\Delta Z_* = 0.02 \pm 0.03$) from NIHAO field systems. However, within the broad dispersions of each distributions, the field and NIHAO-LG dwarfs have statistically matching mean stellar metallicities. We also explored stellar velocity dispersion, mean stellar age, various measures of formation times and SFRs, and no striking differences between NIHAO field and NIHAO-LG dwarfs were found. Within all practical measures, the NIHAO field and NIHAO-LG dwarfs have similar stellar populations.

The interested reader will find further comparisons between NIHAO field and NIHAO-LG dwarfs for the average stellar iron abundance in Appendix 5.9. Different

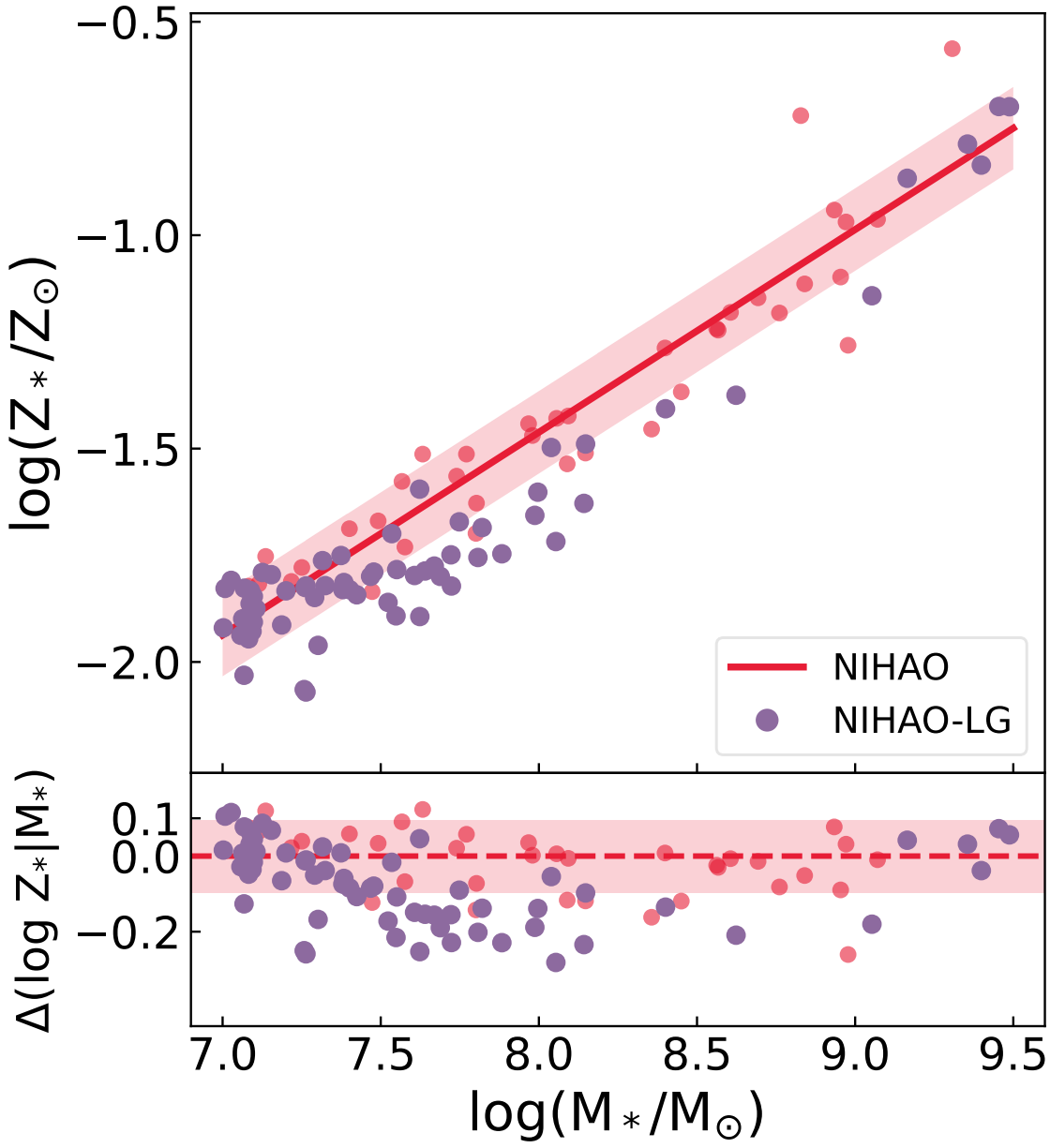

Figure 5.6: Average stellar metallicity versus stellar mass relation for the NIHAO field and NIHAO-LG dwarf galaxies. Both quantities were measured within a spherical radius of $0.2R_{200}$. All other details are as in Fig. 5.4.

		NIHAO		NIHAO-LG
Scaling Relation (1)	Slope (2)	Zero–point (3)	Scatter (4)	Average Difference [dex] (5)
$M_{\rm gas} - M_*$	0.73±0.09	3.47±0.73	0.30±0.06	0.00±0.05
$M_{\rm coldgas} - M_*$	1.09±0.15	0.12±1.27	0.46±0.10	0.41±0.11
$Z_{\rm gas} - M_*$	0.56±0.05	-5.92±0.37	0.12±0.03	0.18±0.06
$Z_{\rm coldgas} - M_*$	0.50±0.06	-5.24±0.49	0.19±0.04	0.00±0.04
$Z_* - M_*$	0.47±0.04	-5.25±0.31	0.09±0.02	0.02±0.03

Table 5.2: Summary of scaling relations used for comparison of the three different simulated dwarf populations. Column (1) lists the scaling relation; columns (2–4) present the slope, zero-point, and scatter, respectively for the NIHAO field dwarfs; and column (5) shows the average difference between the NIHAO field and NIHAO-LG dwarf populations. If the value in column 5 is greater than the scatter of the NIHAO field scaling relations (column 4), the LG dwarf population is considered statistically different. The errors were bootstrapped over 2000 runs.

methods for measuring iron abundance are also discussed.

Finally for this section, Table 5.2 presents a quantitative comparison of NIHAO field and NIHAO-LG dwarf populations. For the scaling relations used here, the slope, zero-point, and scatter for the NIHAO field populations are shown. The average difference between the NIHAO-LG and NIHAO field dwarf populations is also presented in Table 5.2. That difference was calculated by randomly sampling the same number of NIHAO-LG dwarfs as the NIHAO field dwarfs (see Table 5.1) and calculating the median residual with respect to the NIHAO field galaxy scaling relation as presented in Eq. 5.1. This process was bootstrapped 2000 times to estimate the error of the average difference. Table 5.2 reiterates the larger differences in gas properties of the NIHAO-LG dwarfs relative to field systems, especially in the cold gas mass and the total gas metallicity. The stellar properties, such as mean stellar metallicity, velocity dispersion, SFR, etc., of the NIHAO-LG dwarfs show little to no difference with

NIHAO field dwarfs.

5.6 Evolution of the LG

We have found so far that the properties of simulated NIHAO field and NIHAO-LG dwarfs at low redshift ($z = 0$) show non-negligible differences. NIHAO-LG dwarfs have larger (0.2 dex) stellar masses and a larger (0.41 dex) cold gas content within $0.2R_{200}$ than field dwarfs at redshift. The hot gas content for NIHAO-LG dwarfs is also more metal-rich (0.18 dex) than in NIHAO field systems. In this section, we study the evolution of various galaxy properties in an attempt to isolate, if present, evolutionary differences between LG and field dwarf systems.

Motivated by our objective to study the similarities and differences between NIHAO field and NIHAO-LG dwarfs, we wish to trace the evolution of some key dwarf galaxy scaling relations with time. In doing so, we must isolate specific times in the evolutionary history of NIHAO-LG galaxies where environment plays a key role. Ultimately, we constrain the possible influence of LG environment on the evolution of NIHAO-LG dwarf galaxies.

The co-evolution of NIHAO-LG dwarfs in a LG-like environment should be apparent in the gas properties of the NIHAO-LG dwarfs relative to NIHAO field systems. The full set of NIHAO-LG and NIHAO field dwarfs at all redshifts was compared using the average residual from the NIHAO field galaxy scaling relations. The average residuals between NIHAO field and NIHAO-LG samples is calculated using Eq. 5.1 as a function of time. The error on the average residuals are calculated as $\epsilon_{\rm LG} = \sigma(y_{\rm LG}|M_*)/\sqrt{N}$; where $\sigma(y_{\rm LG}|M_*)$ is the standard deviation of the residual

from the field scaling relation and N is the number of data points. In this formalism, we have defined the LG and field dwarfs as different galaxy populations when $\epsilon_{\rm N} < \langle \Delta(y_{\rm LG}|M_*)\rangle_{\rm LG}(t)$, where $\epsilon_{\rm N}$ is the error of the linear fit to the NIHAO field galaxies. In this comparison of the NIHAO-LG and NIHAO field dwarfs, the scatter of the field galaxy scaling relations is also presented. Due to their evolution with time, the slopes of nearly all scaling relations are also expected to evolve; therefore, the forward scatter ($\sigma_{\rm N,f}$) alone is not a robust comparison metric. Instead, we use the orthogonal scatter, defined as $\sigma_{\rm N} = \sigma_{\rm N,f}/\sqrt{1+\alpha_{\rm N}^2}$, for our comparisons.

5.6.1 Gas content

We study the evolution of gas properties, in particular mass and metallicity, for both NIHAO field and NIHAO-LG dwarfs. A comparison of the mass and/or metallicity of the total and/or gas in the NIHAO-LG haloes with the NIHAO field systems at multiple redshifts, can reveal the unique role of the Local Group environment in shaping properties of dwarf galaxies. Fig. 5.7 shows the comparison of the field and LG systems as a function of time for the M_g–M_* relation. The top and bottom panels show all total gas content within R_{200} and the cold gas content within $0.2R_{200}$, respectively. The orthogonal scatter in the total M_g–M_* relation within R_{200} increases from $\sim$0.11 dex at redshift $z \sim 3.2$, to 0.26 dex at present day. Although not presented here, the slope of the relation shows little change over time.

Both NIHAO field and NIHAO-LG dwarfs have the same distribution of total gas content for the complete evolutionary history; the purple shaded band does indeed follow the dark red shaded region (see Fig. 5.7). The NIHAO field systems occupy the central regions of their respective DM halo and are fed gaseous material from

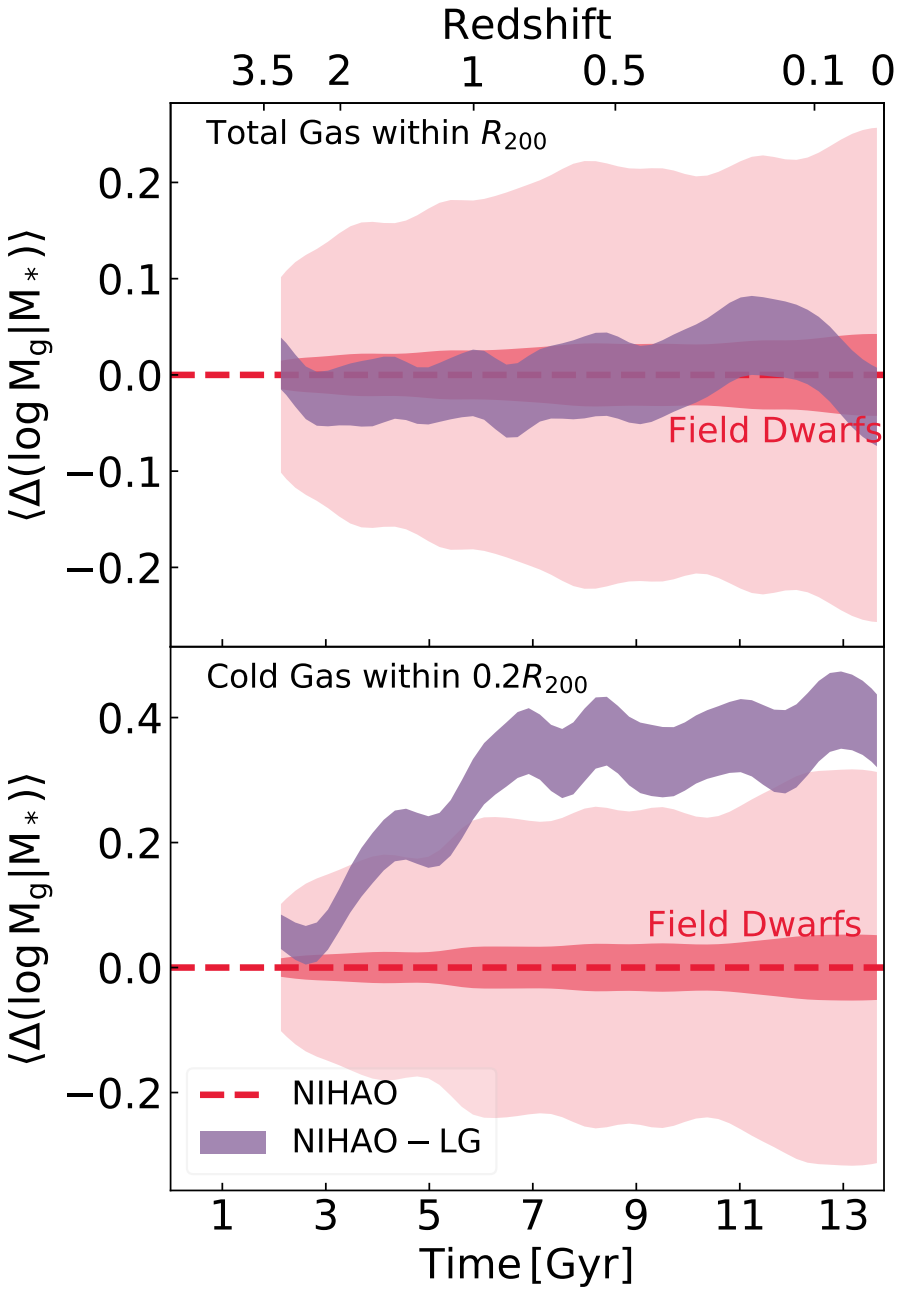

Figure 5.7: Evolution in the residuals of the gas mass–stellar mass relation as a function of time for NIHAO field (red) and NIHAO-LG (purple) dwarfs ($7.0 \leq \log(M_*/M_\odot) \leq 9.5$) shown as shaded regions. The gas mass-stellar mass relation of NIHAO field dwarfs is the horizontal line at $\langle\Delta(M_{\rm Gas}|M_*)\rangle = 0.0$, the dark red region gives the error on the average relation, and the lighter shaded region displays the 1σ scatter of the scaling relation as a function of time. The top and bottom panels show the total and cold gas mass, respectively. Redshift is shown on the top x-axis.

the cosmic filaments, and infrequent gas-rich mergers. Along with similar processes, NIHAO-LG dwarfs are expected to have modified gas content due to the high-density environment of the LG. However, as depicted in Fig. 5.7, the different environment of the LG does not play a significant role in altering the total gas mass of the NIHAO-LG dwarf galaxies (see also Sawala et al. 2012).

While the evolution of the total gas content of the NIHAO-LG and NIHAO field systems is very similar, we find differences between the two dwarf populations for the central cold gas content. For the NIHAO field dwarf sample, the slope and the scatter of the cold M_g–M_* relation in the field evolve significantly with time (see bottom panel of Fig. 5.7). The slope changes range from 0.80 at redshift $z \sim 3.2$ to 1.10 at present day, while the scatter grows from 0.09 dex at redshift $z \sim 3.2$ to 0.31 dex at redshift $z = 0$. Significant differences in the cold gas content between the NIHAO field and NIHAO-LG dwarfs emerge at redshift $z \lesssim 2$ and continue to grow until the present day. At redshift $z = 0$, the NIHAO-LG dwarfs contain ∼0.4 dex more cold gas within $0.2R_{200}$ than the NIHAO field systems. The increasing cold gas mass in the NIHAO-LG dwarfs, compared to the field, is evidence of the unique role that the LG plays. The excess central cold gas through the evolution of NIHAO-LG dwarfs is connected to the gas-phase metallicity evolution of the various star-formation episodes and interactions within the LG environment.

5.6.2 Chemical content

We now consider the evolution of the gas-phase metal content in NIHAO field and NIHAO-LG dwarf galaxies. Fig. 5.8 shows the gas metallicity in the NIHAO field and NIHAO-LG dwarf samples over time. The format of Fig. 5.8 is the same as

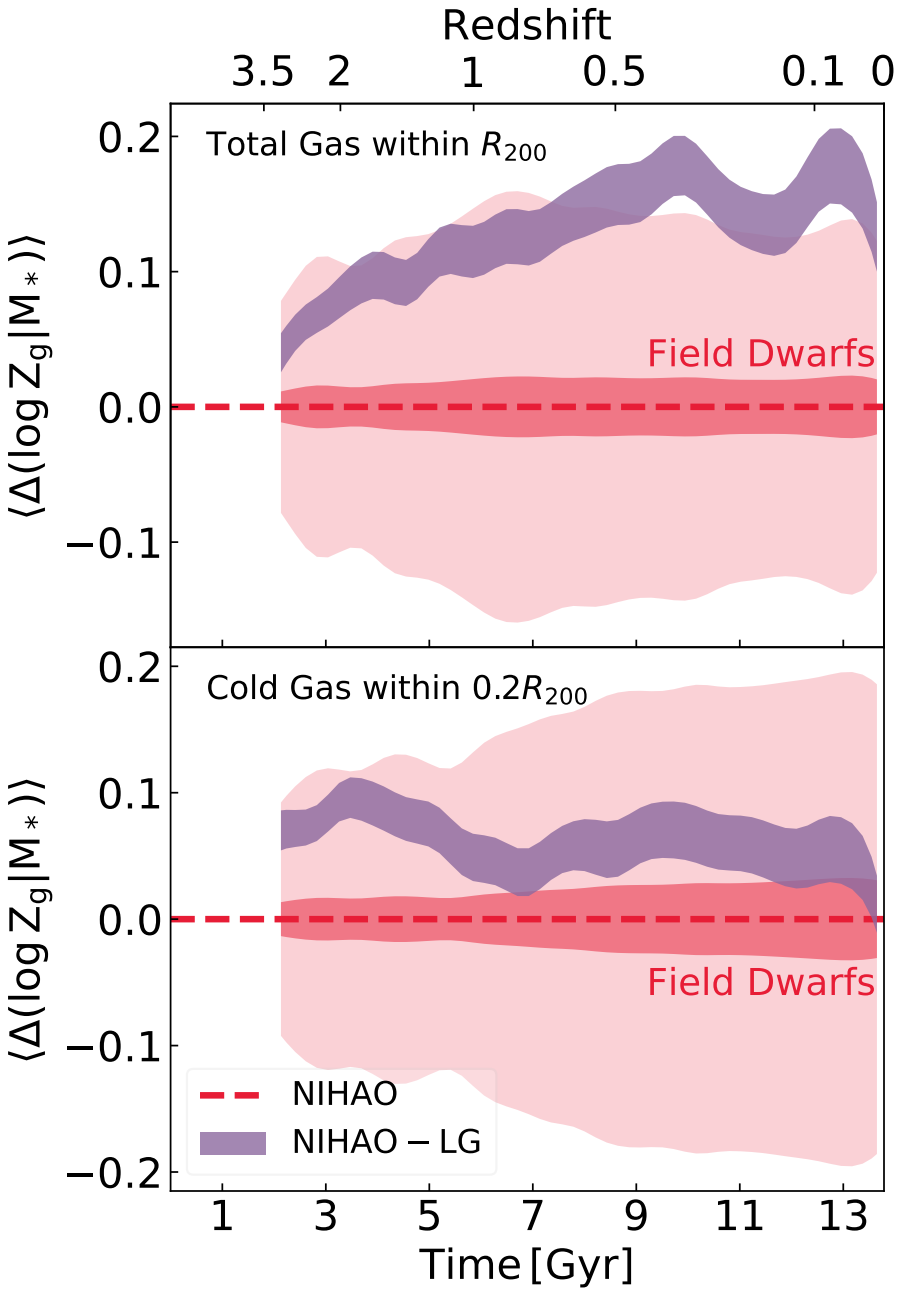

Figure 5.8: Same as Fig. 5.7 for gas metallicity.

Fig. 5.7. In the top panel, where gas metallicity of total gas content is computed within R_{200}, NIHAO field dwarfs display little variation in the scatter of the $Z_{\rm g}$–M_* relation over time. The NIHAO-LG simulations behave slightly differently with time showing dwarfs with more metal-rich gas in the halo than the NIHAO field systems.

From redshift $z \sim 1$ to present day, the NIHAO-LG dwarfs possess a more metal rich gas content (by 0.15 dex, or $3\,\sigma$) than the NIHAO field systems. While the total gas mass of the NIHAO field and NIHAO-LG dwarfs evolve in similar ways (see top panel of Fig. 5.7), the gas content of the NIHAO-LG dwarfs is significantly more metal-enriched. The excess gas-phase metals in NIHAO-LG dwarfs can be attributed to either the interactions within the high-density environment of the LG and/or due to star-formation driven feedback. The next section will investigate the dominance of the environmental (accretion in a high-density environment) and *in-situ* (star formation-driven) processes for the metallicity evolution of the LG.

The bottom panel in Fig. 5.8 depicts the cold gas metallicity evolution of the NIHAO field and NIHAO-LG dwarf galaxies. Unlike the $Z_{\rm g}$–M_* relation for total gas, the cold gas $Z_{\rm g}$–M_* relation for the NIHAO field shows increasing scatter as a function of time. Once again, the NIHAO-LG dwarfs behave differently; over their complete evolution history, NIHAO-LG dwarfs have more cold gas metallicity relative to the NIHAO field systems. The excess metal in the gas within the halo translates into metal-rich cold gas in the central parts ($0.2R_{200}$). The difference between the NIHAO field and NIHAO-LG dwarfs for cold gas metallicity decreases over redshift $z \sim 1{-}2$. During this period, the total gas metallicity (top panel of Fig. 5.8) difference between NIHAO field and NIHAO-LG dwarfs continues to grow.

For redshift $z < 1$, the difference between NIHAO field and NIHAO-LG for cold

gas metallicity remains approximately constant. NIHAO-LG dwarfs show marginal evolutionary differences from the NIHAO field dwarfs for stellar properties, especially for the average stellar metallicity. The lack of evolution in the cold gas metallicity and similar stellar properties is linked to the lack of late star-formation activity in NIHAO-LG dwarfs. Star-formation quenching hinders the recycling of metals in gas and yields a static metal content in the NIHAO-LG cold gas content.

5.6.3 Metal enrichment: *in-situ* versus environment

The metal evolution for these simulated dwarf haloes can come from two sources: *in-situ* star formation (and its associated feedback) as well as interactions within a dense environment of the LG. Fig. 5.9, which attempts to isolate which of these processes is dominant, shows the comparison of gas-phase metals accreted onto a simulated dwarf versus the gas-phase metals produced in-situ, normalized by the gas mass at redshift $z = 0$. It should be noted that only NIHAO-LG dwarfs lying 1.5σ outside of the NIHAO field $Z_{\rm gas} - M_*$ relation presented in Fig. 5.5 are included in Fig. 5.9.

To calculate the accreted and *in-situ* metal masses of a dwarf halo, all gas particles within a halo (at redshift $z = 0$) are traced back to the time when they became bound to the halo progenitor. The metal fraction for gas particles at infall translates to the accreted metal mass and the metals created *in-situ*, $(M_Z(\mathrm{in-situ}))$, according to:

$$M_Z(\mathrm{in-situ}) = M_{Z,0} - M_Z(@\ \mathrm{infall}), \tag{5.2}$$

where $M_{Z,0}$ is the present-day metal mass for gas particles. Fig. 5.9 also shows contours of constant gas-phase metallicity, $\log(Z_g/Z_\odot)$, at redshift $z = 0$ calculated

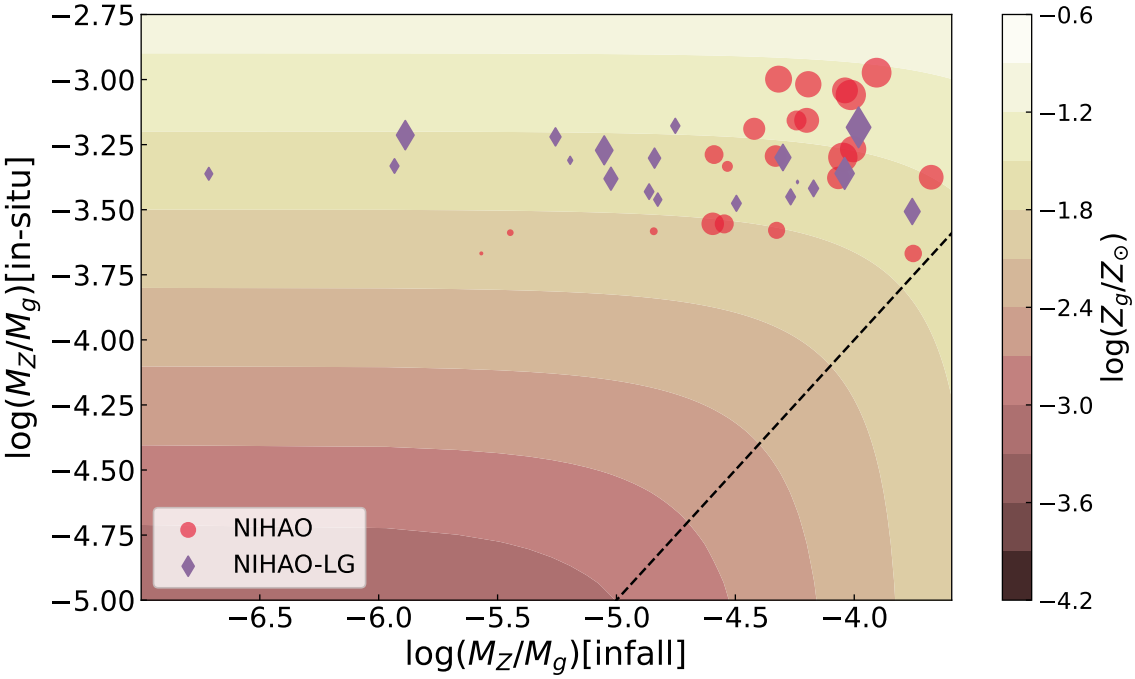

Figure 5.9: Amount of gas-phase metal mass accreted from infall versus gas-phase metal mass generated *in-situ*, for simulated dwarf haloes normalized by the total gas mass at $z = 0$. Red circles correspond to NIHAO field systems, while purple diamonds represent the NIHAO-LG dwarfs. The size of the each point corresponds to the stellar mass at $z = 0$. The contours display present-day constant gas phase metallicity (see color scale to the right). The dashed line represents the line of 50% *in-situ* metal evolution. Only NIHAO-LG galaxies found 1.5σ outside of the NIHAO field $Z_{\rm gas} - M_*$ relation are shown (see Fig. 5.5).

as:

$$\begin{aligned} \log\left(\frac{Z_g}{Z_\odot}\right) &= \log\left(\frac{M_{Z,0}}{M_g}\frac{1}{Z_\odot}\right) \\ &= \log\left(\left[\frac{M_Z(@\ \text{infall})}{M_g} + \frac{M_Z(\text{in}-\text{situ})}{M_g}\right]\frac{1}{Z_\odot}\right). \end{aligned} \tag{5.3}$$

Horizontal or vertical displacements (i.e., metallicity evolution) of dwarf haloes along the contours in Fig. 5.9 are predominantly driven by accretion and/or stellar feedback

related outflows, respectively. Galaxies located on the curved part of these contours also have comparable contributions to their metallicity evolution from both accretion and *in-situ* processes. It should be noted that all galaxies (NIHAO and NIHAO-LG) produce more gas-phase metals through star-formation processes (*in-situ* production) than accretion. The dashed line represents 50 per cent of the metals created through *in-situ* processes. All galaxies (NIHAO field and NIHAO-LG) lie on the left-hand side of the dashed line.

We find that nearly all NIHAO field dwarfs lie on the curved region of the constant gas-phase metallicity contours showing contributions from both *in-situ* and accretion processes. NIHAO haloes with larger stellar mass reside on contours of larger metallicity (a different way to represent the field $Z_{\rm gas} - M_*$ relation), while NIHAO-LG dwarf haloes lie on the horizontal parts of constant contours ($\log(Z_g/Z_\odot \sim -1.7)$). We find that all NIHAO-LG dwarfs (which are outliers of the field $Z_{\rm gas} - M_*$ relation) have constant amounts of metals created via in-situ processes but varying contributions from the environment.

Analysing the accretion of gas-phase metals as a function of time, we find that NIHAO-LG dwarfs accrete gas with high metal content at late times ($t \sim 7\,{\rm Gyr}$). We have also traced the origins of gas particles with high metal fractions. We find that only three NIHAO-LG dwarf haloes with $\log(M_*/M_\odot < 8.5)$ have gas particles that evolved through star formation in the MW/M31 analogues. With the MW/M31 analogues playing minimal roles in the metallicity evolution, the role of environment in this case is a result of the co-evolution of NIHAO-LG dwarfs in a high-density region in the Universe. Throughout their evolution, LG dwarfs co-evolve whilst sharing high metallicity gas released through active star formation feedback. Given that the

accretion in LG dwarfs occurs at a late time, the gas has not had time to cool (the cooling time typically exceeds the Hubble time) and participate in star formation activities.

As a result, no differences are found for the metal content of stars between field and LG dwarfs (see Fig. 5.6). Finally, some NIHAO-LG dwarf halos, show negligible infall metals but high *in-situ* gas-phase metals. Such galaxies accrete a large number of gas particles with low metal fractions early in their evolution and process gas through star formation, resulting in higher metallicities.

We also found that NIHAO-LG dwarfs with excess gas-phase metals are randomly distributed through the simulated LG region; no correlations exist between the excess gas metallicity and distances from MW/M31 analogues or the barycenter of the LG. This is further evidence that MW/M31 analogues play negligible roles in the metallicity evolution of NIHAO-LG dwarfs. It is the full dwarf population in simulated LG regions which goes through star formation at early times to process gas and then exchange it with other NIHAO-LG dwarfs at late times. This creates a unique gas property for NIHAO-LG dwarf populations with respect to NIHAO field systems.

5.7 Summary and Conclusions

The Local Group (LG) is a superb laboratory for the study of the formation and evolution of the dwarf galaxies; the most abundant cosmological structures in the Universe. In this paper, we have examined whether the LG provides an unbiased foil for studies of galaxy formation and evolution. In this comparative study, we have highlighted the similarities and differences between simulated LG and field dwarf galaxies as a function of time/redshift and compared with observations. Our field

control sample relied on dwarf haloes from the NIHAO high resolution zoom-in simulations. For the LG dwarfs, we used the constrained LG simulations run with NIHAO hydrodynamics.

Present-day NIHAO field and NIHAO-LG dwarfs were found to have similar stellar populations; properties like stellar velocity dispersion, mean stellar age, accretion times, and SFRs, etc. Relative to field systems, NIHAO-LG dwarfs show small evolution in cold gas metallicity with time. This is understood in the following way: while the high metallicity gas in the halo should allow for gas to cool efficiently and lead to star-formation events, stellar feedback and outflows in the dwarf systems suppress any further stellar evolution leading to a quenched system and locking metals in the hot halo gas. Therefore, the stellar and cold gas evolution of NIHAO-LG dwarfs is strongly dictated by *in-situ* processes such as stellar feedback, winds, and photoevaporation due to re-ionization, which are not affected by environment (Sawala et al. 2012). A significant fraction of the dwarfs in our constrained LG simulations build up their stellar content early in their evolution history and remain quenched thereafter (e.g. Sand et al. 2010; Simon et al. 2021).

At all times, NIHAO-LG and NIHAO field dwarfs have very similar total gas content. In other words, the total gas content of the LG dwarfs is not influenced by environment, in agreement with findings of Sawala et al. (2012). However, a larger fraction of the gas within NIHAO-LG dwarfs is cold and resides within $0.2R_{200}$. The larger cold gas content is correlated to the higher metal content (relative to the NIHAO field dwarfs) of the gas in the halo; which cools down and enhances the metal content at early times. The higher gas metal content of the NIHAO-LG dwarfs is

expected to be accumulated via interactions within the LG which allows the NIHAO-LG dwarfs to exchange the heavy metal generated during star-formation episodes in other LG systems. The time evolution of the cold gas mass within NIHAO-LG dwarfs shows departures from the field sample around redshift $z \sim 1-2$. This excess cold gas content in NIHAO-LG dwarf through time is related to the metal evolution of the hot gas in NIHAO-LG dwarfs as well; departure for NIHAO-LG gas metallicity emerges around redshift $z \sim 1-2$. Indeed, relative to NIHAO field systems, NIHAO-LG dwarf possess excess metals in the hot gas phase at $R > 0.2R_{200}$ at present day.

We isolate the dominance of *in-situ* metal evolution and/or impact of the LG environment. Most NIHAO-LG dwarf galaxies present excess gas-phase metals relative to simulated NIHAO field dwarfs; these metal-rich gas reside at radii $> 0.2\,R_{200}$. While environment does play a role, the direct influence or presence of the massive haloes (MW/M31) is found to be insignificant; rather, the interaction of dwarfs in a high-density environment such as the LG is the dominant factor. We found that these NIHAO-LG dwarfs accrete high-metallicity gas, processed in other NIHAO-LG dwarfs, at late times ($t \sim 7$Gyr). Because of the late accretion times, the NIHAO-LG dwarf hot gas-phase metals have not had time to cool and participate in star-formation activity. As a result, the gas metallicity evolution of the LG is not reflected in stellar properties of NIHAO-LG dwarfs. The NIHAO-LG dwarfs with excess gas-phase metals are found to have stochastic distribution through the simulated regions; that is, no correlations exist between the excess gas metallicity and the central parts of the simulation LG region.

Given the similar stellar properties of simulated dwarfs, high-resolution dwarf simulations such as NIHAO (Wang et al. 2015) and FIRE (Garrison-Kimmel et al.

2019) may then be compared with the general dwarf population. Our results have demonstrated the value of LG observations, specifically their stellar properties, as constraints for the overall dwarf populations in our Universe. The unique aspects seen in the gas properties of the LG can be examined using high-resolution constrained LG simulations (Gottloeber et al. 2010a; Sorce et al. 2016; Carlesi et al. 2016; Libeskind et al. 2020). Furthermore, with the advent of next generation telescopes such as JWST, Euclid, Rubin/LSST, and SKA, observational signatures of pre-enrichment can ultimately be teased out of high redshift LG analogs and their accompanying dwarfs.

5.8 Appendix: NIHAO-LG(nmd)

Figs. 5.10 and 5.11 reproduce the NIHAO field and NIHAO-LG(nmd) comparisons for various galaxy properties. At redshift $z = 0$, we present different measures of gas masses (total gas within R_{200} and cold gas within $0.2R_{200}$) as well as various measure of metal contents (average gas metallicity within R_{200}, average cold gas metallicity $0.2R_{200}$, and mean stellar metallicity). Similar to NIHAO-LG, we find that the NIHAO-LG(nmd) dwarfs have excess cold gas within $0.2R_{200}$ and total gas-phase metals relative to NIHAO field dwarfs. Independent of the constrained LG simulations used, our conclusions are unchanged.

5.9 Appendix: Iron Abundance in the LG

Observers typically measure stellar chemical abundance of galaxies using bright metal absorption lines such as those of iron or magnesium. Here we present a comparison of

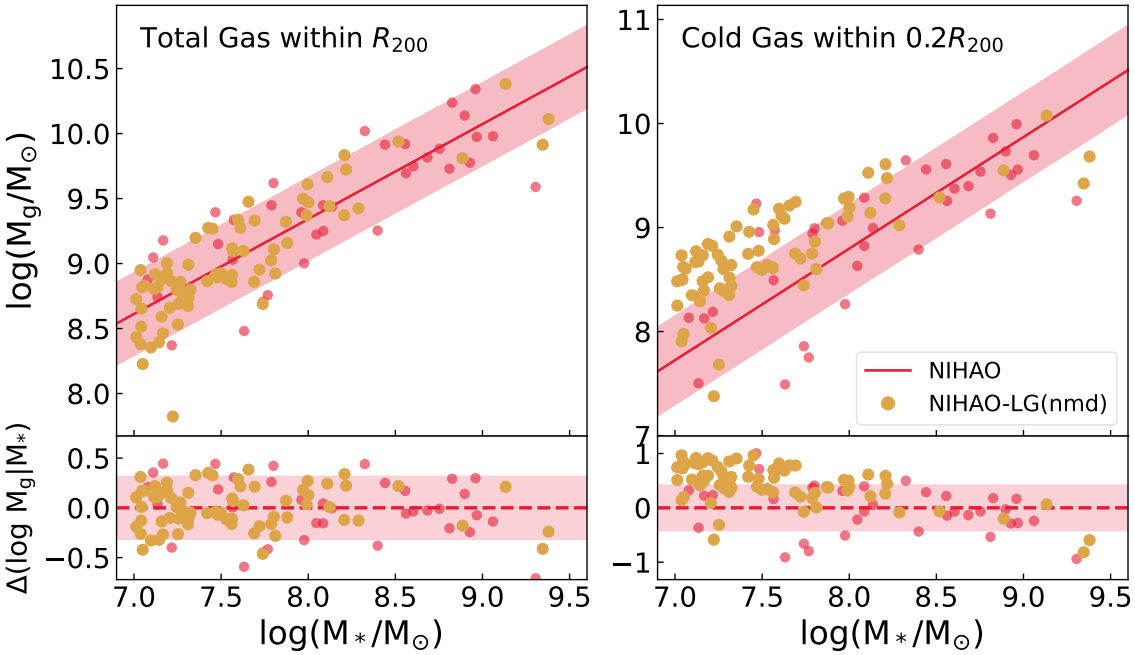

Figure 5.10: Total gas mass (left-hand panel) and cold gas mass ($T < 20000\,\mathrm{K}$; right-hand panel) versus stellar mass at redshift $z = 0$ for NIHAO field (red circles) and NIHAO-LG(nmd) presented as gold circles dwarf galaxies. The solid red line and shaded region represent a best fit of the NIHAO field dwarf galaxies and 1σ scatter about that fit, respectively. Total gas masses were measured within R_{200}, while cold gas and stellar masses were measured within $0.2\mathrm{R}_{200}$. The residuals with respect to the NIHAO field dwarf best fit are shown in both bottom panels.

the stellar iron abundances between NIHAO field and NIHAO-LG dwarfs and observations from Kirby et al. (2013). With most of the iron concentrated in the central parts of the galaxies, the average iron abundance weighted by stellar mass encompasses all star particles within the half-light radius, $R_{1/2}$. An essential aspect of this chemical comparison is the averaging process for the star particles in the simulation. At first, the averaging is carried out with the metallicity in logarithmic space, also called the "geometric mean" (hereafter, log average; Kirby, private communication). The average iron abundance then becomes,

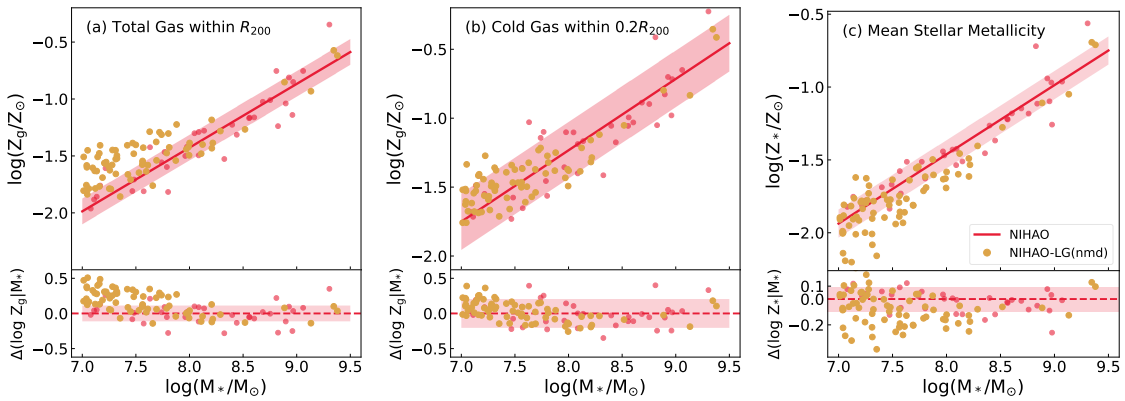

Figure 5.11: Dwarf galaxy comparison between NIHAO field and NIHAO-LG(nmd) for various properties related to metal content. Panel a shows the total gas metallicity within R_{200}, panel b shows the cold gas metallicity within $0.2R_{200}$, and panel c shows the mean stellar metallicity. The red dots, lines, and shaded regions present the NIHAO field galaxies, linear fit, and scatter, respectively. The gold points show dwarfs from the NIHAO-LG(nmd) simulation.

$$\langle [\mathrm{Fe/H}] \rangle_{*,\log} = \frac{\sum_i ([\mathrm{Fe/H}]_{*,i} m_{*,i})}{\sum_i (m_{*,i})}, \tag{5.4}$$

where [Fe/H] is the logarithmic iron abundance and m_* is the stellar mass of the star particle i. However, the averaging process in logarithmic units is inappropriate. A proper expression for the mean iron abundance is given by

$$\langle [\mathrm{Fe/H}] \rangle_{*,\mathrm{lin}} = \log \left(\frac{\sum_i (10^{[\mathrm{Fe/H}]_{*,i}} m_{*,i})}{\sum_i (m_{*,i})} \right). \tag{5.5}$$

In Eq. 5.5, the iron abundance per star particle, i, is calculated in linear space and the logarithm of the complete expression is taken once the average is computed. Our comparison of the simulated dwarf systems uses linear averages presented in Eq. 5.5. For complementarity and comparison with observations, the stellar iron abundances

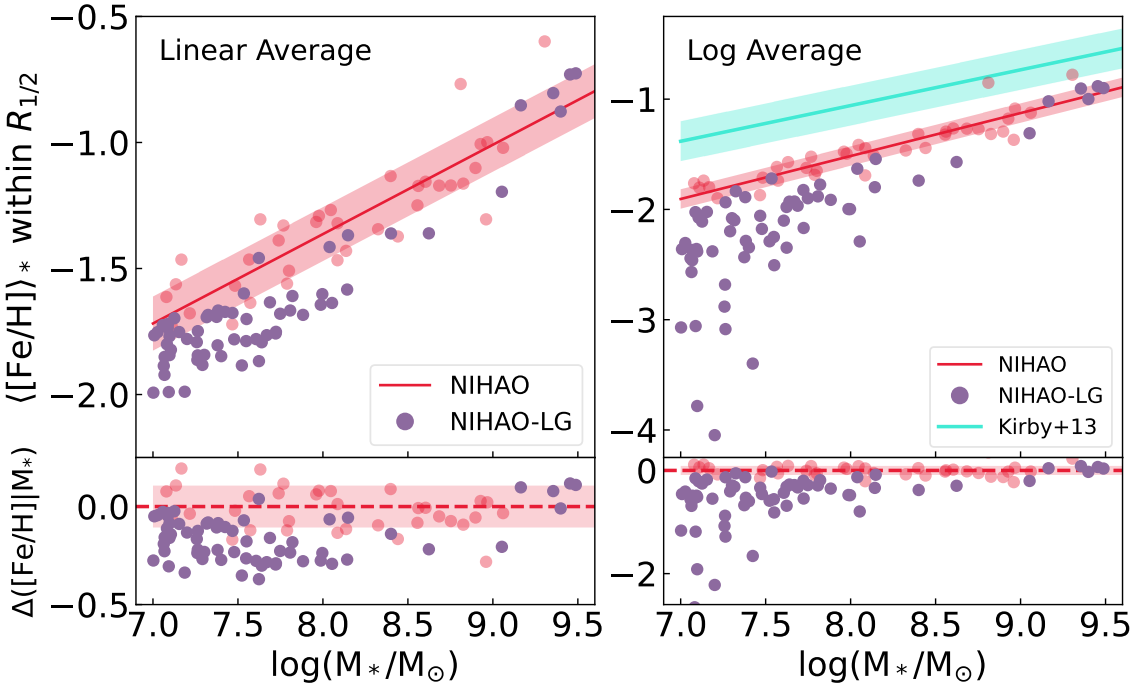

Figure 5.12: Iron abundance, $\langle[\mathrm{Fe/H}]\rangle_*$, versus stellar mass for NIHAO field and NIHAO-LG dwarfs. The color scheme is as in Fig. 5.4. $\langle[\mathrm{Fe/H}]\rangle_*$ was averaged over all stellar particles within the half-light radius, $R_{1/2}$. The left-hand panel shows mass-weighted averages carried out in linear space (see Eq. 5.5 for definition) while the right-hand panel shows mass-weighted averages calculated in log space as presented in Eq. 5.4. In cyan, the right-hand panel shows the observed relation for LG dwarf galaxies from Kirby et al. (2013).

averaged in logarithmic space are also reported.

The left-hand panel of Fig. 5.12 presents the linearly averaged iron abundance versus stellar mass for NIHAO field and NIHAO-LG dwarf samples. Field dwarf galaxies from NIHAO follow $\langle[\mathrm{Fe/H}]\rangle \propto M_*^{0.36\pm0.04}$ with a scatter of 0.09 ± 0.02 dex. NIHAO-LG low-mass dwarfs are somewhat poorer in metals than the field. A linear average for the stellar iron abundance is preferentially biased towards metal-rich stars.

NIHAO-LG shows metal-poor stellar populations relative to field systems. Given the deep potential of the MW and M31, a significant fraction of the outflowing gas and

metals may be retained by the massive halo through galactic fountain effect. With most of the metal retained by the massive halos, the LG dwarf populations would show a metal poorer stellar population relative to expectations due to pre-enrichment. Our result in the left-hand panel of Fig. 5.12 is quantitatively similar to that of FIRE simulations (Escala et al. 2018) or the high-resolution NIHAO simulations (Buck et al. 2019).

The right-hand panel of Fig. 5.12 shows the logarithmic averaged stellar iron abundance for the NIHAO field and NIHAO-LG dwarfs and observed relation from Kirby et al. (2013). With a different averaging technique comes a revised relation; the field galaxies relation, $\langle[\mathrm{Fe/H}]\rangle_*$–$M_*$, is now slightly steeper and tighter with a slope of 0.39 ± 0.04 and scatter 0.09 ± 0.02. The differences between linear and logarithmic averaging of the $\langle[\mathrm{Fe/H}]\rangle_*$–$M_*$ relations are still well within the confidence intervals. The observed relation shows similar linear slope (0.30 ± 0.02) but with a larger scatter (0.17 dex) and lower zero-point. The simulated field galaxies from NIHAO are more iron-poor, as is expected for these low-mass galaxies which cannot retain metal-rich gas due to stellar feedback and winds. The NIHAO-LG dwarfs show an even poorer metal content in stars, with their [Fe/H] distribution lower than observations by a factor 15. The simulations and observations differ only in their zero-point offset (the trends have the same slope) which is directly linked to the implementation of supernova feedback in the simulations (Escala et al. 2018). The study of Buck et al. (2021) provides an improved chemical enrichment scheme for NIHAO simulations that should yield a better match with observations. We shall return to such data-model comparison in a future study.

Chapter 6

Summary and Conclusions

6.1 Summary

In this thesis, we have presented four projects which compare state-of-the-art SAMs and hydrodynamical simulations with rich and robust modern observations. Such comparisons are needed to better understand galaxy formation and evolution and circumscribe future improvements of cosmological models. For the comparison of numerical models (SAMs and cosmological simulations) with observational data, we have (first) compiled large, comprehensive data sets from SDSS and exploited NIHAO, L-GALAXIES and SAGE simulations. These have enabled tests of important galaxy structure and evolutionary processes such as galaxy quenching, baryonic feedback, growth of central densities, etc. What follows is a summary of major results in this thesis and comments on some future works.

Using SDSS central galaxies at $z \sim 0$, the variation of passive fractions in a stellar mass – neighbour density parameter space was studied (Chapter 2). These passive

fractions were then compared to those of central galaxies from various SAMs (L-GALAXIES and SAGE), enabling the study of the dependence of star formation quenching on gas heating processes due to AGN feedback. We found for central galaxies in the SDSS that passive fractions depend on stellar mass and bulge mass, in broad agreement with predictions from SAGE. AGN feedback for SAGE allows for an improved but crude coupling of the gas cooling and heating processes due to AGN feedback. However, some issues matching observed quenched fractions remain in SAGE; especially for high mass field galaxies. These issues likely emerge from the treatment of "orphan" galaxies which leads to a large merger rates and excess cold gas leading to star formation. The passive fractions of L-GALAXIES also show a dependence on halo mass and black hole mass.

In general, the comparisons between observed and simulated properties of galaxies can follow one of two methods. Firstly, one can obtain robust observations of galaxies, correct most observational biases/errors (e.g., sky background, inclination, PSF, internal and external dust extinction, photometric band effects, etc), and compare the resulting corrected data directly with the simulations outputs. Secondly, one can also use simulated galaxies and introduce observational biases (such as atmospheric blur, background sky noise, etc) to generate "mock" observed images and spectra (Torrey et al. 2015; Bottrell et al. 2017; Elagali et al. 2018; Bottrell and Hani 2022) which can be compared with real observations. The next two projects below took advantage of the former approach towards comparing MaNGA observations and NIHAO simulations.

In Chapter 3, we extracted and compiled non-parametric multi-band photometric and environmental catalogues for the MaNGA galaxy survey. Optical *grz* surface

brightness profiles were obtained through the automated isophotal solution software AUTOPROF(Stone et al. 2021b), and shown to reach $\sim$2 mag arcsec^{-2} deeper surface brightness profiles relative to common SDSS imaging. Non-parametric SB profiles were also found to be more robust and reproducible than the parametric modelling of galaxy images (see Fig. 3.4). Galaxian parameters measured relative to total light were also found to be less reliable than those measured relative to an isophotal level.

Rotation curves using the MaNGA Hα velocity maps were also extracted to complement the photometric catalogue of the MaNGA galaxies (Chapter 4). These RCs were extracted by fitting a tanh function to the velocity map. Along with the stellar masses from photometry and gas masses and SFR from Pipe3D (Sánchez et al. 2018), the extracted RCs allowed for the construction of 12 structural galaxy scaling relations. The same galaxy scaling relations were compared with those from the NIHAO zoom-in simulations. While NIHAO galaxies broadly match the same distributions determined for MaNGA galaxies, some important differences were found. Indeed, due to the weak feedback implementation in NIHAO for massive, the central stellar densities (measured using Σ_1) within NIHAO are higher (by $\sim 1\sigma$) than the observed distribution. The spatially-resolved data provided by DESI and MaNGA also enabled an extraction of the spatially-resolved scatter of the VRM$_*$ relations. We found that scatter for parameters measured in the inner galaxian regions was dominated by the great diversity in the inner RC shapes, while the scatter for relations based on outer region measurements was dominated by the large dispersion in stellar surface densities for LTGs (which is due to stochastic star formation). Not only must simulations match global galaxy scaling relations (size-mass, SFMS, TFR),

they should also reproduce spatially-resolved properties and relations (such as the diversity of inner RC slopes, spatially-resolved SFMS, RAR, metallicity gradients, etc.) These detailed comparisons based on spatially-resolved structural information bring together the complex connections between local and global astrophysical processes in galaxies.

Finally, using galaxy scaling relations, we also studied the impact of environment on shaping the dwarf galaxy population in the Universe. We have presented and compared dwarf galaxies from constrained Local Group simulations, NIHAO-LG, with field dwarf galaxies from classic NIHAO simulations. At $z = 0$, we found that simulated LG dwarfs showed very similar stellar properties relative to the simulated field systems. However, the hot gas within LG dwarfs is more enriched than for field dwarfs. The excess hot gas-phase metals in LG dwarfs is the result of interactions amongst LG dwarfs as they live in a denser environment of the LG. Most of the excess-metal within LG dwarfs was accreted at late times ($> 7\,\mathrm{Gyr}$); as a result, this gas did not have time to cool down and be available for star formation. This explains the similar stellar properties between LG and field dwarfs.

6.2 Future Work

The data-model comparisons presented here can be expanded to further refine our understanding of galaxy formation and evolution models. We will pursue the following data-model projects that naturally emerge from this thesis:

1. **Queen's Galaxy Catalogue (QGC)**: The MaNGA photometric catalogue of Arora et al. (2021) consists of multi-band surface-brightness profiles for ∼8000 galaxies. We plan on extending this catalogue to 500,000 galaxies (spanning a

range of stellar mass and environment) using multiple all-sky imaging surveys (GALEX, DESI, WISE). Such an extensive multi-band (FUV to MIR) non-parametric photometric catalogue will enable the:

(a) Derivation of robust inclination corrections (e.g. Holmberg test) for various galaxy properties and their impact on scaling relations. The QGC's multi-band photometry would be used to isolate the effect of geometry, stellar populations, and dust extinction on inclination corrections of galaxies.

(b) Study of the impact of environment on various structural galaxy scaling relations.

2. **Numerical investigations of galaxy scaling relations**: With the update of subgrid physics in the NIHAO simulations (NIHAO2.0), along with the original NIHAO, we will:

(a) Study robust data-model comparisons for higher redshift galaxies (in anticipation of new LSST, JWST, Euclid and Roman data). A test of the slope and scatter between simulations and observations at various key time-steps (such as cosmic noon and reionization) can further guide cosmological models and extragalactic astrophysics.

(b) Isolate the astrophysical drivers of different scaling relations. Using NIHAO simulations with and without SMBH and AGN feedback, we can study the impact of AGN subgrid physics on shaping the slope and scatter of the spatially-resolved SFMS.

While the above projects are obvious extensions of this thesis, the data and techniques presented here allow for numerous new avenues for the study of galaxy formation and evolution.

Bibliography

K. N. Abazajian, J. K. Adelman-McCarthy, M. A. Agüeros, et al. The Seventh Data Release of the Sloan Digital Sky Survey. *ApJS*, 182(2):543–558, June 2009. doi: 10.1088/0067-0049/182/2/543.

Abdurro'uf, K. Accetta, C. Aerts, et al. The Seventeenth Data Release of the Sloan Digital Sky Surveys: Complete Release of MaNGA, MaStar, and APOGEE-2 Data. *ApJS*, 259(2):35, April 2022. doi: 10.3847/1538-4365/ac4414.

M. Ackermann, A. Albert, B. Anderson, et al. Searching for Dark Matter Annihilation from Milky Way Dwarf Spheroidal Galaxies with Six Years of Fermi Large Area Telescope Data. *Phys. Rev. Lett.*, 115(23):231301, December 2015. doi: 10.1103/PhysRevLett.115.231301.

O. Agertz and A. V. Kravtsov. On the Interplay between Star Formation and Feedback in Galaxy Formation Simulations. *ApJ*, 804(1):18, May 2015. doi: 10.1088/0004-637X/804/1/18.

R. Ahumada, C. A. Prieto, A. Almeida, et al. The 16th Data Release of the Sloan Digital Sky Surveys: First Release from the APOGEE-2 Southern Survey and Full Release of eBOSS Spectra. *ApJS*, 249(1):3, July 2020. doi: 10.3847/1538-4365/ab929e.

H. Aihara, C. Allende Prieto, D. An, et al. The Eighth Data Release of the Sloan Digital Sky Survey: First Data from SDSS-III. *ApJS*, 193(2):29, April 2011. doi: 10.1088/0067-0049/193/2/29.

J. T. Allen, S. M. Croom, I. S. Konstantopoulos, et al. The SAMI Galaxy Survey: Early Data Release. *MNRAS*, 446(2):1567–1583, January 2015. doi: 10.1093/mnras/stu2057.

E. Aquino-Ortíz, S. F. Sánchez, O. Valenzuela, et al. A Universal Fundamental Plane and the M_{dyn}-$M_{\star}$ Relation for Galaxies with CALIFA and MaNGA. *ApJ*, 900(2):109, September 2020a. doi: 10.3847/1538-4357/aba94e.

E. Aquino-Ortíz, S. F. Sánchez, O. Valenzuela, et al. A Universal Fundamental Plane and the M_{dyn}-$M_{\star}$ Relation for Galaxies with CALIFA and MaNGA. *ApJ*, 900(2):109, September 2020b. doi: 10.3847/1538-4357/aba94e.

M. Argudo-Fernández, S. Verley, G. Bergond, et al. Catalogues of isolated galaxies, isolated pairs, and isolated triplets in the local Universe. *A&A*, 578:A110, June 2015. doi: 10.1051/0004-6361/201526016.

N. Arora, M. Fossati, F. Fontanot, M. Hirschmann, and D. J. Wilman. On the role of supermassive black holes in quenching star formation in local central galaxies. *MNRAS*, 489(2):1606–1618, October 2019. doi: 10.1093/mnras/stz2266.

N. Arora, C. Stone, S. Courteau, and T. H. Jarrett. MaNGA galaxy properties - I. An extensive optical, mid-infrared photometric, and environmental catalogue. *MNRAS*, 505(3):3135–3156, August 2021. doi: 10.1093/mnras/stab1430.

N. Arora, A. V. Macciò, S. Courteau, et al. NIHAO-LG: the uniqueness of Local Group dwarf galaxies. *MNRAS*, 512(4):6134–6149, June 2022. doi: 10.1093/mnras/stac893.

V. Avila-Reese, P. Colín, A. González-Samaniego, et al. The Specific Star Formation Rate and Stellar Mass Fraction of Low-mass Central Galaxies in Cosmological Simulations. *ApJ*, 736(2):134, August 2011. doi: 10.1088/0004-637X/736/2/134.

R. Bacon, Y. Copin, G. Monnet, et al. The SAURON project - I. The panoramic integral-field spectrograph. *MNRAS*, 326(1):23–35, September 2001. doi: 10.1046/j.1365-8711.2001.04612.x.

I. K. Baldry, M. L. Balogh, R. G. Bower, et al. Galaxy bimodality versus stellar mass and environment. *MNRAS*, 373(2):469–483, December 2006. doi: 10.1111/j.1365-2966.2006.11081.x.

I. K. Baldry, K. Glazebrook, and S. P. Driver. On the galaxy stellar mass function, the mass-metallicity relation and the implied baryonic mass function. *MNRAS*, 388:945–959, August 2008. doi: 10.1111/j.1365-2966.2008.13348.x.

I. K. Baldry, K. Glazebrook, J. Brinkmann, et al. Quantifying the Bimodal Color-Magnitude Distribution of Galaxies. *ApJ*, 600(2):681–694, January 2004. doi: 10.1086/380092.

G. Barro, S. M. Faber, D. C. Koo, et al. Structural and Star-forming Relations since z $\sim$ 3: Connecting Compact Star-forming and Quiescent Galaxies. *ApJ*, 840(1):47, May 2017. doi: 10.3847/1538-4357/aa6b05.

P. S. Behroozi, R. H. Wechsler, and C. Conroy. The Average Star Formation Histories of Galaxies in Dark Matter Halos from z = 0-8. *ApJ*, 770(1):57, June 2013. doi: 10.1088/0004-637X/770/1/57.

A. Beifiori, S. Courteau, E. M. Corsini, and Y. Zhu. On the correlations between galaxy properties and supermassive black hole mass. *MNRAS*, 419:2497–2528, January 2012. doi: 10.1111/j.1365-2966.2011.19903.x.

F. Belfiore, R. Maiolino, K. Bundy, et al. SDSS IV MaNGA - sSFR profiles and the slow quenching of discs in green valley galaxies. *MNRAS*, 477(3):3014–3029, July 2018. doi: 10.1093/mnras/sty768.

R. Bender, D. Burstein, and S. M. Faber. Dynamically Hot Galaxies. I. Structural Properties. *ApJ*, 399:462, November 1992. doi: 10.1086/171940.

A. Benítez-Llambay, J. F. Navarro, M. G. Abadi, et al. The imprint of reionization on the star formation histories of dwarf galaxies. *MNRAS*, 450(4):4207–4220, July 2015. doi: 10.1093/mnras/stv925.

A. Benítez-Llambay, J. F. Navarro, M. G. Abadi, et al. Mergers and the outside-in formation of dwarf spheroidals. *MNRAS*, 456(2):1185–1194, February 2016. doi: 10.1093/mnras/stv2722.

A. J. Benson, R. G. Bower, C. S. Frenk, et al. What Shapes the Luminosity Function of Galaxies? *ApJ*, 599:38–49, December 2003. doi: 10.1086/379160.

M. Bernyk, D. J. Croton, C. Tonini, et al. The Theoretical Astrophysical Observatory: Cloud-based Mock Galaxy Catalogs. *The Astrophysical Journal Supplement Series*, 223:9, March 2016. doi: 10.3847/0067-0049/223/1/9.

T. Bitsakis, S. F. Sánchez, L. Ciesla, et al. The integrated properties of the CALIFA galaxies: model-derived galaxy parameters and quenching of star formation. *MNRAS*, 483:370–380, February 2019. doi: 10.1093/mnras/sty2857.

J. Bland-Hawthorn and O. Gerhard. The Galaxy in Context: Structural, Kinematic, and Integrated Properties. *ARA&A*, 54:529–596, September 2016. doi: 10.1146/annurev-astro-081915-023441.

M. Blank, A. V. Macciò, A. A. Dutton, and A. Obreja. NIHAO - XXII. Introducing black hole formation, accretion, and feedback into the NIHAO simulation suite. *MNRAS*, 487(4):5476–5489, August 2019. doi: 10.1093/mnras/stz1688.

M. Blank, L. E. Meier, A. V. Macciò, et al. NIHAO XXVI: nature versus nurture, the star formation main sequence, and the origin of its scatter. *MNRAS*, 500(1): 1414–1420, January 2021. doi: 10.1093/mnras/staa2670.

M. R. Blanton and J. Moustakas. Physical Properties and Environments of Nearby Galaxies. *ARA&A*, 47(1):159–210, September 2009. doi: 10.1146/annurev-astro-082708-101734.

M. R. Blanton and S. Roweis. K-Corrections and Filter Transformations in the Ultraviolet, Optical, and Near-Infrared. *AJ*, 133(2):734–754, February 2007. doi: 10.1086/510127.

M. R. Blanton, E. Kazin, D. Muna, B. A. Weaver, and A. Price-Whelan. Improved Background Subtraction for the Sloan Digital Sky Survey Images. *AJ*, 142(1):31, July 2011. doi: 10.1088/0004-6256/142/1/31.

A. F. L. Bluck, S. L. Ellison, D. R. Patton, et al. Why do galaxies stop forming stars? I. The passive fraction - black hole mass relation for central galaxies. *ArXiv e-prints*, dec 2014a.

A. F. L. Bluck, J. T. Mendel, S. L. Ellison, et al. Bulge mass is king: the dominant role of the bulge in determining the fraction of passive galaxies in the Sloan Digital Sky Survey. *MNRAS*, 441(1):599–629, Jun 2014b. doi: 10.1093/mnras/stu594.

A. F. L. Bluck, R. Maiolino, J. M. Piotrowska, et al. How do central and satellite galaxies quench? - Insights from spatially resolved spectroscopy in the MaNGA survey. *MNRAS*, 499(1):230–268, September 2020. doi: 10.1093/mnras/staa2806.

G. R. Blumenthal, S. M. Faber, J. R. Primack, and M. J. Rees. Formation of galaxies and large-scale structure with cold dark matter. *Nature*, 311:517–525, October 1984. doi: 10.1038/311517a0.

H. Bondi. On spherically symmetrical accretion. *MNRAS*, 112:195, January 1952. doi: 10.1093/mnras/112.2.195.

C. Bottrell and M. H. Hani. Realistic synthetic integral field spectroscopy with RealSim-IFS. *arXiv e-prints*, art. arXiv:2205.15335, May 2022.

C. Bottrell, P. Torrey, L. Simard, and S. L. Ellison. Galaxies in the Illustris simulation as seen by the Sloan Digital Sky Survey - II. Size-luminosity relations and the deficit of bulge-dominated galaxies in Illustris at low mass. *MNRAS*, 467(3):2879–2895, May 2017. doi: 10.1093/mnras/stx276.

R. G. Bower, A. J. Benson, R. Malbon, et al. Breaking the hierarchy of galaxy

formation. *MNRAS*, 370:645–655, August 2006. doi: 10.1111/j.1365-2966.2006.10519.x.

M. Boylan-Kolchin, V. Springel, S. D. M. White, A. Jenkins, and G. Lemson. Resolving cosmic structure formation with the Millennium-II Simulation. *MNRAS*, 398:1150–1164, September 2009. doi: 10.1111/j.1365-2966.2009.15191.x.

J. D. Bradford, M. C. Geha, and M. R. Blanton. A Study in Blue: The Baryon Content of Isolated Low-mass Galaxies. *ApJ*, 809(2):146, August 2015. doi: 10.1088/0004-637X/809/2/146.

J. Brinchmann, S. Charlot, S. D. M. White, et al. The physical properties of star-forming galaxies in the low-redshift Universe. *MNRAS*, 351(4):1151–1179, July 2004. doi: 10.1111/j.1365-2966.2004.07881.x.

C. B. Brook, G. Stinson, B. K. Gibson, J. Wadsley, and T. Quinn. MaGICC discs: matching observed galaxy relationships over a wide stellar mass range. *MNRAS*, 424(2):1275–1283, August 2012. doi: 10.1111/j.1365-2966.2012.21306.x.

C. B. Brook and A. Di Cintio. Signatures of dark matter halo expansion in galaxy populations. *MNRAS*, 453(2):2133–2143, October 2015. doi: 10.1093/mnras/stv1699.

T. M. Brown, J. Tumlinson, M. Geha, et al. The Primeval Populations of the Ultra-faint Dwarf Galaxies. *ApJ*, 753(1):L21, July 2012. doi: 10.1088/2041-8205/753/1/L21.

S. Brownson, A. F. L. Bluck, R. Maiolino, and G. C. Jones. What drives galaxy quenching? A deep connection between galaxy kinematics and quenching in the

local Universe. *MNRAS*, 511(2):1913–1941, April 2022. doi: 10.1093/mnras/stab3749.

G. Bruzual and S. Charlot. Stellar population synthesis at the resolution of 2003. *MNRAS*, 344(4):1000–1028, October 2003. doi: 10.1046/j.1365-8711.2003.06897.x.

T. Buck. On the origin of the chemical bimodality of disc stars: a tale of merger and migration. *MNRAS*, 491(4):5435–5446, February 2020. doi: 10.1093/mnras/stz3289.

T. Buck, A. V. Macciò, A. Obreja, et al. NIHAO XIII: Clumpy discs or clumpy light in high-redshift galaxies? *MNRAS*, 468(3):3628–3649, July 2017. doi: 10.1093/mnras/stx685.

T. Buck, A. V. Macciò, A. A. Dutton, A. Obreja, and J. Frings. NIHAO XV: the environmental impact of the host galaxy on galactic satellite and field dwarf galaxies. *MNRAS*, 483(1):1314–1341, February 2019. doi: 10.1093/mnras/sty2913.

T. Buck, A. Obreja, A. V. Macciò, et al. NIHAO-UHD: the properties of MW-like stellar discs in high-resolution cosmological simulations. *MNRAS*, 491(3):3461–3478, January 2020. doi: 10.1093/mnras/stz3241.

T. Buck, J. Rybizki, S. Buder, et al. The challenge of simultaneously matching the observed diversity of chemical abundance patterns in cosmological hydrodynamical simulations. *arXiv e-prints*, art. arXiv:2103.03884, March 2021.

K. Bundy, M. A. Bershady, D. R. Law, et al. Overview of the SDSS-IV MaNGA Survey: Mapping nearby Galaxies at Apache Point Observatory. *ApJ*, 798:7, January 2015. doi: 10.1088/0004-637X/798/1/7.

D. Burstein, R. Bender, S. Faber, and R. Nolthenius. Global Relationships Among the Physical Properties of Stellar Systems. *AJ*, 114:1365, October 1997. doi: 10.1086/118570.

P. Camps, A. U. Kapoor, A. Trcka, et al. High-resolution synthetic UV-submm images for Milky Way-mass simulated galaxies from the ARTEMIS project. *MNRAS*, 512 (2):2728–2749, May 2022. doi: 10.1093/mnras/stac719.

M. Cano-Díaz, S. F. Sánchez, S. Zibetti, et al. Spatially Resolved Star Formation Main Sequence of Galaxies in the CALIFA Survey. *ApJ*, 821:L26, April 2016. doi: 10.3847/2041-8205/821/2/L26.

M. Cappellari, E. Emsellem, D. Krajnović, et al. The ATLAS^{3D} project - VII. A new look at the morphology of nearby galaxies: the kinematic morphology-density relation. *MNRAS*, 416(3):1680–1696, September 2011. doi: 10.1111/j.1365-2966.2011.18600.x.

E. Carlesi, J. G. Sorce, Y. Hoffman, et al. Constrained Local UniversE Simulations: a Local Group factory. *MNRAS*, 458(1):900–911, May 2016. doi: 10.1093/mnras/stw357.

B. Catinella, D. Schiminovich, G. Kauffmann, et al. The GALEX Arecibo SDSS Survey - I. Gas fraction scaling relations of massive galaxies and first data release. *MNRAS*, 403(2):683–708, April 2010. doi: 10.1111/j.1365-2966.2009.16180.x.

A. Cattaneo. Feedback and its role in galaxy formation. *Nature Astronomy*, 3:896–897, September 2019. doi: 10.1038/s41550-019-0904-y.

O. Çatmabacak, R. Feldmann, D. Anglés-Alcázar, et al. Black hole-galaxy scaling relations in FIRE: the importance of black hole location and mergers. *MNRAS*, 511(1):506–535, March 2022. doi: 10.1093/mnras/stac040.

G. Chabrier. Galactic Stellar and Substellar Initial Mass Function. *PASP*, 115(809): 763–795, July 2003. doi: 10.1086/376392.

T. K. Chan, D. Kereš, J. Oñorbe, et al. The impact of baryonic physics on the structure of dark matter haloes: the view from the FIRE cosmological simulations. *MNRAS*, 454(3):2981–3001, December 2015. doi: 10.1093/mnras/stv2165.

G. Chen, H.-X. Zhang, X. Kong, et al. The Most Predictive Physical Properties for the Stellar Population Radial Profiles of Nearby Galaxies. *ApJ*, 895(2):146, June 2020a. doi: 10.3847/1538-4357/ab8cc2.

Z. Chen, S. M. Faber, D. C. Koo, et al. Quenching as a Contest between Galaxy Halos and Their Central Black Holes. *ApJ*, 897(1):102, July 2020b. doi: 10.3847/1538-4357/ab9633.

B. Cherinka, B. H. Andrews, J. Sánchez-Gallego, et al. Marvin: A Tool Kit for Streamlined Access and Visualization of the SDSS-IV MaNGA Data Set. *AJ*, 158 (2):74, Aug 2019. doi: 10.3847/1538-3881/ab2634.

C. Chiosi, M. D'Onofrio, E. Merlin, L. Piovan, and P. Marziani. The parallelism between galaxy clusters and early-type galaxies. III. The mass-radius relationship. *A&A*, 643:A136, November 2020. doi: 10.1051/0004-6361/202038773.

C. Chiosi and G. Carraro. Formation and evolution of elliptical galaxies. *MNRAS*, 335(2):335–357, September 2002. doi: 10.1046/j.1365-8711.2002.05590.x.

L. Cicuéndez and G. Battaglia. Appearances can be deceiving: clear signs of accretion in the seemingly ordinary Sextans dSph. *MNRAS*, 480(1):251–260, October 2018. doi: 10.1093/mnras/sty1748.

L. Ciotti. Stellar systems following the R1/m luminosity law. *A&A*, 249:99–106, September 1991.

M. S. Clemens, A. Bressan, B. Nikolic, et al. The star formation history of early-type galaxies as a function of mass and environment. *MNRAS*, 370(2):702–720, August 2006. doi: 10.1111/j.1365-2966.2006.10530.x.

M. E. Cluver, T. H. Jarrett, A. M. Hopkins, et al. Galaxy and Mass Assembly (GAMA): Mid-infrared Properties and Empirical Relations from WISE. *ApJ*, 782 (2):90, February 2014. doi: 10.1088/0004-637X/782/2/90.

M. E. Cluver, T. H. Jarrett, D. A. Dale, et al. Calibrating Star Formation in WISE Using Total Infrared Luminosity. *ApJ*, 850(1):68, November 2017. doi: 10.3847/1538-4357/aa92c7.

M. E. Cluver, T. H. Jarrett, E. N. Taylor, et al. Galaxy and Mass Assembly (GAMA): Demonstrating the Power of WISE in the Study of Galaxy Groups to z ¡ 0.1. *ApJ*, 898(1):20, July 2020. doi: 10.3847/1538-4357/ab9cb8.

C. Conroy and J. E. Gunn. The Propagation of Uncertainties in Stellar Population Synthesis Modeling. III. Model Calibration, Comparison, and Evaluation. *ApJ*, 712 (2):833–857, April 2010. doi: 10.1088/0004-637X/712/2/833.

C. Conroy and R. H. Wechsler. Connecting Galaxies, Halos, and Star Formation Rates

Across Cosmic Time. *ApJ*, 696:620–635, May 2009. doi: 10.1088/0004-637X/696/1/620.

J. W. Cooley and J. W. Tukey. An algorithm for the machine calculation of complex fourier series. *Mathematics of computation*, 19(90):297–301, 1965.

A. P. Cooper, L. Gao, Q. Guo, et al. Surface photometry of brightest cluster galaxies and intracluster stars in ΛCDM. *MNRAS*, 451:2703–2722, Aug 2015. doi: 10.1093/mnras/stv1042.

L. Cortese, B. Catinella, S. Boissier, A. Boselli, and S. Heinis. The effect of the environment on the H I scaling relations. *MNRAS*, 415(2):1797–1806, August 2011. doi: 10.1111/j.1365-2966.2011.18822.x.

S. Courteau. Deep r-Band Photometry for Northern Spiral Galaxies. *ApJS*, 103:363, Apr 1996. doi: 10.1086/192281.

S. Courteau. Optical Rotation Curves and Linewidths for Tully-Fisher Applications. *AJ*, 114:2402, December 1997. doi: 10.1086/118656.

S. Courteau, A. A. Dutton, F. C. van den Bosch, et al. Scaling Relations of Spiral Galaxies. *ApJ*, 671(1):203–225, December 2007. doi: 10.1086/522193.

S. Courteau, M. Cappellari, R. S. de Jong, et al. Galaxy masses. *Reviews of Modern Physics*, 86(1):47–119, January 2014. doi: 10.1103/RevModPhys.86.47.

R. A. Crain, J. Schaye, R. G. Bower, et al. The EAGLE simulations of galaxy formation: calibration of subgrid physics and model variations. *MNRAS*, 450(2):1937–1961, June 2015. doi: 10.1093/mnras/stv725.

D. J. Croton. Evolution in the black hole mass-bulge mass relation: a theoretical perspective. *MNRAS*, 369:1808–1812, July 2006. doi: 10.1111/j.1365-2966.2006.10429.x.

D. J. Croton, G. R. Farrar, P. Norberg, et al. The 2dF Galaxy Redshift Survey: luminosity functions by density environment and galaxy type. *MNRAS*, 356:1155–1167, January 2005. doi: 10.1111/j.1365-2966.2004.08546.x.

D. J. Croton, V. Springel, S. D. M. White, et al. The many lives of active galactic nuclei: cooling flows, black holes and the luminosities and colours of galaxies. *MNRAS*, 365:11–28, January 2006. doi: 10.1111/j.1365-2966.2005.09675.x.

D. J. Croton, A. R. H. Stevens, C. Tonini, et al. Semi-Analytic Galaxy Evolution (SAGE): Model Calibration and Basic Results. *ApJS*, 222(2):22, Feb 2016. doi: 10.3847/0067-0049/222/2/22.

S. Danieli, P. van Dokkum, and C. Conroy. Hunting Faint Dwarf Galaxies in the Field Using Integrated Light Surveys. *ApJ*, 856(1):69, March 2018. doi: 10.3847/1538-4357/aaadfb.

R. Davé, D. Anglés-Alcázar, D. Narayanan, et al. SIMBA: Cosmological simulations with black hole growth and feedback. *MNRAS*, 486(2):2827–2849, June 2019. doi: 10.1093/mnras/stz937.

A. de Graaff, J. Trayford, M. Franx, et al. Observed structural parameters of EAGLE galaxies: reconciling the mass-size relation in simulations with local observations. *MNRAS*, 511(2):2544–2564, April 2022. doi: 10.1093/mnras/stab3510.

G. De Lucia and J. Blaizot. The hierarchical formation of the brightest cluster galaxies. *MNRAS*, 375:2–14, February 2007. doi: 10.1111/j.1365-2966.2006.11287.x.

S. Deeley, M. J. Drinkwater, S. M. Sweet, et al. The two formation pathways of S0 galaxies. *MNRAS*, 508(1):895–911, November 2021. doi: 10.1093/mnras/stab2007.

A. Dekel and J. Silk. The Origin of Dwarf Galaxies, Cold Dark Matter, and Biased Galaxy Formation. *ApJ*, 303:39, April 1986. doi: 10.1086/164050.

A. Dekel, J. Devor, and G. Hetzroni. Galactic halo cusp-core: tidal compression in mergers. *MNRAS*, 341(1):326–342, May 2003. doi: 10.1046/j.1365-8711.2003.06432.x.

DESI Collaboration, A. Aghamousa, J. Aguilar, et al. The DESI Experiment Part I: Science,Targeting, and Survey Design. *arXiv e-prints*, art. arXiv:1611.00036, October 2016.

B. M. Devour and E. F. Bell. Circumventing the Effects of Projection and Dust Using Inclination-independent Infrared Galaxy Structure Measurements: Method, Error Analysis, and a New Public Catalog of Near-infrared Galaxy Structures. *ApJS*, 244 (1):3, September 2019. doi: 10.3847/1538-4365/ab339c.

A. Dey, D. J. Schlegel, D. Lang, et al. Overview of the DESI Legacy Imaging Surveys. *AJ*, 157(5):168, May 2019. doi: 10.3847/1538-3881/ab089d.

A. Di Cintio, R. Mostoghiu, A. Knebe, and J. F. Navarro. Pericentric passage-driven star formation in satellite galaxies and their hosts: CLUES from local group simulations. *MNRAS*, 506(1):531–545, September 2021. doi: 10.1093/mnras/stab1682.

T. Di Matteo, V. Springel, and L. Hernquist. Energy input from quasars regulates the growth and activity of black holes and their host galaxies. *Nature*, 433(7026): 604–607, Feb 2005. doi: 10.1038/nature03335.

A. E. Dolphin, D. R. Weisz, E. D. Skillman, and J. A. Holtzman. Star Formation Histories of Local Group Dwarf Galaxies. *arXiv e-prints*, art. astro-ph/0506430, June 2005.

H. Domínguez Sánchez, M. Huertas-Company, M. Bernardi, D. Tuccillo, and J. L. Fischer. Improving galaxy morphologies for SDSS with Deep Learning. *MNRAS*, 476(3):3661–3676, May 2018. doi: 10.1093/mnras/sty338.

M. D'Onofrio, C. Chiosi, M. Sciarratta, and P. Marziani. The parallelism between galaxy clusters and early-type galaxies. II. Clues on the origin of the scaling relations. *A&A*, 641:A94, September 2020. doi: 10.1051/0004-6361/202038221.

M. D'Onofrio, P. Marziani, and C. Chiosi. Past, Present and Future of the Scaling Relations of Galaxies and Active Galactic Nuclei. *Frontiers in Astronomy and Space Sciences*, 8:157, November 2021. doi: 10.3389/fspas.2021.694554.

C. J. Donzelli, H. Muriel, and J. P. Madrid. The Luminosity Profiles of Brightest Cluster Galaxies. *The Astrophysical Journal Supplement Series*, 195:15, Aug 2011. doi: 10.1088/0067-0049/195/2/15.

T. Doumler, Y. Hoffman, H. Courtois, and S. Gottlöber. Reconstructing cosmological initial conditions from galaxy peculiar velocities - I. Reverse Zeldovich Approximation. *MNRAS*, 430(2):888–901, April 2013. doi: 10.1093/mnras/sts613.

A. Dressler. Galaxy morphology in rich clusters: implications for the formation and evolution of galaxies. *ApJ*, 236:351–365, March 1980. doi: 10.1086/157753.

S. P. Driver, P. Norberg, I. K. Baldry, et al. GAMA: towards a physical understanding of galaxy formation. *Astronomy and Geophysics*, 50(5):5.12–5.19, October 2009. doi: 10.1111/j.1468-4004.2009.50512.x.

A. A. Dutton and F. C. van den Bosch. The impact of feedback on disc galaxy scaling relations. *MNRAS*, 396(1):141–164, June 2009. doi: 10.1111/j.1365-2966.2009.14742.x.

A. A. Dutton, F. C. van den Bosch, A. Dekel, and S. Courteau. A Revised Model for the Formation of Disk Galaxies: Low Spin and Dark Halo Expansion. *ApJ*, 654(1):27–52, January 2007. doi: 10.1086/509314.

A. A. Dutton, C. Conroy, F. C. van den Bosch, F. Prada, and S. More. The kinematic connection between galaxies and dark matter haloes. *MNRAS*, 407(1):2–16, September 2010. doi: 10.1111/j.1365-2966.2010.16911.x.

A. A. Dutton, C. Conroy, F. C. van den Bosch, et al. Dark halo response and the stellar initial mass function in early-type and late-type galaxies. *MNRAS*, 416(1):322–345, September 2011a. doi: 10.1111/j.1365-2966.2011.19038.x.

A. A. Dutton, F. C. van den Bosch, S. M. Faber, et al. On the evolution of the velocity-mass-size relations of disc-dominated galaxies over the past 10 billion years. *MNRAS*, 410(3):1660–1676, January 2011b. doi: 10.1111/j.1365-2966.2010.17555.x.

A. A. Dutton, A. V. Macciò, A. Dekel, et al. NIHAO IX: the role of gas inflows and outflows in driving the contraction and expansion of cold dark matter haloes. *MNRAS*, 461(3):2658–2675, September 2016. doi: 10.1093/mnras/stw1537.

A. A. Dutton, A. Obreja, L. Wang, et al. NIHAO XII: galactic uniformity in a ΛCDM universe. *MNRAS*, 467(4):4937–4950, June 2017. doi: 10.1093/mnras/stx458.

S. A. Eales, M. Baes, N. Bourne, et al. The causes of the red sequence, the blue cloud, the green valley, and the green mountain. *MNRAS*, 481(1):1183–1194, November 2018. doi: 10.1093/mnras/sty2220.

J. Einasto, E. Saar, A. Kaasik, and A. D. Chernin. Missing mass around galaxies - Morphological evidence. *Nature*, 252:111–113, November 1974. doi: 10.1038/252111a0.

K. El-Badry, A. Wetzel, M. Geha, et al. Breathing FIRE: How Stellar Feedback Drives Radial Migration, Rapid Size Fluctuations, and Population Gradients in Low-mass Galaxies. *ApJ*, 820(2):131, April 2016. doi: 10.3847/0004-637X/820/2/131.

A. Elagali, C. D. P. Lagos, O. I. Wong, et al. Ring galaxies in the EAGLE hydrodynamical simulations. *MNRAS*, 481(3):2951–2969, December 2018. doi: 10.1093/mnras/sty2462.

S. L. Ellison, S. F. Sánchez, H. Ibarra-Medel, et al. Star formation is boosted (and quenched) from the inside-out: radial star formation profiles from MaNGA. *MNRAS*, 474(2):2039–2054, February 2018. doi: 10.1093/mnras/stx2882.

P. Erwin. IMFIT: A Fast, Flexible New Program for Astronomical Image Fitting. *ApJ*, 799(2):226, February 2015. doi: 10.1088/0004-637X/799/2/226.

I. Escala, A. Wetzel, E. N. Kirby, et al. Modelling chemical abundance distributions for dwarf galaxies in the Local Group: the impact of turbulent metal diffusion. *MNRAS*, 474(2):2194–2211, February 2018. doi: 10.1093/mnras/stx2858.

J. Etherington and D. Thomas. Measuring galaxy environments in large-scale photometric surveys. *MNRAS*, 451(1):660–679, July 2015. doi: 10.1093/mnras/stv999.

S. M. Faber and R. E. Jackson. Velocity dispersions and mass-to-light ratios for elliptical galaxies. *ApJ*, 204:668–683, March 1976a. doi: 10.1086/154215.

S. M. Faber and R. E. Jackson. Velocity dispersions and mass-to-light ratios for elliptical galaxies. *ApJ*, 204:668–683, March 1976b. doi: 10.1086/154215.

A. C. Fabian. Cooling Flows in Clusters of Galaxies. *ARA&A*, 32:277–318, Jan 1994. doi: 10.1146/annurev.aa.32.090194.001425.

A. C. Fabian. Observational Evidence of Active Galactic Nuclei Feedback. *ARA&A*, 50:455–489, Sep 2012. doi: 10.1146/annurev-astro-081811-125521.

J. J. Fang, S. M. Faber, D. C. Koo, and A. Dekel. A Link between Star Formation Quenching and Inner Stellar Mass Density in Sloan Digital Sky Survey Central Galaxies. *ApJ*, 776(1):63, October 2013. doi: 10.1088/0004-637X/776/1/63.

N. Fanidakis, C. M. Baugh, A. J. Benson, et al. Grand unification of AGN activity in the ΛCDM cosmology. *MNRAS*, 410(1):53–74, Jan 2011. doi: 10.1111/j.1365-2966.2010.17427.x.

L. Ferrarese, F. C. van den Bosch, H. C. Ford, W. Jaffe, and R. W. O'Connell. Hubble Space Telescope Photometry of the Central Regions of Virgo Cluster Elliptical

Galaxies. III. Brightness Profiles. *AJ*, 108:1598, November 1994. doi: 10.1086/117180.

L. Ferrarese and D. Merritt. A Fundamental Relation between Supermassive Black Holes and Their Host Galaxies. *ApJ*, 539:L9–L12, August 2000. doi: 10.1086/312838.

S. P. Fillingham, M. C. Cooper, A. B. Pace, et al. Under pressure: quenching star formation in low-mass satellite galaxies via stripping. *MNRAS*, 463(2):1916–1928, December 2016. doi: 10.1093/mnras/stw2131.

J.-L. Fischer, H. Domínguez Sánchez, and M. Bernardi. SDSS-IV MaNGA PyMorph Photometric and Deep Learning Morphological Catalogues and implications for bulge properties and stellar angular momentum. *MNRAS*, 483:2057–2077, February 2019. doi: 10.1093/mnras/sty3135.

F. Fontanot, P. Monaco, S. Cristiani, and P. Tozzi. The effect of stellar feedback and quasar winds on the active galactic nucleus population. *MNRAS*, 373(3):1173–1187, Dec 2006. doi: 10.1111/j.1365-2966.2006.11094.x.

F. Fontanot, A. Pasquali, G. De Lucia, et al. The dependence of AGN activity on stellar and halo mass in semi-analytic models. *MNRAS*, 413(2):957–970, May 2011. doi: 10.1111/j.1365-2966.2010.18186.x.

F. Fontanot, P. Monaco, and F. Shankar. Interpreting the possible break in the black hole-bulge mass relation. *MNRAS*, 453(4):4112–4120, Nov 2015. doi: 10.1093/mnras/stv1930.

M. Fossati, D. J. Wilman, F. Fontanot, et al. The definition of environment and its relation to the quenching of galaxies at z = 1-2 in a hierarchical Universe. *MNRAS*, 446(3):2582–2598, January 2015. doi: 10.1093/mnras/stu2255.

M. Fossati, D. J. Wilman, J. T. Mendel, et al. Galaxy Environment in the 3D-HST Fields: Witnessing the Onset of Satellite Quenching at z 1-2. *ApJ*, 835(2):153, Feb 2017. doi: 10.3847/1538-4357/835/2/153.

M. Franx, P. G. van Dokkum, N. M. Förster Schreiber, et al. Structure and Star Formation in Galaxies out to z = 3: Evidence for Surface Density Dependent Evolution and Upsizing. *ApJ*, 688(2):770–788, December 2008. doi: 10.1086/592431.

M. Frosst, S. Courteau, N. Arora, et al. The diversity of spiral galaxies explained. *arXiv e-prints*, art. arXiv:2204.02412, April 2022.

J. M. Gabor, R. Davé, K. Finlator, and B. D. Oppenheimer. How is star formation quenched in massive galaxies? *MNRAS*, 407(2):749–771, Sep 2010. doi: 10.1111/j.1365-2966.2010.16961.x.

C. Gallart, M. Monelli, L. Mayer, et al. The ACS LCID Project: On the Origin of Dwarf Galaxy Types—A Manifestation of the Halo Assembly Bias? *ApJ*, 811(2):L18, October 2015. doi: 10.1088/2041-8205/811/2/L18.

A. Gallazzi, S. Charlot, J. Brinchmann, S. D. M. White, and C. A. Tremonti. The ages and metallicities of galaxies in the local universe. *MNRAS*, 362(1):41–58, September 2005. doi: 10.1111/j.1365-2966.2005.09321.x.

R. García-Benito, R. M. González Delgado, E. Pérez, et al. Spatially resolved mass-to-light from the CALIFA survey. Mass-to-light ratio vs. color relations. *A&A*, 621: A120, January 2019. doi: 10.1051/0004-6361/201833993.

S. Garrison-Kimmel, A. Wetzel, P. F. Hopkins, et al. Star formation histories of dwarf galaxies in the FIRE simulations: dependence on mass and Local Group environment. *MNRAS*, 489(4):4574–4588, November 2019. doi: 10.1093/mnras/stz2507.

K. Gebhardt, D. Richstone, E. A. Ajhar, et al. The Centers of Early-Type Galaxies With HST. III. Non-Parametric Recovery of Stellar Luminosity Distribution. *AJ*, 112:105, July 1996. doi: 10.1086/117992.

A. Genina, C. S. Frenk, A. r. Benítez-Llambay, et al. The distinct stellar metallicity populations of simulated Local Group dwarfs. *MNRAS*, 488(2):2312–2331, September 2019. doi: 10.1093/mnras/stz1852.

C. Gilhuly and S. Courteau. An extensive photometric catalogue of CALIFA galaxies. *MNRAS*, 477:845–862, June 2018. doi: 10.1093/mnras/sty756.

R. Giovanelli, M. P. Haynes, J. J. Salzer, et al. Extinction in SC Galaxies. *AJ*, 107: 2036, June 1994. doi: 10.1086/117014.

R. M. González Delgado, R. Cid Fernandes, E. Pérez, et al. Star formation along the Hubble sequence. Radial structure of the star formation of CALIFA galaxies. *A&A*, 590:A44, May 2016. doi: 10.1051/0004-6361/201628174.

A. González-Samaniego, J. S. Bullock, M. Boylan-Kolchin, et al. Dwarf galaxy mass

estimators versus cosmological simulations. *MNRAS*, 472(4):4786–4796, December 2017. doi: 10.1093/mnras/stx2322.

S. Gottloeber, Y. Hoffman, and G. Yepes. Constrained Local UniversE Simulations (CLUES). *arXiv e-prints*, art. arXiv:1005.2687, May 2010a.

S. Gottloeber, Y. Hoffman, and G. Yepes. Constrained Local UniversE Simulations (CLUES). *arXiv e-prints*, art. arXiv:1005.2687, May 2010b.

A. W. Graham and R. Guzmán. HST Photometry of Dwarf Elliptical Galaxies in Coma, and an Explanation for the Alleged Structural Dichotomy between Dwarf and Bright Elliptical Galaxies. *AJ*, 125(6):2936–2950, June 2003. doi: 10.1086/374992.

A. W. Graham and N. Scott. The M $_{BH}$-L $_{spheroid}$ Relation at High and Low Masses, the Quadratic Growth of Black Holes, and Intermediate-mass Black Hole Candidates. *ApJ*, 764(2):151, Feb 2013. doi: 10.1088/0004-637X/764/2/151.

A. W. Graham, I. Trujillo, and N. Caon. Galaxy Light Concentration. I. Index Stability and the Connection with Galaxy Structure, Dynamics, and Supermassive Black Holes. *AJ*, 122(4):1707–1717, October 2001. doi: 10.1086/323090.

M. T. Graham, M. Cappellari, H. Li, et al. SDSS-IV MaNGA: stellar angular momentum of about 2300 galaxies: unveiling the bimodality of massive galaxy properties. *MNRAS*, 477:4711–4737, July 2018. doi: 10.1093/mnras/sty504.

J. Grcevich and M. E. Putman. H I in Local Group Dwarf Galaxies and Stripping by the Galactic Halo. *ApJ*, 696(1):385–395, May 2009. doi: 10.1088/0004-637X/696/1/385.

M. Gu, C. Conroy, and P. Behroozi. Hierarchical Galaxy Growth and Scatter in the Stellar Mass-Halo Mass Relation. *ApJ*, 833(1):2, Dec 2016. doi: 10.3847/0004-637X/833/1/2.

J. E. Gunn and I. Gott, J. Richard. On the Infall of Matter Into Clusters of Galaxies and Some Effects on Their Evolution. *ApJ*, 176:1, August 1972. doi: 10.1086/151605.

Q. Guo, S. White, M. Boylan-Kolchin, et al. From dwarf spheroidals to cD galaxies: simulating the galaxy population in a ΛCDM cosmology. *MNRAS*, 413:101–131, May 2011. doi: 10.1111/j.1365-2966.2010.18114.x.

Q. Guo, S. White, R. E. Angulo, et al. Galaxy formation in WMAP1 and WMAP7 cosmologies. *MNRAS*, 428(2):1351–1365, Jan 2013a. doi: 10.1093/mnras/sts115.

Y. Guo, H. C. Ferguson, M. Giavalisco, et al. CANDELS Multi-wavelength Catalogs: Source Detection and Photometry in the GOODS-South Field. *ApJS*, 207(2):24, August 2013b. doi: 10.1088/0067-0049/207/2/24.

M. Habouzit, M. Volonteri, R. S. Somerville, et al. The diverse galaxy counts in the environment of high-redshift massive black holes in Horizon-AGN. *MNRAS*, 489 (1):1206–1229, October 2019. doi: 10.1093/mnras/stz2105.

C. Hall, S. Courteau, T. Jarrett, et al. Unique Tracks Drive the Scatter of the Spatially Resolved Star Formation Main Sequence. *ApJ*, 865(2):154, October 2018. doi: 10.3847/1538-4357/aadee1.

M. Hall, S. Courteau, A. A. Dutton, M. McDonald, and Y. Zhu. An investigation of Sloan Digital Sky Survey imaging data and multiband scaling relations of spiral

galaxies. *MNRAS*, 425(4):2741–2765, Oct 2012. doi: 10.1111/j.1365-2966.2012.21290.x.

N. Häring and H.-W. Rix. On the Black Hole Mass-Bulge Mass Relation. *ApJ*, 604 (2):L89–L92, Apr 2004. doi: 10.1086/383567.

M. P. Haynes, R. Giovanelli, A. M. Martin, et al. The Arecibo Legacy Fast ALFA Survey: The α.40 H I Source Catalog, Its Characteristics and Their Impact on the Derivation of the H I Mass Function. *AJ*, 142(5):170, November 2011. doi: 10.1088/0004-6256/142/5/170.

B. M. B. Henriques, S. D. M. White, P. A. Thomas, et al. Simulations of the galaxy population constrained by observations from z = 3 to the present day: implications for galactic winds and the fate of their ejecta. *MNRAS*, 431:3373–3395, June 2013. doi: 10.1093/mnras/stt415.

B. M. B. Henriques, S. D. M. White, P. A. Thomas, et al. Galaxy formation in the Planck cosmology - I. Matching the observed evolution of star formation rates, colours and stellar masses. *MNRAS*, 451(3):2663–2680, August 2015a. doi: 10.1093/mnras/stv705.

B. M. B. Henriques, S. D. M. White, P. A. Thomas, et al. Galaxy formation in the Planck cosmology - I. Matching the observed evolution of star formation rates, colours and stellar masses. *MNRAS*, 451(3):2663–2680, Aug 2015b. doi: 10.1093/mnras/stv705.

L. Hernquist. An Analytical Model for Spherical Galaxies and Bulges. *ApJ*, 356:359, June 1990. doi: 10.1086/168845.

J. A. Hester. Ram Pressure Stripping in Clusters and Groups. *ApJ*, 647(2):910–921, August 2006. doi: 10.1086/505614.

M. Hirschmann, G. De Lucia, D. Wilman, et al. The influence of the environmental history on quenching star formation in a Λ cold dark matter universe. *MNRAS*, 444(3):2938–2959, Nov 2014. doi: 10.1093/mnras/stu1609.

M. Hirschmann, G. De Lucia, and F. Fontanot. Galaxy assembly, stellar feedback and metal enrichment: the view from the GAEA model. *MNRAS*, 461(2):1760–1785, Sep 2016. doi: 10.1093/mnras/stw1318.

Y. Hoffman. *Gaussian Fields and Constrained Simulations of the Large-Scale Structure*, volume 665, pages 565–583. 2009. doi: 10.1007/978-3-540-44767-2_17.

Y. Hoffman and E. Ribak. Constrained Realizations of Gaussian Fields: A Simple Algorithm. *ApJ*, 380:L5, October 1991. doi: 10.1086/186160.

M. T. Hogan, B. R. McNamara, F. A. Pulido, et al. The Onset of Thermally Unstable Cooling from the Hot Atmospheres of Giant Galaxies in Clusters: Constraints on Feedback Models. *ApJ*, 851(1):66, Dec 2017. doi: 10.3847/1538-4357/aa9af3.

D. W. Hogg and SDSS Collaboration. The overdensities of galaxy environments as a function of luminosity and color. In *American Astronomical Society Meeting Abstracts #202*, volume 202 of *American Astronomical Society Meeting Abstracts*, page 51.03, May 2003.

E. Holmberg. A photographic photometry of extragalactic nebulae. *Meddelanden fran Lunds Astronomiska Observatorium Serie II*, 136:1, January 1958.

P. F. Hopkins, A. Wetzel, D. Kereš, et al. FIRE-2 simulations: physics versus numerics in galaxy formation. *MNRAS*, 480(1):800–863, October 2018. doi: 10.1093/mnras/sty1690.

S. Huang, M. P. Haynes, R. Giovanelli, and J. Brinchmann. The Arecibo Legacy Fast ALFA Survey: The Galaxy Population Detected by ALFALFA. *ApJ*, 756:113, September 2012. doi: 10.1088/0004-637X/756/2/113.

M. Huertas-Company, S. Mei, F. Shankar, et al. The evolution of the mass-size relation for early-type galaxies from z $\sim$ 1 to the present: dependence on environment, mass range and detailed morphology. *MNRAS*, 428(2):1715–1742, January 2013. doi: 10.1093/mnras/sts150.

K. Jahnke and A. V. Macciò. The Non-causal Origin of the Black-hole-galaxy Scaling Relations. *ApJ*, 734(2):92, Jun 2011. doi: 10.1088/0004-637X/734/2/92.

T. H. Jarrett, T. Chester, R. Cutri, et al. 2MASS Extended Source Catalog: Overview and Algorithms. *AJ*, 119(5):2498–2531, May 2000. doi: 10.1086/301330.

T. H. Jarrett, F. Masci, C. W. Tsai, et al. Constructing a WISE High Resolution Galaxy Atlas. *AJ*, 144(2):68, August 2012. doi: 10.1088/0004-6256/144/2/68.

T. H. Jarrett, F. Masci, C. W. Tsai, et al. Extending the Nearby Galaxy Heritage with WISE: First Results from the WISE Enhanced Resolution Galaxy Atlas. *AJ*, 145(1):6, January 2013. doi: 10.1088/0004-6256/145/1/6.

T. H. Jarrett, M. E. Cluver, M. J. I. Brown, et al. The WISE Extended Source Catalog (WXSC). I. The 100 Largest Galaxies. *ApJS*, 245(2):25, December 2019. doi: 10.3847/1538-4365/ab521a.

G. Kauffmann, S. D. M. White, T. M. Heckman, et al. The environmental dependence of the relations between stellar mass, structure, star formation and nuclear activity in galaxies. *MNRAS*, 353:713–731, September 2004a. doi: 10.1111/j.1365-2966.2004.08117.x.

G. Kauffmann and M. Haehnelt. A unified model for the evolution of galaxies and quasars. *MNRAS*, 311(3):576–588, Jan 2000. doi: 10.1046/j.1365-8711.2000.03077.x.

G. Kauffmann, T. M. Heckman, S. D. M. White, et al. The dependence of star formation history and internal structure on stellar mass for 10^5 low-redshift galaxies. *MNRAS*, 341(1):54–69, May 2003. doi: 10.1046/j.1365-8711.2003.06292.x.

G. Kauffmann, S. D. M. White, T. M. Heckman, et al. The environmental dependence of the relations between stellar mass, structure, star formation and nuclear activity in galaxies. *MNRAS*, 353(3):713–731, September 2004b. doi: 10.1111/j.1365-2966.2004.08117.x.

D. Kawata and J. S. Mulchaey. Strangulation in Galaxy Groups. *ApJ*, 672(2):L103, January 2008. doi: 10.1086/526544.

D. Kawata, B. K. Gibson, D. J. Barnes, R. J. J. Grand, and A. Rahimi. Numerical simulations of bubble-induced star formation in dwarf irregular galaxies with a novel stellar feedback scheme. *MNRAS*, 438(2):1208–1222, February 2014. doi: 10.1093/mnras/stt2267.

J. Kennicutt, Robert C. The Star Formation Law in Galactic Disks. *ApJ*, 344:685, September 1989. doi: 10.1086/167834.

J. Kennicutt, Robert C. The Global Schmidt Law in Star-forming Galaxies. *ApJ*, 498(2):541–552, May 1998. doi: 10.1086/305588.

A. King and K. Pounds. Powerful Outflows and Feedback from Active Galactic Nuclei. *ARA&A*, 53:115–154, August 2015. doi: 10.1146/annurev-astro-082214-122316.

I. R. King and R. Minkowski. Some Properties of Elliptical Galaxies. *ApJ*, 143:1002, March 1966. doi: 10.1086/148580.

E. N. Kirby, J. G. Cohen, P. Guhathakurta, et al. The Universal Stellar Mass-Stellar Metallicity Relation for Dwarf Galaxies. *ApJ*, 779(2):102, December 2013. doi: 10.1088/0004-637X/779/2/102.

A. A. Klypin, S. Trujillo-Gomez, and J. Primack. Dark Matter Halos in the Standard Cosmological Model: Results from the Bolshoi Simulation. *ApJ*, 740(2):102, October 2011. doi: 10.1088/0004-637X/740/2/102.

A. Knebe, D. Stoppacher, F. Prada, et al. MULTIDARK-GALAXIES: data release and first results. *MNRAS*, 474(4):5206–5231, Mar 2018. doi: 10.1093/mnras/stx2662.

E. W. Koch, C. G. Ward, S. Offner, J. L. Loeppky, and E. W. Rosolowsky. Identifying tools for comparing simulations and observations of spectral-line data cubes. *MNRAS*, 471(2):1506–1530, October 2017. doi: 10.1093/mnras/stx1671.

J. Kormendy and L. C. Ho. Coevolution (Or Not) of Supermassive Black Holes and Host Galaxies. *ARA&A*, 51(1):511–653, Aug 2013a. doi: 10.1146/annurev-astro-082708-101811.

J. Kormendy and L. C. Ho. Coevolution (Or Not) of Supermassive Black Holes and Host Galaxies. *ARA&A*, 51(1):511–653, August 2013b. doi: 10.1146/annurev-astro-082708-101811.

J. Kormendy and D. B. Sanders. Ultraluminous IRAS Galaxies: Formation of Elliptical Galaxies by Merger-induced Dissipative Collapse. *ApJ*, 390:L53, May 1992. doi: 10.1086/186370.

A. V. Kravtsov, A. A. Vikhlinin, and A. V. Meshcheryakov. Stellar Mass-Halo Mass Relation and Star Formation Efficiency in High-Mass Halos. *Astronomy Letters*, 44(1):8–34, January 2018. doi: 10.1134/S1063773717120015.

R. Lange, S. P. Driver, A. S. G. Robotham, et al. Galaxy And Mass Assembly (GAMA): mass-size relations of z ¡ 0.1 galaxies subdivided by Sérsic index, colour and morphology. *MNRAS*, 447(3):2603–2630, March 2015. doi: 10.1093/mnras/stu2467.

A. Lapi, P. Salucci, and L. Danese. Precision Scaling Relations for Disk Galaxies in the Local Universe. *ApJ*, 859(1):2, May 2018. doi: 10.3847/1538-4357/aabf35.

T. R. Lauer, E. A. Ajhar, Y. I. Byun, et al. The Centers of Early-Type Galaxies with HST.I.An Observational Survey. *AJ*, 110:2622, December 1995. doi: 10.1086/117719.

F. Lelli, S. S. McGaugh, J. M. Schombert, and M. S. Pawlowski. One Law to Rule Them All: The Radial Acceleration Relation of Galaxies. *ApJ*, 836(2):152, February 2017. doi: 10.3847/1538-4357/836/2/152.

A. K. Leroy, F. Walter, E. Brinks, et al. The Star Formation Efficiency in Nearby Galaxies: Measuring Where Gas Forms Stars Effectively. *AJ*, 136(6):2782–2845, December 2008. doi: 10.1088/0004-6256/136/6/2782.

J. H. Lian, J. R. Li, W. Yan, and X. Kong. The mass-metallicity relation of Lyman-break analogues and its dependence on galaxy properties. *MNRAS*, 446(2):1449–1457, January 2015. doi: 10.1093/mnras/stu2184.

N. I. Libeskind, E. Carlesi, R. J. J. Grand, et al. The HESTIA project: simulations of the Local Group. *MNRAS*, 498(2):2968–2983, October 2020. doi: 10.1093/mnras/staa2541.

L. A. MacArthur, S. Courteau, E. Bell, and J. A. Holtzman. Structure of Disk-dominated Galaxies. II. Color Gradients and Stellar Population Models. *ApJS*, 152 (2):175–199, June 2004. doi: 10.1086/383525.

A. V. Macciò, G. Stinson, C. B. Brook, et al. Halo Expansion in Cosmological Hydro Simulations: Toward a Baryonic Solution of the Cusp/Core Problem in Massive Spirals. *ApJ*, 744(1):L9, January 2012. doi: 10.1088/2041-8205/744/1/L9.

A. V. Macciò, S. M. Udrescu, A. A. Dutton, et al. NIHAO X: reconciling the local galaxy velocity function with cold dark matter via mock H I observations. *MNRAS*, 463(1):L69–L73, November 2016. doi: 10.1093/mnrasl/slw147.

A. V. Macciò, J. Frings, T. Buck, et al. The edge of galaxy formation - I. Formation and evolution of MW-satellite analogues before accretion. *MNRAS*, 472(2):2356–2366, December 2017. doi: 10.1093/mnras/stx2048.

A. V. Macciò, J. Frings, T. Buck, et al. The edge of galaxy formation III: the effects of warm dark matter on Milky Way satellites and field dwarfs. *MNRAS*, 484(4): 5400–5408, April 2019. doi: 10.1093/mnras/stz327.

A. H. Maller, A. A. Berlind, M. R. Blanton, and D. W. Hogg. The Intrinsic Properties of SDSS Galaxies. *ApJ*, 691(1):394–406, January 2009. doi: 10.1088/0004-637X/691/1/394.

M. Martig, F. Bournaud, R. Teyssier, and A. Dekel. Morphological Quenching of Star Formation: Making Early-Type Galaxies Red. *ApJ*, 707:250–267, December 2009. doi: 10.1088/0004-637X/707/1/250.

F. Marulli, S. Bonoli, E. Branchini, L. Moscardini, and V. Springel. Modelling the cosmological co-evolution of supermassive black holes and galaxies - I. BH scaling relations and the AGN luminosity function. *MNRAS*, 385(4):1846–1858, Apr 2008. doi: 10.1111/j.1365-2966.2008.12988.x.

K. L. Masters, R. Nichol, S. Bamford, et al. Galaxy Zoo: dust in spiral galaxies. *MNRAS*, 404(2):792–810, May 2010. doi: 10.1111/j.1365-2966.2010.16335.x.

K. L. Masters, D. V. Stark, Z. J. Pace, et al. H I-MaNGA: H I follow-up for the MaNGA survey. *MNRAS*, 488(3):3396–3405, September 2019. doi: 10.1093/mnras/stz1889.

M. L. Mateo. Dwarf Galaxies of the Local Group. *ARA&A*, 36:435–506, January 1998. doi: 10.1146/annurev.astro.36.1.435.

J. Matthee, J. Schaye, R. A. Crain, et al. The origin of scatter in the stellar mass-halo mass relation of central galaxies in the EAGLE simulation. *MNRAS*, 465(2): 2381–2396, Feb 2017. doi: 10.1093/mnras/stw2884.

I. G. McCarthy, J. Schaye, A. S. Font, et al. Rotation rates, sizes and star formation efficiencies of a representative population of simulated disc galaxies. *MNRAS*, 427 (1):379–392, November 2012. doi: 10.1111/j.1365-2966.2012.21951.x.

A. W. McConnachie. The Observed Properties of Dwarf Galaxies in and around the Local Group. *AJ*, 144(1):4, July 2012. doi: 10.1088/0004-6256/144/1/4.

N. J. McConnell and C.-P. Ma. Revisiting the Scaling Relations of Black Hole Masses and Host Galaxy Properties. *ApJ*, 764(2):184, Feb 2013. doi: 10.1088/0004-637X/764/2/184.

M. McDonald, S. Courteau, and R. B. Tully. Bulge-disc decompositions and structural bimodality of Ursa Major cluster spiral galaxies. *MNRAS*, 393(2):628–640, February 2009. doi: 10.1111/j.1365-2966.2008.14239.x.

M. McDonald, S. Courteau, R. B. Tully, and J. Roediger. A survey of 286 Virgo cluster galaxies at optical griz and near-IR H band: surface brightness profiles and bulge-disc decompositions. *MNRAS*, 414(3):2055–2068, Jul 2011. doi: 10.1111/j.1365-2966.2011.18519.x.

S. S. McGaugh. The Baryonic Tully-Fisher Relation of Galaxies with Extended Rotation Curves and the Stellar Mass of Rotating Galaxies. *ApJ*, 632(2):859–871, October 2005. doi: 10.1086/432968.

S. S. McGaugh. The Baryonic Tully-Fisher Relation of Gas-rich Galaxies as a Test of ΛCDM and MOND. *AJ*, 143(2):40, February 2012. doi: 10.1088/0004-6256/143/2/40.

K. B. W. McQuinn, E. A. K. Adams, J. M. Cannon, et al. The Turn-Down of the Baryonic Tully-Fisher Relation at Low Galaxy Masses. *arXiv e-prints*, art. arXiv:2203.10105, March 2022.

A. J. Mendez, A. L. Coil, J. Lotz, et al. AEGIS: The Morphologies of Green Galaxies at 0.4 ¡ z ¡ 1.2. *ApJ*, 736(2):110, August 2011. doi: 10.1088/0004-637X/736/2/110.

J. Méndez-Abreu, J. A. L. Aguerri, J. Falcón-Barroso, et al. Morpho-kinematic properties of field S0 bulges in the CALIFA survey. *MNRAS*, 474:1307–1334, February 2018. doi: 10.1093/mnras/stx2804.

H. J. Mo, S. Mao, and S. D. M. White. The formation of galactic discs. *MNRAS*, 295(2):319–336, April 1998. doi: 10.1046/j.1365-8711.1998.01227.x.

H. Mo, F. C. van den Bosch, and S. White. *Galaxy Formation and Evolution*. 2010.

M. Molina, N. Ajgaonkar, R. Yan, et al. Swift/UVOT+MaNGA (SwiM) Value-added Catalog. *arXiv e-prints*, art. arXiv:2007.08541, July 2020.

P. Monaco, F. Fontanot, and G. Taffoni. The MORGANA model for the rise of galaxies and active nuclei. *MNRAS*, 375(4):1189–1219, Mar 2007. doi: 10.1111/j.1365-2966.2006.11253.x.

B. P. Moster, A. V. Macciò, and R. S. Somerville. Numerical hydrodynamic simulations based on semi-analytic galaxy merger trees: method and Milky Way-like galaxies. *MNRAS*, 437(2):1027–1044, January 2014. doi: 10.1093/mnras/stt1702.

A. Muzzin, D. Marchesini, M. Stefanon, et al. The Evolution of the Stellar Mass Functions of Star-forming and Quiescent Galaxies to z = 4 from the COSMOS/UltraVISTA Survey. *ApJ*, 777(1):18, November 2013. doi: 10.1088/0004-637X/777/1/18.

D. Nelson, A. Pillepich, V. Springel, et al. First results from the IllustrisTNG simulations: the galaxy colour bimodality. *MNRAS*, 475(1):624–647, March 2018. doi: 10.1093/mnras/stx3040.

A. Obreja, G. S. Stinson, A. A. Dutton, et al. NIHAO VI. The hidden discs of simulated galaxies. *MNRAS*, 459(1):467–486, June 2016. doi: 10.1093/mnras/stw690.

A. Obreja, A. A. Dutton, A. V. Macciò, et al. NIHAO XVI: the properties and evolution of kinematically selected discs, bulges, and stellar haloes. *MNRAS*, 487 (3):4424–4456, August 2019. doi: 10.1093/mnras/stz1563.

D. Obreschkow and K. Glazebrook. Fundamental Mass-Spin-Morphology Relation Of Spiral Galaxies. *ApJ*, 784(1):26, March 2014. doi: 10.1088/0004-637X/784/1/26.

S.-H. Oh, D. A. Hunter, E. Brinks, et al. High-resolution Mass Models of Dwarf Galaxies from LITTLE THINGS. *AJ*, 149(6):180, June 2015. doi: 10.1088/0004-6256/149/6/180.

S. Okamoto, N. Arimoto, Y. Yamada, and M. Onodera. Stellar Populations and Structural Properties of Ultra Faint Dwarf Galaxies, Canes Venatici I, Boötes I, Canes Venatici II, and Leo IV. *ApJ*, 744(2):96, January 2012. doi: 10.1088/0004-637X/744/2/96.

K. A. Oman, J. F. Navarro, A. Fattahi, et al. The unexpected diversity of dwarf galaxy rotation curves. *MNRAS*, 452(4):3650–3665, October 2015. doi: 10.1093/mnras/stv1504.

K. A. Oman, A. Marasco, J. F. Navarro, et al. Non-circular motions and the diversity of dwarf galaxy rotation curves. *MNRAS*, 482(1):821–847, January 2019. doi: 10.1093/mnras/sty2687.

N. N. Q. Ouellette, S. Courteau, J. A. Holtzman, et al. The Spectroscopy and H-band Imaging of Virgo Cluster Galaxies (SHIVir) Survey: Scaling Relations and the Stellar-to-total Mass Relation. *ApJ*, 843(1):74, July 2017. doi: 10.3847/1538-4357/aa74b1.

Z. J. Pace, C. Tremonti, Y. Chen, et al. Resolved and Integrated Stellar Masses in the SDSS-IV/MaNGA Survey. II. Applications of PCA-based Stellar Mass Estimates. *ApJ*, 883(1):83, September 2019. doi: 10.3847/1538-4357/ab3726.

V. Pandya, R. Brennan, R. S. Somerville, et al. The nature of massive transition galaxies in CANDELS, GAMA and cosmological simulations. *MNRAS*, 472(2):2054–2084, December 2017. doi: 10.1093/mnras/stx2027.

M. S. Peeples, J. K. Werk, J. Tumlinson, et al. A Budget and Accounting of Metals at z ~0: Results from the COS-Halos Survey. *ApJ*, 786(1):54, May 2014. doi: 10.1088/0004-637X/786/1/54.

Y.-j. Peng, S. J. Lilly, K. Kovač, et al. Mass and Environment as Drivers of Galaxy Evolution in SDSS and zCOSMOS and the Origin of the Schechter Function. *ApJ*, 721(1):193–221, Sep 2010. doi: 10.1088/0004-637X/721/1/193.

Y.-j. Peng, S. J. Lilly, A. Renzini, and M. Carollo. Mass and Environment as Drivers of Galaxy Evolution. II. The Quenching of Satellite Galaxies as the Origin of Environmental Effects. *ApJ*, 757(1):4, September 2012. doi: 10.1088/0004-637X/757/1/4.

K. Pilkington, B. K. Gibson, C. B. Brook, et al. The distribution of metals in cosmological hydrodynamical simulations of dwarf disc galaxies. *MNRAS*, 425(2): 969–978, September 2012. doi: 10.1111/j.1365-2966.2012.21353.x.

A. Pillepich, D. Nelson, L. Hernquist, et al. First results from the IllustrisTNG simulations: the stellar mass content of groups and clusters of galaxies. *MNRAS*, 475(1):648–675, March 2018. doi: 10.1093/mnras/stx3112.

J. Pizagno, F. Prada, D. H. Weinberg, et al. Dark Matter and Stellar Mass in the Luminous Regions of Disk Galaxies. *ApJ*, 633(2):844–856, November 2005. doi: 10.1086/491614.

Planck Collaboration, P. A. R. Ade, N. Aghanim, et al. Planck 2013 results. XVI. Cosmological parameters. *A&A*, 571:A16, November 2014. doi: 10.1051/0004-6361/201321591.

M. E. Putman, Y. Zheng, A. M. Price-Whelan, et al. The Gas Content and Stripping of Local Group Dwarf Galaxies. *ApJ*, 913(1):53, May 2021. doi: 10.3847/1538-4357/abe391.

M. H. Quenouille. On a method of trend elimination. 36(1/2):75–91, June 1949. ISSN 0006-3444 (print), 1464-3510 (electronic). doi: https://doi.org/10.2307/2332532. URL http://www.jstor.org/stable/2332532.

R.-S. Remus, K. Dolag, T. Naab, et al. The co-evolution of total density profiles and central dark matter fractions in simulated early-type galaxies. *MNRAS*, 464(3): 3742–3756, January 2017. doi: 10.1093/mnras/stw2594.

A. Renzini. Stellar Population Diagnostics of Elliptical Galaxy Formation. *ARA&A*, 44(1):141–192, September 2006. doi: 10.1146/annurev.astro.44.051905.092450.

B. W. Ritchie and P. A. Thomas. Multiphase smoothed-particle hydrodynamics. *MNRAS*, 323(3):743–756, May 2001. doi: 10.1046/j.1365-8711.2001.04268.x.

M. Rodríguez-Baras, A. I. Díaz, F. F. Rosales-Ortega, and S. F. Sánchez. Inner and outer star forming regions over the disks of spiral galaxies. I. Sample characterization. *A&A*, 609:A102, January 2018. doi: 10.1051/0004-6361/201731592.

J. C. Roediger and S. Courteau. On the uncertainties of stellar mass estimates via colour measurements. *MNRAS*, 452(3):3209–3225, September 2015. doi: 10.1093/mnras/stv1499.

A. J. Romanowsky and S. M. Fall. Angular Momentum and Galaxy Formation Revisited. *ApJS*, 203(2):17, December 2012. doi: 10.1088/0067-0049/203/2/17.

R. P. Saglia, P. Sánchez-Blázquez, R. Bender, et al. The fundamental plane of EDisCS galaxies. The effect of size evolution. *A&A*, 524:A6, December 2010. doi: 10.1051/0004-6361/201014703.

R. P. Saglia, M. Opitsch, P. Erwin, et al. The SINFONI Black Hole Survey: The Black Hole Fundamental Plane Revisited and the Paths of (Co)evolution of Supermassive Black Holes and Bulges. *ApJ*, 818(1):47, Feb 2016. doi: 10.3847/0004-637X/818/1/47.

A. Saintonge and K. Spekkens. Disk Galaxy Scaling Relations in the SFI++: Intrinsic Scatter and Applications. *ApJ*, 726(2):77, January 2011. doi: 10.1088/0004-637X/726/2/77.

S. Salim. Green Valley Galaxies. *Serbian Astronomical Journal*, 189:1–14, December 2014. doi: 10.2298/SAJ1489001S.

S. F. Sánchez, E. Pérez, P. Sánchez-Blázquez, et al. Pipe3D, a pipeline to analyze Integral Field Spectroscopy Data: I. New fitting philosophy of FIT3D. *Rev. Mex. Astron. Astrofis.*, 52:21–53, April 2016.

S. F. Sánchez, V. Avila-Reese, H. Hernandez-Toledo, et al. SDSS IV MaNGA - Properties of AGN Host Galaxies. *Rev. Mex. Astron. Astrofis.*, 54:217–260, Apr 2018.

J. Sánchez Almeida. Analysis of the galaxy size versus stellar mass relation. *MNRAS*, 495(1):78–89, April 2020. doi: 10.1093/mnras/staa1108.

L. Sánchez-Menguiano, J. Sánchez Almeida, C. Muñoz-Tuñón, and S. F. Sánchez. Local and Global Gas Metallicity versus Stellar Age Relation in MaNGA Galaxies. *ApJ*, 903(1):52, November 2020. doi: 10.3847/1538-4357/abba7c.

D. J. Sand, A. Seth, E. W. Olszewski, et al. A Deeper Look at Leo IV: Star Formation History and Extended Structure. *ApJ*, 718(1):530–542, July 2010. doi: 10.1088/0004-637X/718/1/530.

P. Santini, A. Fontana, M. Castellano, et al. The Star Formation Main Sequence in the Hubble Space Telescope Frontier Fields. *ApJ*, 847:76, September 2017. doi: 10.3847/1538-4357/aa8874.

I. M. Santos-Santos, A. Di Cintio, C. B. Brook, et al. NIHAO - XIV. Reproducing the observed diversity of dwarf galaxy rotation curve shapes in ΛCDM. *MNRAS*, 473(4):4392–4403, February 2018. doi: 10.1093/mnras/stx2660.

T. Sawala, Q. Guo, C. Scannapieco, A. Jenkins, and S. White. What is the (dark) matter with dwarf galaxies? *MNRAS*, 413(1):659–668, May 2011. doi: 10.1111/j.1365-2966.2010.18163.x.

T. Sawala, C. Scannapieco, and S. White. Local Group dwarf galaxies: nature and nurture. *MNRAS*, 420(2):1714–1730, February 2012. doi: 10.1111/j.1365-2966.2011.20181.x.

T. Sawala, C. S. Frenk, A. Fattahi, et al. The APOSTLE simulations: solutions to the Local Group's cosmic puzzles. *MNRAS*, 457(2):1931–1943, April 2016. doi: 10.1093/mnras/stw145.

K. Schawinski, C. M. Urry, B. D. Simmons, et al. The green valley is a red herring: Galaxy Zoo reveals two evolutionary pathways towards quenching of star formation in early- and late-type galaxies. *MNRAS*, 440(1):889–907, May 2014. doi: 10.1093/mnras/stu327.

J. Schaye, R. A. Crain, R. G. Bower, et al. The EAGLE project: simulating the evolution and assembly of galaxies and their environments. *MNRAS*, 446(1):521–554, January 2015. doi: 10.1093/mnras/stu2058.

P. Schechter. An analytic expression for the luminosity function for galaxies. *ApJ*, 203:297–306, January 1976. doi: 10.1086/154079.

D. J. Schlegel, D. P. Finkbeiner, and M. Davis. Maps of Dust Infrared Emission for Use in Estimation of Reddening and Cosmic Microwave Background Radiation Foregrounds. *ApJ*, 500(2):525–553, June 1998. doi: 10.1086/305772.

N. Scott, A. W. Graham, and J. Schombert. The Supermassive Black Hole Mass-Spheroid Stellar Mass Relation for Sérsic and Core-Sérsic Galaxies. *ApJ*, 768:76, May 2013. doi: 10.1088/0004-637X/768/1/76.

J. A. Sellwood and K. L. Masters. Spirals in galaxies. *arXiv e-prints*, art. arXiv:2110.05615, October 2021.

J. A. Sellwood, K. Spekkens, and C. S. Eckel. Uncertainties in galaxy rotation curves. *MNRAS*, 502(3):3843–3854, April 2021. doi: 10.1093/mnras/stab009.

S. Shalev-Shwartz and S. Ben-David. *Understanding machine learning: From theory to algorithms*. Cambridge university press, 2014.

F. Shankar, M. Bernardi, R. K. Sheth, et al. Selection bias in dynamically measured supermassive black hole samples: its consequences and the quest for the most fundamental relation. *MNRAS*, 460(3):3119–3142, Aug 2016. doi: 10.1093/mnras/stw678.

S. Shen, J. Wadsley, and G. Stinson. The enrichment of the intergalactic medium with adiabatic feedback - I. Metal cooling and metal diffusion. *MNRAS*, 407(3): 1581–1596, September 2010. doi: 10.1111/j.1365-2966.2010.17047.x.

S. Shen, H. J. Mo, S. D. M. White, et al. The size distribution of galaxies in the Sloan Digital Sky Survey. *MNRAS*, 343(3):978–994, August 2003. doi: 10.1046/j.1365-8711.2003.06740.x.

J. Silk and G. A. Mamon. The current status of galaxy formation. *Research in Astronomy and Astrophysics*, 12:917–946, Aug 2012. doi: 10.1088/1674-4527/12/8/004.

J. D. Simon, T. M. Brown, A. Drlica-Wagner, et al. Eridanus II: A Fossil from Reionization with an Off-center Star Cluster. *ApJ*, 908(1):18, February 2021. doi: 10.3847/1538-4357/abd31b.

R. A. Skibba, F. C. van den Bosch, X. Yang, et al. Are brightest halo galaxies central galaxies? *MNRAS*, 410:417–431, Jan 2011. doi: 10.1111/j.1365-2966.2010.17452.x.

M. J. Smith, N. Arora, C. Stone, S. Courteau, and J. E. Geach. Pix2Prof: fast extraction of sequential information from galaxy imagery via a deep natural language 'captioning' model. *MNRAS*, 503(1):96–105, May 2021. doi: 10.1093/mnras/stab424.

Y. Sofue. Dark halos of M 31 and the Milky Way. *PASJ*, 67(4):75, August 2015. doi: 10.1093/pasj/psv042.

R. S. Somerville and R. Davé. Physical Models of Galaxy Formation in a Cosmological Framework. *ARA&A*, 53:51–113, Aug 2015. doi: 10.1146/annurev-astro-082812-140951.

R. S. Somerville, J. R. Primack, and S. M. Faber. The nature of high-redshift galaxies. *MNRAS*, 320:504–528, February 2001. doi: 10.1046/j.1365-8711.2001.03975.x.

R. S. Somerville, P. F. Hopkins, T. J. Cox, B. E. Robertson, and L. Hernquist. A semi-analytic model for the co-evolution of galaxies, black holes and active galactic nuclei. *MNRAS*, 391(2):481–506, Dec 2008. doi: 10.1111/j.1365-2966.2008.13805.x.

J. G. Sorce. Minimization of biases in galaxy peculiar velocity catalogues. *MNRAS*, 450(3):2644–2657, July 2015. doi: 10.1093/mnras/stv760.

J. G. Sorce. Galaxy clusters in local Universe simulations without density constraints: a long uphill struggle. *MNRAS*, 478(4):5199–5208, August 2018. doi: 10.1093/mnras/sty1631.

J. G. Sorce and Q. Guo. The baryonic Tully-Fisher relation cares about the galaxy sample. *MNRAS*, 458(3):2667–2675, May 2016. doi: 10.1093/mnras/stw341.

J. G. Sorce, H. M. Courtois, K. Sheth, and R. B. Tully. Bimodality of galaxy disc central surface brightness distribution in the Spitzer 3.6 μm band. *MNRAS*, 433 (1):751–758, July 2013. doi: 10.1093/mnras/stt768.

J. G. Sorce, H. M. Courtois, S. Gottlöber, Y. Hoffman, and R. B. Tully. Simulations of the Local Universe constrained by observational peculiar velocities. *MNRAS*, 437(4):3586–3595, February 2014. doi: 10.1093/mnras/stt2153.

J. G. Sorce, S. Gottlöber, G. Yepes, et al. Cosmicflows Constrained Local UniversE Simulations. *MNRAS*, 455(2):2078–2090, January 2016. doi: 10.1093/mnras/stv2407.

K. Spekkens, N. Urbancic, B. S. Mason, B. Willman, and J. E. Aguirre. The Dearth of Neutral Hydrogen in Galactic Dwarf Spheroidal Galaxies. *ApJ*, 795(1):L5, November 2014. doi: 10.1088/2041-8205/795/1/L5.

D. N. Spergel, L. Verde, H. V. Peiris, et al. First-Year Wilkinson Microwave

Anisotropy Probe (WMAP) Observations: Determination of Cosmological Parameters. *The Astrophysical Journal Supplement Series*, 148:175–194, September 2003. doi: 10.1086/377226.

V. Springel, J. Wang, M. Vogelsberger, et al. The Aquarius Project: the subhaloes of galactic haloes. *MNRAS*, 391(4):1685–1711, December 2008. doi: 10.1111/j.1365-2966.2008.14066.x.

V. Springel. The cosmological simulation code GADGET-2. *MNRAS*, 364(4):1105–1134, Dec 2005. doi: 10.1111/j.1365-2966.2005.09655.x.

V. Springel, S. D. M. White, A. Jenkins, et al. Simulations of the formation, evolution and clustering of galaxies and quasars. *Nature*, 435:629–636, June 2005. doi: 10.1038/nature03597.

C. M. Springob, M. P. Haynes, R. Giovanelli, and B. R. Kent. A Digital Archive of H I 21 Centimeter Line Spectra of Optically Targeted Galaxies. *ApJS*, 160(1):149–162, September 2005. doi: 10.1086/431550.

C. M. Springob, K. L. Masters, M. P. Haynes, R. Giovanelli, and C. Marinoni. SFI++. II. A New I-Band Tully-Fisher Catalog, Derivation of Peculiar Velocities, and Data Set Properties. *ApJS*, 172(2):599–614, October 2007. doi: 10.1086/519527.

D. V. Stark, S. S. McGaugh, and R. A. Swaters. A First Attempt to Calibrate the Baryonic Tully-Fisher Relation with Gas-Dominated Galaxies. *AJ*, 138:392–401, August 2009. doi: 10.1088/0004-6256/138/2/392.

T. K. Starkenburg, S. Tonnesen, and C. Kopenhafer. What Is Inside Matters: Simulated Green Valley Galaxies Have too Centrally Concentrated Star Formation. *ApJ*, 874(2):L17, April 2019. doi: 10.3847/2041-8213/ab0f34.

M. Steinmetz and J. F. Navarro. The Cosmological Origin of the Tully-Fisher Relation. *ApJ*, 513(2):555–560, March 1999. doi: 10.1086/306904.

G. S. Stinson, C. Brook, A. V. Macciò, et al. Making Galaxies In a Cosmological Context: the need for early stellar feedback. *MNRAS*, 428(1):129–140, January 2013. doi: 10.1093/mnras/sts028.

G. Stinson, A. Seth, N. Katz, et al. Star formation and feedback in smoothed particle hydrodynamic simulations - I. Isolated galaxies. *MNRAS*, 373(3):1074–1090, December 2006. doi: 10.1111/j.1365-2966.2006.11097.x.

C. Stone and S. Courteau. The Intrinsic Scatter of the Radial Acceleration Relation. *ApJ*, 882(1):6, September 2019. doi: 10.3847/1538-4357/ab3126.

C. Stone, S. Courteau, and N. Arora. The Intrinsic Scatter of Galaxy Scaling Relations. *ApJ*, 912(1):41, May 2021a. doi: 10.3847/1538-4357/abebe4.

C. J. Stone, N. Arora, S. Courteau, and J.-C. Cuillandre. AutoProf - I. An automated non-parametric light profile pipeline for modern galaxy surveys. *MNRAS*, 508(2): 1870–1887, December 2021b. doi: 10.1093/mnras/stab2709.

M. A. Strauss and J. A. Willick. The density and peculiar velocity fields of nearby galaxies. *Phys. Rep.*, 261:271–431, January 1995. doi: 10.1016/0370-1573(95)00013-7.

K.-Y. Su, P. F. Hopkins, C. C. Hayward, et al. Feedback first: the surprisingly weak effects of magnetic fields, viscosity, conduction and metal diffusion on sub-L* galaxy formation. *MNRAS*, 471(1):144–166, October 2017. doi: 10.1093/mnras/stx1463.

E. N. Taylor, A. M. Hopkins, I. K. Baldry, et al. Galaxy And Mass Assembly (GAMA): stellar mass estimates. *MNRAS*, 418(3):1587–1620, December 2011. doi: 10.1111/j.1365-2966.2011.19536.x.

D. Thomas, C. Maraston, R. Bender, and C. Mendes de Oliveira. The Epochs of Early-Type Galaxy Formation as a Function of Environment. *ApJ*, 621(2):673–694, March 2005. doi: 10.1086/426932.

P. Torrey, G. F. Snyder, M. Vogelsberger, et al. Synthetic galaxy images and spectra from the Illustris simulation. *MNRAS*, 447(3):2753–2771, March 2015. doi: 10.1093/mnras/stu2592.

S. Tremaine, K. Gebhardt, R. Bender, et al. The Slope of the Black Hole Mass versus Velocity Dispersion Correlation. *ApJ*, 574(2):740–753, Aug 2002. doi: 10.1086/341002.

C. A. Tremonti, T. M. Heckman, G. Kauffmann, et al. The Origin of the Mass-Metallicity Relation: Insights from 53,000 Star- forming Galaxies in the Sloan Digital Sky Survey. *ApJ*, 613:898–913, October 2004. doi: 10.1086/423264.

I. Trujillo, A. W. Graham, and N. Caon. On the estimation of galaxy structural parameters: the Sérsic model. *MNRAS*, 326(3):869–876, September 2001. doi: 10.1046/j.1365-8711.2001.04471.x.

I. Trujillo, N. Chamba, and J. H. Knapen. A physically motivated definition for the size of galaxies in an era of ultradeep imaging. *MNRAS*, 493(1):87–105, March 2020. doi: 10.1093/mnras/staa236.

S. Trujillo-Gomez, A. Klypin, J. Primack, and A. J. Romanowsky. Galaxies in ΛCDM with Halo Abundance Matching: Luminosity-Velocity Relation, Baryonic Mass-Velocity Relation, Velocity Function, and Clustering. *ApJ*, 742(1):16, November 2011. doi: 10.1088/0004-637X/742/1/16.

D. Tuccillo, M. Huertas-Company, E. Decencière, et al. Deep learning for galaxy surface brightness profile fitting. *MNRAS*, 475(1):894–909, March 2018. doi: 10.1093/mnras/stx3186.

R. B. Tully and J. R. Fisher. Reprint of 1977A&A....54..661T. A new method of determining distance to galaxies. *A&A*, 500:105–117, February 1977a.

R. B. Tully and J. R. Fisher. A new method of determining distances to galaxies. *A&A*, 54:661–673, February 1977b.

R. B. Tully and M. A. W. Verheijen. The Ursa Major Cluster of Galaxies. II. Bimodality of the Distribution of Central Surface Brightnesses. *ApJ*, 484(1):145–162, July 1997. doi: 10.1086/304318.

R. B. Tully, M. J. Pierce, J.-S. Huang, et al. Global Extinction in Spiral Galaxies. *AJ*, 115(6):2264–2272, June 1998. doi: 10.1086/300379.

R. B. Tully, H. M. Courtois, A. E. Dolphin, et al. Cosmicflows-2: The Data. *AJ*, 146 (4):86, October 2013. doi: 10.1088/0004-6256/146/4/86.

M. P. van Daalen and M. White. A cross-correlation-based estimate of the galaxy luminosity function. *ArXiv e-prints*, March 2017.

J. van de Sande, C. D. P. Lagos, C. Welker, et al. The SAMI Galaxy Survey: comparing 3D spectroscopic observations with galaxies from cosmological hydrodynamical simulations. *MNRAS*, 484(1):869–891, March 2019. doi: 10.1093/mnras/sty3506.

P. Virtanen, R. Gommers, T. E. Oliphant, et al. SciPy 1.0: Fundamental Algorithms for Scientific Computing in Python. *Nature Methods*, 17:261–272, 2020. doi: 10.1038/s41592-019-0686-2.

M. Vogelsberger, F. Marinacci, P. Torrey, and E. Puchwein. Cosmological simulations of galaxy formation. *Nature Reviews Physics*, 2(1):42–66, January 2020. doi: 10.1038/s42254-019-0127-2.

J. W. Wadsley, G. Veeravalli, and H. M. P. Couchman. On the treatment of entropy mixing in numerical cosmology. *MNRAS*, 387(1):427–438, June 2008. doi: 10.1111/j.1365-2966.2008.13260.x.

J. W. Wadsley, B. W. Keller, and T. R. Quinn. Gasoline2: a modern smoothed particle hydrodynamics code. *MNRAS*, 471(2):2357–2369, October 2017. doi: 10.1093/mnras/stx1643.

D. A. Wake, K. Bundy, A. M. Diamond-Stanic, et al. The SDSS-IV MaNGA Sample: Design, Optimization, and Usage Considerations. *AJ*, 154(3):86, September 2017. doi: 10.3847/1538-3881/aa7ecc.

C. J. Walcher, L. Wisotzki, S. Bekeraité, et al. CALIFA: a diameter-selected sample

for an integral field spectroscopy galaxy survey. *A&A*, 569:A1, September 2014. doi: 10.1051/0004-6361/201424198.

L. Wang, A. A. Dutton, G. S. Stinson, et al. NIHAO project - I. Reproducing the inefficiency of galaxy formation across cosmic time with a large sample of cosmological hydrodynamical simulations. *MNRAS*, 454(1):83–94, November 2015. doi: 10.1093/mnras/stv1937.

W. Wang, S. M. Faber, F. S. Liu, et al. UVI colour gradients of 0.4 ¡ z ¡ 1.4 star-forming main-sequence galaxies in CANDELS: dust extinction and star formation profiles. *MNRAS*, 469(4):4063–4082, August 2017. doi: 10.1093/mnras/stx1148.

A. K. Weigel, K. Schawinski, and C. Bruderer. Stellar mass functions: methods, systematics and results for the local Universe. *MNRAS*, 459(2):2150–2187, June 2016. doi: 10.1093/mnras/stw756.

S. M. Weinmann, A. Pasquali, B. D. Oppenheimer, et al. A fundamental problem in our understanding of low-mass galaxy evolution. *MNRAS*, 426(4):2797–2812, November 2012. doi: 10.1111/j.1365-2966.2012.21931.x.

D. R. Weisz, A. E. Dolphin, E. D. Skillman, et al. The Star Formation Histories of Local Group Dwarf Galaxies. II. Searching For Signatures of Reionization. *ApJ*, 789(2):148, July 2014. doi: 10.1088/0004-637X/789/2/148.

K. B. Westfall, M. Cappellari, M. A. Bershady, et al. The Data Analysis Pipeline for the SDSS-IV MaNGA IFU Galaxy Survey: Overview. *AJ*, 158(6):231, December 2019. doi: 10.3847/1538-3881/ab44a2.

K. E. Whitaker, P. G. van Dokkum, G. Brammer, and M. Franx. The Star Formation Mass Sequence Out to z = 2.5. *ApJ*, 754(2):L29, August 2012. doi: 10.1088/2041-8205/754/2/L29.

K. E. Whitaker, R. Bezanson, P. G. van Dokkum, et al. Predicting Quiescence: The Dependence of Specific Star Formation Rate on Galaxy Size and Central Density at 0.5 < z < 2.5. *ApJ*, 838(1):19, Mar 2017. doi: 10.3847/1538-4357/aa6258.

S. D. M. White and M. J. Rees. Core condensation in heavy halos: a two-stage theory for galaxy formation and clustering. *MNRAS*, 183:341–358, May 1978. doi: 10.1093/mnras/183.3.341.

S. D. M. White and C. S. Frenk. Galaxy Formation through Hierarchical Clustering. *ApJ*, 379:52, September 1991. doi: 10.1086/170483.

D. Williamson, H. Martel, and A. B. Romeo. Chemodynamic Evolution of Dwarf Galaxies in Tidal Fields. *ApJ*, 831(1):1, November 2016. doi: 10.3847/0004-637X/831/1/1.

D. J. Wilman, S. Zibetti, and T. Budavári. A multiscale approach to environment and its influence on the colour distribution of galaxies. *MNRAS*, 406(3):1701–1720, August 2010. doi: 10.1111/j.1365-2966.2010.16845.x.

J. Woo and S. L. Ellison. Two growing modes and the morphology-quiescence relation in isolated galaxies. *MNRAS*, 487(2):1927–1945, August 2019. doi: 10.1093/mnras/stz1377.

J. Woo, S. Courteau, and A. Dekel. Scaling relations and the fundamental line of

the local group dwarf galaxies. *MNRAS*, 390(4):1453–1469, November 2008. doi: 10.1111/j.1365-2966.2008.13770.x.

P. Woods. Feedback gets a stellar review. *Nature Astronomy*, 6:413–413, April 2022. doi: 10.1038/s41550-022-01672-5.

E. L. Wright, P. R. M. Eisenhardt, A. K. Mainzer, et al. The Wide-field Infrared Survey Explorer (WISE): Mission Description and Initial On-orbit Performance. *AJ*, 140(6):1868–1881, December 2010. doi: 10.1088/0004-6256/140/6/1868.

S. Wuyts, N. M. Förster Schreiber, E. J. Nelson, et al. A CANDELS-3D-HST synergy: Resolved Star Formation Patterns at 0.7 ¡ z ¡ 1.5. *ApJ*, 779(2):135, December 2013. doi: 10.1088/0004-637X/779/2/135.

X. Yang, H. J. Mo, and F. C. van den Bosch. Galaxy Groups in the SDSS DR4. II. Halo Occupation Statistics. *ApJ*, 676(1):248–261, Mar 2008. doi: 10.1086/528954.

J. Yin, J. L. Hou, N. Prantzos, et al. Milky Way versus Andromeda: a tale of two disks. *A&A*, 505(2):497–508, October 2009. doi: 10.1051/0004-6361/200912316.

D. G. York, J. Adelman, J. Anderson, John E., et al. The Sloan Digital Sky Survey: Technical Summary. *AJ*, 120(3):1579–1587, September 2000. doi: 10.1086/301513.

S. Zaroubi, Y. Hoffman, K. B. Fisher, and O. Lahav. Wiener Reconstruction of the Large-Scale Structure. *ApJ*, 449:446, August 1995. doi: 10.1086/176070.

H.-X. Zhang, T. H. Puzia, and D. R. Weisz. The Impact of Star Formation Histories on Stellar Mass Estimation: Implications from the Local Group Dwarf Galaxies. *ApJS*, 233(1):13, November 2017. doi: 10.3847/1538-4365/aa937b.

Y. Zheng, V. Wild, N. Lahén, et al. Comparison of stellar populations in simulated and real post-starburst galaxies in MaNGA. *MNRAS*, 498(1):1259–1277, August 2020. doi: 10.1093/mnras/staa2358.